JOURNAL OF THE

AERO/SPACE SCIENCES

VOLUME 27 MAY, 1960 NUMBER 5

MECHANICAL ENGINEERING
MAY 1960
LIBRARY

CONTENTS

Measurements of Skin Friction of the Compressible Turbulent Boundary Layer on a Cone With Foreign Gas Injection ..... CONSTANTINE C. PAPPAS AND ARTHUR F. OKUNO 321

Magnetohydrodynamic Effects on the Formation of Couette Flow ..... L. N. TAO 334

On the Estimation of Structural Damping From Aircraft Resonance Tests ..... RONALD D. MILNE 339

Foucault Pendulum Effect in a Schuler-Tuned System ..... CHARLES BROXMEYER 343

Sweepback Effects in Turbulent Boundary-Layer Shock-Wave Interaction ..... R. J. STALLER 348

On the Use of Normal Coordinates for the Solution of Lumped Parameter Transient Heat-Transfer Problems ..... M. E. GURTIN 357

An Approximate Solution of the Direct Supersonic Blunt-Body Problem for Arbitrary Axisymmetric Shapes ..... STEPHEN C. TRAUGOTT 361

On the Bernoulli-Euler Beam Theory With Random Excitation ..... J. L. BOGDANOFF AND J. E. GOLDBERG 371

Ablation of Reinforced Plastics in Supersonic Flow ..... GEORGE W. SUTTON 377

Readers' Forum 386

PURDUE UNIVERSITY
LIBRARY

Published by
INSTITUTE OF THE AERONAUTICAL SCIENCES, INC.

JOURNAL OF THE AERO/SPACE SCIENCES

Editor: W. R. SEARS
Director, Graduate School of Aeronautical Engineering, Cornell University

Associate Editor: ROBERT R. DEXTER *Managing Editor:* RITA J. TURINO

Editorial Assistant: CAROLINE TAYLOR

Editorial Committee

Aerodynamics and Fluid Mechanics

H. Julian Allen
Holt Ashley
Dean R. Chapman
Francis H. Clauser
Hugh L. Dryden
John C. Evvard
Antonio Ferri
Alexander Flax
Wallace D. Hayes
R. T. Jones
Carl Kaplan
H. W. Liepmann
C. C. Lin
H. F. Ludloff
Harold Luskin
Clark B. Millikan
Henry T. Nagamatsu
H. J. E. Reid
George S. Schairer
G. B. Schubauer
John Stack
Theodore Theodorsen
Arthur N. Tifford
Th. von Kármán

Flight Testing

R. R. Gilruth
Melvin N. Gough
W. L. Howland
W. F. Milliken, Jr.

Rotating Wing Aircraft

F. B. Gustafson
K. H. Hohenemser
Bartram Kelley
R. B. Maloy
Ralph McClarren
R. H. Miller
R. H. Prewitt
Igor I. Sikorsky

Structures

John E. Duberg
R. R. Heldenfels
N. J. Hoff
Samuel Levy
J. F. McBrearty
W. Ramberg
E. E. Sechler
F. R. Shanley
C. R. Strang
S. Timoshenko

Vibration and Flutter

Lee Arnold
M. A. Biot
R. L. Bisplinghoff
Harold A. Cheilek
I. E. Garrick
Martin Goland

Aircraft Design

W. E. Beall
E. H. Heinemann
Hall L. Hibbard
Richard Hutton
C. L. Johnson
A. A. Kartveli
F. K. Teichmann

Electronics

K. C. Black
M. V. Kiebert, Jr.
David S. Little
Paul Rosenberg
Giles J. Strickroth

Physiologic Problems

H. G. Armstrong
Louis H. Bauer
Robert J. Benford
W. Randolph Lovelace, II
Ross A. MacFarland

Flight Propulsion

William Bollay
George W. Brady
R. P. Kroon
Frank E. Marble
Abe Silverstein
E. S. Taylor

Instruments

Alan G. Binnie
Charles H. Colvin
Frank R. Cook
C. S. Draper
S. G. Eskin
C. F. Savage
R. C. Sylvander

SUBSCRIPTION RATES

JOURNAL OF THE AERO/SPACE SCIENCES (formerly Journal of the Aeronautical Sciences), Published Monthly. United States and Possessions: 1 Year, $15.00; Single Copies, $1.50. Foreign Countries Including Canada (American Currency Rates): 1 Year, $16.00; Single Copies, $1.50.

AERO/SPACE ENGINEERING, Published Monthly. United States and Possessions: 1 Year, $5.00; Single Copies, $0.50. Foreign Countries Including Canada (American Currency Rates): 1 Year, $6.00; Single Copies, $0.50.

Notices of change of address should be sent to the Institute at least 30 days prior to actual change of address.

Manuscripts for publication, proofs, and all correspondence should be addressed to the Editorial Office of the JOURNAL.

Publication Office, 20th and Northampton Sts., Easton, Pa. Correspondence regarding subscriptions may be addressed to the Editorial Office of the JOURNAL OF THE AERO/SPACE SCIENCES, 2 East 64th Street, New York 21, N.Y.

© *Copyright, 1960, by the Institute of the Aeronautical Sciences, Inc.*

Second-Class Mail Privileges Authorized at Easton, Pa. Acceptance for mailing at a special rate of postage provided for in Section 1103, Act of October 3, 1917, authorized April 29, 1937.

JOURNAL OF THE AERO/SPACE SCIENCES

VOLUME 27 MAY, 1960 NUMBER 5

Measurements of Skin Friction of the Compressible Turbulent Boundary Layer on a Cone With Foreign Gas Injection†

CONSTANTINE C. PAPPAS* AND ARTHUR F. OKUNO*

Ames Research Center, NASA

Summary

Measurements of average skin friction of the turbulent boundary layer have been made on a 15° total included angle cone with foreign gas injection. Measurements of total skin-friction drag were obtained at free-stream Mach numbers of 0.3, 0.7, 3.5, and 4.7 and within a Reynolds number range from 0.9×10^6 to 5.9×10^6 with injection of helium, air, and Freon-12 (CCl_2F_2) through the porous wall. Substantial reductions in skin friction are realized with gas injection within the range of Mach numbers of this test. The relative reduction in skin friction is in accordance with theory—that is, the light gases are most effective when compared on a mass flow basis. There is a marked effect of Mach number on the reduction of average skin friction; this effect is not shown by the available theories. Limited transition location measurements indicate that the boundary layer does not fully trip with gas injection but that the transition point approaches a forward limit with increasing injection. The variation of the skin-friction coefficient, for the lower injection rates with natural transition, is dependent on the flow Reynolds number and type of injected gas; and at the high injection rates the skin friction is in fair agreement with the turbulent boundary-layer results.

Symbols

A_p = area of porous surface
A_c = total wetted area of cone
C_F = average skin-friction coefficient, (total friction force/qA_c)
c_f = local skin-friction coefficient, (local shear stress/q)
F = dimensionless injection mass flow rate normal to surface, $\rho_w v_w/\rho_c u_c$ for supersonic flow, $\rho_w v_w/\rho_\infty u_\infty$ for subsonic flow
M = Mach number
M_c = cone Mach number, inviscid cone surface value for supersonic flow, free-stream value for subsonic flow
P_c = static pressure on cone
P_t = total pressure
q = dynamic pressure, $(1/2)\rho u^2$
R_c = Reynolds number of cone, $u_c \rho_c x_c/\mu_c$ for supersonic flow, $u_\infty \rho_\infty x_c/\mu_\infty$ for subsonic flow
R_x = Reynolds number of flat plate, $u_\infty \rho_\infty x/\mu_\infty$
T = absolute temperature
T' = reference temperature used in Eq. (1)
u = velocity component parallel to surface in stream direction
v = velocity component normal to the surface
x = coordinate parallel to surface in stream direction
η_r = recovery factor
μ = viscosity of gas
ρ = mass density of gas

Subscripts

c = cone condition
i = incompressible flow condition
0 = zero injection condition
r = adiabatic wall condition
w = condition at surface
∞ = free-stream condition

Introduction

POSSIBLE APPLICATION of transpiration cooling and ablation cooling techniques to the forward areas of high-speed aircraft and missiles has stimulated research to ascertain the effectiveness of these cooling methods. The injection gases (from transpiration or ablation systems) affect the boundary layer in two related ways: the amount of heat which can reach the

† An abbreviated version of this paper was presented at the Aerodynamics—I Session, IAS 27th Annual Meeting, N.Y., Jan. 26–29, 1959, and was published as IAS Report 59-78, entitled, "Effect of Injection of Foreign Gases on the Skin Friction and Heat Transfer of the Turbulent Boundary Layer," by Constantine C. Pappas. Revised and received December 18, 1959.

* Aeronautical Research Scientist.

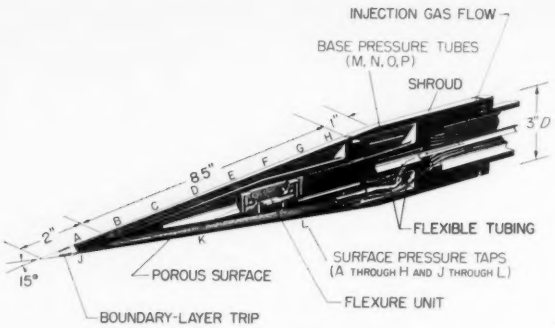

FIG. 1. Cone skin-friction model.

surface is reduced, and the skin friction of the boundary layer is lessened. The objective in this series of tests was to determine the quantitative effect of injection of the foreign gases, helium, air, and Freon-12 (CCl_2F_2), on the total skin friction of the compressible turbulent boundary layer. These gases were chosen to be representative of possible application. Helium represents the light gas injection, air is used as a convenient gas and as a check of some theories which have evaluated the effect of air injection on the compressible turbulent boundary layer, and Freon-12 is similar to some heavy gases which may emanate from ablating plastic materials.

To date, skin-friction measurements for the turbulent boundary layer with only air injection are available. Mickley and Davis[1] have measured local friction on a flat plate with constant mass addition along the wall by the momentum decrement method over a Reynolds number range of 0.04×10^6 to 3×10^6 and at free-stream velocities up to 60 ft. per sec. Hacker[2] measured local skin friction on a flat plate with constant mass addition with a modified Stanton tube at free-stream velocities up to 150 ft. per sec. A marked decrease in local skin friction is indicated with an increase in air injection in the two experiments and general agreement is obtained at the lower injection rates, but there is some disagreement as to the value of the injection parameter, $2F/c_{f_0} = F/0.0289\ R_x^{-1/5}$, at which separation occurs on a flat plate. Hacker gives the value 2.8, but the data of Mickley and Davis indicate no separation for $2F/c_{f_0}$ values up to 5.1.

In supersonic flow, the available skin-friction measurements are again limited to air injection. Tendeland and Okuno[3] obtained the total skin friction on a cone frustum at a cone Mach number of 2.55 by force measurements. Some preliminary measurements of local skin friction obtained on a flat plate at $M = 2.7$ have been reported by Rubesin in reference 4. The data from both sources are in agreement and indicate a sizable reduction in skin friction with air injection. A comparison of the relative reduction in skin friction, C_F/C_{F_0}, for given rates of injection, $2F/C_{F_0}$, at low speeds and at Mach number 2.55 indicates a sizable Mach number effect. The theories of Rubesin[5] and of Dorrance and Dore[6] predict a small effect of Mach number on the relative reduction of skin friction, $C_F \div C_{F_0}$, of the turbulent boundary layer with given rates of air injection $2F/C_{F_0}$.

The present tests were proposed to determine the effect of Mach number on the relative reduction of skin friction with injection of helium, air, and Freon-12.

Description of Equipment

Wind Tunnels

The tests were conducted in the Ames 2 by 2 ft. transonic wind tunnel and in the Ames 10 in. heat-transfer wind tunnel. Pertinent details of these tunnels may be found in references 7 and 8, respectively.

Cone Model

The skin-friction model is shown in Fig. 1. Important dimensions are indicated on the sketch. The model surface was made from three conical segments, each molded from a mat of glass fibers treated with uncured phenolic resin (e.g., see reference 9). Additional phenolic resin was sprayed on the outer surface of the mat to provide a more abrasion-resistant outer surface. These mats were molded into the conical segments and cured in a furnace. The density of the resulting material is about 35 lbs./cu.ft. The three conical segments were trimmed and glued together, and finally glued to the stainless steel nose piece and base mounting ring to form the completed cone. Of a total cone surface of 0.313 sq. ft., 0.284 sq. ft. was porous. The total external conical surface, 0.313 sq. ft., was used in the calculations of the unit injection flow rate, $\rho_w v_w$. The actual unit flow rate is somewhat higher but extends over only the porous area.

The model was instrumented to provide a force balance from which the skin friction was calculated. Eleven pressure taps, of 0.020-in. orifice diameter, were installed to measure the external pressure force on the cone. They were located on two cone rays 180° apart at the positions indicated in Fig. 1. The pressure taps were connected from the base of the porous cone to the cone support through flexible plastic lines.

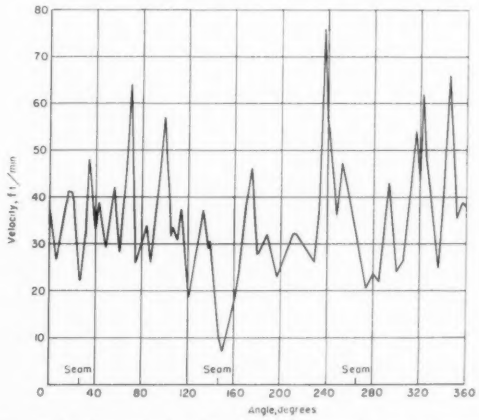

FIG. 2. Injection velocity distribution around cone at constant distance from surface.

Four base pressure orifice tubes with open ends pointing forward were located within the shroud area to measure the base force acting on the model. The porous cone was attached to the base support through a strain-gage instrumented flexure unit. A small gap around the conical surface, 0.004 to 0.006 in. wide, separated the porous cone model from the shroud.

The injection gases were introduced into the porous cone through four flexible tubes, one of which is shown in Fig. 1. The gases were admitted into the flexible tubes at an angle of $82^1/_2°$ to the cone axis in order to minimize the forces on the porous cone due to changes in momentum of the injection gas. The gas emanates from the porous surface on the average at $82^1/_2°$ to the cone axis. It was necessary, however, to correct the strain-gage readings to account for momentum and tube forces (or injection force) at the various tunnel static pressure levels.

The strain-gage unit was mounted on two parallel flexures. One side of the flexures supported the porous cone; the other side was mounted to the stationary cone support. Stops were inserted to limit the flexure travel to prevent damage to the strain-gage elements during start-up and shut-down of the wind tunnels. The whole strain-gage assembly and support pieces were made from 17 PH stainless steel to minimize any differential expansion problems arising from possible variations in temperature level of the structure. Also, the strain-gage elements were temperature compensated to minimize errors due to temperature level.

A boundary-layer trip, 15/16 in. long, made from 2/0 garnet paper with most of the backing removed was used for tests at a free-stream Mach number of 3.5. A double trip made from two 1/2-in. bands of 2/0 garnet paper separated by 1/16 in. was used for the free-stream Mach number 4.7 tests and for the subsonic tests at Mach numbers 0.3 and 0.7. The front end of the trips was located about 1/4 in. back from the cone tip. For the supersonic wind-tunnel tests various trips were tried until the flow appeared to be fully turbulent in the shadowgraph pictures for all test Reynolds numbers. A plot of zero injection skin-friction coefficient versus Reynolds number was also used to substantiate that the flow was turbulent. For

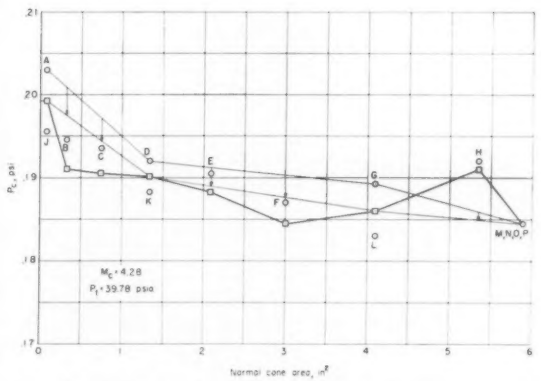

FIG. 3. Weighting method for surface pressures.

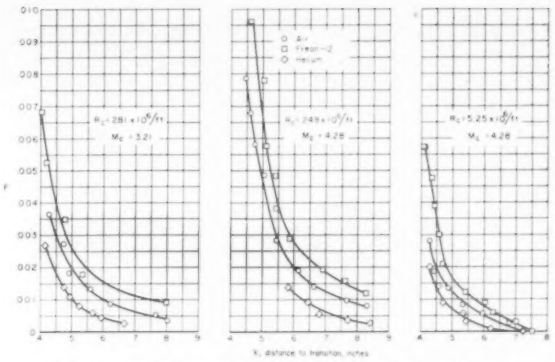

FIG. 4. Variation of transition point with injection.

the subsonic tests the double trip was used to ensure a turbulent boundary layer since the background "hash" of the shadowgraph pictures prevented visualization of boundary-layer turbulence. For some natural transition tests the trip was removed.

It is known that skin friction is affected by surface roughness. Any porous surface when viewed on a large enough scale can not be considered as smooth, but the porous fibrous glass surface when new was aerodynamically smooth. Surface erosion occurred during the testing at supersonic velocities and the porous surface required smoothing before the subsonic tests were conducted. The surface roughness probably has the most effect on the skin friction with zero injection since with injection the outward flow of the injected gases would tend to shield the surface irregularities from the main stream flow over the cone. Another possible unknown effect on skin friction may be caused by the individual jets of gas emanating from the surface. Whether this effect is essentially an introduction of roughness elements is not known from these tests. An examination of the representative injection velocity measurements shown in Fig. 2 readily shows the existence of higher speed jets coming out of the surface. These measurements indicating relative porosity were made with an Alnor heated thermocouple anemometer circumferentially around the cone at a constant distance of 1/16 in. from the surface.

Three gases were injected through the porous surface; they were grade-A helium, dry air, and commercial Freon-12. The gases were metered with rotometers prior to entering the model and were passed through a fibrous glass filter twice the thickness of the conical porous wall. An examination of the model after extensive testing revealed no dirt particles or appreciable discoloration on the inner surface of the porous cone; therefore, it was believed that no significant porosity variations were introduced as a result of accumulation of matter within the porous surface material.

Test Conditions and Procedures

Skin-friction measurements were made at nominal free-stream Mach numbers of 0.3, 0.7, 3.5, and 4.7. The range of Reynolds numbers was from 0.9×10^6

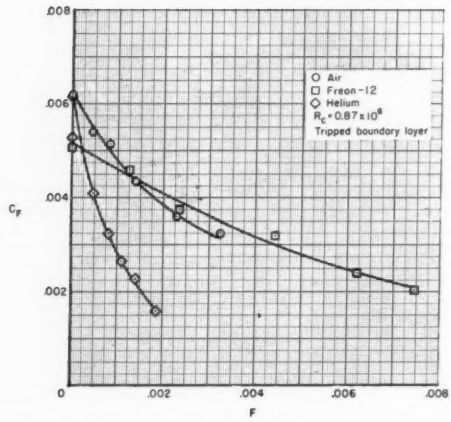

FIG. 5(a). Variation of average skin-friction coefficient with injection. $M_e = 0.3$; $R_e = 0.87 \times 10^6$.

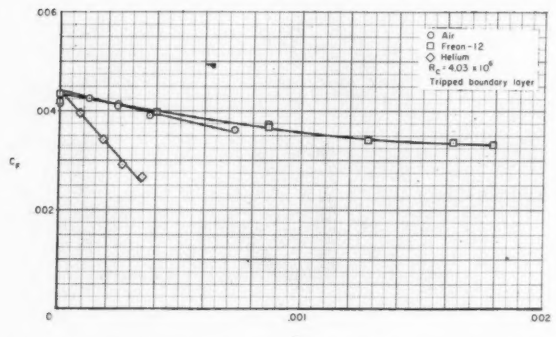

FIG. 5(b). Variation of average skin-friction coefficient with injection. $M_e = 0.3$; $R_e = 4.03 \times 10^6$.

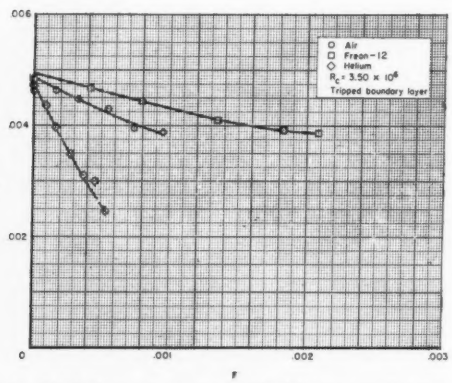

FIG. 5(c). Variation of average skin-friction coefficient with injection. $M_e = 0.7$.

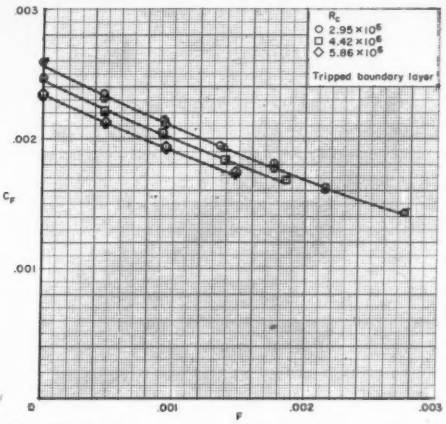

FIG. 5(d). Variation of average skin-friction coefficient with injection. $M_e = 3.21$; air injection.

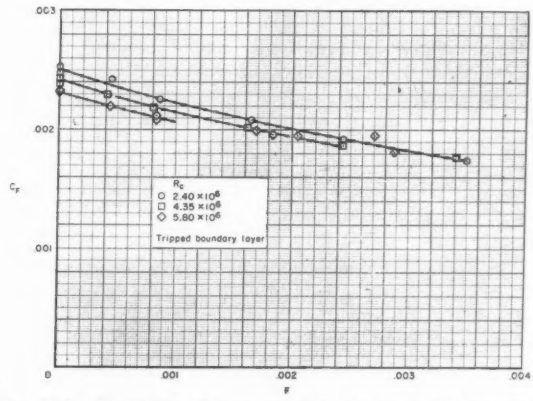

FIG. 5(e). Variation of average skin-friction coefficient with injection. $M_e = 3.21$; Freon-12 injection.

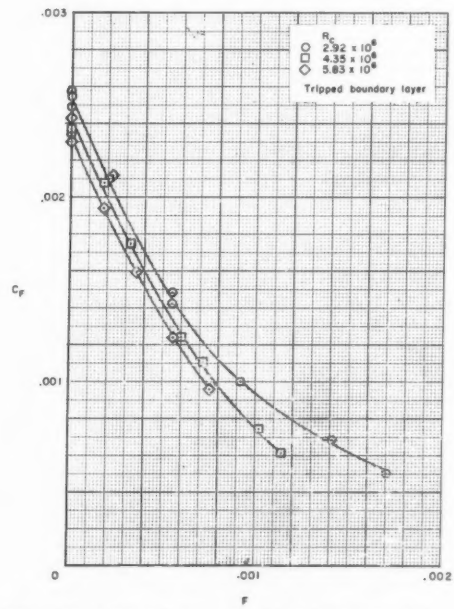

FIG. 5(f). Variation of average skin-friction coefficient with injection. $M_e = 3.21$; helium injection.

to 5.9 × 10^6 based on free-stream conditions for subsonic flow and inviscid cone surface conditions after the conical shock wave for supersonic flow. The characteristic length in the Reynolds number is the cone ray length of $10^1/_2$ in.

The necessary measurements used to determine total skin friction were the surface pressures along the cone, the base pressures, the gas injection rates, the strain-gage output (or force), the standard wind-tunnel conditions of stagnation pressure and temperature, and test section static pressure. The free-stream Mach number was determined from the ratio of free-stream static to stagnation pressure for all tests. The cone Mach number for supersonic flow was obtained from reference 10 for a 15° total angle cone.

Calibrations of the strain-gage flexure unit were made before and/or after each daily test run. Also, the injection force exerted on the cone due to the passage of the injection gases through the porous cone was measured. These individual measurements of indicated strain-gage force as a function of injection weight rate of each gas were made at static pressures near to the wind-tunnel static pressure test conditions. Linear interpolations or extrapolations of the correction were made to match actual test static pressures. These corrections were an appreciable portion of the total skin-friction force only in the case of high helium injection rates where the skin-friction force was quite small.

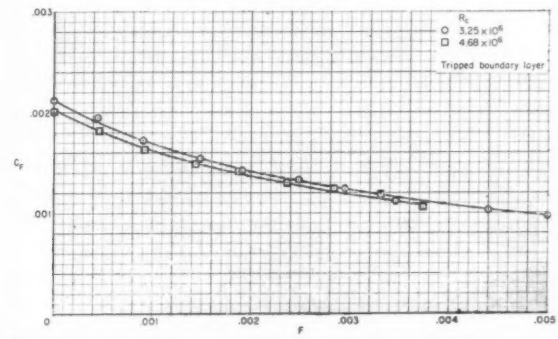

FIG. 5(g). Variation of average skin-friction coefficient with injection. M_e = 4.30; air injection.

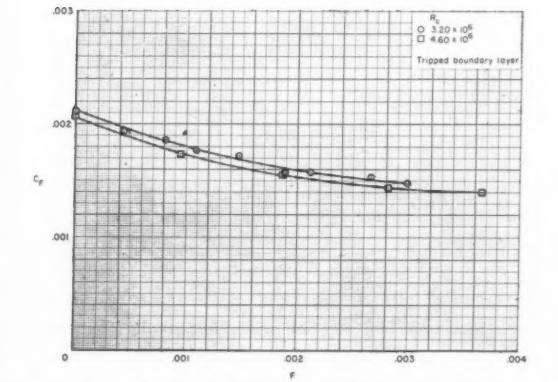

FIG. 5(h). Variation of average skin-friction coefficient with injection. M_e = 4.30; Freon-12 injection.

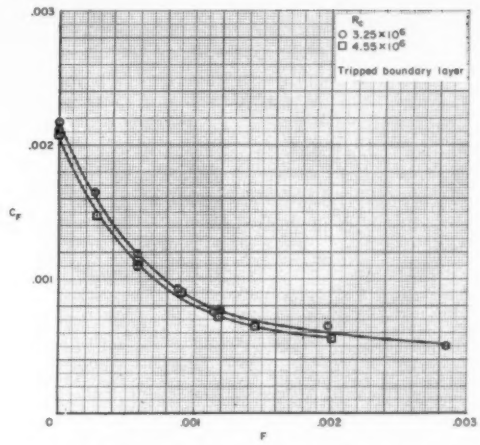

FIG. 5(i). Variation of average skin-friction coefficient with injection. M_e = 4.30; helium injection.

Zero shift of the strain-gage output was usually negligible during the tests.

Static pressure distributions on the cone exterior are sensitive to the gas injection rate in two ways: (1) the effective external geometry of the cone is changed with rate of injection of each gas, and (2) local jets of gas emanating from the surface can cause an expansion or compression region near to the pressure orifice which thereby indicates a pressure not representative of the cone surface. Only one of many static pressure distributions along the cone exterior is presented in this report (see Fig. 3), and this is to demonstrate the method for determining the net external pressure force on the cone. Pressures indicated by circular symbols A through H exist along one cone ray and J, K, L along a ray 180° around the cone, and base pressures M, N, O, P are within the cone shroud. Pressure taps J, K, L are at the same distance back from the tip as are taps A, D, G, respectively (see Fig. 1). The pressures are plotted as a function of the cross-sectional area of the cone normal to the axis, and the area under the curve (to the zero ordinate value) connecting the square symbols (weighted values) is the axial pressure force acting in the stream direction. Because of the many static pressure distributions obtained in these tests, a systematic pressure weighting and curve fairing method was adopted. The final curve, composed of the heavy straight line segments connecting the square symbols, was defined by the average of pressures A and J, D and K, G and L, and pressures B, C, E, F, and H shifted by the amount and direction indicated by the vertical arrows on the figure.

Average Skin-Friction Coefficients

The average skin-friction coefficient is defined for the cone as total friction drag divided by qA_c where the dynamic pressure q is defined as $(1/2)\rho_\infty u_\infty^2$ for subsonic flow and $(1/2)\rho_e u_e^2$ for the supersonic flow tests. The total skin-friction drag is defined in this report to be the axial component of the skin-friction

TABLE 1
Magnitude of Forces Used to Determine Skin Friction

M_∞	$R_e \times 10^{-6}$	Helium injection rate, F	Cone-minus-base force, lb.	Strain-gage force, lb.	Maximum strain gage zero shift, lb.	Injection force, lb.	Skin-friction force, lb.	Weighting shift, lb.	Possible fairing change, lb.	Ratio of cone force to skin-friction force
0.3	4.02	0	0.166	0.552	±0.004	0	0.386	0.015	0.013	456
0.3	4.02	0.000344	0.395	0.616	±0.004	0.015	0.236	0.002	0.009	744
0.7	3.51	0	0.440	1.226	±0.001	0	0.786	0.023	0.029	80.5
0.7	3.48	0.000532	1.317	1.668	±0.001	0.057	0.408	0.004	0.015	155
3.5	2.91	0	3.444–3.555	0.376	±0.001	0	0.487	0.041	0.001	7.14
3.5	2.91	0.00170	3.571–3.072	0.578	±0.001	0.018	0.097	0.044	0.024	36.9
4.7	3.18	0	1.634–1.684	0.283	±0.009	0	0.333	0.023	0.003	4.92
4.7	3.14	0.00285	1.792–1.424	0.428	±0.009	0.020	0.080	0.023	0.017	22.3

force. The axial friction force is equal to the resultant of the external pressure force, the base pressure force, and the corrected strain-gage force. The total wetted area of the cone is A_c.

Effect of Boundary-Layer Trip

The use of a boundary-layer trip introduces uncertainties into the skin-friction measurements. The effective start of the fully developed turbulent boundary layer may be displaced, and the pressure and skin-friction drag of the trip (which are not accounted for) may introduce errors in the calculation of the total skin friction of the cone. These effects were minimized in these tests because the trip was thin and covered a very small part of the total cone area, and the shift in effective origin of the turbulent boundary layer was in a region of diminishing area at the tip. For the skin-friction tests with gas injection, the actual injection did not extend to the cone tip, so the effect of boundary layer thickening that would result from this missing injection may have been partially compensated for by the boundary-layer thickening resulting from the trip.

It was not possible to measure the drag of the nonporous nose region (including trip) of the cone. The skin friction of the nose area ($x_c = 2$ in.) is estimated to be 3.6 per cent of the total skin-friction drag. The skin friction of the trip region (including cone tip, $x_c = 1^1/_4$ in.) is estimated to be about 2 per cent of the total skin friction; therefore, an uncertainty of 100 per cent in trip drag introduces an uncertainty of only 2 per cent in the total drag.

Effect of External Pressure Distribution and Other Factors

The cone pressure force and the base pressure force are the largest involved in the model force balance. For the subsonic tests, the cone pressure force and base pressure force were from 80 to 744 times larger than the skin-friction force and, for the supersonic tests, from 5 to 37 times larger. Rather than measure the external cone pressures directly in the subsonic tests, the difference between cone and base pressures was measured, and this difference in pressure forces was of the same order of magnitude as the skin friction. For the supersonic tests the external pressures were measured directly. Accuracy for pressure measurements was ±0.000755 lb. per sq. in.; this is equivalent to 0.00445 lb. base or cone pressure force, if the error is in one direction for all pressure measurements. A tabulation of the uncertainties and of the corrections which enter into the skin-friction determination is shown in Table 1. The extreme cases are presented—that is, the largest and smallest skin-friction values for each Mach number and for a representative Reynolds number are shown. All forces are tabulated in pounds force rather than per cent of friction force in order to show what absolute accuracy is required for these force measurements. Some explanation of the tabulation is necessary. The cone-minus-base force was the difference in the axial components of the pressure forces acting on the wetted area and the base area of the cone. The strain-gage force was the indicated force on the flexures. The strain-gage readings taken with gas injecting into the model and flowing over the strain gage were considered more reliable than the zero injection readings because the gage temperature with injection was near the calibration temperature. The strain-gage zero shift was the change in gage reading with zero loading, noted over the period of a day's run and was probably due to temperature changes of the strain gage. The injection force was the force exerted on the cone by the injection gases and has been described in the section titled "Test Procedures." The weighting shift is not an error but is the shift in external cone force from that obtained from the pressure-area straight line curve connecting pressures A through H to M, N, O, P along one cone ray to the heavy straight line curve connecting the weighted pressures (square symbols), as shown in Fig. 3. Some individual pressures were affected by the local gas injection through the porous wall and it was necessary to adopt a modified weighting of the individual pressures. Now, in all similar cases a consistent fairing method was followed; therefore, the relative magnitudes of the external cone forces of a series of runs are probably good, but the absolute value of this pressure force is dependent on the fairing method by an amount indicated by the possible fairing change. The last column of the table is the ratio of the axial cone force divided by the axial skin-friction force and is shown to emphasize the relative magnitude of the forces involved in the force balance used to determine skin friction.

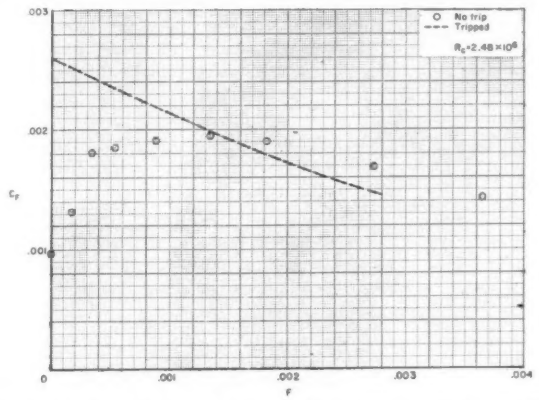

FIG 6(a). Comparison of average skin-friction coefficients with and without boundary-layer trip. $M_c = 3.21$; air injection.

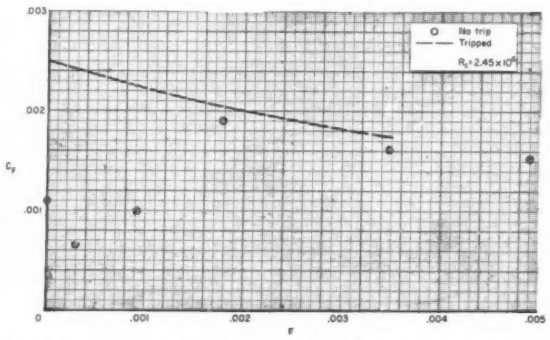

FIG 6(b). Comparison of average skin-friction coefficients with and without boundary-layer trip. $M_c = 3.21$; Freon-12 injection.

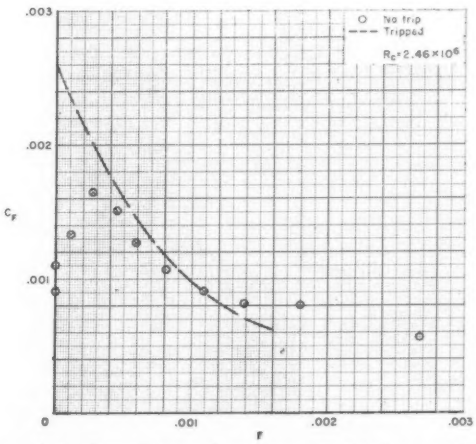

FIG. 6(c). Comparison of average skin-friction coefficients with and without boundary-layer trip. $M_c = 3.21$; helium injection; $R_c = 2.46 \times 10^6$.

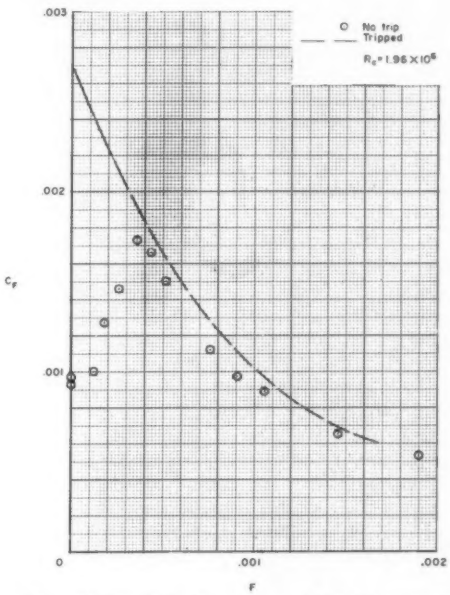

FIG. 6(d). Comparison of average skin-friction coefficients with and without boundary-layer trip. $M_c = 3.21$; helium injection; $R_c = 1.96 \times 10^6$.

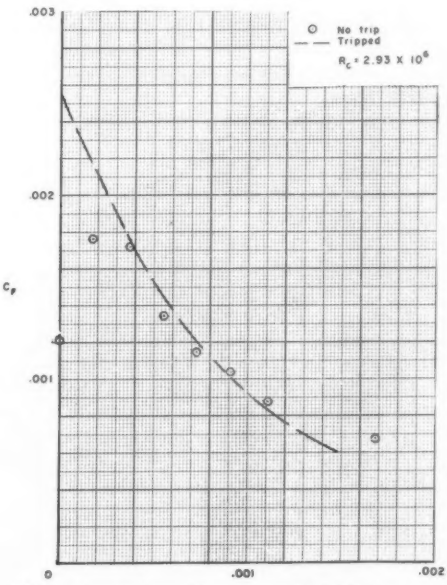

FIG. 6(e). Comparison of average skin-friction coefficients with and without boundary-layer trip. $M_c = 3.21$; helium injection; $R_c = 2.93 \times 10^6$.

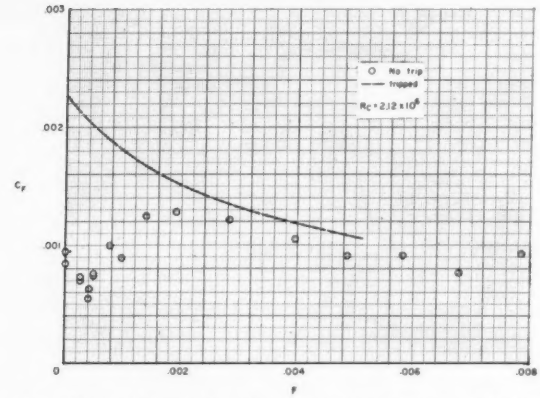

FIG. 7(a). Comparison of average skin-friction coefficients with and without boundary-layer trip. $M_e = 4.30$; air injection; $R_e = 2.12 \times 10^6$.

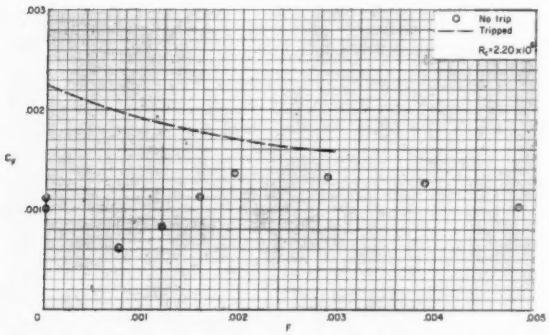

FIG. 7(b). Comparison of average skin-friction coefficients with and without boundary-layer trip. $M_e = 4.30$; Freon-12 injection; $R_e = 2.20 \times 10^6$.

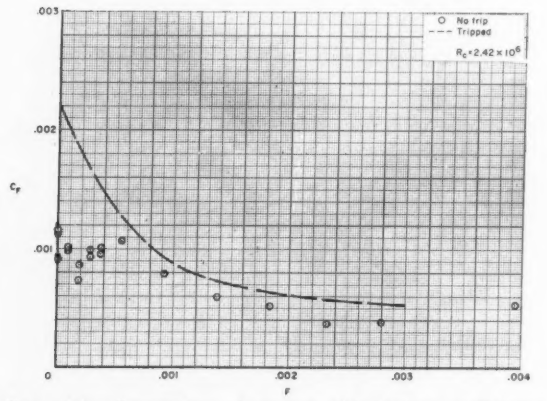

FIG. 7(c). Comparison of average skin-friction coefficients with and without boundary-layer trip. $M_e = 4.30$; helium injection; $R_e = 2.42 \times 10^6$.

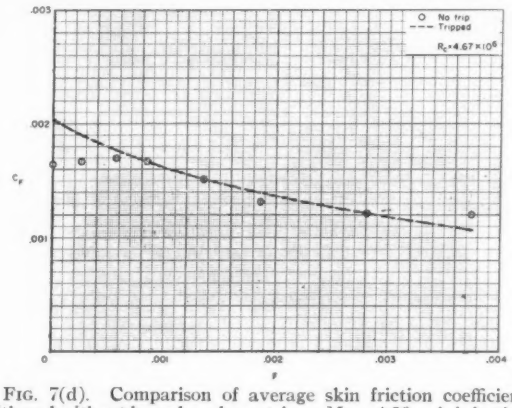

FIG. 7(d). Comparison of average skin friction coefficients with and without boundary-layer trip. $M_e = 4.30$; air injection; $R_e = 4.67 \times 10^6$.

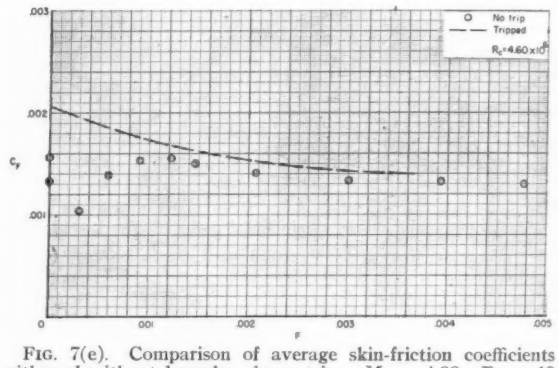

FIG. 7(e). Comparison of average skin-friction coefficients with and without boundary-layer trip. $M_e = 4.30$; Freon-12 injections; $R_e = 4.60 \times 10^6$.

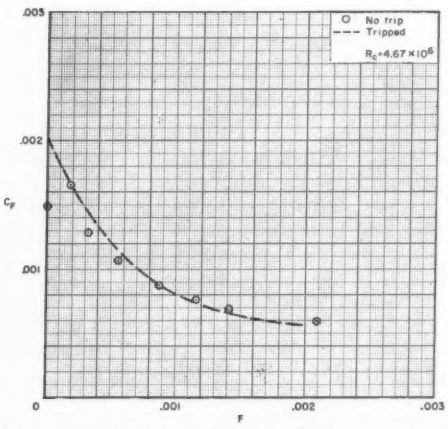

FIG. 7(f). Comparison of average skin-friction coefficients with and without boundar-layer trip. $M_e = 4.30$; helium injection; $R_e = 4.67 \times 10^6$.

Presentation of Basic Data

Some limited transition data were obtained on the test cone without a trip at cone Mach numbers of 3.21 and 4.28. These results are presented in Fig. 4. The actual point of transition is defined where the first turbulent eddies appear in the boundary-layer shadowgraph pictures. It is apparent that transition does not occur immediately at the initial point of injection, $x_c = 2$ in., and that the transition point of the boundary layer moves forward on the cone with increased injection. As might be expected when compared on a mass basis, helium injection initially causes the largest change in transition location; air and Freon-12 have less effect. The transition location seems to approach a forward asymptotic value for the high injection rates of air and Freon-12, and complete tripping does not occur. Limitations in viewing the model prevented extension of these curves for the whole cone.

The fundamental data of this report are the average skin-friction coefficients obtained on the cone with a tripped turbulent boundary layer. These data are presented on graphs in Figs. 5(a) to 5(i), as a function of the dimensionless injection rate F. For the subsonic tests $F = \rho_w v_w / \rho_\infty u_\infty$ and for the supersonic tests $F = \rho_w v_w / \rho_c u_c$. Curves have been faired through each set of data to indicate the scatter in the basic data and to show the faired curve zero injection skin-friction coefficients, C_{F_0}. These faired curve C_{F_0} values are used subsequently as reference values in the correlation of the data. The curves require little discussion except to note that in Fig. 5(a) there are shown two faired curve C_{F_0} values for the same Mach number and Reynolds number. These data, represented by each of the faired curves, are consistent within themselves. The differences noted in the C_{F_0} values of Fig. 5(a) are a direct result of a slight measured change in the external cone pressure distribution. The only significant variation in C_{F_0} values was obtained at a Mach number of 0.3.

In conjunction with the transition studies, total skin-friction coefficients were measured for the cone under conditions of natural transitiion. These average skin-friction coefficients for the untripped boundary layer are presented as a function of the injection rate F and are compared in Fig. 6 with the skin-friction coefficients of a tripped boundary layer obtained at the same cone Reynolds number. The skin-friction coefficients for the tripped boundary layer were corrected for the effect of Reynolds number in some cases in order to make comparison at the same Reynolds number of the nontripped flow. Air, Freon-12, and helium were injected through the cone at $R_c \approx 2.46 \times 10^6$ and $M_c = 3.21$, and the skin-friction results are shown in figs. 6(a), 6(b), and 6(c). For Freon injection, the skin friction decreases initially from the zero injection value and then rises almost to the tripped boundary-layer values. Up to an injection rate $F = 0.001$ [Fig. 6(b)], the effect of injection to decrease the skin friction is greater than the increase in skin friction caused by the forward shift in transition location. For air and helium injection an immediate increase in skin friction occurs with injection [Figs. 6(a) and 6(c)], and for high rates of injection the skin friction obtained without a trip slightly exceeds the fully turbulent results. For helium injection at cone Reynolds numbers of 1.96×10^6 and 2.93×10^6 [Figs. 6(d) and 6(e)], the skin-friction values rise from the zero injection value to the turbulent skin-friction coefficient curve and then fall off in good agreement with the curve. Generally, with the higher Reynolds number tests, the skin-friction coefficients obtained with no trip come into approximate coincidence with the curve of the tripped boundary layer at lower values of F than those obtained with no trip at lower Reynolds numbers.

Some skin-friction results obtained with no trip at a higher Mach number, $M_c = 4.28$, with injection of Freon, air, and helium are presented in Figs. 7(a), 7(b), and 7(c), for $R_c \approx 2.2 \times 10^6$ and Figs. 7(d), 7(e), and 7(f) for $R_c \approx 4.65 \times 10^6$. For the $R_c \approx 2.2 \times 10^6$ results, the skin friction initially decreases from the zero injection value for all gases and then rises to come into approximate coincidence with the tripped-boundary layer curve. Here again the skin-friction coefficients for helium injection obtained with no trip rise most quickly and come into approximate agreement with the tripped values as would be expected. For the results obtained with no trip at $R_c \approx 4.6 \times 10^6$, only for the Freon injection do the skin-friction coefficients initially decrease in value. For the air and helium injection the skin-friction values initially rise and then come into agreement with the tripped skin-friction curve with increased injection.

Some general statements may be made concerning the skin friction obtained with no trip. For the higher rates of injection the nontripped and tripped-boundary-layer skin-friction coefficients are in fair agreement. This does not mean, however, that transition occurs at the start of the porous region on the cone surface, but that the skin-friction contribution of the laminar portion of the boundary layer is in approximate agreement with the turbulent skin friction of the same fore part of the cone. Also, the contribution of the turbulent skin friction of the fore part of the cone, $x_c < 4$ in., is calculated to be $16^1/_2$ per cent of the total turbulent

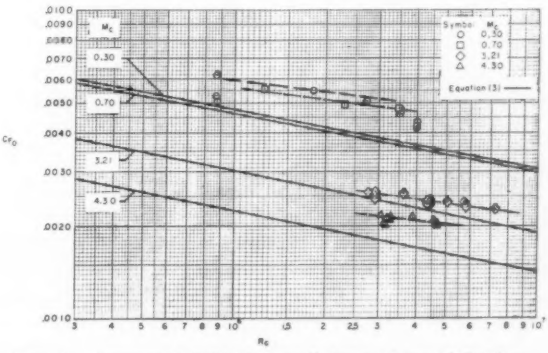

FIG. 8. Average skin-friction coefficients without injection.

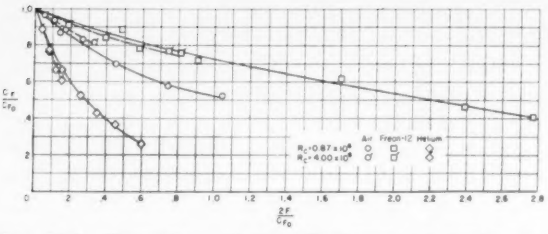

FIG. 9(a). Comparison of the effectiveness of foreign gas injection on skin friction. $M_e = 0.3$.

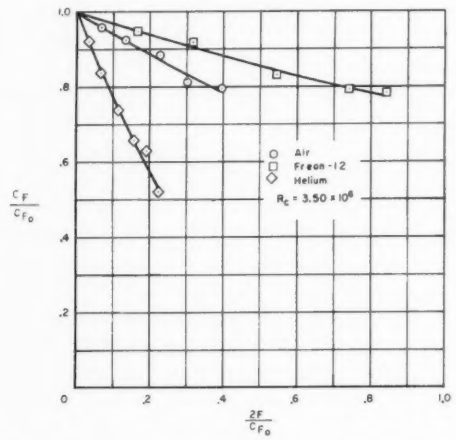

FIG. 9(b). Comparison of the effectiveness of foreign gas injection on skin friction. $M_e = 0.7$.

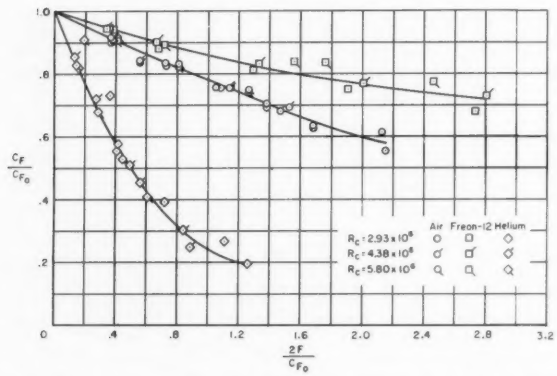

FIG. 9(c). Comparison of the effectiveness of foreign gas injection on skin friction. $M_e = 3.21$.

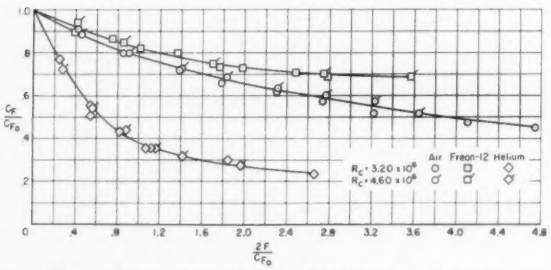

FIG. 9(d). Comparison of the effectiveness of foreign gas injection on skin friction. $M_e = 4.30$.

skin friction. Even if the skin friction of the fore part of the cone were changed considerably the total skin friction would still be in fair agreement at the higher injection rates. A check on the reliability of the total skin-friction measurements was made, but is not shown, by comparing the total skin friction obtained with no trip at low Reynolds numbers with the laminar theory. A plot of all the zero injection skin-friction coefficients with no trip revealed that these values are just within the transition region between laminar and turbulent flow.

Skin-Friction Coefficients With Zero Injection and Tripped Boundary Layer

Average skin-friction coefficients without injection obtained at cone Mach numbers of 0.3, 0.7, 3.21, and 4.30 are presented in Fig. 8. These cone values are compared with flat-plate skin friction transformed to cone values for all test Mach numbers, even though a pressure gradient exists along the surface of the cone in subsonic flow. The solid line curves are obtained from a modified form of the incompressible flow flat-plate Blasius equation, $c_{f_0}/2 = 0.0296\ R_x^{-0.2}$, valid in the region $10^5 < R_x < 10^7$. This equation is adapted to cone flow to give the total skin-friction coefficient $C_{F_{0_i}} = 0.0754\ R_c^{-0.2}$. The effect of Mach number on the skin-friction coefficient is calculated by the intermediate temperature method (T' method, reference 11) where the air-stream properties are evaluated at an intermediate temperature, T', and

$$T'/T_e = 1 + 0.035\ M_e^2 + 0.45[(T_w/T_e) - 1] \quad (1)$$

or

$$T'/T_e = 1 + 0.115\ M_e^2 \quad \text{for } T_w = T_r; \quad \eta_r = 0.89 \quad (2)$$

Finally, the actual computation of the solid curves is made from the equation

$$C_{F_0} = \frac{0.0754}{R_c^{0.2}} \frac{1}{(T'/T_e)^{1/2}} \left[\frac{1 + (S/T_e)}{(T'/T_e) + (S/T_e)}\right]^{0.2} \quad (3)$$

where $S \backsimeq 200°$R. is the constant in the Sutherland viscosity formula.

The experimental data for Mach numbers 0.3, 0.7, 3.21, and 4.30 are fitted in Fig. 8 by dashed curves of the type $C_{F_0} = KR_c^{-n}$, where $K = K(M_e)$ for $T_w = T_r$, and $n = 0.133$ best represents the experimental results. The representation of the data by these curves, corresponding to $n = 0.133$, is strengthened by the fact that the faired curve values of C_{F_0} obtained from the C_F vs. F curves of Fig. 5 fall on these dashed curves. The possibility has been considered that this low value of n may have been caused by surface roughness. One would expect that surface roughness would have less influence on the skin friction with gas injection, but here again the presence of finite jets of injected gas may perpetuate the roughness effect even with injection. The variation of the average skin-friction coefficient with Reynolds number is somewhat less than that obtained on flat plates (where $n \backsimeq 0.2$). Whether

this different variation is due to effects of the boundary-layer trip and surface roughness or is a genuine cone effect is not known from these limited experiments. There are some other experimental results available. The data of Tendeland and Okuno[3] obtained by force measurements on a conical surface, which was not smooth, were over a small Reynolds number range and show no consistent variation with Reynolds number. Bradfield, DeCoursin, and Blumer[12] measured average skin friction of a tripped turbulent boundary layer on a smooth cone and show no variation of C_{F_0} over a limited range of Reynolds numbers. The value of the average skin-friction coefficient of the turbulent boundary layer on a cone is still in doubt. The present C_{F_0} test results are consistently higher than the flat-plate skin friction transformed to cone C_{F_0} values. The skin-friction measurements of tripped turbulent boundary layers of references 3 and 12 are not adequate to define skin friction on cones over an extended Reynolds number and Mach number range.

Final Results and Discussion

A comparison of the effectiveness in reducing skin friction of the various injection gases at each test Mach number is presented in Figs. 9(a), 9(b), 9(c), and 9(d). The ordinate is the ratio of the skin-friction coefficient with injection to that with zero injection. The abscissa is the dimensionless mass injection flow rate F divided by one half the skin-friction coefficient for zero injection. This comparison is made on an equivalent mass flow basis, and when presented on this basis, the effects of Reynolds number, wall to free-stream temperature ratio, and Mach number are expected from the theories for air injection to be minimized. The effect of wall to free-stream temperature ratio variation is not considered in these tests because the model wall temperature was always near recovery temperature. The reduction in skin friction due to gas injection obtained at free-stream Mach number $M_\infty = 0.3$ [Fig. 9(a)] is indicative of the results at the higher Mach numbers. The effectiveness of the light gas, helium, is immediately apparent; reductions in skin friction of 75 per cent were realized at relatively low injection rates. For the same injection rate, F, reductions of 36 and 20 per cent were obtained with air and Freon. The data, obtained at Reynolds numbers of 0.87×10^6 and 4.0×10^6, are distinguished in the figure by two sets of curves faired through the experimental points. The effect of Reynolds number on the relative reduction of skin friction is small when compared in this coordinate system but this comparison is made for limited injection rates. The variation of skin friction with injection for $M_\infty = 0.7$ [Fig. 9(b)] shows similar initial trends, but limitations of the model prevented extension to higher injection rates. The measurements of skin friction at a cone Mach number $M_c = 3.21$ are presented in Fig. 9(c). The data were obtained at three cone Reynolds numbers within the Reynolds number range of 2.93×10^6 to 5.80×10^6. The skin-friction results correlate reasonably well in this coordinate system. The highest Mach number results, $M_c = 4.30$, are presented in Fig. 9(d). Maximum relative injection rates were attained for these test conditions, and no indication of boundary-layer separation was seen in any of the shadowgraph pictures.

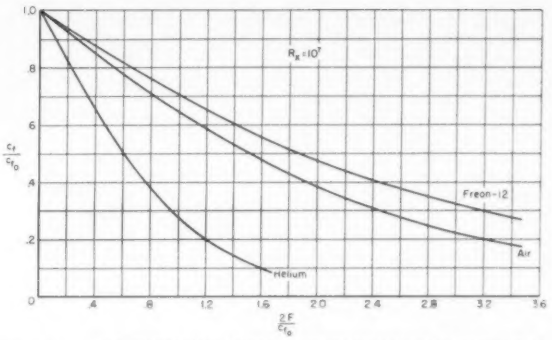

FIG. 10. Theoretical skin-friction variation for a flat plate with injection (see reference 13); $M = 0$, $T = 500°$R.

The skin-friction data generally show that (1) substantial reductions in skin friction are attained with gas injection, (2) the relative effectiveness of the gases is in accordance with the theory of reference 13, and (3) heavy gases similar to Freon-12 which may emit from ablating plastics are not very effective in reducing skin friction. The theoretical local skin-friction results of reference 13 are shown in Fig. 10 for a comparison of only the relative gas effectiveness for reducing skin friction. The theory is for an incompressible nearly isothermal flow over a flat plate with gas properties evaluated at a temperature of 500°R. Note that the comparison of relative gas effectiveness is made between the present total skin-friction results of Fig. 9 obtained on a cone and the theoretical local skin friction on a flat plate of Fig. 10. It can be shown for uniform injection and for distributed injection varying as $x^{-1/5}$, that the c_f/c_{f_0} vs. $2F/c_{f_0}$ and C_F/C_{F_0} vs. $2F/C_{F_0}$ relationships are essentially the same for flat plate flow and both relationships are essentially the same for cone flow. Also, it can be shown that the c_f/c_{f_0} vs. $2F/c_{f_0}$ relation is essentially the same for both flat plate and cone flow; therefore, comparison may be made between local and average skin friction for both cone and flat plate flow for equivalent external flow conditions at the edge of the boundary layer.

The effect of Mach number on the reduction in skin friction is not easily ascertained from the previous Figs. 9(a) through 9(d); but before the Mach number effect is discussed, comparison between the present data and other available skin-friction results should be made. To the writers' knowledge, only a limited number of experiments which measure the effects of gas injection on skin friction are available. They are the low speed data of Mickley and Davis[1] and the data of Tendeland and Okuno[3] obtained at $M = 2.55$. All these tests were with air injection. The local skin-friction measurements of Hacker are in agreement with Mickley and

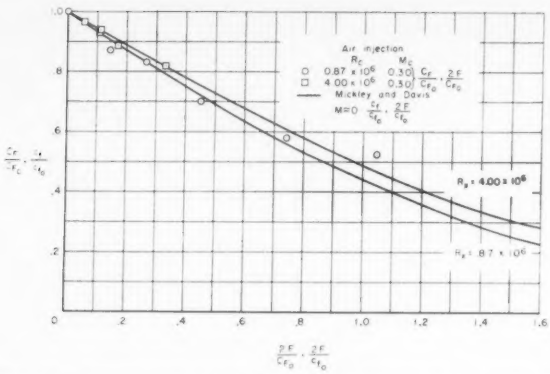

FIG. 11. Comparison of the effect of air injection of skin friction at low speeds.

Davis at the low injection rates, but at the higher injection rates Hacker indicates a separated boundary layer. A comparison is made of the present $M_\infty = 0.3$ results with those of Mickley and Davis in Fig. 11. The agreement is generally good for the injection rates of the present tests.

The representative experimental skin-friction data with air injection are compared with some of the theories in Fig. 12. The conditions for comparison are a wall temperature near recovery temperature for the experiments, a wall temperature equal to total temperature for the theories, a Mach number range from 0 to 5, and a Reynolds number within the range of 0.9×10^6 to 10×10^6. Two theories, one of Rubesin[5] and the other of Dorrance and Dore,[6] are shown as shaded regions between the indicated Mach number ranges. The dashed curves are the available experimental skin-friction measurements. The experimental result is that the relative reduction in skin friction with air injection shows a marked Mach number dependence. Neither of the theories considered predicts the extent of this measured dependence of skin friction on Mach number. It is of some interest to note that much of the earlier research to measure effects of air injection on the turbulent boundary layer at supersonic speeds reported in references 3, 4, 14, and 15 was in the Mach number range of 2.5 to 3.0, where the theory of Rubesin[5] predicts the outcome quite well. The low-speed results of Mickley and Davis combined with the present results show the Mach number effects clearly.

The effect of Mach number on the experimental variation of the skin-friction ratio, C_F/C_{F_0}, is shown in Figs. 13(a), 13(b), and 13(c) for air, Freon-12, and helium injection. Fig. 13 is a cross plot of the faired curve values of Fig. 9. The local skin-friction measurements of Mickley and Davis, obtained on a flat plate with air injection, are used to augment the present test results at the low Mach numbers in Fig. 13(a). The effectiveness of air injection in reducing skin friction generally decreases with increasing Mach number. For Freon-12 injection [Fig. 13(b)] the reduction in the skin-friction ratio appears to be least in the Mach number range of 2.5 to 3.5. For helium injection [Fig. 13(c)] decreasing effectiveness is noted with increasing Mach number for all injection rates, $2F/C_{F_0}$.

It can be expected that the heat transfer with injection should generally follow these skin-friction trends and that one possible application of gas injection is to alleviate high rates of heat transfer from within the turbulent boundary layer. The probable regions of application of transpiration cooling are blunt leading edges of wings and blunt nose regions of missiles, and in these regions the local Mach number at the edge of the boundary layer is much reduced below the free-stream Mach number, thereby allowing the application of these test results.

Conclusions

Total skin friction of the turbulent boundary layer was measured on a porous cone with foreign gas injection of helium, air, and Freon-12 at an average Reynolds number of about 3×10^6 and up to a cone Mach number of 4.3. A number of measurements of boundary-layer skin friction with natural transition were made in conjunction with limited studies of transition movement with foreign gas injection. It was found that:

(1) Helium injection initially causes the largest change in transition location; air and Freon-12 have less effect on transition. The boundary layer is not completely tripped even for the higher rates of injection of air and Freon, and the transition location appears to approach an asymptotic position at high rates of injection.

(2) The average skin-friction coefficients, C_F, obtained with natural transition come into fair agreement with the tripped boundary-layer results at the high injection rates. The variation of C_F with injection rate, F, at the lower F values is dependent on the Reynolds number of the flow and the type of injection gas.

(3) Substantial reductions in skin friction of the turbulent boundary layer were realized with foreign gas injection of helium, air, and Freon-12. Reductions of 80 per cent in skin friction were obtained at the highest helium injection rates of the tests without inducing boundary-layer separation.

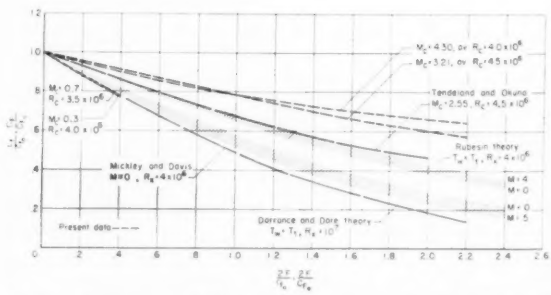

FIG. 12. Comparison of skin-friction theory and experiment with air injection.

(4) The relative effectiveness of helium, air, and Freon-12 in reducing skin friction as predicted by the theory of Rubesin and Pappas is in agreement with experiment.

(5) The present experimental results show an appreciable change in relative skin-friction reduction with change in Mach number. This variation is not predicted by the theories of Rubesin and of Dorrance and Dore for air injection.

References

[1] Mickley, H. S., and Davis, R. S., *Momentum Transfer for Flow Over a Flat Plate With Blowing*, NACA TN 4017, 1957.

[2] Hacker, D. S., *Empirical Prediction of Turbulent Boundary Layer Instability Along a Flat Plate With Constant Mass Addition at the Wall*, Jet Propulsion, Vol. 26, No. 9, pp. 786–787, September, 1956.

[3] Tendeland, Thorval, and Okuno, Arthur F., *The Effect of Fluid Injection on the Compressible Turbulent Boundary Layer—The Effect on Skin Friction of Air Injected Into the Boundary Layer of a Cone at $M = 2.7$*, NACA RM A56DO5, 1956.

[4] Rubesin, Morris W., *The Influence of Surface Injection on Heat Transfer and Skin Friction Associated With the High-Speed Turbulent Boundary Layer*, NACA RM A55L13, 1956.

[5] Rubesin, Morris W., *An Analytical Estimation of the Effect of Transpiration Cooling on the Heat-Transfer and Skin-Friction Characteristics of a Compressible, Turbulent Boundary Layer*, NACA TN 3341, 1954.

[6] Dorrance, William H., and Dore, Frank J., *The Effect of Mass Transfer on the Compressible Turbulent Boundary-Layer Skin Friction and Heat Transfer*, Journal of the Aeronautical Sciences, Vol. 21, No. 6, pp. 404–410, June, 1954.

[7] Spiegel, Joseph M., and Lawrence, Leslie F., *A Description of the Ames 2- by 2-Foot Transonic Wind Tunnel and Preliminary Evaluation of Wall Interference*, NACA RM A55121, 1956.

[8] Tendeland, Thorval, *Effect of Mach Number and Wall-Temperature Ratio on Turbulent Heat Transfer at Mach Numbers From 3 to 5*, NACA TN 4236, 1958.

[9] Dannenberg, Robert E., Weiberg, James A., and Gambucci, Bruno J., *A Fibrous-Glass Compact as a Permeable Material for Boundary-Layer-Control Applications Using Area Suction*, NACA TN 3388, 1955.

[10] Staff of the Computing Section (under the direction of Zdeněk Kopal); *Tables of Supersonic Flow Around Cones*, Tech. Rep. 1, Center of Analysis, M.I.T., Cambridge, 1947.

[11] Sommer, Simon C., and Short, Barbara J., *Free-Flight Measurements of Turbulent-Boundary-Layer Skin Friction in the Presence of Severe Aerodynamic Heating at Mach Numbers From 2.8 to 7.0*, NACA TN 3391, 1955.

[12] Bradfield, W. S., DeCoursin, D. G., and Blumer, C. F., *Characteristics of Laminar and Turbulent Boundary Layer at Supersonic Velocity*, Res. Rep. 83, Inst. of Tech., Univ. of Minnesota, July, 1952.

[13] Rubesin, Morris W., and Pappas, Constantine C., *An Analysis of the Turbulent Boundary-Layer Characteristics on a Flat Plate With Distributed Light-Gas Injection*, NACA TN 4149, 1958.

[14] Leadon, B. M., and Scott, C. J., *Measurement of Recovery Factors and Heat Transfer Coefficients With Transpiration Cooling in a Turbulent Boundary Layer at $M = 3.0$ Using Air and Helium as Coolants*, Res. Rep. 126, Inst. of Tech., Univ. of Minnesota, February, 1956.

[15] Rubesin, Morris W., Pappas, Constantine C., and Okuno, Arthur F., *The Effect of Fluid Injection on the Compressible Turbulent Boundary Layer—Preliminary Tests on Transpiration Cooling of a Flat Plate at $M = 2.7$ With Air as the Injected Gas*, NACA RM A55I19, 1955.

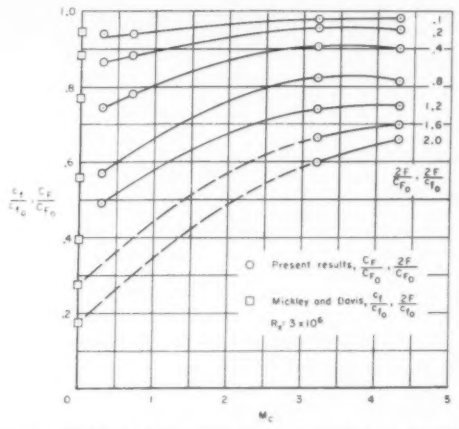

FIG. 13(a). Effect of Mach number on the relative reduction in skin friction; air injection.

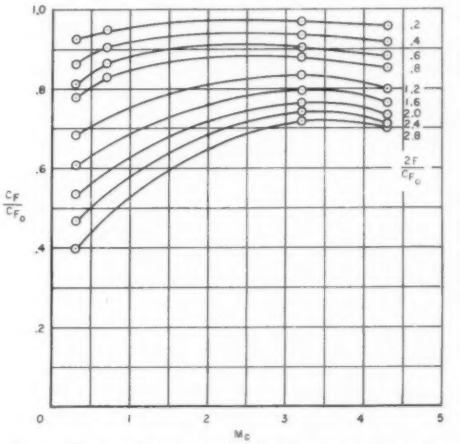

FIG. 13(b). Effect of Mach number on the relative reduction in skin friction; Freon-12 injection.

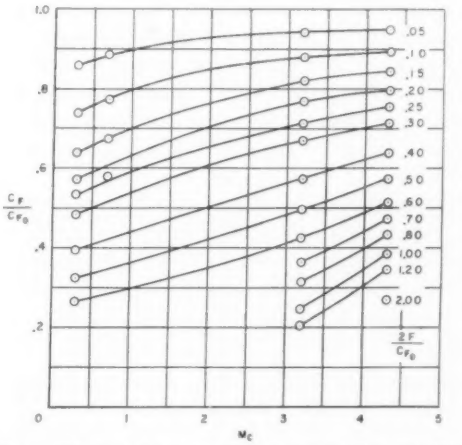

FIG. 13(c). Effect of Mach number on the relative reduction in skin friction; helium injection.

Magnetohydrodynamic Effects on the Formation of Couette Flow

L. N. TAO*

Illinois Institute of Technology

Summary

This paper is concerned with the problem of the formation of Couette flow—i.e., the problem of how the velocity profile varies with the time tending asymptotically to that of the steady flow of an electrically conducting viscous fluid in the presence of a magnetic field. The governing equations and boundary conditions are established and discussed. The cases of both vanishing and nonvanishing mean induced electric field strengths are solved in terms of complimentary error functions as well as some elementary functions. It is shown that the solutions are reducible to that of the steady case as the time approaches infinity, and to that of the nonmagnetic field as the Hartmann number becomes zero. Some numerical calculations are given. The results indicate that in the presence of a magnetic field the flow rate is reduced depending on the magnitude of the Hartmann number, and that the magnetic field "assists" the flow to reach its steady condition.

(1) Introduction

THE PROBLEM of the formation of Couette flow in a nonmagnetic field—i.e., the problem of how the velocity profile varies with time tending asymptotically to the linear distribution of the steady case—is well known.[1] The solution may be expressed by a series of complimentary error functions. It is the purpose of this paper to generalize the problem covering the case of the formation of Couette flow of an electrically conducting viscous fluid in the presence of a magnetic field.

In a magnetic field the motion of an electrically conducting fluid is subjected to the electromagnetic forces of the field. Meanwhile, the motion induces an electric current and consequently causes a change of the electromagnetic field and forces. This interrelation between forces and motion is one of the main features of magnetohydrodynamics. The basic hydrodynamic equations must be modified to include this interrelation. A problem related to this study on steady hypersonic Couette flow in a magnetic field has been studied by Bleviss.[2]

In Section (2) we list the basic equations of the electromagnetic field and of hydrodynamic flow. Section (3) shows the proper reduction of these equations to the problem of unsteady Couette flow. The problem of the formation of Couette flow with vanishing electric field intensity is then solved in Section (4). The solution is reducible to that of the steady case as the time approaches infinity, and to that of the nonmagnetic field as the magnetic strength becomes zero. The problem with nonvanishing electric field intensity is studied in Section (5) with an assumption that the effect of electric field intensity may be averaged over a section of the channel. Finally, some numerical results are given in Section (6).

Received May 25, 1959. Revised and received July 25, 1959.

* Associate Professor of Mechanics, Department of Mechanics.

The author wishes to thank the Graduate School of the Illinois Institute of Technology and the Esso Educational Foundation, for a faculty research fellowship which made this investigation possible, and Professor P. Chiarulli and D. W. Prosser, for their valuable suggestions and comments.

(2) Basic Equations

First, we record the relevant electromagnetic equations without the displacement currents[3] for constant magnetic permeability μ and electric conductivity σ in the system of consistent m.k.s. units:

$$\text{curl } \mathbf{H} = \mathbf{j} \tag{2.1}$$

$$\text{div } \mathbf{j} = 0 \tag{2.2}$$

$$\text{curl } \mathbf{E} = -\partial \mathbf{B}/\partial t \tag{2.3}$$

$$\mathbf{B} = \mu \mathbf{H} \tag{2.4}$$

$$\text{div } \mathbf{B} = \text{div } \mathbf{H} = 0 \tag{2.5}$$

$$\mathbf{j} = \sigma(\mathbf{E} + \mathbf{q} \times \mathbf{B}) \tag{2.6}$$

where **B, H, j, E,** and **q** are the magnetic induction, magnetic field, current intensity, electric field intensity, and velocity, respectively.

The basic equations of an incompressible magnetohydrodynamically interacting fluid are

$$\text{div } \mathbf{q} = 0 \tag{2.7}$$

$$D\mathbf{q}/Dt = -(1/\rho) \text{ grad } p + \nu \nabla^2 \mathbf{q} + (\mu/\rho)\mathbf{j} \times \mathbf{H} \tag{2.8}$$

where p, ρ, and ν are the pressure, density, and kinematic viscosity, respectively. D/Dt is the usual material derivative. In the momentum equation, Eq. (2.8), the gravity force has been neglected.

(3) Unsteady Couette Flow

Consider a laminar flow of an electrically conducting liquid between two parallel plates, one of which suddenly executes a constant speed u_0. Let the plates be at $y = 0$ and $y = h$. We assume that the flow is in the x direction only and that a uniform magnetic field H_0 is imposed perpendicular to the plates. And we further assume that the walls are nonconducting.

With the above hypotheses we may say that all physical quantities are, at most, functions of y and t. Using Eqs. (2.2) and (2.5) and the assumption that the

walls are nonconducting, we conclude that

$$H_y = H_0, \quad j_y = 0 \tag{3.1}$$

Therefore, Eq. (2.8), expressed in component forms, is

$$\partial u/\partial t = \nu(\partial^2 u/\partial y^2) - (\mu/\rho) j_z H_0 \tag{3.2}$$

$$\partial p/\partial y = \mu j_z H_x \tag{3.3}$$

From Eqs. (2.1) and (2.3) we get

$$j_z = -(\partial H_x/\partial y) \tag{3.4}$$

$$\partial E_z/\partial y = -\mu(\partial H_x/\partial t) \tag{3.5}$$

Furthermore, from Ohm's law, Eq. (2.6), we have

$$j_z = \sigma(E_z + \mu H_0 u) \tag{3.6}$$

Combining Eqs. (3.3) and (3.4), we obtain

$$p = -\mu H_x^2/2 + C(t)$$

where H_x may be found from Eqs. (3.4) and (3.6) after the flow field is determined. This pressure is known as the "magnetic pressure.[4]"

Finally, by combining Eqs. (3.2) and (3.6), we conclude that the flow field is governed by

$$\partial u/\partial t = \nu(\partial^2 u/\partial y^2) - (\sigma\mu/\rho) H_0 E_z - (\sigma\mu^2 H_0^2/\rho) u \tag{3.7}$$

In general, E_z of the problem is a function of both y and t. Its magnitude is directly related to the electric resistance of the fluid, or, in dimensionless form, to the magnetic Reynolds number,[4, 5] which may be interpreted as the ratio of motion-induced magnetic field to applied magnetic field. When the electric resistance or the magnetic Reynolds number is small, we may neglect E_z entirely from the consideration of order of magnitude. This assumption has been used in some previous investigations.[2, 6, 7] Physically, this corresponds to the case where the lines of magnetic force were frozen in the field.

With $E_z = 0$, Eq. (3.7) is reduced to

$$\partial u/\partial t = \nu(\partial^2 u/\partial y^2) - mu \tag{3.8}$$

where

$$m = \sigma\mu^2 H_0^2/\rho \tag{3.9}$$

The solution to this equation is given in Section (4).

If we retain the E_z term in Eq. (3.7), the complete solution is undoubtedly quite complicated. In this study a simplifying assumption will be adopted. It is known that in the steady case E_z is independent of y (a pure constant), since

$$\partial E_z/\partial y = -\mu(\partial H_x/\partial t) = 0 \tag{3.10}$$

Also the present study is an investigation of the time effect on the flow in the presence of a magnetic field. We shall assume that E_z may be taken as constant at a particular time. In other words, E_z may be treated as the integrated mean over a section. This means that E_z in Eq. (3.7) may be replaced by the average value $\bar{E}_z$, which is a function of t only. The validity of this assumption may be seen from a rough estimate of the order

$$(\partial E_z/\partial t)/(\partial E_z/\partial y) = 0(h/\tau) \tag{3.11}$$

where τ is the time of decay[4] which is of the order of

$$\tau \approx \rho/(\sigma\mu^2 H_0^2) \tag{3.12}$$

With

$$\bar{E}_z(t) = (1/h)\int_0^h E_z(y, t)\,dy \tag{3.13}$$

Eq. (3.7) may be written as

$$\partial u/\partial t = \nu(\partial^2 u/\partial y^2) - A(t) - mu \tag{3.14}$$

where

$$A(t) = (\sigma\mu/\rho) H_0 \bar{E}_z(t), \quad m = \sigma\mu^2 H_0^2/\rho \tag{3.15}$$

The solution to this equation is given in Section (5).

(4) Formation of Couette Flow With Vanishing E_z

In this section we will discuss the solution of the formation of Couette flow with $E_z = 0$. The simplification of $E_z = 0$ has been used by some investigators on various magnetohydrodynamics problems; for example, the hypersonic Couette flow by Bleviss,[2] the impulse motion of an infinite flat plate by Rossow,[6] and motion near an oscillating flat plate by Ong and Nicholls.[7] Furthermore, it will be shown in the next section that the solution with $E_z = 0$—i.e., with frozen magnetic field—is useful for that with nonvanishing $\bar{E}_z$.

The basic equation with $E_z = 0$ is

$$(\partial u/\partial t) + mu = \nu(\partial^2 u/\partial y^2) \tag{4.1}$$

and the boundary conditions are

$$\left.\begin{array}{lll} t \le 0, & 0 \le y \le h; & u = 0 \\ t > 0, & y = 0; & u = u_0 \\ t > 0, & y = h; & u = 0 \end{array}\right\} \tag{4.2}$$

Clearly the problem can be solved by the use of the Laplace transform. However, the procedure, though straightforward, is quite tedious. In the following we will solve the problem by means of a general theorem about differential equations of the parabolic type—namely, Duhamel's theorem.[8]

Introducing

$$v = u\, e^{mt} \tag{4.3}$$

Eq. (4.1) becomes

$$\partial v/\partial t = \nu(\partial^2 v/\partial y^2) \tag{4.4}$$

and the boundary conditions are

$$\left.\begin{array}{lll} t \le 0, & 0 \le y \le h; & v = 0 \\ t > 0, & y = 0; & v = u_0\, e^{mt} \\ t > 0, & y = h; & v = 0 \end{array}\right\} \tag{4.5}$$

First, we seek the solution with boundary conditions independent of t;

$$\left.\begin{array}{lll} t \le 0, & 0 \le y \le h; & v = 0 \\ t > 0, & y = 0; & v = u_0 \\ t > 0, & y = h; & v = 0 \end{array}\right\} \tag{4.6}$$

The solution[1] satisfying Eq. (4.4) and the time independent boundary conditions (4.6) is

$$v/u_0 = \sum_{n=0}^{\infty} \operatorname{erfc}\,[2n\eta_1 + \eta] - \sum_{n=0}^{\infty} \operatorname{erfc}[2(n+1)\eta_1 - \eta] \quad (4.7)$$

where

$$\eta_1 = h/2(\nu t)^{1/2}, \quad \eta = y/2(\nu t)^{1/2} \quad (4.8)$$

and $\operatorname{erfc}(z)$ is the complimentary error function—i.e.,

$$\operatorname{erfc}(z) = 2\pi^{-(1/2)} \int_z^{\infty} e^{-s^2}\, ds \quad (4.9)$$

By applying Duhamel's theorem, the solution satisfying Eq. (4.4) and conditions (4.5) is

$$\frac{v}{u_0} = \int_0^t e^{mt'} \frac{\partial}{\partial t} \left\{ \sum_{n=0}^{\infty} \operatorname{erfc}\left[\frac{2nh + y}{2\sqrt{\nu(t-t')}}\right] - \sum_{n=0}^{\infty} \operatorname{erfc}\left[\frac{2(n+1)h - y}{2\sqrt{\nu(t-t')}}\right] \right\} dt' \quad (4.10)$$

Changing the variables of integrations,

$$s_n = \frac{2nh + y}{2\sqrt{\nu(t-t')}} \quad \text{and} \quad s_n = \frac{2(n+1)h - y}{2\sqrt{\nu(t-t')}} \quad (4.11)$$

for the first and second series, respectively, we have

$$\frac{v}{u_0} = \frac{2}{\pi^{1/2}} \left\{ \sum_{n=0}^{\infty} \int_{(2nh+y)/2\sqrt{\nu t}}^{\infty} \exp\left[mt - \frac{m(2nh+y)^2}{4\nu s_n^2} - s_n^2 \right] ds_n - \sum_{n=0}^{\infty} \int_{[2(n+1)h-y]/2\sqrt{\nu t}}^{\infty} \exp\left[mt - \frac{m[2(n+1)h - y]^2}{4\nu s_n^2} - s_n^2 \right] ds_n \right. \quad (4.12)$$

Performing the integrations leads to

$$\begin{aligned} \frac{v}{u_0} = \frac{e^{mt}}{2} \left\{ \sum_{n=0}^{\infty} \exp\left[\left(\frac{m}{\nu}\right)^{1/2} (2nh + y) \right] \operatorname{erfc}\left[\frac{2nh+y}{2(\nu t)^{1/2}} + (mt)^{1/2} \right] + \right. \\ \sum_{n=0}^{\infty} \exp\left[- \left(\frac{m}{\nu}\right)^{1/2} (2nh + y) \right] \operatorname{erfc}\left[\frac{2nh+y}{2(\nu t)^{1/2}} - (mt)^{1/2} \right] - \sum_{n=0}^{\infty} \exp\left[\left(\frac{m}{\nu}\right)^{1/2} \{2(n+1)h - y\} \right] \times \\ \operatorname{erfc}\left[\frac{2(n+1)h - y}{2(\nu t)^{1/2}} + (mt)^{1/2} \right] - \sum_{n=0}^{\infty} \exp\left[- \left(\frac{m}{\nu}\right)^{1/2} \{2(n+1)h - y\} \right] \times \\ \left. \operatorname{erfc}\left[\frac{2(n+1)h - y}{2(\nu t)^{1/2}} - (mt)^{1/2} \right] \right\} \end{aligned} \quad (4.13)$$

Introducing

$$\alpha = (\nu t)^{1/2}/\mathrm{h}, \quad \xi = y/h, \quad M = (m/\nu)^{1/2} h \quad (4.14)$$

where M is the Hartmann number,[4, 5] which may be interpreted as the ratio of "induction drag" to viscous drag.

The solution of Eq. (4.1) is then

$$\begin{aligned} \frac{u}{u_0} = \frac{1}{2} \left\{ \sum_{n=0}^{\infty} \exp\,[M(2n + \xi)] \operatorname{erfc}\left[\frac{2n+\xi}{2\alpha} + \alpha M \right] + \sum_{n=0}^{\infty} \exp\,[-M(2n + \xi)] \times \right. \\ \operatorname{erfc}\left[\frac{2n+\xi}{2\alpha} - \alpha M \right] - \sum_{n=0}^{\infty} \exp\,[M\{2(n+1) - \xi\}] \operatorname{erfc}\left[\frac{2(n+1) - \xi}{2\alpha} + \alpha M \right] - \\ \left. \sum_{n=0}^{\infty} \exp\,[-M\{2(n+1) - \xi\}] \operatorname{erfc}\left[\frac{2(n+1) - \xi}{2\alpha} - \alpha M \right] \right\} \end{aligned} \quad (4.15)$$

The convergence of these series can be easily established since $|\operatorname{erfc}(z)| \leq 2$ and the remaining parts are combinable in the form of hyperbolic functions.

As $\alpha = (\nu t)^{1/2}/h \to \infty$, using

$$\operatorname{erfc}(\infty) = 0 \quad \text{and} \quad \operatorname{erfc}(-\infty) = 2 \quad (4.16)$$

we have the solution of steady Couette flow

$$\left. \begin{aligned} \frac{u}{u_0} = \sum_{n=0}^{\infty} \exp[-M(2n + \xi)] - \sum_{n=0}^{\infty} \exp\,[-M(2n + 2 - \xi)] \\ = \sinh M(1 - \xi)/\sinh M \end{aligned} \right\} \quad (4.17)$$

Also, as $M \to 0$, Eq. (4.15) is reduced to Eq. (4.7)—i.e., the solution in a nonmagnetic field.

(5) Formation of Couette Flow With Nonvanishing $\bar{E}_z$

With nonvanishing $\bar{E}_z$, the governing equation is

$$(\partial u/\partial t) + A(t) + mu = \nu(\partial^2 u/\partial y^2) \quad (5.1)$$

and the boundary conditions are

$$\left.\begin{array}{lll} t \le 0, & 0 \le y \le h; & u = 0 \\ t > 0, & y = 0; & u = u_0 \\ t > 0, & y = h; & u = 0 \end{array}\right\} \tag{5.2}$$

Let $$u = w\, e^{-mt} - e^{-mt} \int_0^t A(t)\, e^{mt}\, dt \tag{5.3}$$

$w(y, t)$ must satisfy

$$\partial w/\partial t = \nu(\partial^2 w/\partial y^2) \tag{5.4}$$

and boundary conditions

$$\left.\begin{array}{lll} t \le 0, & 0 \le y \le h; & w = 0 \\ t > 0, & y = 0; & w = u_0\, e^{mt} + f(t) \\ t > 0, & y = h; & w = f(t) \end{array}\right\} \tag{5.5}$$

where $$f(t) = \int_0^t A(t)\, e^{mt}\, dt \tag{5.6}$$

Write $$w(y, t) = w_1(y, t) + w_2(y, t) \tag{5.7}$$

such that $w_1(y, t)$ corresponds to the solution $E_z = 0$. The solution of $w_1(y, t)$ is given in the previous section.

$w_2(y, t)$ must satisfy

$$\partial w_2/\partial t = \nu(\partial^2 w_2/\partial y^2) \tag{5.8}$$

and the boundary conditions

$$\left.\begin{array}{lll} t \le 0, & 0 \le y \le h; & w_2 = 0 \\ t > 0, & y = 0; & w_2 = f(t) \\ t > 0, & y = h; & w_2 = f(t) \end{array}\right\} \tag{5.9}$$

Again we first seek the solution which satisfies Eq. (5.8) and the boundary conditions

$$\left.\begin{array}{lll} t \le 0, & 0 \le y \le h; & w_2 = 0 \\ t > 0, & y = 0 \text{ and } y = h; & w_2 = 1 \end{array}\right\} \tag{5.10}$$

By means of the Fourier expansion, it can be easily found that the solution satisfying Eq. (5.8) and conditions (5.10) is

$$w_2 = 1 - (4/\pi) \sum_{n=0}^{\infty} [1/(2n+1)] \times \exp[-\nu(2n+1)^2\pi^2 t/h^2] \sin [(2n+1)\pi y/h] \tag{5.11}$$

Again Duhamel's theorem shows that the solution which satisfies (5.8) and (5.9) is

$$w_2 = \int_0^t f(s)(\partial/\partial t) F(y, t-s) ds \tag{5.12}$$

where $$F(y, t-s) = 1 - \frac{4}{\pi} \sum_{n=0}^{\infty} \frac{1}{2n+1} \exp\left[-\frac{\nu(2n+1)^2\pi^2(t-s)}{h^2}\right] \sin \frac{(2n+1)\pi y}{h} \tag{5.13}$$

or

$$w_2 = \frac{4\pi\nu}{h^2} \sum_{n=0}^{\infty} (2n+1) \exp\left[-\frac{\nu(2n+1)^2\pi^2 t}{h^2}\right] \sin \frac{(2n+1)\pi y}{h} \cdot \int_0^t f(s) \exp\left[\frac{\nu(2n+1)^2\pi^2 s}{h^2}\right] ds \tag{5.14}$$

Therefore, the complete solution of the problem with nonvanishing $\bar{E}_z$ is

$$\begin{aligned} u &= (w_1 + w_2)e^{-mt} - f(t)e^{-mt} \\ &= \frac{u_0}{2} \left\{ \sum_{n=0}^{\infty} \exp[M(2n+\xi)] \operatorname{erfc}\left[\frac{2n+\xi}{2\alpha} + \alpha M\right] + \sum_{n=0}^{\infty} \exp[-M(2n+\xi)] \times \right. \\ &\qquad \operatorname{erfc}\left[\frac{2n+\xi}{2\alpha} - \alpha M\right] - \sum_{n=0}^{\infty} \exp[M(2n+2-\xi)] \operatorname{erfc}\left[\frac{2n+2-\xi}{2\alpha} + \alpha M\right] - \\ &\qquad \left. \sum_{n=0}^{\infty} \exp[-M(2n+2-\xi)] \operatorname{erfc}\left[\frac{2n+2-\xi}{2\alpha} - \alpha M\right] \right\} + 4\pi\alpha^2 e^{-\alpha^2 M^2} \sum_{n=0}^{\infty} (2n+1) \times \\ &\qquad \exp[-(2n+1)^2\pi^2\alpha^2] \cdot \sin[(2n+1)\pi\xi] \int_0^1 f(t\zeta) \exp[(2n+1)^2\pi^2\alpha^2\zeta] d\zeta - f(t)e^{-\alpha^2 M^2} \end{aligned} \tag{5.15}$$

When $\bar{E}_z$ may be taken as constant, $f(t)$ and the integral in Eq. (5.15) can be readily obtained. Let $\bar{E}_z = K$, then

$$f(t) = (K/\mu H_0)(e^{mt} - 1) = (K/\mu H_0)(e^{\alpha^2 M^2} - 1) \tag{5.16}$$

and

$$\int_0^1 f(t\zeta) \exp[(2n+1)^2\pi^2\alpha^2\zeta] d\zeta = \frac{K}{\mu H_0} \left\{ \frac{\exp[(2n+1)^2\pi^2\alpha^2 + \alpha^2 M^2] - 1}{(2n+1)^2\pi^2\alpha^2 + \alpha^2 M^2} - \frac{\exp[(2n+1)^2\pi^2\alpha^2] - 1}{(2n+1)^2\pi^2\alpha^2} \right\} \tag{5.17}$$

The convergence of Eq. (5.15) can be established by the same approach mentioned in the previous section, since both $\sin z$ and $f(z)$ are bounded.

In order to complete the problem, the function $\bar{E}_z(t)$ must be determined from the relevant equations and the boundary conditions. Since the walls are nonconducting, we have

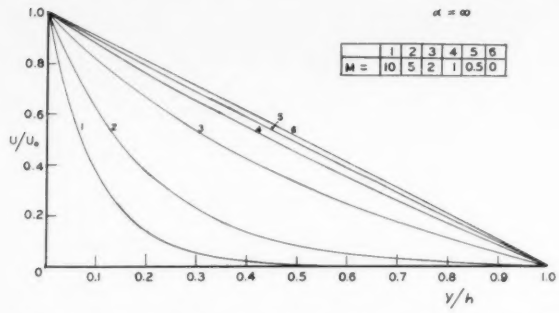

FIG. 1. Velocity profiles—steady flow with different Hartmann numbers.

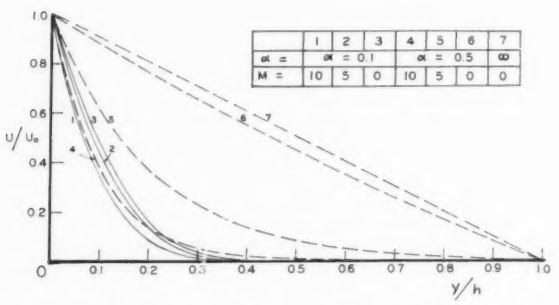

FIG. 2. Velocity profiles—different Hartmann numbers and fixed time parameters.

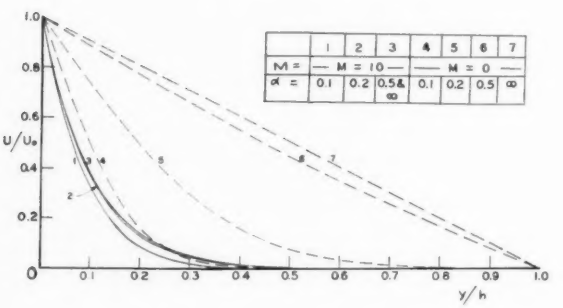

FIG. 3. Velocity profiles—different time parameters and fixed Hartmann numbers.

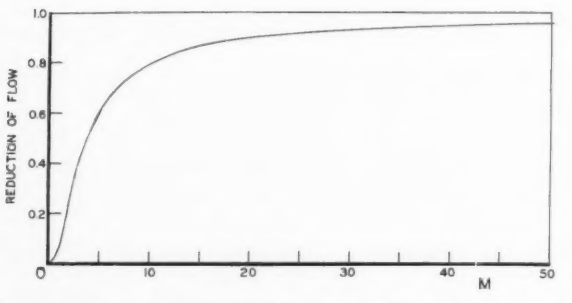

FIG. 4. Relation between reduction of flow and Hartmann number, $(Q_{M=0} - Q_{M=M})/Q_{M=0}$ vs. M; steady flow.

$$\int_0^h j_z\,dy = \sigma \int_0^h (\bar{E}_z + \mu H_0 u)\,dy = 0 \quad (5.18)$$

or

$$\bar{E}_z(t) = -\mu H_0 \int_0^1 u\,d\xi \quad (5.19)$$

Furthermore, as we take $\bar{E}_z$ = constant, we have

$$\lim_{\tau\to\infty} \frac{1}{\tau} \int_0^\tau \int_0^h (\bar{E}_z + \mu H_0 u)\,dy\,dt = 0 \quad (5.20)$$

or

$$\bar{E}_z = K = -\lim_{\tau\to\infty} (\mu H_0/\tau) \int_0^\tau \int_0^1 u\,d\xi\,dt \quad (5.21)$$

(6) Numerical Results

Due to the lengthy solution of the problem, only the numerical results with vanishing E_z will be given here. Fig. 1 shows a comparison of the steady cases with different Hartmann numbers. It can be readily seen that the magnetic force has the effect of retarding the motion. This is one of the features of fluid motion in the presence of a magnetic field.[4, 5] In the momentum equation, Eq. (2.8), we may observe that the term

$$\mathbf{j} \times \mathbf{H} = \sigma\mu(\mathbf{q} \times \mathbf{H}) \times \mathbf{H}$$

always has a component opposite to the direction of flow.

Figs. 2 and 3 give the velocity profiles at different Hartmann numbers with fixed α, and at different α with fixed Hartmann numbers. These two figures clearly indicate that the motion in the presence of a strong magnetic field will approach its steady case in a shorter time, and that for a given magnetic field the decrease of flow at the early stage is less than that at the later time. Fig. 4 gives in dimensionless form the reduction of the flow of steady cases due to the presence of a magnetic field.

References

[1] Schlichting, H., *Boundary Layer Theory*, p. 66; McGraw-Hill Book Company, Inc., New York, 1955.

[2] Bleviss, Z. O., *Magnetogasdynamics of Hypersonic Couette Flow*, Journal of the Aero/Space Sciences, Vol. 25, No. 10, pp. 601–615, October, 1958.

[3] Landshoff, R. K. (Ed.), *Magnetohydrodynamics*, Elsasser, W. M., "Some Dimensional Aspects of Hydromagnetic Phenomena," pp. 16–28, Stanford University Press, Stanford, Calif., 1957.

[4] Cowling, T. G., *Magnetohydrodynamics*, Interscience Publishers, Inc., New York, 1957.

[5] Resler, E. L., Jr., and Sears, W. R., *The Prospects for Magneto-Aerodynamics*, Journal of the Aeronautical Sciences, Vol. 25, No. 4, pp. 235–245, 258, April, 1958.

[6] Rossow, V. J., *On Flow of Electrically Conducting Fluids Over a Flat Plate in the Presence of a Transverse Magnetic Field*, NACA TN 3971, May, 1957.

[7] Ong, R. S., and Nicholls, J. A., *On the Flow of a Hydromagnetic Fluid Near an Oscillating Flat Plate*, Journal of the Aero/Space Sciences, Readers' Forum, Vol. 26, No. 5, pp. 313–314, May, 1959.

[8] Sneddon, I. N., *Fourier Transform*, p. 164, McGraw-Hill Book Company, Inc., New York, 1951.

On the Estimation of Structural Damping From Aircraft Resonance Tests

RONALD D. MILNE*

Queen Mary College, University of London

Summary

The inclusion of an allowance for structural damping in flutter calculations is becoming increasingly necessary. Within the framework of linearized "complex" damping, a method is proposed for estimating, from ground resonance tests on the prototype aircraft, appropriate damping coefficients for incorporation into the flutter equations. The revised flutter calculations normally undertaken at this stage may thus include a realistic allowance for structural damping; in particular, account may be taken of the coupling which normally exists in practice between undamped normal modes.

The method is developed from a theoretical standpoint, but with reference to probable practical difficulties. The relationship between the theoretical semirigid approach and the measured responses taken from the actual aircraft is illustrated by a simplified theoretical example.

(1) Introduction

THE USUAL theoretical procedure for predicting the flutter speed of an aircraft is well known. The aircraft is replaced by a dynamic model having a finite number of degrees of freedom and a set of linear differential equations of motion is set up, embodying the structural, inertial, and aerodynamic attributes of the model. These equations are solved under conditions of simple harmonic motion to yield flutter speed, frequency, and mode.

It may be very important to include some estimate of structural damping in the equations, and recent practice has been to use measured or calculated normal modes as coordinate functions for the model and to add to the equations of motion quadrature terms representing the effect of "complex" damping in simple harmonic motion. However, because of a fundamental lack of knowledge as to the distribution of such structural damping, only direct damping terms, of a magnitude consistent with experimental results obtained from simple structural elements, are normally included. Such damping terms do nothing to couple the normal modes used as coordinate functions, and this coupling may be important in altering the flutter mode and so the flutter speed. It is in an attempt to estimate both direct and coupling terms appropriate to the dynamic model adopted that the present method is proposed.

Extensive resonance testing of a prototype aircraft is mandatory, and current flutter calculations are normally revised using information obtained from such tests. By measuring the complex response of the aircraft to a number of harmonic forcing systems it is suggested that a set of damping coefficients may be estimated for inclusion in the revised flutter equations. The tests would not involve equipment additional to that normally required for the application of multipoint vibration techniques to the estimation of undamped normal modes.

The method is not dependent on the use of normal modes as coordinate functions, although these are convenient and would tend to yield more accurate estimates of the damping coefficients than arbitrary functions.

Success is obviously consequent upon how well the concept of linear "complex" damping may describe the internal dissipation of energy in complicated aircraft structures.

Received May 12, 1959.

*Lecturer, Department of Aeronautical Engineering.

(2) Analysis

The aircraft structure is replaced by a semirigid model having n degrees of freedom characterized by n chosen coordinate functions and their associated amplitudes $c_r(t)$. The choice of the coordinate functions and their number will be governed by the nature of the flutter problem to be investigated; they may be arbitrarily chosen but physically likely functions, interpolation functions (in which case the $c_r(t)$ are the actual displacements at n points of the structure), or undamped normal modes based on calculation or measurement. Functions having zero strain energy are not considered.

The analysis deals only with the steady-state response of the model to an harmonic force input of circular frequency ω. Accordingly, putting

$$c_r(t) = (a_r + ib_r)e^{i\omega t} \tag{1}$$

the algebraic response equations are

$$(-\omega^2[m] + [k] + i[g])\{a + ib\} = \{p\} \tag{2}$$

where $[m]$, $[k]$, $[g]$ are, respectively, the matrices of generalized inertia, stiffness, and (complex) damping coefficients, and $\{p\}$ is the column matrix of generalized force amplitudes chosen for convenience to be entirely "in-phase."

An alternative form of Eq. (2) consists of the simultaneous equations

$$[e]\{a\} - [g]\{b\} = \{p\} \tag{3a}$$

$$[g]\{a\} + [e]\{b\} = 0 \tag{3b}$$

with $$[e] = -\omega^2[m] + [k]$$

It is assumed that the mass distribution of the structure has been assessed and that the generalized inertia coefficients have been estimated therefrom; in addition, either by structural analysis or by measurement of undamped normal modes and their frequencies, it is assumed that the generalized stiffness coefficients have also been estimated. Thus, at any frequency ω the matrix $[e]$ is determined at least within a framework of those assumptions usually involved in classical flutter calculations.

Let the known force distribution $\{p\}_s$ of circular frequency ω_s be applied to the actual structure; then, by measurement of the complex response at n points and the use of a suitable geometric coordinate transformation based on the particular semirigid model adopted, the response vectors $\{a\}_s$, $\{b\}_s$ may be estimated. Since the semirigid model can only approximate the actual response of the structure the use of more than n measuring points will not, in general, yield a consistent transformation; clearly, then, the choice of the n measuring points will influence the estimation of the response vectors. This is a consideration to be reckoned with in the practical application.

For every force-frequency combination $\{p\}_s$, ω_s, the response equations are

$$[e]_s\{a\}_s - [g]\{b\}_s = \{p\}_s \tag{4a}$$

$$[g]\{a\}_s + [e]_s\{b\}_s = 0 \tag{4b}$$

wherein, according to the foregoing discussion, only the elements of the matrix $[g]$ are unknown. Premultiply each of Eqs. (4) by a row matrix having ciphers everywhere except for unity in the rth column giving the scalar equations,

$$[e_r]_s\{a\}_s - [g_r]\{b\}_s = p_{rs} \tag{5a}$$

$$[g_r]\{a\}_s + [e_r]_s\{b\}_s = 0 \tag{5b}$$

where the row matrices $[e_r]_s$, $[g_r]$ represent, respectively, the rth row of the matrices $[e]_s$, $[g]$. Let m force-frequency combinations be applied to the structure yielding m response columns $\{a\}_s$, $\{b\}_s$. Let the (n, k) matrices $[a_k]$, $[b_k]$ be formed by columns from any k columns of the complete set; similarly, the matrices $[a_l]$, $[b_l]$ are formed from any l columns ($k, l \leq m$).

Writing Eq. (5a) for each of the selected l column pairs and Eq. (5b) for each of the selected k column pairs and rearranging, then

$$[g_r]\,[b_l] = \left[\,[e_r]_s\{a\}_s - p_{rs}\right], \quad s = 1 \text{ to } l \tag{6a}$$

$$[g_r]\,[a_k] = \left[\,-[e_r]_s\{b\}_s\right], \quad s = 1 \text{ to } k \tag{6b}$$

Eqs. (6a) and (6b) may be combined in terms of partitioned matrices to give

$$[g_r]\left[\,[a_k],\ [b_l]\,\right] = \left[\,-[e_r]_s\{b\}_s,\ [e_r]_s\{a\}_s - p_{rs}\right] \tag{7}$$

Eq. (7) represents a set of simultaneous equations for the elements of the rth row of $[g]$ provided the equations are consistent and the rank of

$$[a_k,\ b_l] = \left[\,[a_k]\,,\ [b_l]\,\right]$$

is not less than n. Consistency is ensured in the theoretical case by the fact that the response columns satisfy Eqs. (4); however, in the practical case, this condition is not likely to be satisfied exactly and it becomes necessary to select only n of the equations for solution. This selection is obviously important to the success of the method and is best made by choosing, at the outset, a suitable set of force-frequency combinations.

Accordingly, the rank of $[a_k,\ b_l]$ is considered only when $l = n - k$ under two sets of k force-frequency combinations which may in the general case be combined (the number of force-frequency combinations need not exceed k or l, whichever is the greater; here, $k > l$): Set (a), at one frequency, k linearly independent force columns $\{p\}_s$; Set (b), one force column at k distinct frequencies ω_s.

In the case of excitation by Set (a) it is convenient to use certain results based on Characteristic Phase Lag Theory.[1] Thus at any given frequency there exists a complete n-fold vector base of real forcing columns $\{y\}_j$ whereby if any arbitrary n-element forcing column $\{p\}$ is expressed in terms of this base, for example,

$$\{p\} = \sum_{j=1}^{n} \beta_j\{y\}_j = [y_n]\{\beta\} \tag{8}$$

then the response vectors are given by

$$\{a\} = \sum_{j=1}^{n} \beta_j \cos\varphi_j\{r\}_j = [r_n]\,[\cos\varphi_n]\,\{\beta\} \tag{9a}$$

$$-\{b\} = \sum_{j=1}^{n} \beta_j \sin\varphi_j\{r\}_j = [r_n]\,[\sin\varphi_n]\,\{\beta\} \tag{9b}$$

where the $\{r\}_j$ are n linearly independent frequency response modes and the φ_j are the n characteristic phase angles for the system; both the $\{r\}_j$ and the φ_j are functions of the frequency of excitation.

For k independent forcing columns $\{p\}_s$ Eqs. (8) and (9) may be written in the forms

$$[p_k] = [y_n]\,[\beta_k] \tag{10}$$

$$[a_k] = [r_n]\,[\cos\varphi_n]\,[\beta_k] \tag{11a}$$

$$-[b_k] = [r_n]\,[\sin\varphi_n]\,[\beta_k] \tag{11b}$$

where the matrix $[\beta_k]$ is of order (n, k).

Without loss of generality consider the rank of the matrix [cf. Eq. (7)],

$$[a_k,\ b_{n-k}] = [r_n]\,[\sin\varphi_n]\left[\,[\cot\varphi_n]\,[\beta_k],\ -[\beta_{n-k}]\,\right]$$

wherein one of the φ_j may be $\pi/2$ if the chosen frequency is coincident with an undamped natural frequency. The matrices $[r_n]$, $[\sin\varphi_n]$ being nonsingular the rank of $[a_k,\ b_{n-k}]$ is not less than the rank of

$$\left[\,[\cot\varphi_n]\,[\beta_k],\ -[p_{n-k}]\,\right]$$

A Laplacian expansion in the first k columns of the

determinant of this matrix gives

$$\left|\,[\cot \varphi_n]\,[\beta_k],\ -[\beta_{n-k}]\,\right| = \sum_j \left(\prod_i \cot \varphi_i\right)_j \left(\left|\beta_k\right|\ \left|\beta_{n-k}\right|\right)_j$$

where $|\beta_k|$, $|\beta_{n-k}|$ are, respectively, any kth order minor and its $(n-k)$th order complementary minor, the continued product contains any k cot φ from n and the summation contains as many terms as there are combinations of k from n. Since the k $\{p\}_s$ are chosen to be independent then $[\beta_k]$ is of rank k and will contain at least one minor of order k which is not zero. In addition, at least one product $(|\beta_k|\ |\beta_{n-k}|)$ will not be zero except in the particular case when two columns appearing both in $[\beta_k]$ and $[\beta_{n-k}]$ differ in one element only; this in turn implies that the difference of two forcing columns $\{p\}_r$, $\{p\}_s$ is proportional to one of the base forcing columns $\{y\}_j$. In this case it cannot be asserted that $[a_k,\ b_{n-k}]$ is of rank n.

Since it may be irksome to avoid such a hazard in practice a safer procedure is to use n independent forcing columns $\{p\}_s$ and to solve Eq. (7) either with $l = n$, $k = 0$ or with $k = n$, $l = 0$. The independence of the $\{p\}_s$ then ensures that both $[a_n]$ and $[b_n]$ are of rank n [Eq. (11)] except when one of the characteristic angles is $\pi/2$ and $[a_n]$ may contain a null column.

The above and later considerations point to the equation

$$[g_r]\,[b_n] = \left[\,[e_r]_s\{a\}_s - p_{rs}\right],\ s = 1 \text{ to } n \qquad (12)$$

as the most suitable for the determination of the damping coefficients.

Following these considerations the case of excitation by Set (b) will be discussed only with reference to Eq. (12)—i.e., rank of $[b_n]$—and when ω_s takes n different values. Solving Eqs. (4) for $\{b\}_s$ then,

$$\left[I + ([g]^{-1}[e]_s)^2\right]\{b\}_s = -[g]^{-1}\{p\} \qquad (13)$$

or

$$[D]_s\{b\}_s = \{k\}$$

where $\{k\}$ is a column of constants. The solution for $\{b\}_s$ is

$$\{b\}_s = \left\{\frac{|D_r|_s}{|D|_s}\right\}$$

where $|D_r|_s$ is the determinant of $[D]_s$ with the rth column replaced by $\{k\}$. For each of the n frequencies the matrix of response columns is

$$[b_n] = \left[\frac{|D_r|_s}{|D|_s}\right],\quad s = 1 \text{ to } n.$$

Since $\prod_s^n |D|_s \neq 0$, then $[b_n]$ will be nonsingular if

$$\left|\ |D_r|_s\ \right| \neq 0$$

This determinant may be written

$$\left|f_r(\omega_s^2)\right|$$

where f_r is a polynomial in ω_s^2 of order $(2n-1)$. So long as the n ω_s are different, then the columns of this determinant are independent and $[b_n]$ is of rank n.

The successive rows of $[g]$ may thus be determined by equations like (12) using a set of n independent force-frequency combinations. The complete expression for $[g]$ is

$$[g] = [b_n]^{-1}[h]$$

where

$$h_{rs} = [e_r]_s\{a\}_s - p_{rs}$$

In a recent paper by Traill-Nash[2] a procedure is given for exciting normal modes by determining at each undamped natural frequency that member of the base of forcing columns $[y_n]$ associated with a characteristic phase angle of $\pi/2$. This procedure may be used to estimate the damping coefficients.

Let excitation be at an undamped natural frequency ω_j with forcing column $\{y\}_j$. Response is then entirely in quadrature and the second equation of (3) indicates that the response column $\{b\}_j$ must have the form of the jth normal mode. The first equation of (3) reduces to

$$-[g]\{b\}_j = \{y\}_j$$

and, writing this equation for each undamped natural frequency and corresponding forcing column, then

$$-[g]\,[b_n] = [y_n]$$

or

$$[g] = -[b_n]^{-1}[y_n] \qquad (14)$$

Thus, a knowledge of the n undamped normal modes and the n forcing columns $\{y\}_j$ yields a direct estimate of the damping matrix $[g]$.

(3) A Theoretical Example

The usefulness of the semirigid representation lies in the fact that within a frequency range of interest it is possible to approximate the motion of the aircraft by a finite, usually small, number of degrees of freedom. The quality of this approximation at any frequency used for response measurement will clearly affect the estimation of the model damping coefficients from responses of the actual structure.

With this point in mind a simple theoretical example is worked through in which the responses of a chosen system in five degrees of freedom are used to calculate the damping coefficients belonging to "model" systems which are assumed to have less than five degrees of freedom. Here the responses in five degrees of freedom represent those measured from the actual structure while the various "models" represent semirigid approximations of varying order.

The system chosen is a uniform pinned beam whose uncoupled bending and torsional modes are sine curves. The uncoupled frequencies are chosen as

$$(\omega_i)_b = 1, 4, 9, 16, \ldots i^2$$

$$(\omega_i)_t = 3, 6, 9, 12, \ldots 3i$$

TABLE 1
Matrix of Damping Coefficients

0.1189	0.4478	0.0581	0.2618	0.4826
0.4478	2.6026	0.2838	1.9678	2.0215
0.0581	0.2838	1.3081	0.7873	0.6806
0.2618	1.9678	0.7873	6.6732	0.8392
0.4826	2.0215	0.6806	0.8392	7.9980

TABLE 2
In-Phase Response Columns

−1.244651	0.066187	0.061370	0.007762	0.007531
0.307190	0.090226	−0.156274	−0.070435	−0.040584
−0.016341	−0.173922	0.092150	0.005135	0.008427
−0.023049	−0.089679	−0.087093	0.014481	0.134421
0.036081	−0.019129	−0.016448	0.042750	−0.005016

the frequency coincidence $(\omega_3)_b = (\omega_3)_t = 9$ is deliberately chosen. Inertial coupling is introduced between these modes by offsetting the sectional center of mass. The basic system chosen for the example has as its five degrees of freedom the first five (coupled) normal modes of this beam. The relevant (coupled) frequencies are

$$\omega_1 = 0.981$$
$$\omega_2 = 3.66$$
$$\omega_3 = 3.74$$
$$\omega_4 = 7.16$$
$$\omega_5 = 8.10$$

the generalized inertia matrix is normalized to the unit matrix and the stiffness matrix is the diagonal matrix $[\omega_i^2]$. Damping is introduced in the following ways: (a) uniform damping in bending with angle of loss 0.05 rad., (b) uniform damping in torsion with angle of loss 0.03 rad., (c) concentrated damping at 1/6 and 1/3 span in bending with angle of loss 0.075 rad., and (d) concentrated damping at 1/6 and 1/3 span in torsion with angle of loss 0.150 rad. These sources of damping lead to the matrix of generalized damping coefficients shown in Table 1.

A single force column is used, derived from the use of two in-phase linear exciters—one placed on the flexural axis at 2/3 span and one offset from the flexural axis and located at 5/6 span. The responses to this force column at the five undamped natural frequencies are used as the basis for the recalculation of the damping coefficients. The response matrices $[a_5]$, $[b_5]$ are shown in Tables 2 and 3.

Using Eq. (12), the full damping matrix (Table 1) is readily reproduced, but interest is fixed on the calculation of the appropriate damping matrix when the system is assumed to have only one, two, three, or four degrees of freedom, consisting of the normal (coupled) modes taken in successive order. For these calculations only those terms of the response columns (Tables 2 and 3) corresponding to the retained degrees of freedom are used and only the responses at one, two, three, or four undamped frequencies. Thus, in these cases, the parts of the response columns which are used in the calculation are derived from the response of a more complete system as would be the case in practice. Eq. (12) now leads to damping matrices which are only approximately symmetrical, and these are rendered symmetrical by averaging corresponding elements. On this basis the various approximations to the relevant parts of the full damping matrix belonging to the "model" systems are shown in Table 4.

The approximations to the elements of the full damping matrix are quite acceptable in this case despite the fact that two of the natural (excitation) frequencies are very close together. The use of Eq. (6b), $(k = n)$, instead of Eq. (12) does not yield such a set of satisfactory approximations.

The example does not take into account the changes in the elements of the response columns which would result from the fitting of a reduced number of coordinate functions (in this case the undamped normal modes) to just a sufficient number of measured displacements.

(4) Conclusions

The proposed method could readily form an extension to standard multi-point resonance testing; indeed, when the procedure suggested by Traill-Nash is used the information required is already at hand once the normal modes have been obtained.

Practical difficulties may be severe and the results obtained will depend on the choice of coordinate functions, the choice of measuring points, and the choice of exciting points. The use of normal modes as coordinate functions seems to be preferable to any other set since then the diagonal damping coefficients would probably predominate; furthermore, the effect of neglected (higher frequency) modes will be minimized if responses are measured near resonant frequencies. The exciting forces need not be large in number provided they are capable of exciting adequately all the chosen modes.

(*Continued on page 376*)

TABLE 3
Quadrature Response Columns

−4.037047	−0.000451	0.006716	0.000115	−0.000249
0.021352	0.855556	0.832410	0.001673	−0.003007
0.000001	−0.420396	−0.497447	−0.000736	−0.002030
0.002806	−0.014644	−0.021736	−0.325266	−0.061868
0.004370	−0.002571	−0.008438	0.016484	0.061137

TABLE 4
Approximations to the Damping Coefficients

Damping Coeffs.	Number of Degrees of Freedom 1	2	3	4
g_{11}	0.1158	0.1180	0.1183	0.1184
g_{12}		0.4283	0.4566	0.4542
g_{22}		2.4234	2.7113	2.6657
g_{13}			0.0846	0.0747
g_{23}			0.4546	0.3664
g_{33}			1.4205	1.3567
g_{14}				0.2491
g_{24}				1.9293
g_{34}				0.8000
g_{44}				6.6307

Foucault Pendulum Effect in a Schuler-Tuned System†

CHARLES BROXMEYER*
Massachusetts Institute of Technology

Summary

Three-axis analysis of an undamped, Schuler-tuned, inertial navigation system, carried by a vehicle moving near the Earth's surface, leads to a set of six simultaneous linear differential equations of the first order. Solution of the sixth degree characteristic equation of this set shows that the system errors oscillate with the eighty-four minute period predictable from single-axis analysis and that, in addition, the errors exhibit beats with a period which varies with latitude and velocity. It is shown that this behavior has an analog in the behavior of a Foucault pendulum.

Symbols

$\mathbf{a}$	= acceleration
α, β, γ	= x, y, and z components respectively of $\boldsymbol{\epsilon}$ referred to the indicated coordinate system
$\boldsymbol{\epsilon}$	= vector error angle
$\mathbf{f}$	= specific force
f_x, f_y, f_z	= components of $\mathbf{f}$ referred to the geographic coordinate system
f_x', f_y', f_z'	= components of $\mathbf{f}$ referred to the indicated coordinate system
$\mathbf{g}$	= gravity vector
g	= $g_z = \lvert\mathbf{g}\rvert$
$\mathbf{G}$	= gravitational attraction per unit mass
λ	= geographic latitude
λ'	= computed geographic latitude
r	= length of pendulum
$\mathbf{R}$	= Earth radius vector
R	= $\lvert\mathbf{R}\rvert$
$\mathbf{T}$	= tension
T_x, T_y, T_z	= components of $\mathbf{T}$ referred to the geographic coordinate system
T_s	= Schuler period
T_f	= Foucault period
U_x, U_y, U_z	= gyro drift rates referred to the indicated coordinate system
$\boldsymbol{\omega}$	= angular velocity of the geographic coordinate system
$\omega_x, \omega_y, \omega_z$	= components of $\boldsymbol{\omega}$ referred to the geographic coordinate system
$\boldsymbol{\omega}'$	= angular velocity of the indicated coordinate system
$\omega_x', \omega_y', \omega_z'$	= components of $\boldsymbol{\omega}'$ referred to the indicated coordinate system
ω_e	= longitude rate $\times \cos\lambda$
ω_e'	= computed longitude rate $\times \cos\lambda'$
ω_n	= geographic latitude rate
ω_n'	= computed geographic latitude rate
Δ	= Earth rate vector
Ω	= $\lvert\Delta\rvert$

Subscripts

e	= east
n	= north
x, y, z	= Cartesian components

Received April 16, 1959.

† The material in this paper appeared originally as Report E-654, Instrumentation Laboratory, M.I.T.

* Staff Member, Instrumentation Laboratory.

(1) Introduction

An aspect of the behavior of Schuler-tuned inertial navigation systems which has been of particular interest is the analogy which such systems display to a hypothetical Earth-radius pendulum. The analogy can be expressed by showing that under certain conditions, (single-axis model, nonrotating Earth) the stabilized platform of an undamped inertial navigation system indicates the vertical with an oscillating error that satisfies an equation of the form

$$\ddot{\alpha} + (g/R)\alpha = 0 \tag{1.1}$$

where the period of the oscillation is

$$T_s = 2\pi\sqrt{R/g} \cong 84 \text{ minutes} \tag{1.2}$$

If the analysis of a practicable Schuler-tuned system, having compensation for Coriolis and centrifugal forces, is extended to a three-axis reference system, and the rotation of the Earth taken into account, a further parallel to a simple pendulum is found to exist in that the eighty-four minute error oscillations exhibit long period beats. This behavior is identical with that of a Foucault pendulum tuned to an eighty-four minute period.

Error equations of the pendulum and navigation system problems show the analogy in cross-coupling terms which leads to the parallel behavior. The inertial navigation system does not exhibit the modulated oscillations if the interchannel inertial force compensation is not mechanized.

(2) The Foucault Pendulum

A Foucault pendulum is a spherical pendulum set in motion in a plane and allowed to swing so that the effect of the rotation of the Earth is evident on its behavior. It is found that such a pendulum oscillates in a plane which rotates with constant velocity around the vertical. The period of rotation is

$$T_f = 2\pi/\Omega \sin\lambda \tag{2.1}$$

If the pendulum is observed with respect to a geo-

graphic reference system* with origin at the point of support, the projection of its oscillations on the x and y axes will have the appearance of beat waves with short period

$$T_s = 2\pi\sqrt{R/g} \tag{1.2}$$

and long period

$$T_f = 2\pi/\Omega \sin \lambda \tag{2.1}$$

(3) Analysis of a Foucault Pendulum

The total force acting on the bob of a pendulum is

$$\mathbf{F} = \mathbf{T} + m\mathbf{G} \tag{3.1}$$

where $\mathbf{T}$ is the tension in the pendulum and $\mathbf{G}$ is the gravitational attraction per unit mass. Using Newton's second law,

$$\mathbf{T}/m + \mathbf{G} = \ddot{\mathbf{R}}\big|_s \tag{3.2}$$

where $\mathbf{R}$ extends from a fixed point in an inertial coordinate system to the bob. If $\mathbf{R}$ is referred to a geographic coordinate system with origin at the surface of the Earth, at the point of support, then

$$\mathbf{T}/m + \mathbf{G} = \ddot{\mathbf{R}} + 2\boldsymbol{\Omega} \times \dot{\mathbf{R}} + \boldsymbol{\Omega} \times (\boldsymbol{\Omega} \times \mathbf{R}) \tag{3.3}$$

The gravity vector $\mathbf{g}$ is defined by

$$\mathbf{g} = \mathbf{G} - \boldsymbol{\Omega} \times (\boldsymbol{\Omega} \times \mathbf{R}) \tag{3.4}$$

Substituting Eq. (3.4) into Eq. (3.3)

$$\mathbf{T}/m + \mathbf{g} = \ddot{\mathbf{R}} + 2\boldsymbol{\Omega} \times \dot{\mathbf{R}} \tag{3.5}$$

Let

$$\mathbf{R} = \mathbf{R}_0 + \mathbf{R}_1 \tag{3.6}$$

where $\mathbf{R}_0$ extends from the center of the Earth to the origin of the geographic coordinate system and $\mathbf{R}_1$ extends from the pendulum point of support to the bob. Since $\mathbf{R}_0$ is a constant in the geographic system

$$\mathbf{T}/m + \mathbf{g} = \ddot{\mathbf{R}}_1 + 2\boldsymbol{\Omega} \times \dot{\mathbf{R}}_1 \tag{3.7}$$

If the length of the pendulum is r, then for small oscillations

$$\mathbf{R}_1 \cong ix + jy + kr \tag{3.8}$$

and the rectangular form of Eq. (3.7) is

$$\left.\begin{aligned} T_x/m &= \ddot{x} + 2\Omega\dot{y} \sin \lambda \\ T_y/m &= \ddot{y} - 2\Omega\dot{x} \sin \lambda \\ T_z/m &= 2\Omega\dot{y} \cos \lambda - g \end{aligned}\right\} \tag{3.9}$$

The relations between the components of tension are

$$T_x = (x/r)T_z, \quad T_y = (y/r)T_z \tag{3.10}$$

From the third equation of (3.9)

$$T_z/m + g = 2\Omega\dot{y} \cos \lambda \cong 0 \tag{3.11}$$

Substituting Eqs. (3.10) and (3.11) into Eqs. (3.9),

$$\left.\begin{aligned} 0 &= \ddot{x} + (g/r)x + 2\Omega\dot{y} \sin \lambda \\ 0 &= -2\Omega\dot{x} \sin \lambda + \ddot{y} + (g/r)y \end{aligned}\right\} \tag{3.12}$$

The characteristic equation of this system is

$$0 = p^4 + [4\Omega^2 \sin^2 \lambda + 2(g/r)]\, p^2 + (g/r)^2 \tag{3.13}$$

Its roots are

$$p \cong \begin{cases} \pm[\sqrt{g/r} + \Omega \sin \lambda] \\ \pm[\sqrt{g/r} - \Omega \sin \lambda] \end{cases} \tag{3.14}$$

and a solution of Eqs. (3.12) has the form

$$\left.\begin{aligned} x &= A_0 \cos(\Omega t \sin \lambda) \sin \sqrt{g/r}\, t \\ y &= A_0 \sin(\Omega t \sin \lambda) \sin \sqrt{g/r}\, t \end{aligned}\right\} \tag{3.15}$$

If $u = x + iy$, then

$$u = A_0 \sin \sqrt{g/r}\, t \exp[i\Omega t \sin \lambda] \tag{3.16}$$

which is the equation of a vector in the x, y plane rotating with constant angular velocity $\Omega \sin \lambda$, and with amplitude $A_0 \sin \sqrt{g/r}\, t$.

(4) Inertial Navigation Systems

A detailed treatment of the principles of inertial navigation is outside the scope of this discussion; however, a brief description of the kind of navigation system being considered here will be given.

A platform called the controlled member, connected to a vehicle through a set of gimbals, is given an initial alignment with respect to north and the horizontal. As the vehicle then moves through space in any manner, torque motors, driving the gimbals, maintain the platform with the same orientation relative to north and the horizontal. Latitude and longitude are com puted from the information processed.

The controlled member mounts three single degree of freedom integrating gyros with input axes aligned along north, east, and along the normal to the platform. There are also two pendulous accelerometers with input axes aligned along the north and east directions.

The system consisting of the controlled member, associated gimbal system, and three gyros alone, is sometimes referred to as a space stabilization system, or stabilized platform. It is capable of maintaining the controlled member with fixed orientation relative to inertial space when its gyros have no command signal applied, or of causing the controlled member to have three angular velocity components along the gyro input axes which are proportional to the respective gyro input signals.

An inertial navigation system of the type analyzed here consists of a stabilized platform with additional elements to produce continuously the desired platform orientation with respect to the Earth, regardless of vehicle motion. To control the platform orientation,

* A system of right-handed, orthogonal, Cartesian coordinates with origin at some point external to the International Ellipsoid of Reference, z axis normal to the Ellipsoid, x axis intercepting the Earth's polar axis in a northerly sense, and y axis pointing east.

three angular rate command signals are derived from the accelerometers and other elements and applied as torquing signals to the three gyros mounted on the platform. Feedback in this system consists of change of orientation of the controlled member, and, therefore, of the accelerometer input axes.

The accelerometers measure two components of a quantity called the specific force which depends on the gravitational attraction of the Earth and on the kinematic acceleration of the vehicle. The specific force associated with any moving point is

$$\mathbf{f} = -\mathbf{a} + \mathbf{G} \tag{4.1}$$

where $\mathbf{a}$ is acceleration and $\mathbf{G}$ the gravitational attraction per unit mass. The computation of the motion of the system depends on the kinematic term, while the selected platform orientation enables separation of the gravitational and kinematic components of specific force.

A block diagram of an inertial navigation system is shown in Fig. 1.

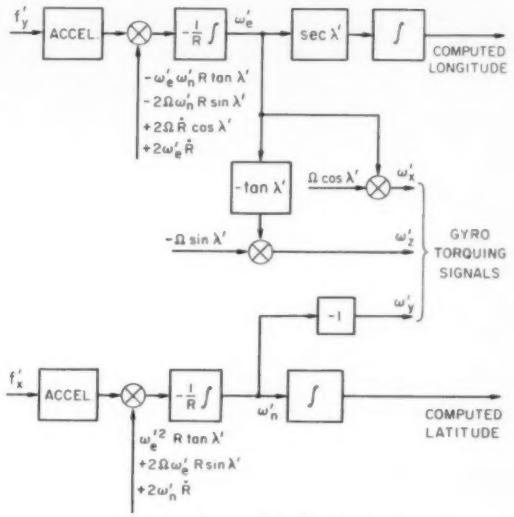

FIG. 1. System block diagram.

(5) Error Analysis of an Inertial Navigation System

The system shown in Fig. 1 mechanizes the equations

$$\left.\begin{aligned} \dot{\omega}_n' &= -(1/R)(f_x' + \omega_e'^2 R \tan\lambda' + 2\Omega\omega_e' R \sin\lambda' + 2\omega_n' \dot{R}) \\ \dot{\omega}_e' &= -(1/R)(f_y' - \omega_e'\omega_n' R \tan\lambda' - 2\Omega\omega_n' R \sin\lambda' + 2\Omega\dot{R}\cos\lambda' + 2\omega_e' \dot{R}) \end{aligned}\right\} \tag{5.1}$$

The angular rates of the controlled member are

$$\left.\begin{aligned} \omega_x' &= \Omega\cos\lambda + \omega_e' \\ \omega_y' &= -\omega_n' \\ \omega_z' &= -\Omega\sin\lambda' - \omega_e'\tan\lambda' \end{aligned}\right\} \tag{5.2}$$

The mechanization equations (5.1) are postulated and then justified by analysis of the resultant system. The form of Eqs. (5.1) is based on (4.1) which becomes

$$\mathbf{f} = -\ddot{\mathbf{R}} - 2\boldsymbol{\omega} \times \dot{\mathbf{R}} - \dot{\boldsymbol{\omega}} \times \mathbf{R} - \boldsymbol{\omega} \times (\boldsymbol{\omega} \times \mathbf{R}) + \mathbf{G} \tag{5.3}$$

when referred to a coordinate system which is rotating with angular velocity $\boldsymbol{\omega}$, and has its origin at the terminus of the position vector $\mathbf{R}$ from the center of the Earth. Eqs. (5.1) are obtained when Eq. (5.3) is referred to a geographic coordinate system, the x and y components are solved for $\dot{\omega}_n$ and $\dot{\omega}_e$, respectively, and the unprimed (geographic) quantities are replaced by primed (computed) quantities. In deriving Eqs. (5.1) certain small correction terms resulting from the Earth's oblateness have been neglected.

In Eqs. (5.1), terms in $\dot{R}$ are called Coriolis force compensation terms, and terms containing products of angular velocities are called centrifugal force compensation terms, corresponding to the names usually given to the terms in Eq. (5.3) from which they arise. There is no essential difference in the nature of the Coriolis terms and centrifugal force terms, and their relative magnitudes depend only on the motion of the selected reference frame.

In the case analyzed, the system will be assumed to be carried by a vehicle which flies at constant ground speed, and at constant altitude on a parallel of latitude. For this case,

$$\dot{\omega}_n = \omega_n = \dot{\omega}_e = \dot{R} = 0 \tag{5.4}$$

The condition $\dot{R} = 0$ reduces the Coriolis terms of Eqs. (5.1) to zero. The centrifugal terms remain, however, and the demonstration of Foucault pendulum-like behavior of the system depends on retaining the centrifugal force terms in the analysis.

The conditions (5.4) are imposed for simplicity in the analysis and are not essential to the derivation of the system error equations. Using Eq. (5.4), the three components of specific force, referred to a geographic reference frame, which act on the system are

$$\left.\begin{aligned} f_x &= -2\Omega\omega_e R\sin\lambda - \omega_e^2 R\tan\lambda \\ f_y &= 0 \\ f_z &= -2\Omega\omega_e R\cos\lambda - \omega_e^2 R + g \end{aligned}\right\} \tag{5.5}$$

The specific forces sensed by the accelerometers are related to the quantities in (5.5) by the transformations

$$\left.\begin{aligned} f_x' &= \cos(x', x)f_x + \cos(x', y)f_y + \cos(x', z)f_z \\ f_y' &= \cos(y', x)f_x + \cos(y', y)f_y + \cos(y', z)f_z \end{aligned}\right\} \tag{5.6}$$

If the angular displacement of the indicated and geographic systems is small, then Eqs. (5.6) may be written

$$\left.\begin{aligned} f_x' &= f_x + \gamma f_y - \beta f_z \\ f_y' &= -\gamma f_x + f_y + \alpha f_z \end{aligned}\right\} \tag{5.7}$$

where the angles α, β, and γ are the components of a vector rotation which would instantaneously bring the geographic system into coincidence with the indicated system.

TABLE 1
System Oscillation Periods

ω_e knots	T_1 hrs	T_2 min	T_3 min	T_s min	T_f hrs
2000 east	6.13	99.86	73.94	84.97	9.49
0	23.93	87.68	81. 27	84.36	37.09
2000 west	12. 58	91.04	78.78	84.47	19. 50

$T_s = 2T_2T_3/(T_2 + T_3)$ = Schuler period

$T_f = 2T_2T_3/(T_2 - T_3)$ = Foucault period

All values at $\lambda = 40^\circ$

Substituting Eqs. (5.5) into Eqs. (5.7),

$$\left.\begin{aligned} f_x' &= -2\Omega\omega_e R \sin\lambda - \omega_e^2 R \tan\lambda + \\ &\qquad \beta(2\Omega\omega_e R\cos\lambda + \omega_e^2 R - g) \\ f_y' &= \gamma(2\Omega\omega_e R\sin\lambda + \omega_e^2 R\tan\lambda) - \\ &\qquad \alpha(2\Omega\omega_e R\cos\lambda + \omega_e^2 R - g) \end{aligned}\right\} \tag{5.8}$$

Combining Eqs. (5.1) and Eqs. (5.8)

$$\left.\begin{aligned} \dot\omega_n' &= (2\Omega\omega_e\sin\lambda - 2\Omega\omega_e'\sin\lambda') + \\ &\qquad (\omega_e^2\tan\lambda - \omega_e'^2\tan\lambda') - \\ &\qquad \beta(2\Omega\omega_e\cos\lambda + \omega_e^2 - g/R) \\ \dot\omega_e' &= -\gamma(2\Omega\omega_e\sin\lambda + \omega_e^2\tan\lambda) + \\ &\qquad \alpha(2\Omega\omega_e\cos\lambda + \omega_e^2 - g/R) + \\ &\qquad 2\Omega\omega_n'\sin\lambda' + \omega_e'\omega_n'\tan\lambda' \end{aligned}\right\} \tag{5.9}$$

The set (5.9) can be reduced to a set of linear equations by the following procedure: put

$$\left.\begin{aligned} \delta\dot\omega_n &= \dot\omega_n' - \dot\omega_n = \dot\omega_n' \\ \delta\dot\omega_e &= \dot\omega_e' - \dot\omega_e = \dot\omega_e' \\ \delta\omega_n &= \omega_n' - \omega_n = \omega_n' \\ \delta\omega_e &= \omega_e' - \omega_e \\ \delta\lambda &= \lambda' - \lambda \end{aligned}\right\} \tag{5.10}$$

Then

$$\left.\begin{aligned} 2\Omega\omega_e'\sin\lambda' &= 2\Omega(\omega_e + \delta\omega_e)\sin(\lambda + \delta\lambda) \\ &\cong 2\,\Omega\omega_e\sin\lambda + 2\Omega\,\delta\omega_e\sin\lambda + \\ &\qquad 2\Omega\omega_e\delta\lambda\cos\lambda \end{aligned}\right\} \tag{5.11}$$

if terms containing products, and powers of δ's higher than the first, are neglected. In the same way,

$$\omega_e'^2\tan\lambda' \cong \omega_e^2\tan\lambda - 2\omega_e\delta\omega_e\tan\lambda + \delta\lambda\omega_e^2\sec^2\lambda \tag{5.12}$$

$$2\Omega\omega_n'\sin\lambda' \cong 2\Omega\delta\omega_n\sin\lambda \tag{5.13}$$

$$\omega_e'\omega_n'\tan\lambda' \cong \omega_e\delta\omega_n\tan\lambda \tag{5.14}$$

Replacing the corresponding terms in Eqs. (5.9) by Eqs. (5.11), (5.12), (5.13), and (5.14),

$$\left.\begin{aligned} \delta\dot\omega_n &= -\delta\omega_e(2\Omega\sin\lambda + 2\omega_e\tan\lambda) - \\ &\qquad \delta\lambda(2\Omega\omega_e\cos\lambda + \omega_e^2\sec^2\lambda) - \\ &\qquad \beta(2\Omega\omega_e\cos\lambda + \omega_e^2 - g/R) \\ \delta\dot\omega_e &= \delta\omega_n(2\Omega\sin\lambda + \omega_e\tan\lambda) + \\ &\qquad \alpha(2\Omega\omega_e\cos\lambda + \omega_e^2 - g/R) - \\ &\qquad \gamma(2\Omega\omega_e\sin\lambda + \omega_e^2\tan\lambda) \end{aligned}\right\} \tag{5.15}$$

The differential equations (5.15) contain six variables. Four additional equations are obtained from the definition

$$\left.\begin{aligned} \omega_n' - \omega_n &= (d/dt)(\lambda' - \lambda) \\ \delta\omega_n &= \delta\dot\lambda \end{aligned}\right\} \tag{5.16}$$

and from the relationships connecting the error angles.

The vector error angle $\boldsymbol{\epsilon}$, which defines the relative orientation of the indicated and geographic coordinate systems, has a rate of change which is given by

$$\mathbf{d\epsilon}/dt = \boldsymbol{\omega}' - \boldsymbol{\omega} \tag{5.17}$$

where $\boldsymbol{\omega}'$ is the angular velocity of the indicated coordinate system and $\boldsymbol{\omega}$ the angular velocity of the geographic coordinate system. If $\boldsymbol{\omega}$ is given in geographic coordinates, and $\boldsymbol{\omega}'$ in indicated coordinates, then Eq. (5.17) can be written in indicated coordinates by resolving the components of $\boldsymbol{\omega}$ into the indicated system. Using the same transformation as in Eq. (5.7), Eq. (5.17) may be written

$$\left.\begin{aligned} \dot\alpha &= \omega_x' - \omega_x - \gamma\omega_y + \beta\omega_z \\ \dot\beta &= \omega_y' - \omega_y - \alpha\omega_z + \gamma\omega_x \\ \dot\gamma &= \omega_z' - \omega_z - \beta\omega_x + \alpha\omega_y \end{aligned}\right\} \tag{5.18}$$

For the stated conditions (5.4)

$$\left.\begin{aligned} \omega_x &= \Omega\cos\lambda + \omega_e \\ \omega_y &= 0 \\ \omega_z &= -\Omega\sin\lambda - \omega_e\tan\lambda \end{aligned}\right\} \tag{5.19}$$

Using Eqs. (5.18), (5.2), and (5.19), and adding the gyro uncertainties U_x, U_y, and U_z,

$$\left.\begin{aligned} \dot\alpha &= \Omega(\cos\lambda' - \cos\lambda) + \omega_e' - \omega_e - \\ &\qquad \beta(\Omega\sin\lambda + \omega_e\tan\lambda) + U_x \\ \dot\beta &= -\omega_n' + \alpha(\Omega\sin\lambda + \omega_e\tan\lambda) + \\ &\qquad \gamma(\Omega\cos\lambda + \omega_e) + U_y \\ \dot\gamma &= -\Omega(\sin\lambda' - \sin\lambda) - \\ &\qquad (\omega_e'\tan\lambda' - \omega_e\tan\lambda) - \\ &\qquad \beta(\Omega\cos\lambda + \omega_e) + U_z \end{aligned}\right\} \tag{5.20}$$

Neglecting second-order terms as before, Eqs. (5.20) simplify to

$$\left.\begin{aligned} \dot\alpha &= -\Omega\delta\lambda\sin\lambda + \delta\omega_e - \\ &\qquad \beta(\Omega\sin\lambda + \omega_e\tan\lambda) + U_x \\ \dot\beta &= -\delta\omega_n + \alpha(\Omega\sin\lambda + \omega_e\tan\lambda) + \\ &\qquad \gamma(\Omega\cos\lambda + \omega_e) + U_y \\ \dot\gamma &= -\delta\lambda(\Omega\cos\lambda + \omega_e\sec^2\lambda) - \\ &\qquad \delta\omega_e\tan\lambda - \beta(\Omega\cos\lambda + \omega_e) + U_z \end{aligned}\right\} \tag{5.21}$$

The six equations (5.15), (5.16), and (5.21) may now be solved by any of the usual methods for the solution of systems of linear differential equations of the first order.

Written as a single matrix equation, the system appears as in (5.22). All analytical methods for the solution of such an equation require the determination of the characteristic values of the six-by-six matrix. To see this, note that if the Laplace transform is applied throughout, Eq. (5.22) could be written with zero on

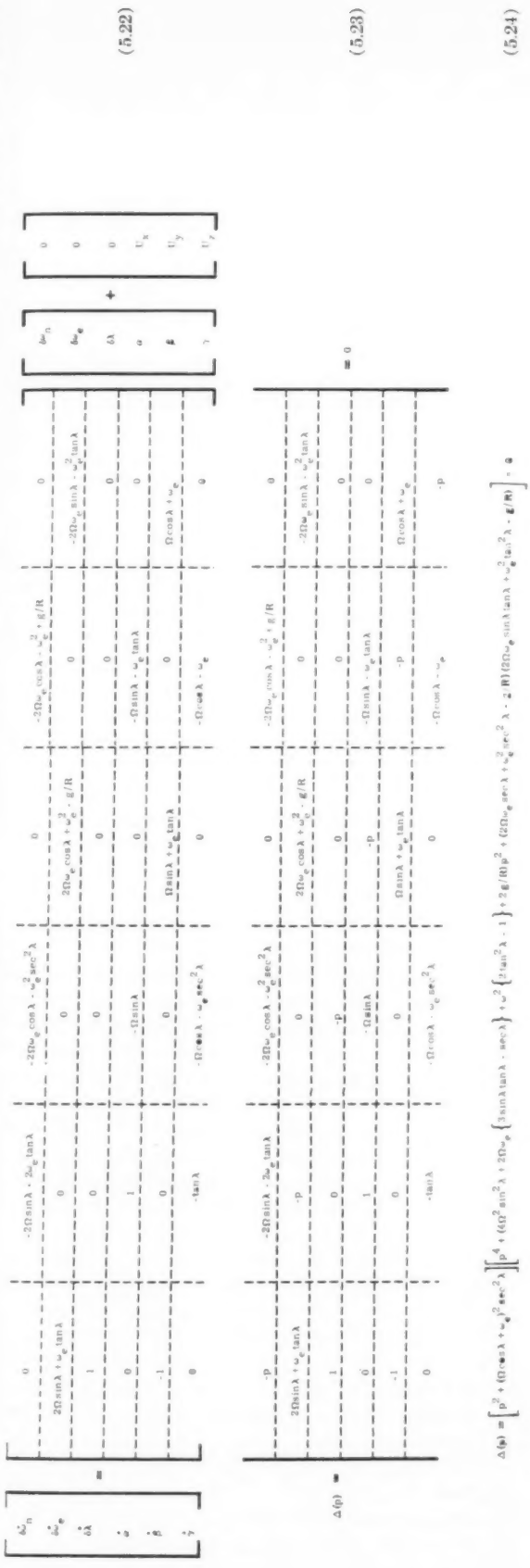

(5.22) (5.23) (5.24)

the left-hand side and an element $-p$ added to each diagonal element of the six-by-six matrix. The system could then be solved by Cramer's rule, and an inversion back into the time domain would require a knowledge of the zeros of Eq. (5.23). Reduction of the determinant in (5.23) yields the characteristic equation (5.24). The zeros of this equation are the angular frequencies of the various system oscillations. A complete solution of (5.22) will not be given here; however, the characteristic values are found for some special cases listed in Table 1.

(6) Conclusion

Examinatian of the characteristic equation (5.24) shows the following:

(a) The second factor of the characteristic equation is a generalized form of the right-hand side of (3.13), and becomes identical with it if $\omega_e = 0$. This circumstance shows the analogy with the Foucault pendulum analyzed in Section (3).

(b) The zeros of the second factor are (neglecting second-order terms)

$$p = \begin{cases} \pm i[\sqrt{g/R} + (\Omega + \omega_e \sec \lambda) \sin \lambda] \\ \pm i[\sqrt{g/R} - (\Omega + \omega_e \sec \lambda) \sin \lambda] \end{cases}$$

if $$(\Omega + \omega_e \sec \lambda) \ll \sqrt{g/R}$$

The zeros lie slightly above and slightly below the eighty-four minute points on the imaginary axis. The system error angles, therefore, contain two sinusoidal components having almost the same frequency, which together produce a beat wave.

(c) The period of the modulating wave is

$$T_f = 2\pi/(\Omega + \omega_e \sec \lambda) \sin \lambda$$

where $(\Omega + \omega_e \sec \lambda)$, the celestial longitude rate, is the total angular velocity of the geographic reference system for the case considered.

(d) The first factor of the characteristic equations shows that the system also has a pure sinusoidal oscillation with period

$$T_1 = 2\pi/(\Omega + \omega_e \sec \lambda)$$

Table 1 summarizes the numerical results for the cases 2,000 knots east, zero velocity, and 2,000 knots west.

The conditions (5.4), which restricted the vehicle to a constant speed path on a small circle of latitude, were assumed in order that the coefficients of (5.22) should be strictly constant and the theory of linear differential equations with constant coefficients be applicable. If general maneuvers of the vehicle are allowed, (5.22) must be generalized so that the coefficients are appropriate functions of the rates and accelerations. This can be accomplished by starting with the complete specific force expressions instead of the abbreviated ex-

(*Continued on page 385*)

Sweepback Effects in Turbulent Boundary-Layer Shock-Wave Interaction

R. J. STALKER*
University of Sydney, Australia

Summary

Experiments are reported on the interaction of turbulent boundary layers and shock waves with sweptback configurations. They show that the peak pressure rise at separation, the upstream influence ahead of separation, and the pressure rise at reattachment for moderate sweep angles can all be understood by simple extensions of available two-dimensional theories.

Symbols

p = static pressure
δ = undisturbed boundary-layer thickness upstream of interaction
h = step height
M_1 = upstream normal component of Mach number
θ = inverse logarithmic decrement of upstream influence
α = sweep angle
U = normal component of mainstream velocity
p_d = "base" pressure
p_f = pressure after reattachment
M_a = normal component of Mach number immediately before reattachment
$\bar{M}$ = normal component of Mach number on dividing stream sheet

Subscripts

1 = undisturbed conditions upstream of interaction
2 = conditions downstream of interaction

(A) Introduction

ONLY after considerable effort have most of the phenomena observed in the interaction of a shock in a supersonic mainstream with an adjacent boundary layer been understood, and studies have naturally been directed at the simplest two-dimensional problems. As a result of these studies, the processes involved are now understood sufficiently to warrant an approach to the interaction problem in three dimensions.

When the boundary layer is laminar, this approach may be expected to be predominantly theoretical, for indeed, there has already been considerable success in obtaining solutions to the laminar boundary-layer equations alone for useful three-dimensional configurations.[1] However, interest is here centered on the turbulent boundary layer, in which case no such promise of a successful theoretical approach exists, and knowledge of three-dimensional effects must be derived from experimental evidence.

The two special complicating features of a general three-dimensional interaction are the cross flow within the boundary layer and the fact that changes in flow quantities occur in both of any two mutually perpendicular directions parallel to the surface on which the interaction is taking place. The present study was concerned with the effects of cross flow, whence it was decided to confine attention to configurations for which the flow pattern was invariant in one of the directions parallel to the surface. Such configurations are said to possess cylindrical symmetry, and are exemplified by the straight swept wing of infinite span. Though interesting cross-flow behavior was observed, it was found that important aspects of separating and reattaching flows could be understood, using appropriate extensions of two-dimensional theories, without specific reference to the cross flow.

Treating the separation phenomenon first, the experiments clearly showed two features variant to sweepback. The first, the peak pressure rise, decreased with increasing sweep angle in a manner such that it was approximately dependent only on the normal component of Mach number. This was seen to accord with an approximate two-dimensional theory, due to Crocco and Probstein,[2] which was extended to the sweepback case. The second feature was the upstream influence, or the rate at which pressure decreases with distance upstream, and this was found to increase with sweep angle in a manner consistent with a two-dimensional small perturbations theory, due to Lighthill,[3] which was found to apply to the sweepback case.

The experiments on reattaching flow were concerned with the effect of sweepback on the reattachment pressure rise behind a swept, back step of height such that this pressure rise was independent of step height. For moderate sweep angles, this was again found to be roughly dependent only on the normal component of upstream Mach number, in agreement with a two-dimensional theory proposed by Chapman[4] and Korst,[5] which was extended to swept configurations.

Received May 15, 1959. Revised and received September 29, 1959.

* Formerly, Research Student, William and Agnes Bennett Supersonics Laboratory. Now, Assistant Research Officer, Division of Mechanical Engineering, National Research Council, Ottawa, Canada.

The author gratefully acknowledges the guidance of Dr. R. E. Meyer, together with the encouragement of Prof. A. V. Stephens and his successor, Prof. W. H. Wittrick. The study was conducted under a research grant made available by the University of Sydney, and was initiated while the author was on leave of absence from Australian National Airways.

(B) Separating Flow

(1) *Experimental Configurations*

The tests were conducted in a 6 × 3 in. intermittent blowdown type wind tunnel, at $M = 2.36$ and a Reynold's number of 9×10^5 per in.

The experimental configurations are shown in Fig. 1. Fig. 1(a) represents a step attached to a rotatable steel plate, which replaced the window at the test section on the 6 in. sidewall of the tunnel. Both the height and sweep angle of the step were varied, and pressure distributions taken along a line normal to the step face, meeting it at the centerline of the sidewall.

Fig. 1(b) shows a flat plate, with leading edge swept at 45°, mounted to span the 6 in. dimension of the test section. Steps of varying height were mounted on the plate, with upstream step face parallel to the leading edge, and pressure distributions were obtained along the tunnel centerline and traverse lines parallel to it 1.5 in. on either side. In order to avoid choking of the flow on the underside of the plate, and consequent "spillage" onto the upper, testing surface, provision was made for expanding the flow there by the step in the sidewall shown in the figure. China film tests on the sidewall confirmed that this was effective.

Fig. 1(c) shows a wooden ramp attached to one of the contoured nozzle liners. This ramp formed a sudden change in angle at the surface of the liner, generating an ordinary two-dimensional oblique shock, which made an interaction at the sidewall with sweep angle equal to the shock angle. This interaction was investigated using pressure plotting, and was utilized to provide information on upstream influence at large sweep angles.

(2) *Incident Boundary Layers*

(*a*) *Tunnel Sidewall*—Using the china film technique, it was first confirmed that cross flows within the sidewall boundary layer were sufficiently small to be disregarded, and then pitot traverses of the boundary layer were made at the test section, 0.2 in. and 1.7 in. to one side of the sidewall centerline. The Mach number profiles obtained were identical, indicating a uniform boundary layer, of thickness 0.25 in. One of the profiles is shown in Fig. 2.

(*b*) *Swept Plate*—China film tests on the swept plate indicated that the skin-friction direction was identical with the direction of the mainstream, and, from momentum considerations, it then follows that all the flow within the boundary layer is in the direction of the mainstream.[6] Having established this, the Mach number profile was made the subject of a separate study,[7] and the results of a pitot traverse of the boundary layer, at a streamwise distance of 4.65 in. from the leading edge, are presented here in Fig. 2.* Comparing these with the results of the traverse on the tunnel wall, it is seen that the Mach number profile is as in two dimensions, and the results of the interaction studies in the two cases may therefore be directly compared.

* These results are reproduced with the kind permission of the author of reference 7.

It may be noted that this result supplements those of Ashkenas and Riddell,[8] who have shown, at low subsonic speeds, that in a zero pressure gradient turbulent boundary layer initiated at a swept leading edge the flow is closely parallel to the mainstream, and the velocity profile is as in two dimensions.

(3) *Results*

Static pressure distributions obtained in the tests on the sidewall and on the swept plate are shown in Figs. 3 and 4, respectively. It would be expected in either case that some part of the flow would be subject to an "end effect," arising from the upstream junction of the step face with the adjacent nozzle liner, and, indeed, this is evidenced on traverse A in Fig. 4 by the large drop in pressure toward the step at a height of 0.150 in. However, Fig. 4 also shows that the spanwise distance over which this end effect is felt is reduced with step height, and therefore indicates that in seeking results which are free of end effects, a sufficient condition is that the shape of the pressure distribution curve is invariant to a reduction in step height. The results for the two lesser step heights at traverse B and traverse C in Fig. 4, and at sweep angles of 45° and 57° in Fig. 3, are thus all free of end effects. The remaining results at lesser sweep angles in Fig. 3 do not show evidence of a large end effect, and since they are used only for determination of peak pressure, which, as may be seen from traverse A in Fig. 4, is not strongly sensitive to end effect, they may be regarded as adequate.

(4) *Peak Pressure Rise*

The variation of the peak pressure rise with sweepback can be obtained from Fig. 3. For correlation with the theory following, the results should represent "free" separation, which takes place when the separation is independent of the agency inducing it.

First, at zero sweep, the results of other investigators[9] indicate that the peak pressure rise becomes invariant to increasing step height, and is therefore representative of free separation, when $h/\delta = 2.0$, but is only a little below its ultimate value when $h/\delta = 1.2$, as in these tests. Further, at sweep angles of 45° and 57° in Fig. 3, because the shape of the pressure distribution curve is unchanged by change in step height, the separation must be independent of the agency invoking it, and free separation is therefore obtained when $h/\delta = 0.5$. Thus the step height necessary to yield a value of peak pressure corresponding to free separation decreases with increasing sweep angle, indicating that in the tests at sweep angles in the intermediate zone between 0° and 45°, the step height is adequate.

These peak pressures are presented in Fig. 5, plotted against the normal component of upstream Mach number. Comparing these with the results obtained by other investigators in two dimensions, it is seen that, within the somewhat wide limits of the consistency of the results, a sweepback principle can be formulated—that is, the peak pressure rise is roughly dependent only on the normal component of Mach number.

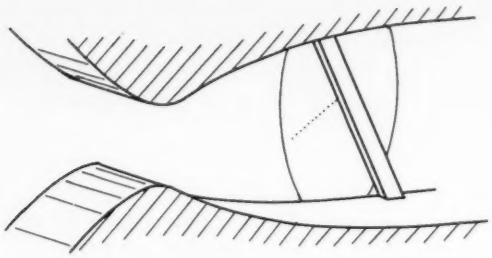

FIG. 1 (a). Test configuration—step on sidewall.

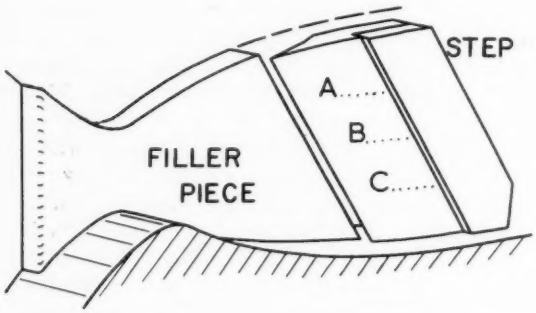

FIG. 1 (b). Test configuration—step on swept plate.

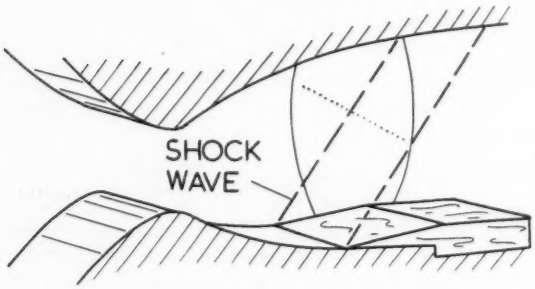

FIG. 1 (c). Test configuration—ramp on nozzle liner.

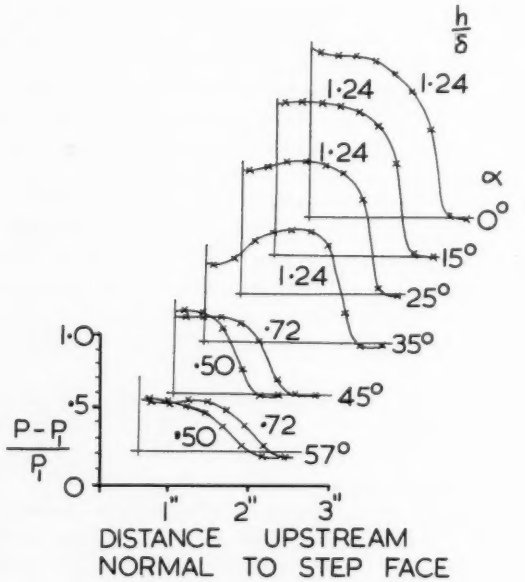

FIG. 3. Results of tests on sidewall.

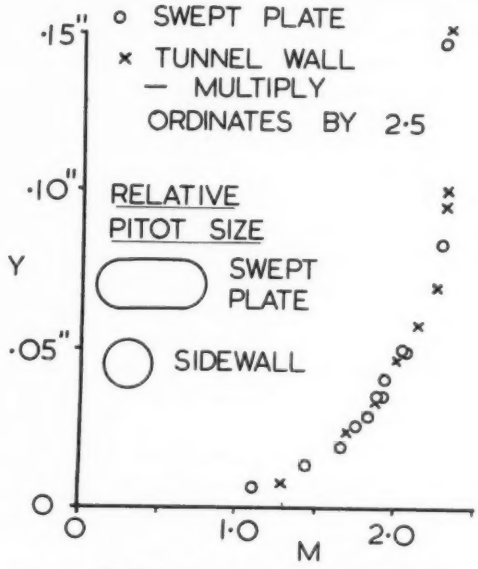

FIG. 2. Boundary-layer traverses.

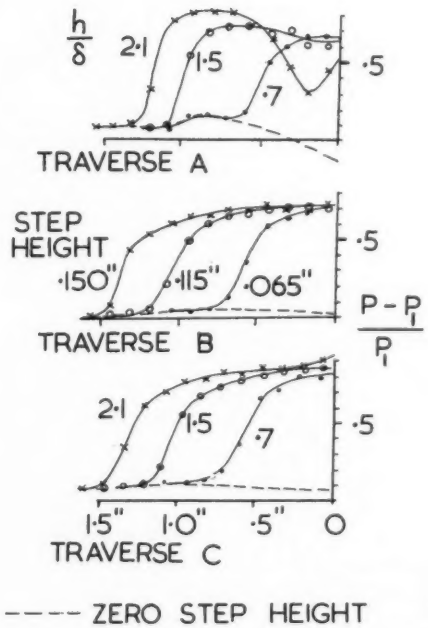

FIG. 4. Results of tests on swept plate.

Crocco-Probstein Theory: Review—A simple theory, which may be readily extended to the sweepback case, has been presented for the two-dimensional free interaction by Crocco and Probstein.[2] Relying on evidence from schlieren photographs, it is assumed that, as shown in Fig. 6, the outer edge of the boundary layer deflects sharply where it meets the shock, and that all the mainstream pressure rise takes place through the shock. Initial and final control surfaces "1" and "2" are taken at stations, a few boundary-layer thicknesses apart, where the pressure is approximately constant. Guided by an analysis of experimental results presented by Hammitt,[12] the effect of skin friction, mass addition, and momentum addition are neglected in balancing the mass flow and momentum for the boundary layer between these two stations, and the equations

$$m_1 = m_2 \tag{1}$$

for the mass flow, and

$$\delta(p_2 - p_1) = I_1 - I_2 = I_1[1 - (r_2U_2/r_1U_1)] \tag{2}$$

for the momentum balance, are obtained. Here,

$$m = \int_0^\delta \rho u \, dy \quad \text{and} \quad I = \int_0^\delta \rho u^2 \, dy$$

where δ is the boundary-layer thickness, y is distance normal to the surface, ρ is density, and u is velocity. p and U are local static pressure and mainstream velocity, respectively, and $r = I/mU$ is a convenient boundary-layer momentum ratio.

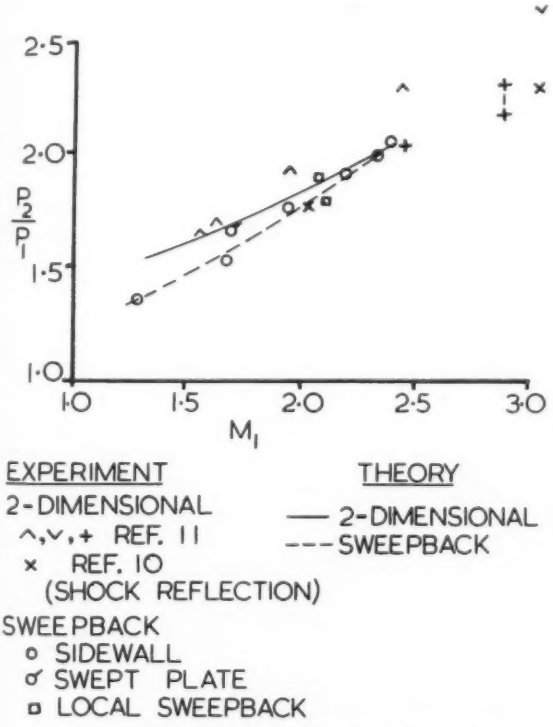

FIG. 5. Effect of sweepback on peak pressure ratio.

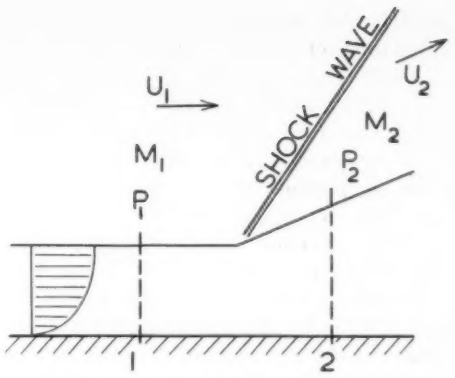

FIG. 6. Crocco-Probstein interaction model.

Putting $I = \rho_e U^2 \delta I'$, where ρ_e is the mainstream density, Eq. (2) becomes

$$p_2/p_1 = 1 + \gamma M_1^2 I_1'[1 - (r_2U_2/r_1U_1)] \tag{3}$$

The shock equations provide another relation between p_2/p_1, U_2/U_1, and M_1, and, hence, if I_1' is fixed by choosing an incident boundary layer of specific nondimensional velocity and density profiles, the pressure ratio is dependent only on the incident Mach number and the final value of the ratio r_2/r_1. Crocco and Probstein obtained a satisfactory correlation with experimental results with r_2/r_1 constant.

Sweepback Effect—The experiments have indicated the interaction in three dimensions to be similar in kind to that in two dimensions, and therefore, provided that changes in the flow variables over a distance $0(\delta)$ in the spanwise direction are negligible compared with changes occurring in the normal direction, the model used above will be equally suitable here. Thus, using definitions of m, I, r, U, and M based on the normal component of velocity, Eq. (3) may be obtained as before. The shock relations between p_2/p_1, U_2/U_1, and M_1 are unaltered by sweep, so determination of the pressure ratio rests on knowledge of I_1' and r_2/r_1.

Two curves are presented in Fig. 5, one showing the variation of peak pressure rise with Mach number in two-dimensional flow, and the other showing the variation of peak pressure rise with normal Mach number for swept configurations. For both these curves, I_1' is obtained by assuming uniform total temperature across the boundary layer, together with a 1/7 power law velocity distribution, while r_2/r_1 is assumed constant, thereby arbitrarily extending the result of Crocco and Probstein to the sweepback case. The actual value of r_2/r_1 is here chosen to yield the experimentally observed pressure rise at zero sweep. Two points are illustrated by these curves. First, between themselves they support the experimental approximation that the peak pressure rise is dependent only on the normal component of Mach number, but indicate that at large sweep angles, this can be expected to be only a rough approximation indeed. Second, the close agreement between the experimental results and the sweepback

effect predicted by the theory confirms the assumption that r_2/r_1 is unaffected by sweepback.*

In retrospect, the result that r_2/r_1 is independent of Mach number and sweepback angle is, perhaps, not so surprising. A feature common to nearly all theories regarding flow over a blunt base or a back step in a surface is that the pressure there, normally referred to as the "base" pressure, is controlled by the pressure rise at reattachment, and hence by the momentum distribution in the mixing layer approaching the reattachment zone. Therefore, when the step height is such that the length of the mixing layer is sufficient to allow an equilibrium mixing layer profile to form, further increases in step height will not alter the base pressure, and the "asymptotic" step height will have been achieved. In practice, this occurs at a step height which is somewhat less than the upstream boundary-layer thickness, implying that the internal mixing forces are strong enough to effectively complete the change to a mixing layer profile in only a few boundary-layer thicknesses. These same mixing forces are also acting to produce a mixing layer profile in the region downstream of a separation, and hence may be expected to be effective over a distance small enough for skin friction, and mass and momentum addition from the mainstream, to have little effect. The profile at station "2" may therefore be expected to be fairly close to an equilibrium mixing layer profile, yielding a value of r_2, which is not strongly dependent on Mach number nor, from the discussion in Section (C.2), strongly dependent on sweepback effects.

Local Sweepback—In view of the strong mixing forces discussed above, it will be expected that r_2 will not be very sensitive to small departures from cylindrical symmetry in the region near separation, and the theory should therefore predict the peak pressure rise at a curved separation line, provided the radius of curvature is large compared with the incident boundary-layer thickness. Two results are presented in Fig. 5 where the separation line, as indicated by the china film technique, was far from parallel to the step face in the region where the pressure traverse was taken. When these results are plotted using the local sweep angle of the separation line, they are seen to be consistent with the theory.

(5) *Upstream Influence*

Apart from the peak pressure rise, a noteworthy feature displayed by the pressure distributions of Fig. 3 is that the distance over which the pressure rise takes place increases with sweep angle. This distance is connected with the upstream influence treated by Lighthill[3] in a two-dimensional small perturbations theory of shock-wave boundary-layer interaction, and by showing below that this theory also applies to the flow normal to the line of sweepback, a means is provided for correlating the results.

* In fact, the agreement between theory and experiment is so close as to suggest mutual compensation of the sources of error engendered by the crude nature of the theory itself.

Theory—The basic, unperturbed flow assumed by Lighthill was parallel to the surface, with all derivatives in that direction equal to zero. A similar basic flow may be assumed for the sweepback case, with the interaction generated in such a way that although the isobars are straight and parallel, they are oblique to the incident flow—in fact, just as though the interaction were taking place on an infinite swept wing.

Lighthill pointed out that in a small perturbations type of analysis, disturbances to the viscous forces in the boundary layer would be negligible compared with disturbances to the inertia forces, except in a thin layer adjacent to the surface, where the flow could be taken to be incompressible. The boundary layer could thus be treated in two parts—an outer, rotational, inviscid layer, and an inner, viscous incompressible layer which provided the effective wall boundary conditions for the outer layer.

The behavior of the inner, viscous layer is, of course, subject to the Navier-Stokes equations which become, for steady incompressible flow in two dimensions,

$$\left.\begin{aligned} &(\partial u/\partial x) + (\partial v/\partial y) = 0 \\ &\rho[u(\partial u/\partial x) + v(\partial u/\partial y)] = \\ &\qquad -(\partial p/\partial x) + \mu[(\partial^2 u/\partial x^2) + (\partial^2 u/\partial y^2)] \\ &\rho[u(\partial v/\partial x) + v(\partial v/\partial y)] = \\ &\qquad -(\partial p/\partial y) + \mu[(\partial^2 v/\partial x^2) + (\partial^2 v/\partial y^2)] \end{aligned}\right\} \quad (4)$$

where x and y are coordinates parallel and normal to the surface, respectively, and u and v are corresponding velocities. Lighthill showed that these equations yielded the boundary condition for the outer, inviscid layer that the surface may be regarded as displaced to

$$y = 0.78[\theta \nu_w / U'(0)]^{1/3}$$

and, more importantly, the Mach number of the basic flow at the surface may be taken as

$$M_e = 0.78 M'(0)[\theta \nu_w / U'(0)]^{1/3} \quad (5)$$

Here ν_w is the kinematic viscosity at the surface, $M'(0)$ and $U'(0)$ are the gradients, normal to the surface, of the Mach number and velocity there in the basic flow, and θ is the inverse logarithmic decrement of the upstream influence, being the distance over which the perturbation pressure is reduced by a factor e^{-1}.

In the sweepback case, because the flow possesses cylindrical symmetry, and all derivatives with respect to the spanwise coordinate are zero, the equations for the inner viscous layer are identical with Eq. (4), with x and u now measured normal to the line of sweepback. Lighthill's analysis therefore applies, leading again to Eq. (5), with M_e now interpreted as the component, normal to the sweepback line, of the Mach number at the effective surface, and $M'(0)$ and $U'(0)$ as gradients of the components of Mach number and velocity in the same direction.

The outer, inviscid layer was treated by Lighthill as a steady rotational flow of an inviscid non-heat-conducting fluid, and he showed[13] that when small perturba-

tions of the flow variables are taken, the equations of the flow in two dimensions become

$$\left.\begin{aligned}[1 - M^2(y)](\partial p/\partial x) &= \gamma p_1 M^2(y)(\partial \eta/\partial y)\\ M^{-2}(y)(\partial p/\partial y) &= -\gamma p_1(\partial n/\partial x)\end{aligned}\right\} \quad (6)$$

where p is the pressure, p_1 its upstream value, η is the local direction of flow, and $M(y)$ is the Mach number at distance y from the surface. Then, using these equations, together with the boundary conditions at the effective surface, and the condition that deflections and pressures at the outer edge of the boundary layer must match those in the mainstream, he derived the expression for the inverse logarithmic decrement[3]

$$\theta = (M_1^2/\beta)[1/M'(0)M_e] + (\delta/\beta)\{[1/(1 - 2n)] - M_1^2 + [\beta^2/(1 + 2n)]\} \quad (7)$$

for a boundary layer whose undisturbed Mach number profile is given by

$$M(y) = \{[M'(0)y]^{-2} + [M_1(y/\delta)^n]^{-2}\}^{-1/2} \quad (8)$$

δ is the boundary-layer thickness, M_1 is the mainstream Mach number, and $\beta = \sqrt{M_1^2 - 1}$.

In considering the outer, inviscid layer in a sweptback interaction, the condition that spanwise derivatives are zero can be shown to yield basic equations of the flow which are as in two dimensions, and thus, when the perturbation equations are derived by following Lighthill's procedure, these are found to be identical with Eq. (6), with $M(y)$ and η now interpreted as components normal to the line of sweepback. The relation between deflection and pressure for the normal component of flow in the mainstream at the outer edge of the boundary layer is as in two dimensions, and therefore, when the boundary conditions at the effective surface are used, the perturbation equations will yield an expression identical with Eq. (7) for the upstream influence in the sweepback case, with all Mach numbers interpreted as components normal to the line of sweepback.

To determine n, Lighthill used the formula $n = (1/7) + (1/70)M_1^2$ based on a 1/7 power law, and the assumption of constant stagnation temperature across the boundary layer. The same assumptions for the undisturbed boundary layer in the present case lead to the formula

$$n = (1/7) + (1/70)M_1^2 \cos^{-2}\alpha \quad (9)$$

The inverse logarithmic decrement can now be expressed as a function of Reynolds' number, mainstream Mach number and sweep angle by using the formula for the resultant skin friction[3]

$$\tau = 0.029\ \rho_1 U_1^2 \cos^{-2}\alpha\ R_\delta^{-(1/4)}(T_w/T_1)^{0.35}$$

together with the relations

$$\mu_w/\mu_1 = (T_w/T_1)^{0.8}, \quad \rho_w/\rho_1 = T_1/T_w,$$
$$T_w/T_1 = 1 + 0.18M_1^2 \cos^{-2}\alpha$$

Here R_δ is the Reynolds number based on boundary-layer thickness, U_1 is the normal component of mainstream velocity, T is the absolute temperature, μ is the coefficient of viscosity, and subscript w signifies conditions at the surface. Using these relations, together with Eqs. (5) and (7), and remembering that $\mu_w U'(0) = \tau \cos\alpha$, it is found that

$$\theta/\delta = (470/\beta)R_\delta^{-(11/12)}(T_w/T_1)^{2.2}(\cos^{1/3}\alpha)(\theta/\delta)^{1/3} + (1/\beta)\{[1/(1 - 2n)] - M_1^2 + [\beta^2/(1 + 2n)]\} \quad (10)$$

This is shown plotted in Fig. 7 for the conditions of the present experiments, the value of θ at $\alpha = 60°$ being used as a reference length. As outlined by Lighthill, the theory is not expected to apply for small values of θ, whence the doubtful part of the curve is shown by a broken line.

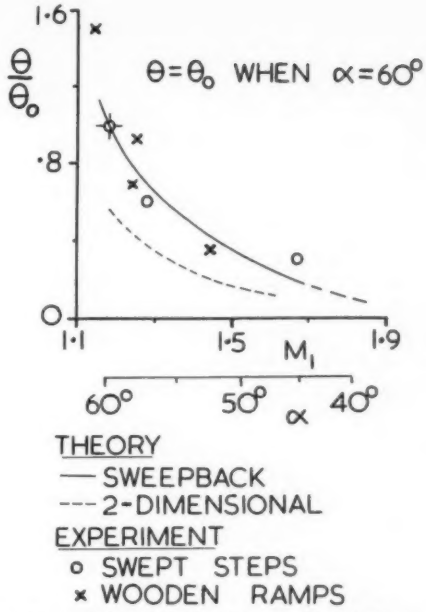

FIG. 7. Effect of sweepback on upstream influence.

For comparison, the variation of θ with Mach number in two dimensions is also shown in Fig. 7, at the same Reynolds number as in the present tests. As might be expected, the fact that, in the sweepback case, the normal component of flow has lower boundary-layer Mach numbers associated with a given mainstream Mach number than in two dimensions, leads to a larger upstream influence, but in both cases there is a similar type of dependence on the normal component of mainstream Mach number.

Comparison With Experiment—Making the comparison between theory and experiment, it should be noted at the outset that the experimental results are for separating flows, and therefore involve large perturbations of the basic boundary layer. For this reason, only a rough correlation will be expected.

The experimental estimates of θ were obtained by drawing a straight line parallel to the pressure distribution curve in the region of constant pressure gradient, and measuring the distance, along the line of the pressure traverse, for the pressure ratio on this straight line to rise from 1:10 to 1:27; that is, for the perturbation

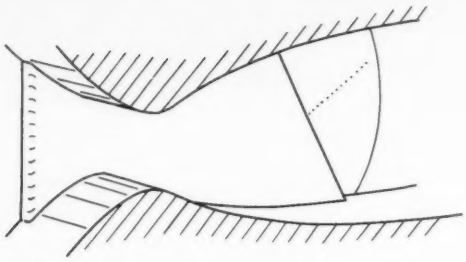

FIG. 8. Test configuration—swept back step.

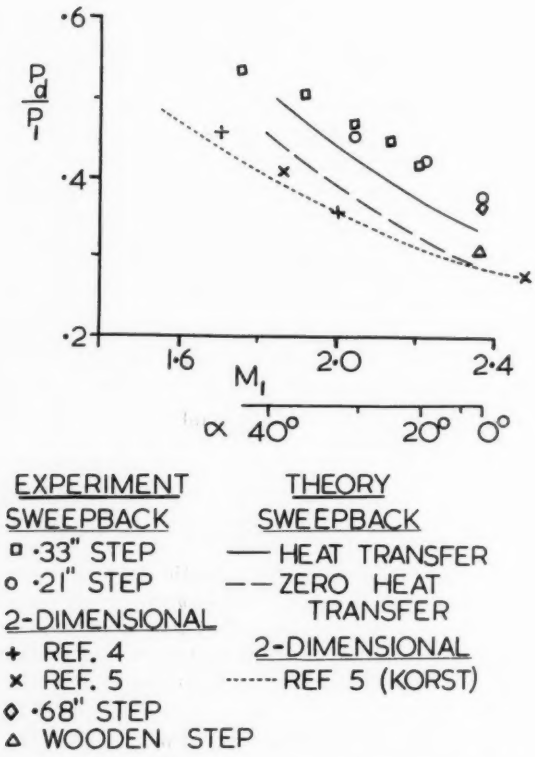

FIG. 9. Effect of sweepback on reattachment pressure rise.

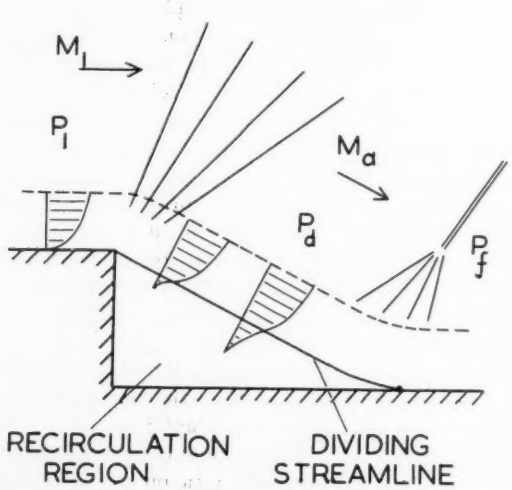

FIG. 10. Reattaching flow downstream of step.

pressure to increase by a factor e. In this manner, values were obtained which were associated with the flow upstream of the separation, where the disturbances were not too large, and yet which were defined with reasonable accuracy from a sufficient number of experimental points.

It is seen from the figure that theory and experiment agree as well as may be expected.

(C) Reattaching Flow

(1) *Experiment*

The tests on the reattachment over a sweptback step were conducted by placing a plate, of uniform thickness, on the tunnel sidewall. This extended upstream into the subsonic portion of the nozzle, as shown in Fig. 8, and was terminated at the test section in such a way that it formed a back step with the desired sweep angle. Then, by replacing the window at the test section by a rotatable steel plate carrying a line of static pressure orifices, it was possible to measure the variation of static pressure along a number of traverse lines immediately downstream of the step face. From these measurements, the variation of the base pressure and a number of isobars in the reattachment zone were obtained for a spanwise distance of about 1.5 in. midspan.

The results, which are presented in detail in reference 6, showed isobars which were parallel to the step face, together with a very slow spanwise variation in base pressure. It was therefore possible to estimate values of the base pressure corresponding to cylindrical symmetry with an expected accuracy of ± 0.02 on pressure ratio, and it is these values which are plotted in Fig. 9.

For comparison with the theory presented below, it was desired that the "asymptotic" step height, or the step height such that further increases did not affect the base pressure, should be obtained. The majority of the results in Fig. 9 are for step heights of 0.21 in. and 0.33 in., and these show no consistent difference, while a further check at zero sweep with a step height of 0.68 in. yielded the same base pressure, whence it is concluded that the asymptotic step height was indeed achieved.

Results obtained by other investigators[4, 14] in two dimensions are also presented in Fig. 9, and it is seen that the base pressure ratios at zero sweep for the present tests are about 0.07 greater than would be expected. Comparison with the test conditions of the other investigators suggested that the present results may be much more prone to a heat-transfer effect, arising from incomplete temperature recovery in the boundary layer and the thermal inertia of the walls, and, to check this, a wooden replica, of step height 0.46 in., of the zero sweep configuration was made. This was mounted on a wooden backing piece extending roughly 9 in. downstream of the step, and when tested, yielded a pressure ratio reduced by 0.05. It was therefore concluded that the present results were indeed subject to a heat-transfer effect, which must be ac-

counted for in comparing with the theory presented below.

(2) *Theory*

Chapman-Korst Mechanism: Review—The nature of the flow immediately downstream of the step is illustrated in Fig. 10. The mainstream flow deflects through an expansion over the salient corner of the step, and flows adjacent to a recirculation region which is separated from the mainstream by a mixing layer. The recirculation region is terminated by reattachment, and the magnitude of the pressure rise supported by this reattachment dictates the base pressure.

In two dimensions, the base pressure can be determined according to a mechanism proposed independently by Chapman[4] and Korst.[5] Since the mass flow scavenged from the recirculation region by the mixing layer will be balanced by that returned through the reattachment pressure rise, a dividing streamline must exist, separating the recirculating flow from that which passes downstream. Assuming that viscous effects may be neglected during the recompression along the dividing streamline, it then follows that the total pressure there must be just sufficient to penetrate the recompression zone, and is therefore equal to the final static pressure when the recompression is complete—i.e.,

$$p_f = p_d\{1 + [(\gamma - 1)/2]\bar{M}^2\}^{\gamma/(\gamma-1)} \qquad (11)$$

For turbulent mixing, by considering a simplified form of the mixing layer equations, Korst obtained a relation between $\bar{M}$ and M_a when the streamwise length of the mixing layer was large, and was thus able to provide an expression for p_d/p_f in terms of M_a. Mainstream relations then allow this ratio, or p_d/p_1, to be determined by the upstream Mach number.

Sweepback Effect—A configuration with cylindrical symmetry is now envisaged, and, since the flow in all planes normal to the step face and the surface is identical, Fig. 10 may be taken to represent the flow in any such plane. The dividing streamline then represents the trace, in the plane, of a dividing stream sheet which, as before, separates the flow with a recirculating component from that which passes downstream, and which meets the surface at a line parallel to the step face.

Following Chapman and Korst, it is assumed that viscous effects at the dividing stream sheet may be ignored during the recompression. The spanwise flow then has no effect on the normal flow, and the normal flow behaves exactly as in two dimensions. Eq. (11) then applies, with $\bar{M}$ now signifying the component of Mach number on the dividing stream sheet normal to the reattachment line. If M_a is now interpreted as the corresponding mainstream component of Mach number, a relation between $\bar{M}$ and M_a will, as before, permit the dependence of p_d/p_1 on upstream flow conditions to be ascertained.

As in two dimensions, this relation is obtained by considering a constant pressure mixing layer, which is, however, initiated at a swept leading edge. In the case of a laminar mixing layer, it is readily shown,[6] by following Moore,[15] that leading-edge sweepback has no effect, and in any streamwise plane normal to the surface the boundary layer develops as in two dimensions. Unfortunately, the turbulent mixing layer is not amenable to theoretical consideration, nor are any experimental results available showing the effect of a swept leading edge. It is therefore necessary to be guided by the results for the turbulent boundary layer in Section (B.2), and this leads to the view that the flow in the mixing layer is parallel to the mainstream, with Mach number distribution identical with that in two dimensions. Thus, for zero heat transfer, the results of Korst's calculations for two-dimensional mixing may be used, yielding a relation between $\bar{M}$ and M_a for any given resultant mainstream Mach number immediately upstream of the recompression.

Calculation of p_d/p_1 may now proceed by a trial and error process. Alternatively, as pointed out by Chapman, negligible error is involved in assuming the recompression in the mainstream to be isentropic, and some algebraic manipulation, following the procedure of reference 4, then produces the explicit expression

$$(p_d/p_1)^{(1-\gamma)/\gamma} = 1 + \frac{\bar{u}^2}{1 - \bar{u}^2} \times \frac{[(\gamma - 1)/2]M_1^2}{1 + [(\gamma - 1)/2]M_1^2 \cos^2 \alpha} \qquad (12)$$

where $\bar{u}$ is the ratio between the velocity on the dividing stream sheet and the mainstream velocity.

This relation is plotted on Fig. 9, and as the sweep angle is increased it is seen to diverge from the corresponding two-dimensional theory of Korst.

(3) *Comparison of Theory With Experiment*

Heat-Transfer Effect—As pointed out above, the tests at zero sweep indicate that the experimental results are unfortunately subject to a heat-transfer effect, and some adjustment to the theory must be made to indicate how this is influenced by sweepback.

Maintaining the assumption that viscous effects may be ignored during recompression, Eq. (11) remains valid, and the base pressure is seen to be influenced through the effect of heat transfer on $\bar{M}$. Now, the difference between the lowest value of the boundary-layer recovery temperature during a test, and the ambient temperature of the tunnel walls, is no greater than 35°C., whence the temperature differences involved in the heat transfer are small, and the changes induced may be regarded as small perturbations of a basic flow with zero heat transfer. $\Delta\bar{M}$, the change in $\bar{M}$, has, therefore, a zero pressure gradient boundary-layer type of dependence on the basic flow. This basic flow has already been taken as insensitive to leading-edge sweepback, and may also be expected to be negligibly affected by the small changes in resultant mainstream Mach number occasioned by the sweepback, wherefore it follows that $\Delta\bar{M}$ is independent of sweepback.

Thus, Eq. (12) may be used to compute the value of $\Delta\bar{M}$ required to cause the observed change in p_d/p_1 at

zero sweep, and this amount added to the zero heat-transfer value of $\bar{M}$ at any other sweep angle, to calculate the value of p_d/p_1 with heat transfer. The resulting corrected curve is shown in Fig. 9, and, allowing for the experimental error in determining the effect of heat transfer at zero sweep, it is seen to be consistent with the experimental results up to a sweep angle of about 40°.

It may be noted that at a sweep angle of 42°, the experimental value of p_d/p_1 is slightly below that expected. This is indicative of a trend which was more pronounced in other, much less accurate results, obtained at larger sweep angles, which are not presented here. Therefore, there is reason to expect that the present analysis will not be effective at large sweep angles.

(D) Conclusions

In previous theoretical approaches to compressible boundary layers with sweepback it has been found that, because of the interdependence of the spanwise and the chordwise flow, it is not generally possible to use simple extensions of appropriate two-dimensional theories. Nevertheless, the present investigations have shown that this can be done for certain important features of turbulent boundary-layer shock-wave interaction in supersonic flows.

For the first of these features, the peak pressure rise, a discontinuity analysis due to Crocco and Probstein is used. In this the influence of the boundary layer is incorporated through certain momentum parameters upstream and downstream of the interaction, which, as indicated by experimental evidence, adjust so rapidly through the interaction that they may be taken to have their zero pressure gradient values. Extension from two dimensions to the sweepback case may therefore be effected without regard to details of the interaction process—specifically, without regard to interdependence in development of the spanwise flow and the flow normal to the line of sweepback.

The upstream influence is treated in Lighthill's small perturbations theory by considering the boundary layer in two parts—an outer layer of rotational but inviscid flow and an inner layer where viscous effects are important but velocities are sufficiently low for the flow to be regarded as incompressible. Since a characteristic of each of these layers is that the flow normal to the line of sweepback develops independently of the spanwise flow, the theory extends simply to the sweepback case.

The Chapman-Korst theory for reattaching flows rests upon the assumption of isentropic recompression along a "dividing streamline," and this aspect has been discussed by the originators of the theory in reference 16. Both are agreed that the probable reason for success of the theory in two dimensions is that the effect of the viscous losses which occur along the dividing streamline is compensated for by reattachment of this streamline before the pressure rise is complete, and the successful use of the theory here implies that this is equally true for cases of moderate sweepback.

References

[1] Moore, F. K., *Three Dimensional Boundary Layer Theory*, "Advances in Applied Mechanics," Vol. IV, Academic Press, Inc., 1956.

[2] Crocco, L., and Probstein, R. F., *The Peak Pressure Rise Across an Oblique Shock Emerging From a Turbulent Boundary Layer Over a Plane Surface*, Princeton Aero. Lab. Report 254, March, 1954.

[3] Lighthill, M. J., *On Boundary Layers and Upstream Influence. II. Supersonic Flows Without Separation*, Proc. Roy. Soc., Series A, Vol. 217, p. 478, 1953.

[4] Chapman, D. R., Kuehn, D. M., and Larson, H. K., *Investigation of Separated Flows in Supersonic and Subsonic Streams With Emphasis on the Effect of Transition*, NACA TN 3869, 1957.

[5] Korst, H. H., *Theory for Base Pressures in Transonic and Supersonic Flow*, J. Appl. Mech. Mech., Vol. 23, No. 4, pp. 593–600, 1956.

[6] Stalker, R. J., *Shock Boundary Layer Interaction in Three Dimensions*, Ph.D. Thesis, Dept. Aero. Engrg., Univ. of Sydney (also to be published as report by Aeronautical Research Laboratories, Melbourne, Australia).

[7] Fisher, R. S., *Investigation of the Turbulent Boundary Layer on a Swept Flat Plate at $M = 2.4$*, Graduation Thesis, Dept. Aero. Engrg., Univ. of Sydney, 1958.

[8] Ashkenas, H., and Riddell, F. R., *Investigations of the Turbulent Boundary Layer on a Yawed Flat Plate*, NACA TN 3383, 1955.

[9] Bogdonoff, S. M., and Kepler, C. E., *Separation of a Supersonic Turbulent Boundary Layer*, Journal of the Aeronautical Sciences, Vol. 22, No. 6, p. 414, June, 1955.

[10] Gadd, G. E., Holder, D. W., and Regan, J. D., *An Experimental Investigation of the Interaction Between Shock Waves and Boundary Layers*, Proc. Roy. Soc., Series A, No. 1165, Vol. 226, p. 227, 1953.

[11] Lange, R. H., *Present Status of Information Relative to the Prediction of Shock-Induced Boundary Layer Separation*, NACA TN 3065, 1954.

[12] Hammitt, A. G., *The Interaction of Shock Waves and Turbulent Boundary Layers*, Journal of the Aeronautical Sciences, Vol. 25, No. 6, p. 345, June, 1958.

[13] Lighthill, M. J., *Reflection at a Laminar Boundary Layer of a Weak, Steady Disturbance to a Supersonic Stream, Neglecting Viscosity and Heat Conduction*, Quart. J. Mech. & Appl. Math., Vol. 3, p. 303, 1950.

[14] Beastall, D., and Eggink, H., *Some Experiments on Breakaway in Supersonic Flow (Part II)*, RAE TN Aero. 2061, 1950.

[15] Moore, F. K., *Three Dimensional Compressible Laminar Boundary Layer Flow*, NACA TN 2279, 1951.

[16] Chapman, D. R., and Korst, H. H., *Discussion on "Theory for Base Pressures in Transonic and Supersonic Flow,"* J. Appl. Mech., Vol. 24, No. 3, p. 484, 1957.

On the Use of Normal Coordinates for the Solution of Lumped Parameter Transient Heat-Transfer Problems

M. E. GURTIN*

General Electric Company

Introduction

THE USE of normal coordinates in solving lumped parameter forced vibration problems has been a valuable asset to the vibration analyst. The same method may be applied to the lumped parameter transient heat-transfer problem. Standard digital computer programs are available which will solve the matrix eigenvalue problem. Using a method such as the serial Jacobi method,[1, 2] the eigenvalues and eigenvectors of a 45 × 45 matrix can be obtained in about 6 minutes on an IBM 704 computer.

This report shows how the matrix eigenvalue problem for heat transfer is set up and how the eigenvalues and eigenvectors are used to construct the transient solution.

Matrix Definitions

$[\ ]$	denotes a matrix
$\bar{\phi}$	the bar denotes a vector or column matrix
$[\ ]^*$	denotes the transpose
$[\ ]_D$	denotes a diagonal matrix
$\dot{(\phi)}$	the dot signifies differentiation with respect to time
I	is the unit diagonal matrix

Basic Equations

Using an electrical-thermal analogy, a set of linear differential equations with constant coefficients can be written for the system to be analyzed. The analogy is shown below:

Electrical	Thermal	
$i = GE$	$q = GT$	(1)
$i = B(dE/dt)$	$q = B(dT/dt)$	

The conductance, G, and susceptance, B, for the thermal analogy are:

$$\begin{aligned} G\ (\text{conduction}) &= KA/l \\ G\ (\text{convection}) &= hA \\ B &= C_p V \rho \end{aligned} \qquad (2)$$

A portion of a typical thermal circuit is shown in Fig. 1.

For the solution, it is desirable to employ heat flow equilibrium equations and solve for the temperatures. This method is known as the nodal method and consists essentially in writing Kirchhoff's current law at the nodes or junctions of the network. The number of independent nodes of a network is the number of junctions minus one.[4] The nodal equations for the node shown in Fig. 2 are:

$$\Sigma q = 0 \qquad (3a)$$

$$q_{ba} + q_{ca} + q_{da} + q_{ea} + q_{a-gnd} + q_a = 0 \qquad (3b)$$

$$(T_b - T_a)G_{ba} + (T_c - T_a)G_{ca} + (T_d - T_a)G_{da} + (T_e - T_a)G_{ea} - (dT_a/dt)B_a + q_a = 0 \qquad (3c)$$

If a nodal analysis is carried out for a complete network, the result will be a set of simultaneous linear differential equations. These equations may be represented by the following matrix equation:

$$[\mathrm{B}]\,\dot{\bar{T}}(t) + [G]\,\bar{T}(t) = \bar{q}(t) \qquad (4)$$

where

$[G]$ = conductance matrix ($q_{ij} = q_{ji}$ = the net heat flow out of node i due to a unit temperature at node j, the temperatures at all other nodes being zero)

$[B]$ = susceptance matrix ($b_{ij} = b_{ji}$ = the net heat flow out of node i due to a unit temperature change with time at node j, the temperature changes with time at all other nodes being zero)

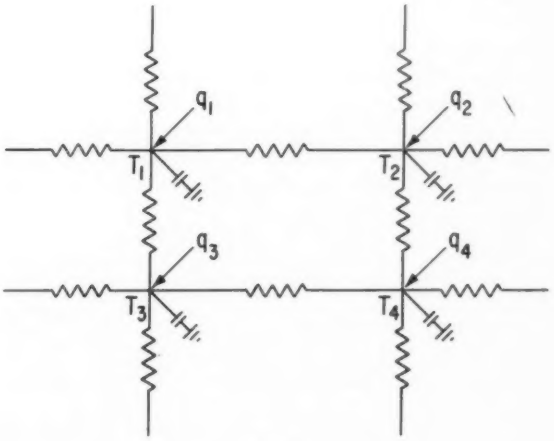

FIG. 1.

Received May 21, 1959.

* Formerly, Engineer—Vibration, General Engineering Laboratory, G-E. Now, National Defense Fellow, Brown University, Providence, R.I.

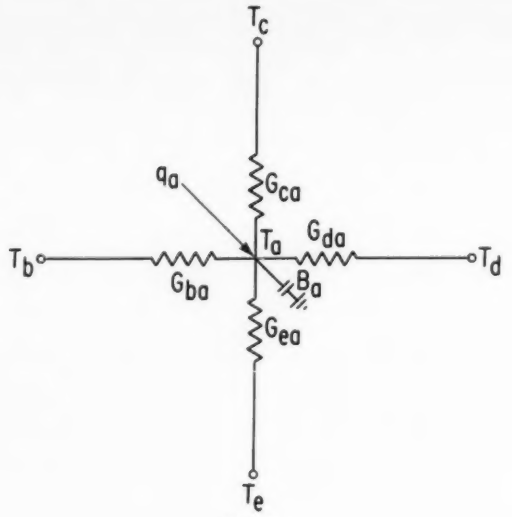

FIG. 2.

$\bar{T}$ = vector or column matrix of temperature coordinates, T_i being the temperature of the ith node

$\bar{q}$ = vector or column matrix of heat flow into the system, q_i being the heat flowing into node i from external sources

To solve Eq. (4), a coordinate transformation is sought which will diagonalize both $[B]$ and $[G]$. These new coordinates are known as normal coordinates. To determine this transformation, the characteristic equation

$$[B]\dot{\bar{T}} + [G]\bar{T} = 0 \tag{5}$$

is solved. The solution is of the form

$$\bar{T} = \bar{\phi}e^{-\lambda t} \tag{6}$$

Combining Eqs. (5) and (6),

$$-\lambda[B]\bar{\phi} + [G]\bar{\phi} = 0 \tag{7}$$

which is the basic matrix eigenvalue problem for lumped parameter thermal circuits. If the number of independent nodes is r, then the solution consists of r values of λ, which need not all be distinct[1,5] and are referred to as the eigenvalues of Eq. (7). Corresponding to each value, λ_n, there exists a vector solution, $\bar{\phi}^n$, referred to as an eigenvector. The eigenvalue problem determines the eigenvectors to within an arbitrary multiplicative constant. Different methods of determining the eigenvalues and eigenvectors of Eq. (7) are given in references 1 and 2.

Now multiply Eq. (7) by $\bar{\phi}^*$ and solve for λ

$$\lambda = \bar{\phi}^*[G]\bar{\phi}/\bar{\phi}^*[B]\bar{\phi} \tag{8}$$

From energy considerations, it is clear that $\bar{\phi}^*[G]\bar{\phi}$, which is proportional to the energy dissipated in the equivalent electrical circuit, must be non-negative. Also, by definition, $\dot{\bar{T}}^*[B]\dot{\bar{T}} > 0$ for values of $\dot{\bar{T}}$ not equal to the null vector. Therefore, $[B]$ must be positive definite. From the above two considerations, we can conclude that $\lambda \geq 0$ and that $\lambda = 0$ corresponds to cases where there is no energy dissipated—i.e., where $\bar{\phi}^*[G]\bar{\phi} = 0$.

An important property of the eigenvectors is orthogonality.[2, 3, 5] If λ_n and λ_p are two different eigenvalues, their corresponding eigenvectors satisfy

$$\begin{aligned} \bar{\phi}^{n*}[B]\bar{\phi}^p &= 0 \\ \bar{\phi}^{n*}[G]\bar{\phi}^p &= 0 \end{aligned} \tag{9}$$

To facilitate solution, the eigenvectors will be normalized such that

$$\bar{\phi}^{n*}[B]\bar{\phi}^n = 1 \tag{10}$$

Then, if a modal matrix is constructed (the nth column being the eigenvector associated with the nth eigenvalue),

$$[M] = \begin{bmatrix} \phi_1{}^1 & \phi_1{}^2 & \cdot & \phi_1{}^n & \cdot & \cdot & \phi_1{}^r \\ \phi_2{}^1 & \phi_2{}^2 & \cdot & \phi_2{}^n & \cdot & \cdot & \phi_2{}^r \\ \cdot & \cdot & & \cdot & & & \cdot \\ \cdot & \cdot & & \cdot & & & \cdot \\ \cdot & \cdot & & \cdot & & & \cdot \\ \cdot & \cdot & & \cdot & & & \cdot \\ \cdot & \cdot & & \cdot & & & \cdot \\ \phi_r{}^1 & \phi_r{}^2 & \cdot & \phi_r{}^n & \cdot & \cdot & \phi_r{}^r \end{bmatrix} \tag{11}$$

It follows directly from the orthogonality relations and from Eq. (10) that

$$[M]^*[B][M] = I \tag{12}$$

It is also apparent that

$$[M]^*[G][M] = \begin{bmatrix} \lambda_1 & 0 & 0 & \cdot & \cdot & 0 \\ 0 & \lambda_2 & \cdot & \cdot & \cdot & \cdot \\ 0 & \cdot & \cdot & & & \cdot \\ \cdot & \cdot & & \cdot & & \cdot \\ \cdot & \cdot & & & \cdot & \cdot \\ 0 & \cdot & \cdot & \cdot & \cdot & \lambda_r \end{bmatrix}_D \equiv [\lambda_n]_D \tag{13}$$

A method is now available to diagonalize $[B]$ and $[G]$ simultaneously. This method will be used for the solution of Eq. (4). The Laplace transform of Eq. (4) is now taken (all initial conditions assumed to be zero).

$$\{s[B] + [G]\}\bar{T}(s) = \bar{q}(s) \tag{14}$$

Premultiplying Eq. (14) by $[M]^*$ and defining

$$\bar{T}(s) = [M]\bar{A}(s) \tag{15}$$

results in the following equation:

$$\{s[M]^*[B][M] + [M]^*[G][M]\}\bar{A}(s) = [M]^*\bar{q}(s) \tag{16}$$

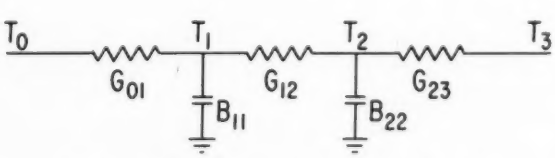

FIG. 3. T_0 and T_3 are specified functions of time.

But, from Eqs. (12) and (13),

$$[Is + [\lambda_n]_D]\ \bar{A}(s) = [M]^*\bar{q}(s) \tag{17}$$

As the matrix,

$$[Is+[\lambda_n]_D]_D=\begin{bmatrix} s+\lambda_1 & 0 & 0 & . & . & 0 \\ 0 & s+\lambda_2 & . & . & . & . \\ 0 & . & . & & & . \\ . & . & & . & & . \\ . & . & & & . & . \\ 0 & . & . & . & . & \lambda_r \end{bmatrix}_D \tag{18}$$

is diagonal. Its inverse will be:

$$[Is + [\lambda_n]_D]\bar{D}^{-1} = \begin{bmatrix} \frac{1}{s+\lambda_1} & 0 & 0 & . & . & 0 \\ 0 & \frac{1}{s+\lambda_2} & . & . & . & . \\ 0 & . & . & . & & . \\ . & . & & . & & . \\ . & . & & & . & . \\ 0 & . & . & . & . & \frac{1}{s+\lambda_r} \end{bmatrix}_D \equiv \left[\frac{1}{s+\lambda_n}\right]_D \tag{19}$$

Eq. (17) is now solved for $\bar{A}(s)$:

$$\bar{A}(s) = [1/(s+\lambda_n)]_D[M]^*\bar{q}(s) \tag{20}$$

and

$$\bar{T}(s) = [M]\bar{A}(s) = [M][1/(s+\lambda_n)]_D[M]^*\bar{q}(s) \tag{21}$$

which may also be written

$$\bar{T}(s) = \sum_{n=1}^{n=r} \frac{\bar{\phi}^{n*}\bar{q}(s)\bar{\phi}^n}{s+\lambda_n} \tag{22}$$

Taking the inverse Laplace transform of Eq. (22)

$$\bar{T}(t) = \mathfrak{L}^{-1} \sum_{n=1}^{n=r} \frac{\bar{\phi}^{n*}\bar{q}(s)\bar{\phi}^n}{s+\lambda_n} \tag{23}$$

which is the closed-form solution of the original problem in terms of the eigenvalues and eigenvectors of the characteristic equation.

Solutions for Different Types of Inputs

If the inputs are all step functions applied at time zero,

$$\bar{q}(s) = \bar{Q}/s \tag{24}$$

Eq. (23) becomes

$$\bar{T}(t) = \mathfrak{L}^{-1} \sum_{n=1}^{n=r} \frac{\bar{\phi}^{n*}\bar{Q}\bar{\phi}^n}{s(s+\lambda_n)} \tag{25}$$

or

$$\bar{T}(t) = \sum_{n=1}^{n=r} \frac{\bar{\phi}^{n*}\bar{Q}\bar{\phi}^n}{\lambda_n}\,[1 - e^{-\lambda_n t}] \tag{26}$$

If the inputs are all ramp functions applied at time zero,

$$\bar{q}(s) = \bar{Q}/s^2 \tag{27}$$

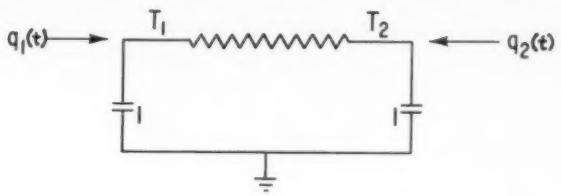

FIG. 4. $q_1(t) = 1, \quad t \geqq 0$
$= 0, \quad t < 0$
$q_2(t) = 2, \quad t \geqq 0$
$= 0, \quad t < 0$

Eq. (23) becomes

$$\left.\begin{aligned} \bar{T}(t) &= \mathfrak{L}^{-1} \sum_{n=1}^{n=r} \frac{\bar{\phi}^{n*}\bar{Q}\bar{\phi}^n}{s^2(s+\lambda^n)} \\ \bar{T}(t) &= \sum_{n=1}^{n=r} \frac{\bar{\phi}^{n*}\bar{Q}\bar{\phi}^n}{{\lambda_n}^2}\,[e^{-\lambda_n t} + \lambda_n t - 1] \end{aligned}\right\} \tag{28}$$

If temperatures at certain points are specified as a function of time instead of heat flow, the problem is solved in the same manner. As an example, the equations for the problem shown in Fig. 3 will be written:

$$\left.\begin{aligned} (T_1 - T_0)G_{01} + (T_1 - T_2)G_{12} + (dT_1/dt)B_{11} = 0 \\ (T_2 - T_1)G_{12} + (T_2 - T_3)G_{23} + (dT_2/dt)B_{22} = 0 \end{aligned}\right\} \tag{29}$$

or

$$\begin{bmatrix} B_{11} & 0 \\ 0 & B_{22} \end{bmatrix}\begin{pmatrix} \dot{T}_1 \\ \dot{T}_2 \end{pmatrix} + \begin{bmatrix} G_{01}+G_{12} & -G_{12} \\ -G_{12} & G_{12}+G_{23} \end{bmatrix}\begin{pmatrix} T_1 \\ T_2 \end{pmatrix} = \begin{pmatrix} G_{01}\,T_0 \\ G_{23}\,T_3 \end{pmatrix} \tag{30}$$

If we define

$$\bar{q}(t) = \begin{pmatrix} G_{01}T_0 \\ G_{23}T_3 \end{pmatrix} \tag{31}$$

We have an equation identical to Eq. (4), and, therefore, the solution is identical.

An Example

The equivalent circuit shown in Fig. 4 will be solved. The number of junctions is three, and, therefore, the number of independent nodes is two. Then,

$$[B] = \begin{bmatrix} 1 & 0 \\ 0 & 1 \end{bmatrix} \tag{32}$$

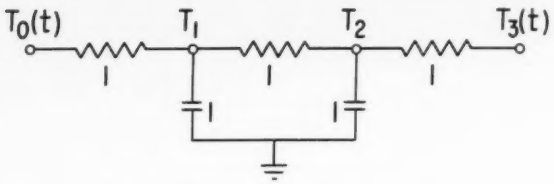

FIG. 5. $T_0(t) = 1,\ t \geqq 0;\ = 0,\ t < 0\} \quad T_0(s) = 1/s$
$T_3(t) = 2,\ t \geqq 0;\ = 0,\ t < 0\} \quad T_3(s) = 2/s$

$$[G] = \begin{bmatrix} 1 & -1 \\ -1 & 1 \end{bmatrix} \tag{33}$$

Substituting Eqs. (32) and (33) into Eq. (7),

$$\left[-\lambda\begin{bmatrix}1 & 0\\ 0 & 1\end{bmatrix} + \begin{bmatrix}1 & -1\\ -1 & 1\end{bmatrix}\right]\begin{pmatrix}\phi_1\\ \phi_2\end{pmatrix} = 0 \tag{34}$$

For a problem as small as this, a direct solution is the most practical.* The characteristic equation is

$$\begin{vmatrix} 1-\lambda & -1 \\ -1 & 1-\lambda \end{vmatrix} = 0 \tag{35}$$

or

$$\left.\begin{aligned}(1-\lambda)(1-\lambda) - 1 &= 0\\ \lambda_1 &= 0\\ \lambda_2 &= 2\end{aligned}\right\} \tag{36}$$

$$\begin{array}{ll|ll} \multicolumn{2}{c|}{\text{for } \lambda = 0} & \multicolumn{2}{c}{\text{for } \lambda = 2} \\ \phi_1 - \phi_2 &= 0 & -\phi_1 - \phi_2 &= 0 \\ \phi_1 &= \phi_2 & \phi_1 &= -\phi_2 \\ \multicolumn{2}{c|}{\bar{\phi}^{(1)} = \begin{pmatrix}0.707\\ 0.707\end{pmatrix}\dagger} & \multicolumn{2}{c}{\bar{\phi}^{(2)} = \begin{pmatrix}0.707\\ -0.707\end{pmatrix}\dagger} \end{array} \tag{37}$$

From Fig. 4,

$$\left.\begin{aligned}q_1(s) &= 1/s, \quad Q_1 = 1\\ q_2(s) &= 2/s, \quad Q_2 = 2\end{aligned}\right\} \tag{38}$$

Then, from Eq. (26), which is the temperature distribution due to step function inputs,

$$\bar{T}(t) = (0.707,\ 0.707)\begin{pmatrix}1\\2\end{pmatrix}\begin{pmatrix}0.707\\0.707\end{pmatrix}\left\{\lim_{\lambda_1 \to 0}\frac{1-e^{-\lambda_1 t}}{\lambda_1}\right\} + (0.707,\ -0.707)\begin{pmatrix}1\\2\end{pmatrix}\begin{pmatrix}0.707\\-0.707\end{pmatrix}\left\{\frac{1-e^{-2t}}{2}\right\} \tag{39}$$

* Actually, for a problem as small as this, the use of normal coordinates is not necessary. However, the use of normal coordinates can be most easily demonstrated on a simple system.

† Normalized as per Eq. (10).

or

$$\bar{T}(t) = \begin{pmatrix}1.5t\\1.5t\end{pmatrix} + \begin{pmatrix}-0.25 + 0.25e^{-2t}\\ +0.25 - 0.25e^{-2t}\end{pmatrix} \tag{40}$$

or

$$\left.\begin{aligned}T_1(t) &= 1.5t - 0.25 + 0.25e^{-2t}\\ T_2(t) &= 1.5t + 0.25 - 0.25e^{-2t}\end{aligned}\right\} \tag{41}$$

Another Example

A circuit in which the temperatures are specified will now be solved (see Fig. 5). The susceptance and conductance matrices are:

$$\left.\begin{aligned}[B] &= \begin{bmatrix}1 & 0\\ 0 & 1\end{bmatrix}\\ [G] &= \begin{bmatrix}2 & -1\\ -1 & 2\end{bmatrix}\end{aligned}\right. \tag{42}$$

The characteristic equation is:

$$\left.\begin{aligned}\begin{vmatrix}2-\lambda & -1\\ -1 & 2-\lambda\end{vmatrix} &= 0\\ \lambda_1 &= 1\\ \lambda_2 &= 3\end{aligned}\right. \tag{43}$$

And the corresponding eigenvectors are:

$$\bar{\phi}^{(1)} = \begin{pmatrix}0.707\\0.707\end{pmatrix}, \quad \bar{\phi}^{(2)} = \begin{pmatrix}0.707\\-0.707\end{pmatrix} \tag{44}$$

and

$$\bar{q}(s) = \begin{pmatrix}G_1 T_0(s)\\ G_3 T_3(s)\end{pmatrix} = \begin{pmatrix}1/s\\ 2/s\end{pmatrix} \tag{45}$$

From Eq. (26),

$$\bar{T}(t) = [0.707,\ 0.707]\begin{pmatrix}1\\2\end{pmatrix}\begin{pmatrix}0.707\\0.707\end{pmatrix}\{1 - e^{-t}\} + (0.707,\ -0.707)\begin{pmatrix}1\\2\end{pmatrix}\begin{pmatrix}0.707\\-0.707\end{pmatrix}\{0.33 - 0.33e^{-3t}\} \tag{46}$$

or

$$\left.\begin{aligned}T_1(t) &= 1.333 - 1.5e^{-t} + 0.1667e^{-3t}\\ T_2(t) &= 1.667 - 1.5e^{-t} - 0.1667e^{-3t}\end{aligned}\right\} \tag{47}$$

which are the required temperature-time relations.

References

[1] White, P. A., *The Computation of Eigenvalues and Eigenvectors of a Matrix*, J. Soc. Indus. Appl. Math., Vol. 6, No. 4, December, 1958.

[2] Crandall, S. H., *Engineering Analysis, A Survey of Numerical Procedures*, McGraw-Hill Book Co., Inc., 1956.

[3] Frazer, R. A., Duncan, W. J., and Collar, A. R., *Elementary Matrices*, Cambridge University Press, 1955.

[4] Kerchner, R. M., and Corcoran, G. F., *Alternating Current Circuits*, John Wiley and Sons, 1956.

[5] Hildebrand, F. B., *Methods of Applied Mathematics*, Prentice-Hall, Inc., 1956.

An Approximate Solution of the Direct Supersonic Blunt-Body Problem for Arbitrary Axisymmetric Shapes

STEPHEN C. TRAUGOTT*

The Martin Company

Summary

The integral method of Belotserkovskii has been carried out to the first approximation for arbitrary blunt axisymmetric bodies in supersonic or hypersonic flight. This method is direct, in that it gives the surface-pressure distribution and shock shape for a prescribed body. Results obtained by numerical integration for several body shapes at several Mach numbers are compared to experimental results with good agreement. It is also shown that the method can be successfully applied to pointed bodies with attached shock. In the stagnation region, simple relationships are found from the equations of the first approximation which connect the surface-velocity gradient, shock curvature, shock-detachment distance, and body curvature. These relations are also correlated with experiment for a variety of shapes as a function of Mach number. The correlations permit a rapid estimate of the stagnation-point velocity gradient, important for heat-transfer calculations, for any blunt body from the shock stand-off distance. A method for a higher approximation is described, for which, in contrast to the higher approximations of Belotserkovskii, a large number of simultaneous total differential equations with unknown parameters does not occur. One form of this method has been studied numerically. Results are given which, though only partially successful, indicate the amount of improvement to be expected from a higher approximation.

Symbols

Nondimensionalizing quantities are: maximum body radius l, stagnation pressure and density ahead of shock, and maximum velocity $U_{max} = U_\infty \sqrt{[2 + (\gamma - 1)M_\infty^2]/(\gamma - 1)M_\infty^2}$, with U_∞ the flight velocity.

a = dimensionless body radius in the plane normal to the body axis
M = Mach number
n = dimensionless coordinate normal to the body surface, measured from the surface
p = dimensionless pressure
r = dimensionless radial coordinate in the plane normal to the body axis
R = dimensionless body radius of curvature $= -[1/(d\theta/ds)]$
$\mathfrak{R}$ = dimensionless shock radius of curvature
s = dimensionless coordinate along the body surface, measured from the stagnation point
v_s = dimensionless velocity parallel to the body surface
v_n = dimensionless velocity normal to the surface
w = $\sqrt{v_s^2 + v_n^2}$
X = dimensionless distance from the stagnation point along the body axis
δ = dimensionless shock layer thickness measured normal to the body surface
ρ = dimensionless density
θ = angle from axis of symmetry to body-surface tangent
x = angle from normal to axis of symmetry to shock tangent
ψ = stream function defined in Eq. (9)
φ = p/ρ^γ
γ = ratio of specific heats (assumed constant)
τ = dimensionless time

Subscripts

∞ referring to conditions just behind the shock
δ referring to conditions just behind the shock
0 referring to conditions on the body surface
sp referring to conditions at the stagnation point

(1) Introduction

IT IS WELL KNOWN that a blunt shape in supersonic flight is accompanied by a detached shock wave with a resultant mixed flow field between body and shock. The practical importance of blunt-nosed bodies has led to many recent investigations of supersonic flow with detached shocks, and these have been both of the inverse and direct type. In the inverse problem, the shape of the shock is considered given and the associated body shape follows from the solution. The problems associated with boundary conditions specified along an otherwise unknown shock location are thus avoided. This approach is taken in the studies of Zlotnick and Newman,[1] Garabedian and Lieberstein,[2] and Van Dyke,[3] where numerical solutions of the exact inviscid equations are obtained. It is shown there that the shape of the shock can be selected to give, within limits, body shapes of practical interest. Nevertheless, it seems that prescribed variations in body curvature would be very difficult to approximate with a suitable shock. The direct method, by which the shock and flow field are found for a given body, would permit greater practical utilization. Examples of this latter approach are given by Maslen and Moeckel,[4] Li and Geiger,[5] and Lees and Kubota.[6] However, these studies consider only hypersonic flow and approximations are made which are not valid at low supersonic Mach numbers. Although, for obvious reasons, hypersonic flow is receiving a great deal of attention, it nevertheless is desirable to have methods available which are valid for relatively low supersonic Mach numbers as well, since blunt re-entry shapes must also fly supersonically. Uchida and Yasuhara[7] and Cabannes[8] consider the direct problem without restriction to hypersonic flow, but in the former case the method

Received May 15, 1959.

* Scientist, Research and Development, Aerophysics Research Staff, BL.

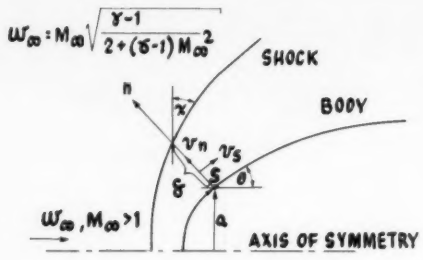

FIG. 1. Coordinate system.

is not suited to numerical machine work, while the latter approach appears quite cumbersome.

A straightforward method for the direct problem, well suited to numerical computation, was given by Belotserkovskii.[9] In this study, an approximate integral theory without restrictions on Mach number is applied to plane supersonic flow about a cylinder. The inviscid equations of motion are first integrated across the shock layer to give a system of simultaneous total differential equations from which the shock shape and the surface-pressure distribution may then be determined.* Results are presented for several Mach numbers and degrees of approximation. It is shown that, for flow about a cylinder, the first approximation should be satisfactory for most purposes.

Blunt-body shapes of current practical interest are characterized by large variations of the meridional radius of curvature, and it seemed worthwhile to extend the integral method described above to blunt axisymmetric bodies of arbitrary shape. The present work is concerned with this extension, and with the determination of how well the relatively simple first approximation describes the flow field for such bodies. The higher approximations of Belotserkovskii lead rapidly to the difficult problem of solving a large number of simultaneous differential equations in which a number of unknown parameters must be simultaneously determined by the condition that no singularities occur in the solution. A scheme will be described here for obtaining higher approximations which avoids this difficulty and involves, as in the first approximation, only three simultaneous differential equations with the shock detachment distance as the only free parameter. Further, simple and useful relations are derived from the formulation of the first approximation which relate the stagnation-point velocity gradient, shock-detachment distance, and shock curvature for arbitrary body shapes.

(2) Fundamental Equations

To accommodate an arbitrary body contour, coordinates along and normal to the axisymmetric surface are chosen. Following Belotserkovskii, all variables are made dimensionless: lengths with the maximum body radius in the plane normal to the body axis, velocities with the maximum velocity U_{max}, and pressure and density with stagnation pressure and stagnation density ahead of the shock where the Mach number is M_∞ and the dimensionless uniform velocity is w_∞. In Fig 1, s is the distance to any point on the body along the surface, n is in the direction normal to the surface, θ is the angle between the axis of symmetry and the surface tangent, x is the angle between the normal to the axis of symmetry and the shock tangent, and δ is the shock layer thickness along n. The body is prescribed by the variation of a, the body radius in the plane normal to the axis, with s. The body radius of curvature in the meridional plane is

$$R = -[1/(d\theta/ds)]$$

We neglect viscosity and heat conduction, and assume constant specific heats, with ratio γ. To obtain the equations of motion in a form suitable for our purposes, let

$$\begin{aligned} t &= (1 - w^2)^{1/(\gamma-1)}v_s \\ h &= (1 - w^2)^{1/(\gamma-1)}v_n \\ z &= \rho v_s v_n \\ H &= \rho v_n^2 + [(\gamma - 1)/2\gamma]p \\ g &= \rho v_s^2 + [(\gamma - 1)/2\gamma]p \end{aligned}$$

Then the governing differential equations for steady motion can be written as follows.

Continuity:

$$[\partial(rt)/\partial s] + (\partial/\partial n)\{[1 + (n/R)]rh\} = 0 \quad (1)$$

Momentum in the n Direction:

$$[\partial(rz)/\partial s] + (\partial/\partial n)\{[1 + (n/R)]rH\} - (r/R)g - [1 + (n/R)]\cos\theta[(\gamma - 1)/2\gamma]p = 0 \quad (2)$$

Integrated Momentum (Bernoulli Equation):

$$p/\rho = 1 - w^2 \quad (3)$$

Energy:

$$(D/D\tau)(p/\rho^\gamma) = 0 \quad (4)$$

These four equations are sufficient to determine the four unknowns v_s, v_n, p, and ρ.

Eqs. (1) and (2) may be integrated over n across the shock layer, from $n = 0$ to $n = \delta$. One finds, making use of the Leibnitz rule and the fact that on the surface $h_0 = z_0 = 0$,

$$r_\delta h_\delta[1 + (\delta/R)] - r_\delta t_\delta(d\delta/ds) + (d/ds)\int_0^\delta (rt)dn = 0 \quad (5)$$

$$r_\delta H_\delta[1 + (\delta/R)] - aH_0 - r_\delta z_\delta(d\delta/ds) + (d/ds)\int_0^\delta (rz)dn - \int_0^\delta (r/R)gdn - \cos\theta\,[(\gamma - 1)/2\gamma]\int_0^\delta [1 + (n/R)]pdn = 0 \quad (6)$$

* This publication was brought to the author's attention by Dr. Maurice Holt of Brown University. Dr. Holt has since extended Belotserkovskii's first approximation to spheres and spherical caps.

It follows from Eq. (4) that p/ρ^γ is constant along a streamline—thus,

$$p/\rho^\gamma = \varphi(\psi) \tag{7}$$

(with ψ, the stream function, defined below).

Then, making use of Eq. (3),

$$\left.\begin{aligned} p &= (1 - u^2)^{\gamma/(\gamma-1)}\varphi^{-1/(\gamma-1)} \\ \rho &= (1 - w^2)^{1/(\gamma-1)}\varphi^{-1/(\gamma-1)} \end{aligned}\right\} \tag{8}$$

If Eq. (8) is used in Eqs. (5) and (6), these latter equations will contain as unknown variables v_s, v_n, φ, and ψ. The introduction of ψ as a new unknown requires an additional equation. This is supplied by the definition of the stream function, here written along any line in the n–s plane prescribed by $n = n(s)$ as

$$d\psi/ds = \rho\{rv_s(dn/ds) - [1 + (n/R)]rv_n\} \tag{9}$$

Eqs. (5) through (9) then determine the problem.

Suppose the functional form of the integrands in Eqs. (5) and (6) were known, so that these integrands are given in terms of their values at the boundaries—that is, body surface and shock. Then these equations would be total differential equations in s containing δ, v_{s_δ}, v_{n_δ}, φ_δ, φ_0, v_{s_0}, and v_{n_0}. But $v_{n_0} = 0$, and, since the body surface is also a streamline, $\varphi_0 = \varphi_{sp}$ is known from the normal shock relations. The oblique shock relations yield v_{s_δ}, v_{n_δ}, and φ_δ as functions of x [see Eq. (12)]; thus, only three unknowns remain—δ, x, and v_{s_0}. A third equation for use with Eqs. (5) and (6) is supplied as an additional relation between δ and x from the geometry of Fig. 1:

$$d\delta/ds = [1 + (\delta/R)]/\tan(\theta + x) \tag{10}$$

Integration of Eqs. (5), (6), and (10) will then determine the shock as a function of distance along the surface from δ and x, and the pressure distribution is obtained from v_{s_0}.

The knowledge necessary to evaluate the integrands in Eqs. (5) and (6) must come from Eqs. (7) and (9). These are available to supply the required information about variations of the flow field in the n direction, normal to the surface.

(3) First Belotserkovskii Approximation

A first approximation to the problem can be obtained by taking the integrands in the integrated continuity and momentum Eqs. (5) and (6) to be linear in n. Since this takes the place of information which should come from Eqs. (7) and (9), these equations are no longer necesary. If any one of the integrands is $f(n, s)$, then

$$f(n, s) = f_0(s) + (n/\delta)[f_\delta(s) - f_0(s)]$$

and

$$\int_0^\delta f(n, s)dn = (\delta/2)[f_\delta + f_0] \tag{11}$$

The equations for the first approximation are obtained by substituting Eq. (11) into Eqs. (5) and (6). For example,

$$(d/ds)\int_0^\delta (rt)dn = (1/2)[(rt)_\delta + (rt)_0]\,(d\delta/ds) + (\delta/2)[d(rt)_0/ds] + (\delta/2)[d(rt)_\delta/ds]$$

With

$$(rt)_0 = a(1 - v_{s_0}^2)^{1/(\gamma-1)}v_{s_0}$$

$$(rt)_\delta = (a + \delta\cos\theta)(1 - w_\delta^2)^{1/(\gamma-1)}v_{s_\delta}$$

All quantities immediately behind the shock are related to x by use of the oblique shock relations, which here take the form (see, for instance, reference 10)

$$\varphi_\delta = \left[\frac{2\gamma M_\infty^2\cos^2 x - (\gamma - 1)}{\gamma + 1}\right]\times \left[\frac{2 + (\gamma - 1)M_\infty^2\cos^2 x}{(\gamma + 1)M_\infty^2\cos^2 x}\right]^\gamma \tag{12a}$$

$$v_{s_\delta} = M_\infty\sqrt{\frac{\gamma - 1}{2 + (\gamma - 1)M_\infty^2}}\times \left\{\left[1 - \frac{2}{\gamma + 1}\left(\cos^2 x - \frac{1}{M_\infty^2}\right)\right]\cos\theta + \left[\frac{2}{\gamma + 1}\tan x\left(\cos^2 x - \frac{1}{M_\infty^2}\right)\right]\sin\theta\right\} \tag{12b}$$

$$v_{n_\delta} = M_\infty\sqrt{\frac{\gamma - 1}{2 + (\gamma - 1)M_\infty^2}}\times \left\{\left[1 - \frac{2}{\gamma + 1}\left(\cos^2 x - \frac{1}{M_\infty^2}\right)\right](-\sin\theta) + \left[\frac{2}{\gamma + 1}\tan x\left(\cos^2 x - \frac{1}{M_\infty^2}\right)\right]\cos\theta\right\} \tag{12c}$$

Because the surface is a streamline along which the entropy is constant, we have

$$\varphi_0 = \left[\frac{2\gamma M_\infty^2 - (\gamma - 1)}{\gamma + 1}\right]\left[\frac{2 + (\gamma - 1)M_\infty^2}{(\gamma + 1)M_\infty^2}\right]^\gamma \tag{13}$$

Together with Eq. (10), three first-order total differential equations result, containing as unknowns $\delta(s)$, $x(s)$, $v_{s_0}(s)$, and their s derivatives.

These differential equations are easily solved for the derivatives of the unknown quantities in the form

$$d\delta/ds = [1 + (\delta/R)]/\tan(\theta + x) \tag{10}$$

$$\frac{dv_{s_0}}{ds} = \frac{F[D - A(d\delta/ds)] - C[G + E(d\delta/ds)]}{BF} \tag{14}$$

$$dx/ds = [G + E(d\delta/ds)]/F \tag{15}$$

where the individual terms on the right-hand side of the last two equations are given below.

$$A = (a/2)\{(1 - v_{s_0}^2)^{1/(\gamma-1)}v_{s_0} - (1 - w_\delta^2)^{1/(\gamma-1)}v_{s_\delta}\}$$

$$B = (\delta a/2)(1 - v_{s_0}^2)^{(2-\gamma)/(\gamma-1)}\times \{1 - [(\gamma + 1)/(\gamma - 1)]v_{s_0}^2\}$$

$$C = \frac{\delta}{2}(a + \delta\cos\theta)(1 - w_\delta^2)^{1/(\gamma-1)}\frac{4}{\gamma+1}M_\infty\sqrt{\frac{(\gamma-1)}{2+(\gamma-1)M_\infty^2}}\left(\left[1 - \frac{2v_{s_\delta}^2}{(\gamma-1)(1-w_\delta^2)}\right]\times\right.$$
$$\left\{\left[\frac{1}{2}\left(1 - \frac{1}{M_\infty^2\cos^2 x}\right) - \sin^2 x\right]\sin\theta + (\sin x\cos x)\cos\theta\right\} - \left[\frac{2v_{s_\delta}v_{n_\delta}}{(\gamma-1)(1-w_\delta^2)}\right]\times$$
$$\left.\left\{\left[\frac{1}{2}\left(1 - \frac{1}{M_\infty^2\cos^2 x}\right) - \sin^2 x\right]\cos\theta - (\sin x\cos x)\cos\theta\right\}\right)$$

$$D = -[1 - (\delta/2)(d\theta/ds)](a + \delta\cos\theta)(1 - w_\delta^2)^{1/(\gamma-1)}v_{n_\delta} - (\delta/2)\sin\theta\{(1 - v_{s_0}^2)^{1/(\gamma-1)}v_{s_0} +$$
$$(1 - w_\delta^2)^{1/(\gamma-1)}v_{s_\delta}[1 - \delta(d\theta/ds)]\}$$

$$E = (a/2)(1 - w_\delta^2)^{1/(\gamma-1)}\varphi_\delta^{-[1/(\gamma-1)]}v_{s_\delta}v_{n_\delta}$$

$$F = \frac{\delta}{2}(a + \delta\cos\theta)(1 - w_\delta^2)^{1/(\gamma-1)}\frac{4}{\gamma+1}M_\infty\sqrt{\frac{\gamma-1}{2+(\gamma-1)M_\infty^2}}\left(v_{n_\delta}\left[1 - \frac{2v_{s_\delta}^2}{(\gamma-1)(1-w_\delta^2)}\right]\times\right.$$
$$\left\{\left[\frac{1}{2}\left(1 - \frac{1}{M_\infty^2\cos^2 x}\right) - \sin^2 x\right]\sin\theta + (\sin x\cos x)\cos\theta\right\} + v_{s_\delta}\left[1 - \frac{2v_{n\delta}^2}{(\gamma-1)(1-w_\delta^2)}\right]\times$$
$$\left.\left\{\left[\frac{1}{2}\left(1 - \frac{1}{M_\infty^2\cos^2 x}\right) - \sin^2 x\right]\cos\theta - (\sin x\cos x)\sin\theta\right\}\right)\varphi_\delta^{-[1/(\gamma-1)]} + \frac{\delta}{2}(a + \delta\cos\theta)\times$$
$$(1 - w_\delta^2)^{1/(\gamma-1)}2v_{s_\delta}v_{n_\delta}\tan x\frac{\gamma}{\gamma+1}\frac{(M_\infty^2\cos^2 x - 1)^2}{2+(\gamma-1)M_\infty^2\cos^2 x}\left[\frac{2+(\gamma-1)M_\infty^2\cos^2 x}{(\gamma+1)M_\infty^2\cos^2 x}\right]^\gamma\varphi_\delta^{-[\gamma/(\gamma-1)}$$

$$G = -\varphi_\delta^{-[1/(\gamma-1)]}(1 - w_\delta^2)^{1/(\gamma-1)}\{v_{n_\delta}^2[1 - (\delta/2)(d\theta/ds)](a + \delta\cos\theta) + v_{s_\delta}v_{n_\delta}[1 - \delta(d\theta/ds)](\delta/2)\sin\theta\} -$$
$$\varphi_0^{-[1/(\gamma-1)]}(1 - v_{s_0}^2)^{1/(\gamma-1)}\{v_{s_0}^2(\delta/2)(d\theta/ds)a\} - [(\gamma-1)/2\gamma][a + (\delta/2)\cos\theta - (\delta/2)(d\theta/ds)a]\times$$
$$[(1 - w_\delta^2)^{\gamma/(\gamma-1)}\varphi_\delta^{-[1/(\gamma-1)]} - (1 - v_{s_0}^2)^{\gamma/(\gamma-1)}\varphi_0^{-[1/(\gamma-1)]}]$$

with

$$M_\infty\sqrt{(\gamma-1)/[2+(\gamma-1)M_\infty^2]} = u_\infty$$

Considered together with Eqs. (12) and (13), Eqs. (10), (14), and (15) are of the form:

$$d\delta/ds = (d\delta/ds)[\delta, x, \theta, (d\theta/ds)]$$
$$dv_{s_0}/ds = (dv_{s_0}/ds)[\delta, x, v_{s_0}, \theta, (d\theta/ds), a, \gamma, M_\infty]$$
$$dx/ds = (dx/ds)[\delta, x, v_{s_0}, \theta, (d\theta/ds), a, \gamma, M_\infty]$$

The solution of this system of coupled nonlinear equations with proper initial values constitutes the first approximation. The initial values are, for $s = 0$,

$$\delta = \delta_{sp}, \quad v_{s_0} = 0, \quad x = 0$$

The stagnation-point shock detachment distance, δ_{sp}, is unknown; it must be determined as part of the solution. This is done in the following way.

It can be seen from Eqs. (14) and (15) that both dv_{s_0}/ds and dx/ds become infinite when F vanishes, while a vanishing B makes dv_{s_0}/ds infinite. No physical interpretation readily appears for F, and one cannot say a priori whether it will vanish or not. However, B will vanish when

$$v_{s_0} = \sqrt{(\gamma-1)/(\gamma+1)}$$

which is sonic velocity. If the velocity gradient at the sonic point on the surface is to remain finite, we must require that both the numerator and the denominator of Eq. (14) vanish at this point. That is, when $B = 0$,

$$D - A(d\delta/ds) = C(dx/ds)$$

This condition is used to determine δ_{sp} by an iterative procedure. The details of this procedure are given in reference 11. Of course, it is possible that an infinite velocity gradient does physically occur on the surface when a sharp corner exists. However, due to the nature of the coordinate system chosen, any sharp corner must be slightly rounded if the shock shape is to be specified everywhere, as shown by Sketch 1.

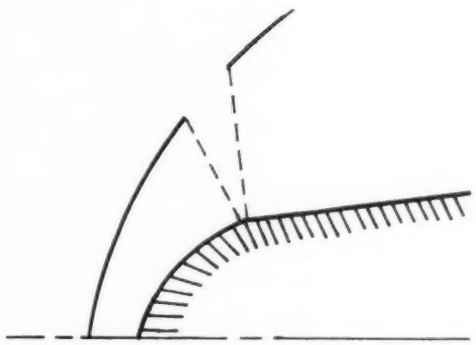

SKETCH 1.

Thus, the condition which determines the stagnation-point shock-detachment distance will always be taken here to be a finite velocity gradient at the sonic point and the equations then can be integrated to give δ, x, v_{s_0}. The surface pressure is finally calculated from the first of Eq. (8), which becomes at the body surface

$$p_0 = \left[(1 - v_{s_0}^2)\frac{(\gamma+1)M_\infty^2}{2+(\gamma-1)M_\infty^2}\right]^{\gamma/(\gamma-1)}\times$$
$$\left[\frac{2\gamma M_\infty^2 - (\gamma-1)}{\gamma+1}\right]^{-[1/(\gamma-1)]} \qquad (16)$$

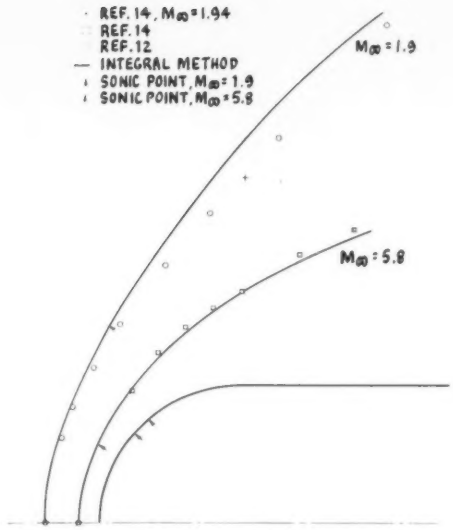

FIG. 2. Shock shapes, hemisphere-cylinder.

(4) First-Approximation Results and Discussion

Several examples have been worked out numerically on an IBM 704 digital calculator.* A spherical nose is the most simple blunt-body shape; furthermore, a considerable amount of data exists for spheres and hemisphere-cylinders. Data for both shock shape and surface-pressure distribution for a hemisphere-cylinder at $M_\infty = 1.9$ have been obtained from Moeckel.[12] Data for the same body shape at $M_\infty = 5.8$ have been taken from Oliver[13] and Love[14] for the pressure distribution and shock shape, respectively. At $M_\infty = 1.9$, the iteration scheme described converges to $\delta_{sp} = 0.3963$, which compares to an experimental value of 0.38 determined from reference 12 (see also Fig. 6 of reference 15). At $M_\infty = 5.8$, δ_{sp} converges to 0.1498, compared to $\delta_{sp} = 0.15$ determined from Oliver. A comparison of measured and calculated shock shapes is given in Fig. 2 for both Mach numbers. To indicate the reliability of the experimental data, a point at $M_\infty = 1.94$ is also shown from Love. Figs. 3 and 4 show a comparison of measured pressures with those obtained by the first approximation. In these examples γ has been taken as 1.4. The Newtonian pressure calculated from $C_p/C_{p_{max}} = \sin^2\theta$ is also shown.

Experiments on bodies with large variations of meridional curvature along the surface are reported by Hastings, et al.[16] The bodies tested are flat-faced, 30° half-angle cones with shoulders of various radii. Body No. 2 has been selected for comparison with the present integral method, at $M_\infty = 1.79$ and $M_\infty = 4.84$. For these Mach numbers, respectively, $\delta_{sp} = 0.43$ and $\delta_{sp} = 0.215$ were determined by the author from the shadowgraphs of reference 16. From the iteration, corresponding values are found to be 0.5031 and 0.2200.

* Fred H. Scaife of the Martin-Baltimore Digital Group was instrumental in establishing a workable digital program.

Fig. 5 shows Body No. 2 and the measured and calculated shock shapes for both Mach numbers. The results for the pressure distributions are given in Figs. 6 and 7.

It can be seen that the calculated shock shapes are good, even for the relatively complex body shape of Fig. 5. The agreement between theory and experiment becomes better as M_∞ increases, as far as the shock shape is concerned. The same is not true, however, of the surface pressure distributions. For the hemispherical body, the lower free-stream Mach number gives better agreement of pressures with experiment, although it would appear for both Mach numbers that up to values of s considerably past the sonic piont on the surface the results of the first approximation are excellent for this body. For the flat-faced cone, a better sur-

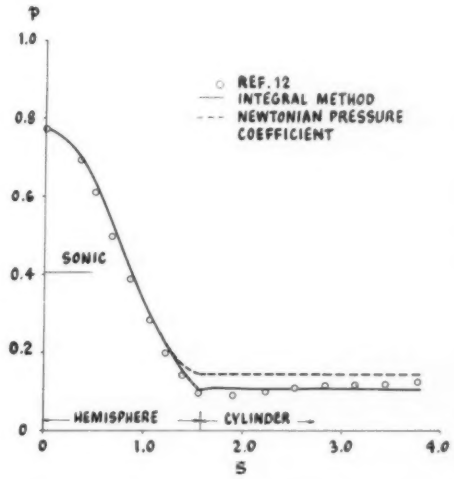

FIG. 3. Pressure distribution, hemisphere-cylinder at $M\infty = 1.9$.

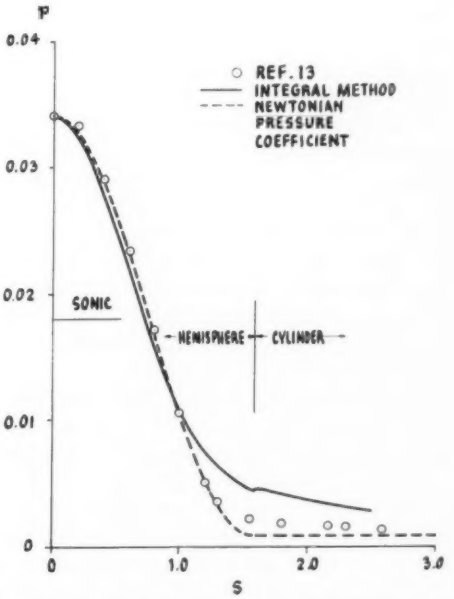

FIG. 4. Pressure distribution, hemisphere-cylinder at $M_\infty = 5.8$.

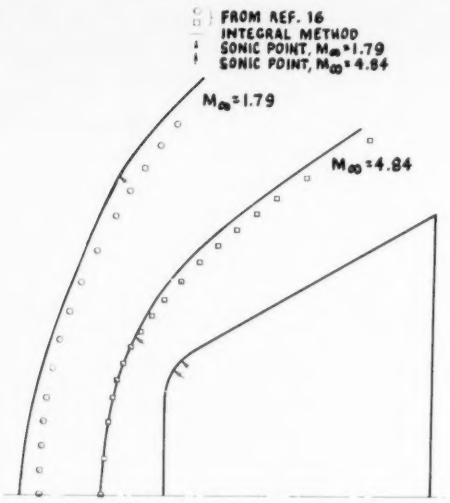

FIG. 5. Shock shapes, flat-faced cone.

face pressure in front is obtained at the higher free-stream Mach number; again it would seem that the results are reliable well into the supersonic regime on the surface.

The effect of a sudden change in body curvature is noticeable for all the calculated pressures. A rapid change in the slope of the pressure distribution is seen to occur whenever the surface curvature changes discontinuously from a finite value to zero. This is due to the fact that with the linear variation in n of the first approximation it is not possible to enforce the condition that a discontinuity in R should not result in a discontinuity in the solution. The effect is most pronounced for the flat-faced cone (Figs. 6 and 7). At the higher Mach number, this jump causes a departure from the experimental points farther back on the body; however, at the lower Mach number, qualitative agreement with experiment is obtained, since the experimental values here follow the same sort of jump. It must be pointed out that at the lower Mach number for Body No. 2 the photographs[16] show the existence of a second shock on the body some distance behind the shoulder on the conical portion. The gradients normal to the surface introduced by such a shock are of course not taken into account in this first approximation, and the results of Fig. 6 are believed to be fortuitous in the region just downstream of the second curvature discontinuity. It appears that a higher approximation will prove useful for bodies with sudden changes in curvature, especially at low Mach numbers.

It can also be seen from Fig. 6 that one cannot expect the first approximation to be valid when carried through in all cases for pressure distribution over the entire body. No explanation for the sudden rise in pressure at $s = 1.45$ can be given at this time. Caution is therefore in order in the use of the first approximation for very large distances from the stagnation point. Nevertheless, the method would not in any case be expected to be useful over the entire body for all bodies, since concave portions of the surface may be present to give rise to a second shock. A very useful application to such bodies, however, would be to use it only until the flow has become supersonic, then the results can be taken as initial conditions for other methods valid for entirely supersonic flow fields. The first approximation appears satisfactory for this purpose for the body shapes and Mach number range described.

Since the present method should also be applicable to flow over a pointed body with an attached shock, with $\delta_{sp} = 0$, a 30° half-angle cone was studied at $M_\infty = 4.0$ as an additional example. For this body, both shock angle and surface pressure should be constant with s. It was found from an integration from $s = 0.1$ to $s = 1.5$ that, over this range, x varied only 0.2 per cent and the surface pressure 0.5 per cent from the Kopal Table values. The shock layer thickness should be linear with s for this problem, and $d\delta/ds$ constant. This parameter was found from the integration to be constant within 1.4 per cent. Thus the Belotserkovskii first approximation may also be applied to pointed bodies of revolution.

(5) Stagnation Region

The first approximation, embodied in Eqs. (10), (14), and (15), has been shown to yield useful results upon numerical integration. The equations themselves are quite complicated, however, and contribute little to the physical understanding of the problem. It will now be shown that, by considering the stagnation region, simple analytical relations between shock and body curvature, shock detachment distance, and velocity gradient can be directly obtained. These relations lead to correlations which make both shock curvature $\mathcal{R}_{sp}$ and stagnation-point velocity gradient independent of overall body shape and which provide a rapid means for estimating these quantities from either optical information or from other theoretical results on shock detachment distance. The importance of the stagnation-point velocity gradient is well known, while the shock vertex radius of curvature is an essential parameter for the calculation of the inviscid, shock-generated vorticity on the body surface which can influence both skin friction and heat transfer.

Since the following considerations are specialized to the stagnation region, the subscript sp is dropped for this section.

In the stagnation region, we put

$$\cos x = \sin \theta = 1$$

To first order in a:

$$\cos \theta = a/R, \quad \therefore (a + \delta \cos \theta) = a[1 + (\delta/R)]$$

$$\sin x = \tan x = x = a(dx/ds)$$

$$v_{s_0} = a(dv_{s_0}/ds)$$

$$v_{s_\delta} = -\frac{a}{R} v_{n\delta} \left[1 + \frac{2(M_\infty^2 - 1)}{2 + (\gamma - 1)M_\infty^2} R \frac{dx}{ds} \right]$$

The difference between φ_δ and φ_0 is second order in a. Thus, $\varphi_0 = \varphi_\delta$. With these substitutions, Eqs. (14) and (15) can be written as

$$\frac{dv_{n_\delta}}{ds} = -\frac{v_{n\delta}}{\delta}(1 - v_{n\delta}^2)^{1/(\gamma-1)}\left(1 + \frac{\delta}{R}\right) \times \left[1 - \delta\frac{dx}{ds}\frac{2(M_\infty^2 - 1)}{2 + (\gamma - 1)M_\infty^2}\right] \quad (17)$$

$$\frac{dx}{ds} = \frac{1}{\delta}\left\{\frac{v_{n\delta}^2 + [(\gamma-1)/2\gamma](1 - v_{n\delta}^2) - [(\gamma-1)/2\gamma][1/(1 - v_{n\delta}^2)^{1/(\gamma-1)}]}{2v_{n\delta}^2\{(M_\infty^2 - 1)/[2 + (\gamma-1)M_\infty^2]\}}\right\} \quad (18)$$

with

$$v_{n\delta} = -M_\infty\sqrt{(\gamma-1)/[2 + (\gamma-1)M_\infty^2]} \times \{1 - [2/(\gamma+1)][1 - (1/M_\infty^2)]\}$$

Eq. (10) becomes

$$d\delta/ds = (a/R)[1 + (\delta/R)][1 - R(dx/ds)] \quad (19)$$

The relation between $\mathcal{R}$ and dx/ds from the geometry of Fig. 1 is

$$1/\mathcal{R} = (dx/ds)\{\sin(\theta + x)/[1 + (\delta/R)]\} \quad (20)$$

At the stagnation point

$$1/\mathcal{R} = (dx/ds)/[1 + (\delta/R)] \quad (21)$$

Thus, Eqs. (17) and (18) give, at the stagnation point, relations between shock curvature, shock detachment distance, body curvature, and velocity gradient as functions of γ and M_∞.

Using Eq. (21), Eqs. (17) and (18) may be written as

$$(1/w_\infty)\{\delta/[1 + (\delta/R)]\}(dv_{n_\delta}/ds) = \pi(M_\infty, \gamma) \quad (22)$$

$$(\delta/\mathcal{R})[1 + (\delta/R)] = \Gamma(M_\infty, \gamma) \quad (23)$$

where

$$\pi(M_\infty, \gamma) = \frac{2 + (\gamma-1)M_\infty^2}{(\gamma+1)M_\infty^2}\left\{1 - \Gamma\left[\frac{2(M_\infty^2 - 1)}{2 + (\gamma-1)M_\infty^2}\right]\right\}\left[\frac{4\gamma M_\infty^2 - 2(\gamma-1)}{(\gamma+1)^2 M_\infty^2}\right]^{1/(\gamma-1)}$$

$$\Gamma(M_\infty, \gamma) = \frac{2(\gamma+1) + 2\gamma(\gamma+1)M_\infty^2 - (\gamma+1)^2 M_\infty^2\{(\gamma+1)^2 M_\infty^2/[4\gamma M_\infty^2 - 2(\gamma-1)]\}^{1/(\gamma-1)}}{4\gamma(M_\infty^2 - 1)}$$

Eqs. (22) and (23) contain the body shape explicitly only in the factor $[1 + (\delta/R)]$. Both equations state that the proper nondimensionalizing length for shock radius of curvature and stagnation-point velocity gradient is δ, and that with the additional factor $1 + (\delta/R)$ both quantities can be made independent of body shape. The way in which this factor occurs can be made plausible on physical grounds.

Consider Eq. (23). It is known for low supersonic flight Mach numbers and blunt convex bodies that changes in the body shape upstream of the sonic point have little effect on the shock shape. (See references 17 and 18.)

Changes in R for a given M_∞ result in changes of δ but not of $\mathcal{R}$. The ratio $\delta/\mathcal{R}$ cannot therefore be independ-

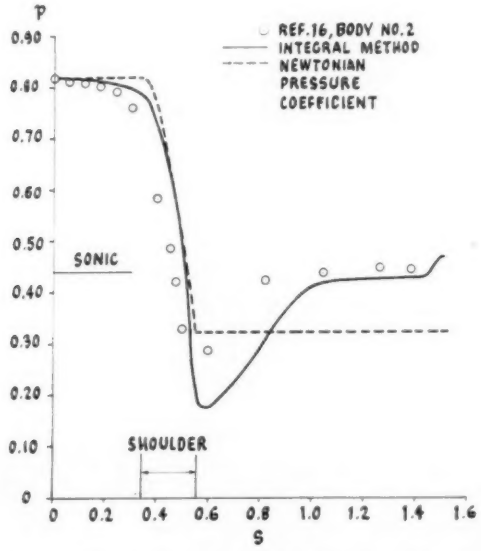

FIG. 6. Pressure distribution, flat-faced cone at $M_\infty = 1.79$.

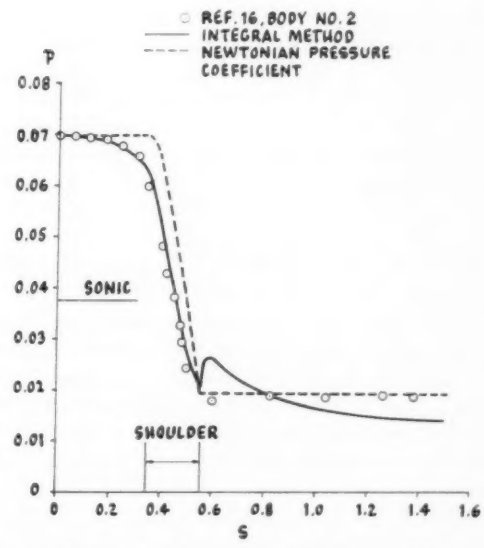

FIG. 7. Pressure distribution, flat-faced cone at $M_\infty = 4.84$.

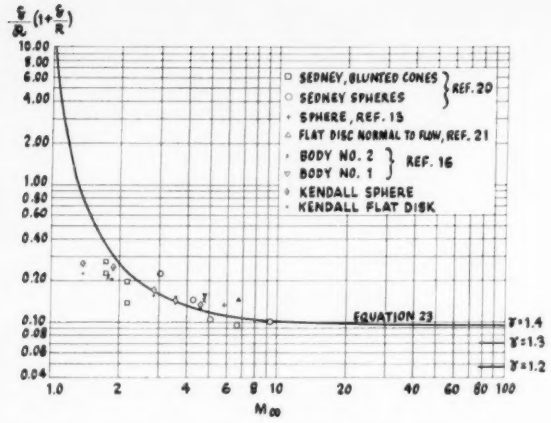

FIG. 8. Dimensionless stagnation-point shock curvature.

ent of body shape for low Mach numbers but in fact must increase with R. Since $1 + (\delta/R)$ decreases with increasing R under these conditions, it is seen that this factor must appear in the numerator of Eq. (23). It should be noted that Eq. (23) must break down as the transonic regime is approached where $\delta/\mathcal{R}$ should be independent of nose shape. At very large Mach numbers δ/R is small, $1 + (\delta/R) \to 1$, and $\delta/\mathcal{R}$ again becomes independent of body shape, in agreement with the hypersonic behavior pointed out by Hayes.[19]

For the velocity gradient in Eq. (22), consider again first the low supersonic regime. For essentially spherical bodies, for $M_\infty \to 1$, $\delta/R \gg 1$, and

$$(1/w_\infty)\{\delta/[1 + (\delta/R)]\}(dv_{s_0}/ds) \to (R/w_\infty)(dv_{s_0}/ds)$$

Since for low Mach numbers many different nose shapes are possible in the stagnation region with the same shock, the local surface velocity gradient in this region must depend essentially only on the body shape there, that is, on R. This argument must fail for flat-nosed bodies, $R \to \infty$, since the statement that $(R/w_\infty)(dv_{s_0}/ds)$ is independent of body shape implies then incorrectly that $dv_{s_0}/ds \to 0$. Of the three length scales available, $\mathcal{R}$, R, and δ, only two are left for $R \to \infty$, and $\mathcal{R}$ clearly is not significant at low Mach numbers due to its invariance with nose shape. This leaves δ as the only proper parameter, in agreement with Eq. (22) under these conditions.

For hypersonic flow, $\delta/R \ll 1$ for any R and

$$(1/w_\infty)\{\delta/[1 + (\delta/R)]\}(dv_{s_0}/ds) \to (\delta/w_\infty)(dv_{s_0}/ds) \sim (\mathcal{R}/w_\infty)(dv_{s_0}/ds)$$

Since both δ and $\mathcal{R}$ are functions of body shape for large Mach numbers, either one of these shock parameters then serves to indirectly include body shape in the dimensionless velocity gradient, and the explicit appearance of R is no longer required.

In order to compare Eqs. (22) and (23) with experiment, simultaneous data are needed for δ, R, and $\mathcal{R}$, or δ, R, and dv_{s_0}/ds for a variety of body shapes and Mach numbers. In Fig. 8, Eq. (23) for the shock curvature is plotted with $\gamma = 1.4$. The value of γ should more properly be taken as a function of Mach number to account for real gas effects, but, since no single such function exists universally, only asymptotic values for $M_\infty \to \infty$ are indicated for other values or γ. For comparison, data are shown for the following shapes: spheres from Sedney[20] and Kendall;* hemisphere-cylinder, from Oliver;[13] flat disc normal to the flow direction, from Serbin[21] and Kendall; spherically blunted cones, from Sedney; and the flat-faced cones of Hastings, et al.[16] It should be noticed that the scatter for significantly different shapes in such a plot is no worse than that for a single shape.

Fig. 9 shows Eq. (22) for the dimensionless velocity gradient with $\gamma = 1.4$. Again, only asymptotic values for other values of γ are shown. Experimental data for both velocity gradient and shock stand-off distance were obtained for the following shapes: hemisphere-cylinder, from Korobkin and Gruenewald;[22] spheres, from Kendall; flat disc, from Kendall; flat-faced cones from Hastings, et al.[16] and, finally, a family of cylinders capped by spherical segments of various radii, from Boison and Curtiss.[23] While the variation with M_∞ is not precisely matched, it seems that a significant parameter has been obtained which is valid over a wide range of Mach numbers for correlating the velocity gradients on widely differing body shapes.

(6) Second Approximation

The results presented so far show that in certain cases it will prove worthwhile to use a better approximation than the first. Specifically, Eq. (11) must be improved.

Eq. (11) may be generalized to an Nth degree polynomial in n; that is, any integrand $f(n, s)$ of Eqs. (5) and (6) is written as

$$f(n, s) = \sum_{i=0}^{N} A_i(s)[n/\delta(s)]^i \qquad (24)$$

where

$$A_0(s) = f(0, s) = f_0(s)$$

* J. M. Kendall, Jr., as yet unpublished data.

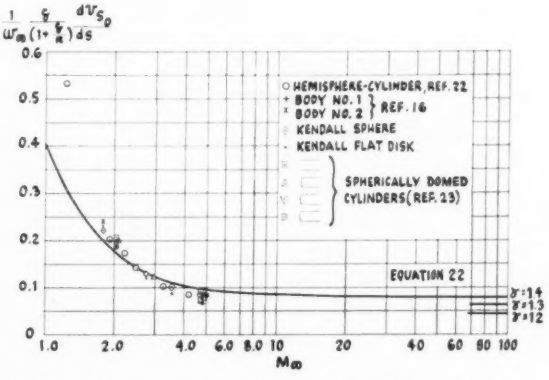

FIG. 9. Dimensionless stagnation-point velocity gradient.

The method used by Belotserkovskii for obtaining higher approximations is to divide the shock layer into N strips in the Nth approximation, obtained by dividing δ at each s into N equal parts. An Nth degree polynomial, Eq. (24), is used with its coefficients A_i so determined that the function being approximated takes on unknown strip values at the $N-1$ strip boundaries. That is, f must be f_δ at the shock, f_0 at the surface, and $f_{m/N}$ at $n = (m/N)\,\delta$ for the mth strip boundary, where $1 \leq m \leq N-1$.

Since there are four unknowns at each strip boundary (v_s, v_n, φ, ψ), there will be $4(N-1)+3 = 4N-1$ unknowns in the Nth approximation, counting δ, v_{s_0}, x. The $4N-1$ equations necessary to make the problem determinate are obtained by integrating Eqs. (1) and (2) from the surface to each strip boundary, giving $2N$ equations similar to Eqs. (5) and (6). Eqs. (7) and (9) yield $2(N-1)$ additional relations, and Eq. (10) is one more. Thus, there are $2N + 2(N-1) + 1 = 4N - 1$ equations, of which $2N + (N-1) + 1 = 3N$ are first-order total differential equations. The initial values at $s = 0$ are $x_{sp} = \psi_{sp} = v_{s_{sp}} = 0$. However, δ_{sp} and $v_{n_{sp}}$ are not known, and these remain as parameters to be determined by the condition that no singularities occur in the solution, as before. In the Nth approximation there will be $(N-1)+1 = N$ parameters which must be simultaneously so chosen that no singularities occur in the solution. Thus, for any approximation higher than the first, the Belotserkovskii method requires the solution of a large number of simultaneous equations under the proper simultaneous choice of a number of parameters, and although Belotserkovskii gives results for the third approximation (eleven equations, three undetermined parameters) it appears that this method would prove very tedious in practice. With this formulation no lower order approximations are required for the determination of a higher one, since each approximation is formulated in a completely determinate manner.

To avoid the complications of this method, an alternative approach was used to evaluate the coefficients in Eq. (24), using only data at the boundaries, body surface, and shock. Then no additional unknowns are introduced, and again only three equations serve to evaluate the three unknowns δ, x, and v_{s_0}. δ_{sp} remains as a single unknown parameter. No details are presented here due to space limitations. It was found that from the definition of vorticity and the equation of continuity it was possible to express the derivatives with respect to n of the integrands in Eqs. (5) and (6) at both body surface and shock in terms of δ, x, v_{s_0}, (dx/ds), (dv_{s_0}/ds). Then both the values and n derivatives of these integrands are given at the boundaries, and this is sufficient to specify a cubic in Eq. (24), corresponding to the third Belotserkovskii approximation, in terms of the same three unknowns that occur in the first approximation.

Then, one finds for any integrand

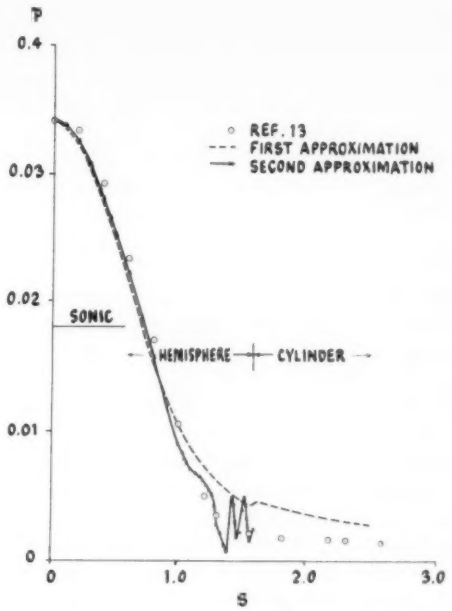

FIG. 10. Pressure distribution, hemisphere-cylinder at $M_\infty = 5.8$ (second approximation).

$$f(n,s) = f_0(s) + \delta(\partial f/\partial n)_0\,(n/\delta) + \delta\{[3(f_\delta - f_0)/\delta] - [2(\partial f/\partial n)_0 + (\partial f/\partial n)_\delta]\}(n/\delta)^2 - \delta\{[2(f_\delta - f_0)/\delta] - [(\partial f/\partial n)_0 + (\partial f/\partial n)_\delta]\}(n/\delta)^3 \times$$

$$\int_0^\delta f(n,s)\,dn = (\delta/2)[f_\delta + f_0] + (\delta^2/12) \times [(\partial f/\partial n)_0 - (\partial f/\partial n)_\delta] \quad (25)$$

If $f(n, s)$ varies linearly with n/δ, so that the first approximation is exact, Eq. (25) reduces to Eq. (11). The second term on the right of Eq. (25) may thus be regarded as a correction term to the first approximation.

As is seen from Eqs. (5) and (6), some of the approximate integrals calculated from Eq. (25) must be differentiated with respect to s. Since the n derivatives in Eq. (25) are related to s derivatives of the dependent variables, this differentiation will generate second derivative terms in s for the cubic approximation which are not present in the first. For example, the vorticity at the shock, related to dx/ds, is used to calculate $(\partial v_s/\partial n)_\delta$ as well as $(\partial v_n/\partial n)_\delta$. When these terms are inserted into Eqs. (5) and (6), d^2x/ds^2 will appear, and the equations become second order in s. Thus, this formulation will lead to the solution of two second-order equations for x and v_{s_0}, with Eq. (10) retained as a first-order equation.

An attempt was made to bypass the labor involved in programing this system of equations and to use instead the system already coded for the first approximation in an iterative scheme. It has already been established that for certain conditions the first approximation is quite satisfactory, which implies that under these conditions the second term on the right of Eq. (25) must be small compared to the first. This term was therefore evaluated from the results of the first

approximation and a new integration performed of the first approximation system of equations to which these correction terms were added. This was intended as the first step in a sequence of similar steps. Again, no details can be given here. It was found, however, that this method is extremely sensitive to any irregularities occurring in the first approximation results and strongly amplifies them. It was not possible to pass by discontinuities of body curvature such as exist in all the examples treated by the first approximation.

For the flat-faced cones this trouble prevented the integration from preceding very far, but for the hemisphere-cylinder significant results were obtained up to $s = \pi/2$. An example for $M_\infty = 5.8$ is shown in Fig. 10. Except for the amplification of irregularities due to the iteration scheme described the pressure distribution of Fig. 10 comes closer, especially past the sonic point, to the experimental values than the first approximation. This is considered as an indication that with a second approximation based on the solution of the second-order equations, which are obtained by treating the correction term as unknown rather than determined from the previous approximation, there is a good chance for excellent results.

(7) Conclusions

The first-approximation integration method described yields results for both surface pressure and shock shape which give good agreement with experiment for arbitrary axisymmetric bodies over regions with continuous surface curvature. The shock shapes are more accurately given at higher Mach numbers. The surface pressures well back from the stagnation region would be improved by the indicated second approximation, and it appears that this second approximation would be considerably less complicated than the higher approximations of Belotserkovskii. By itself, the first approximation is also very useful as a method for determining initial conditions for other techniques valid for entirely supersonic flow fields.

The first approximation suggests that the surface velocity gradient at the stagnation point, as well as the shock curvature, may be determined for axisymmetric bodies of arbitrary shape with only the shock-detachment distance required from experiment, as indicated by Eqs. (22) and (23). The limited experimental data available makes it desirable to test this tentative conclusion obtained from the first approximation by further experiments on a variety of bodies over a wide range of Mach numbers.

If the existence of such a relationship is substantiated by further experiments or more elaborate analysis, it would be useful in a wide range of heat-transfer calculations for arbitrary body shapes.

References

[1] Zlotnick, M., and Newman, D. J., *Theoretical Calculation of the Flow on Blunt-Nosed Axisymmetric Bodies in a Hypersonic Stream*, AVCO Rep. RAD-TR-2-57-29, September 19, 1957.

[2] Garabedian, P. R., and Lieberstein, H. M., *Examples of Detached Bow Shock Waves in Hypersonic Flow*, Journal of the Aeronautical Sciences, Vol. 25, No. 2, p. 109, February, 1958.

[3] Van Dyke, M. D., *The Supersonic Blunt Body Problem—Review and Extension*, Journal of the Aeronautical Sciences, Vol. 25, No. 8, p. 485, August, 1958.

[4] Maslen, S. H., and Moeckel, W. E., *Inviscid Hypersonic Flow Past Blunt Bodies*, Journal of the Aeronautical Sciences, Vol. 24, No. 9, p. 683, September, 1957.

[5] Li, T. Y., and Geiger, R. E., *Stagnation Point of a Blunt Body in Hypersonic Flight*, Journal of the Aeronautical Sciences, Vol. 24, No. 1, p. 25, January, 1957.

[6] Lees, L., and Kubota, T., *Inviscid Hypersonic Flow Over Blunt-Nosed Slender Bodies*, Journal of the Aeronautical Sciences, Vol. 24, No. 3, p. 195, March, 1957.

[7] Uchida, S., and Yasuhara, M., *The Rotational Field behind a Curved Shock Wave Calculated by the Method of Flux Analysis*, Journal of the Aeronautical Sciences, Vol. 23, No. 9, p. 830, September, 1956.

[8] Cabannes, H., *Theoretical Determination of Fluid Flow behind a Detached Shock*, ONERA TN No. 5, 1951 (in French).

[9] Belotserkovskii, O. M., *Flow Past a Circular Cylinder with a Detached Shock Wave*, Doklady, AN USSR, Vol. 113, No. 3, p. 509, 1957 (in Russian; translation available from Morris D. Friedman, Inc., Needham Heights, Mass.).

[10] Chester, W., *Supersonic Flow Past a Bluff Body with a Detached Shock, Part II*, J. Fluid Mech., Vol. 1, Part 5, p. 490, November, 1956.

[11] Traugott, S., *An Approximate Solution of the Supersonic Blunt-Body Problem for Prescribed Arbitrary Asixymmetric Shapes*, Research Report RR-13, The Martin Company, August, 1958.

[12] Moeckel, W. E., *Experimental Investigation of Supersonic Flow with Detached Shock Waves for Mach Numbers between 1.8 and 2.9*, NACA RM E 50 DO5, July, 1950.

[13] Oliver, R. E., *An Experimental Investigation of Flow about Simple Blunt Bodies at a Nominal Mach Number of 5.8*, Journal of the Aeronautical Sciences, Vol. 23, No. 2, p. 177, February, 1956.

[14] Love, E. S., *A Reexamination of the Use of Simple Concepts for Predicting the Shape and Location of Detached Shock Waves*, NACA TN 4170, December, 1957.

[15] Heberle, J., Wood, G. P., and Gooderum, P. B., *Data on Shape and Location of Detached Shock Waves on Cones and Spheres*, NACA TN 2000, January, 1950.

[16] Hastings, S. M., Persh, J., and Redmann, E. J., *Experimental Investigation of the Pressure Distribution on Axisymmetric Flat-Face Cone Type Bodies at Supersonic and Hypersonic Speeds*, NAVORD Report 5659, October, 1957.

[17] Moeckel, W. E., *Approximate Method for Predicting Form and Location of Detached Shock Waves Ahead of Plane or Axially Symmetric Bodies*, NACA TN 1921, July, 1949.

[18] Busemann, A., *A Review of Analytical Methods for the Treatment of Flows with Detached Shocks*, NACA TN 1858, April, 1949.

[19] Hayes, W. D., *Some Aspects of Hypersonic Flow*, The Ramo-Wooldridge Corporation, January, 1955.

[20] Sedney, R., *Shock Wave Curvature for Hypersonic Axisymmetric Flow*, Journal of the Aeronautical Sciences, Vol. 24, No. 8, p. 630, August, 1957.

[21] Serbin, H., *Supersonic Flow around Blunt Bodies*, Journal of the Aeronautical Sciences, Vol. 25, No. 1, p. 58, January, 1958.

[22] Korobkin, I., and Gruenewald, K. H., *Investigation of Local Laminar Heat Transfer on a Hemisphere for Supersonic Mach Numbers at Low Rates of Heat Flux*, Journal of the Aeronautical Sciences, Vol. 24, No. 3, p. 188, March, 1957.

[23] Boison, J. C., and Curtiss, H. A., *An Experimental Investigation of Blunt Body Stagnation Point Velocity Gradient*, ARS Journal, Vol. 29, No. 2, p. 130, February, 1959.

On the Bernoulli-Euler Beam Theory With Random Excitation

J. L. BOGDANOFF* AND J. E. GOLDBERG**
Purdue University

Summary

Mean square displacement and stress are calculated in a simply supported Bernoulli-Euler beam with distributed external viscous damping for several types of random excitations. Contrary to a recently published conclusion, the mean square values are found be finite except for two types of excitations which do not appear to have appreciable physical significance in engineering problems.

The mean square calculus of random processes is used in the analysis.

(1) Introduction

A NUMBER of papers (e.g., see references 1–7) have appeared recently discussing the response of linear elastic systems to various types of random excitations. Two of these papers[4, 7] presented theoretical analyses for beams and plates under the assumption that the excitation was completely random in time as well as completely random in space. The mean square of the bending stress in a simply supported Bernoulli-Euler beam with external viscous damping was found to be infinite, and the conclusion was advanced[7] that the Bernoulli-Euler beam was adequate when only mean square displacement is of interest. Two points come to mind immediately. First, random processes of the type assumed are restricted in the scope of their applications, second, to have to give up the Bernoulli-Euler theory in beam problems when there are random excitations would complicate a number of technical problems to quite an extent. Hence, the question arises as to what the results of such an analysis would have been if a more realistic assumption had been made regarding the random process. The present paper presents results bearing on this question.

We shall only consider a simply supported uniform Bernoulli-Euler beam having uniformly distributed constant external viscous damping, and we shall further assume that the excitation $m\ P(x, t)$ per unit length has the form

$$m\ P(x, t) = m\ R(x)\ Q(t) \tag{1}$$

where $R(x)$ is either deterministic [Case (A)] or random [Case (B)] and $Q(t)$ is random in time. When $R(x)$ is random, we assume that $R(x)$ and $Q(t)$ are independent.

Second-order random processes, having finite total power (or variance) do occur in nature. Hence, we shall assume that $R(x)$ (when random) and $Q(t)$ are of this type.

The m.s. (mean square) calculus[8, 9] of random processes will be used in our analysis rather than the method of generalized harmonic analysis. While this calculus is not too familiar to engineers, we shall use it since it permits the analysis to follow the same pattern already familiar in the dynamic analysis of linear systems under deterministic excitation. We shall not constantly cite these two references in what follows, the reader understanding that for answers to questions relating to theory, he must refer to them.

(2) Analysis

Let the length of the beam be L, its bending stiffness EI, its depth $2h$, and its mass per unit length m. With damping constant c, the equation of motion and boundary conditions become, respectively,

$$a^2(\partial^4 W/\partial x^4) + 2\beta(\partial W/\partial t) + (\partial^2 W/\partial t^2) = P(x, t) \tag{2}$$

$$\left.\begin{aligned} W(0, t) &= W(l, t) = 0 \\ \left.\frac{\partial^2 W}{\partial x^2}\right|_{x=0} &= \left.\frac{\partial^2 W}{\partial x^2}\right|_{x=l} = 0 \end{aligned}\right\} \tag{3}$$

where $W(x, t)$ is the transverse displacement and

$$a^2 = EI/m, \quad 2\beta = c/m \tag{4}$$

We write[10]

$$R(x) = \sum_{j=1}^{\infty} R_j \sin\ (j\pi x/L) \tag{5}$$

Where $R(x)$ is deterministic, the R_j are constants; where $R(x)$ is random, the R_j are random variables. More will be said about this later. Eq. (1) now becomes

$$P(x, t) = Q(t) \sum_{j=1}^{\infty} R_j \sin\ (j\pi x/L) \tag{6}$$

We now seek a solution of the form

$$W(x, t) = \sum_{j=1}^{\infty} T_j(t) \sin\ (j\pi x/L) \tag{7}$$

This equation satisfies the boundary conditions. The substitution of Eqs. (6) and (7) into Eq. (2) leads to the system of equations

Received April 6, 1959.

* Professor of Engineering Sciences.
** Professor of Structural Engineering.

The authors wish to express their indebtedness to Profs. S. S. Shu and F. Kozin of the Division of Engineering Sciences, Purdue University, for helpful discussions during the preparation of their paper.

$$\ddot{T}_j + 2\beta\dot{T}_j + p_j^2 T_j = R_j\, Q(t), \quad j = 1, 2, \ldots \tag{8}$$

where $$p_j^2 = a^2(j\pi/L)^4 \tag{9}$$

and the dots indicate differentiation (in a sense to be described below).

For positive values of time, let $h_j(t)$ be the solution of the equation

$$\left.\begin{aligned} &\ddot{h}_j + 2\beta\dot{h}_j + p_j^2 h_j = 0 \\ &h_j(0) = 0, \quad \dot{h}_j(0) = 1 \end{aligned}\right\} \tag{10}$$

and let $h_j(t)$ be zero for negative time. Then, assuming $p_j^2 > \beta^2$ for $j = 1, 2, \ldots$

$$h_j(t) = e^{-\beta t} \sin p_j' t/p_j' \tag{11}$$

where $$p_j' = \sqrt{p_j^2 - \beta^2}$$

The covariance $\Gamma_Q(t, t_1)$ of $Q(t)$, with $E\{Q(t)\} = 0$, is given by the equation

$$\Gamma_Q(t_1, t_2) = E\{Q(t_1)Q(t_2)\} \tag{12}$$

the E before the curly brackets denoting expectation. Since $Q(t)$ is of second order and m.s. continuous, $\Gamma_Q(t_1, t_2)$ is bounded and continuous.

The ordinary Riemann integral

$$\int_{t_0}^{t}\int_{t_0}^{t} h_j(t - \tau_1)h_j(t - \tau_2)\, Q(\tau_1, \tau_2)d\tau_1, d\tau_2 \tag{13}$$

exists and is finite. Hence, the m.s. Riemann integral

$$\int_{t_0}^{t} h_j(t - \tau)\, Q(\tau)d\tau \tag{14a}$$

exists. Moreover, Eq. (14a) possesses two m.s. derivatives

$$\left.\begin{aligned} &\int_{t_0}^{t} \dot{h}_j(t - \tau)\, Q(\tau)\, d\tau \\ &\int_{t_0}^{t} \ddot{h}_j(t - \tau)\, Q(\tau)\, d\tau + Q(t) \end{aligned}\right\} \tag{14b}$$

Hence, if the derivatives in Eq. (8) are interpreted as m.s. derivatives, the mean square solution of Eq. (8) is

$$T_j(t) = A_j \cos \omega_j' t + B_j \sin \omega_j' t + R_j \int_{t_0}^{t} h_j(t - \tau)Q(\tau)d\tau, \quad j = 1, 2, \ldots \tag{15}$$

where A_j and B_j are arbitrary. Assuming, as we shall, that the beam is at rest at $t = t_0$, we may replace Eq. (15) by

$$T_j(t) = R \int_{t_0}^{t} h_j(t - \tau)\, Q(\tau)d\tau, \quad j = 1, 2, \ldots \tag{16}$$

The substitution of Eq. (16) into Eq. (7) yields the equation

$$W(x, t) = \sum_{1}^{\infty} R_j \sin (j\pi x/L) \int_{t_0}^{t} h_j(t - \tau)\, Q(\tau)d\tau \tag{17}$$

provided we assume, as we shall, that

$$\lim_{m,n\to\infty} \sum_{j=1}^{m}\sum_{k=1}^{n} E\{R_jR_k\} \sin (j\pi x/L) \sin (k\pi x/L) \times \int_{t_0}^{t}\int_{t_0}^{t} h_j(t - \tau_1)h_k(t - \tau_2)\Gamma_Q(\tau_1, \tau_2)d\tau_1 d\tau_2 \tag{18}$$

exists and is finite for all approaches to the limit. Eq. (17) may be regarded as the m.s. solution of Eqs. (2) and (3) provided the beam is at rest at $t = t_0$. The mean of $W(x, t)$ is zero, since the mean of $Q(t)$ is zero, expectation and "limit in mean" commute and the mean of $Q(t)$ is zero; its covariance is given by

$$\Gamma_w(x, t_1, t_2) = E\{W(x, t_1)W(x, t_2)\} = \sum_{j=1}^{\infty}\sum_{k=1}^{\infty} E\{R_jR_k\} \sin (j\pi x/L) \sin (k\pi x/L) \times \int_{t_0}^{t_1}\int_{t_0}^{t_2} h_j(t_1 - \tau_1)\, h_k(t_2 - \tau_2)\cdot\Gamma_Q(\tau_1, \tau_2)d\tau_1 d\tau_2 \tag{19}$$

What has been said so far is applicable to stationary as well as nonstationary processes. Typical examples of random disturbances which are nonstationary are those arising from blasts, earthquakes, shocks, etc. While such disturbances are of considerable technical interest, there does not appear sufficient information at this time concerning their covariance, probability distributions, etc., to warrant attempting significant calculations. For this reason, we shall now assume $Q(t)$ is at least weakly stationary.

Let $P_Q(\omega)$ denote the power spectral density of $Q(t)$. Then we have the well-known relations

$$\left.\begin{aligned} &\Gamma_Q(t, t + \tau) = \Gamma_Q(\tau) \\ &\Gamma_Q(\tau) = (1/2) \int_{-\infty}^{\infty} P_Q(\omega)e^{+i\omega\tau}\, d\omega \\ &P_Q(\omega) = (1/\pi) \int_{-\infty}^{\infty} \Gamma_Q(\tau)e^{-\omega\tau}\, d\tau \end{aligned}\right\} \tag{20}$$

Although the last two of Eqs. (20) are somewhat restrictive in their range of application, they suffice for most engineering purposes.

We shall also put $t_0 = -\infty$ which means that we disregard the starting transient. The integrals in Eqs. (14) still exist as m.s. Riemann integrals if we replace t_0 by $-\infty$. We now write Eq. (17) as

$$W(x, t) = \sum_{j=1}^{\infty} R_j \sin (j\pi x/L) \int_{0}^{\infty} h_j(\tau) \times Q(t - \tau)d\tau \tag{21}$$

This series converges in m.s. if we assume that the

$$\lim_{m,n\to\infty} \sum_{j=1}^{m}\sum_{k=1}^{n} E\{R_jR_k\} \sin (j\pi x/L) \sin (k\pi x/L) \times \int_{0}^{\infty}\int_{0}^{\infty} h_1(\tau_1)h_n(\tau_2)\cdot\Gamma_Q(\tau - \tau_2 + \tau_1)d\tau_1 d\tau_2$$

converges to a finite limit regardless of how the limit is approached for $\tau = 0$. Then, Eq. (19) becomes

$$\Gamma_W(x, \tau) = \sum_{j=1}^{\infty} \sum_{k=1}^{\infty} E\{R_j R_k\} \sin(j\pi x/L) \times \sin(k\pi x/L) \int_0^{\infty} \int_0^{\infty} h_j(\tau_1) h_k(\tau_2) \times \Gamma_Q(\tau - \tau_2 + \tau_1) d\tau_1 d\tau_2 \quad (22)$$

Since the mean of $Q(t)$ is zero, Eq. (22) shows that $W(x, t)$ is weakly stationary. Eq. (22) takes the form

$$\Gamma_W(x, \tau) = (1/2) \sum_{j=1}^{\infty} \sum_{k=1}^{\infty} E\left\{\int_{-\infty}^{\infty} g_j(x, -i\omega) \times g_k(x, i\omega) P_Q(\omega) e^{+i\omega\tau} d\omega\right\} \quad (23)$$

upon employing the last of Eqs. (20). Here,

$$g_j(x, i\omega) = R_j \frac{\sin(j\pi x/L)}{p_j^2 - \omega^2 + i2\beta\omega} \quad (24)$$

If we may interchange the order of summation and integration in Eq. (23), it becomes

$$\Gamma_W(x, \tau) = (1/2) \int_{-\infty}^{\infty} E\{|G_W(x, i\omega)|^2\} \times P_Q(\omega) e^{+i\omega\tau} d\omega \quad (25)$$

where $$G_W(x, i\omega) = \sum_{j=1}^{\infty} \frac{R_j \sin(j\pi x/L)}{(p_j^2 - \omega^2 + i2\beta\omega)} \quad (26)$$

and this is the displacement frequency response at x when the beam is subject to the fluctuating excitation $R(x)e^{i\omega\tau}$. The covariance $\Gamma_W(x, \tau)$ and power spectral density $P_W(x, \tau)$ are related through equations similar to the last two of Eqs. (20):

$$\left.\begin{aligned} \Gamma_W(x, \tau) &= (1/2) \int_{-\infty}^{\infty} P_W(x, \omega) e^{+i\omega\tau} d\omega \\ P_W(x, \omega) &= (1/\pi) \int_{-\infty}^{\infty} \Gamma_W(x, \tau) e^{-i\omega\tau} d\tau \end{aligned}\right\} \quad (27)$$

With these and Eq. (25), we find that

$$P_W(x, \omega) = |G(x, i\omega)|^2 P_Q(\omega) \quad (28)$$

Formulas analogous to Eq. (21) and Eqs. (25)–(28) may be obtained for maximum bending stress $S(x, t)$ at x; they are

$$\left.\begin{aligned} S(x, t) &= -(Eh\pi^2/L^2) \sum_{j=1}^{\infty} j^2 R_j \sin(j\pi x/L) \int_0^{\infty} h_j(\tau) Q(t - \tau) d\tau \\ \Gamma_S(x, \tau) &= (1/2) \int_{-\infty}^{\infty} E\{|H(x, i\omega)|^2\} P_Q(\omega) e^{+i\omega\tau} d\omega \\ H(x, i\omega) &= -\frac{Eh\pi^2}{L^2} \sum_{j=1}^{\infty} \frac{j^2 R_j \sin(j\pi x/L)}{p_j^2 - \omega^2 + i2\beta\omega} \\ \Gamma_S(x, \tau) &= (1/2) \int_{-\infty}^{\infty} P_S(x, \omega) e^{+i\omega\tau} d\omega \\ P_S(x, \omega) &= (1/\pi) \int_{-\infty}^{\infty} \Gamma_S(x, \tau) e^{-i\omega\tau} d\tau \\ P_S(x, \omega) &= E\{|H(x, i\omega)|^2\} P_Q(\omega) \end{aligned}\right\} \quad (29)$$

where $\Gamma_S(x, \tau)$ is the covariance and $P_S(x, \omega)$ is the power spectral density for $S(x, t)$.

The random process $Q(t)$ determines the spectral density $P_Q(\omega)$. In spite of the differences which may occur in the spectra of processes occurring in nature, they all possess the common feature that their total power is finite—i.e.,

$$(1/2) \int_{-\infty}^{\infty} P_Q(\omega) d\omega < \infty$$

A simple form which we shall use in the following and which has this feature is

$$P_Q(\omega) = \bar{P}_Q \omega_0^2/(\omega_0^2 + \omega^2) \quad (30)$$

where $\bar{P}_Q$ and ω_0 are real constants. Thus,

$$\left.\begin{aligned} (1/2) \int_{-\infty}^{\infty} \bar{P}_Q(\omega) d\omega &= (\pi P_Q \omega_0/2) = \sigma_Q^2 \\ \Gamma_Q(\omega) &= (\pi \bar{P}_Q \omega_0/2) e^{-\omega_0|\tau|} \end{aligned}\right\} \quad (31)$$

Fig. 1 shows $P_Q(\omega)$ and $\Gamma_Q(\tau)$. Since $\Gamma_Q(\tau)$ is continuous at $\tau = 0$ but not differentiable, $Q(t)$ is m.s. continuous, but not m.s. differentiable. By selecting values of ω_0, we can alter the spread of $P_Q(\omega)$ and the sharpness of $\Gamma_Q(\tau)$ at 0.

The spectrum and covariance of a white noise process may be obtained by letting $\omega_0 \to \infty$:

$$\left.\begin{aligned} P_Q^{\infty}(\omega) &= \bar{P}_Q, \quad \sigma_Q^2 = \infty \\ \Gamma_Q^{\infty}(\tau) &= \bar{P}_Q \pi \delta(t) \end{aligned}\right\} \quad (32)$$

where δ is the usual delta function. These are shown in Fig. 2. White noise is a completely random process. While no process exists in nature with the characteristics given in Eqs. (32), since its total power or variance is infinite, it is sometimes convenient to use it as an approximation to a real process especially when the rapidity of the fluctuations in the excitation are orders of magnitude faster than any which can occur naturally in the system under consideration. In the theory of Brownian motion[8] of a particle, for example, the use of a completely random excitation

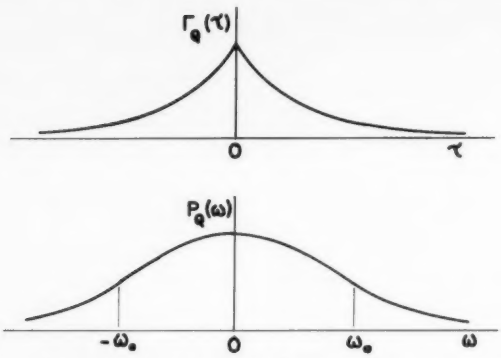

FIG. 1. Covariance and spectral density corresponding to Eqs. (30) and (31).

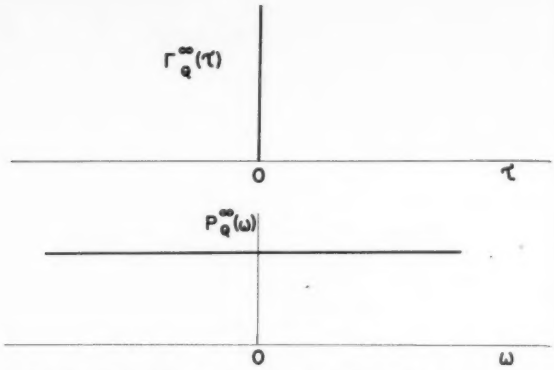

FIG. 2. Covariance and spectral density of white noise.

with spectral density and covariance as in Eq. (32) leads to predictions of mean square displacement in conformity with observation. Intuitively, one would expect that if independent random disturbances having band limited white noise types of spectra act upon a lumped parameter viscously damped linear system and if the lowest cutoff frequency is much larger than the highest undamped natural frequency of the system, the mean square values of displacement (absolute and relative) would be very close to those predicted on assuming the disturbances completely random. This is the case. A similar remark obviously cannot be made for a continuous system; hence, the use of Eqs. (32) in engineering calculations requires careful justification.

The double integral appearing in Eq. (13), with the second upper limit replaced by $t + \tau$ and the lower limit replaced by $-\infty$ may be rewritten in terms of $\bar{P}_Q(\omega)$ and with Eq. (30) evaluated:

$$\frac{1}{2}\int_{-\infty}^{\infty} \frac{\bar{P}_Q\omega_0^2 e^{i\omega\tau}\,d\omega}{(\omega^2+\omega_0^2)(\omega^2-p_j^2-i2\beta\omega)(\omega^2-p_j^2+i2\beta\omega)} = \frac{\pi\bar{P}_Q}{2}\,[(p_j^2+\omega_0^2)^2-(2\beta\omega_0)^2]^{-1}\times$$

$$\left\{\omega_0 e^{-\omega_0\tau}+\frac{\omega_0^2 e^{-\beta\tau}}{2\beta p_j^2}\,[p_j^2+\omega_0^2-(2\beta)^2]\cos p_j'\tau+\frac{\omega_0^2 e^{-\beta\tau}}{2p_j' p_j^2}\,[3p_j^2+\omega_0^2-(2\beta)^2]\sin p_j'\tau\right\} \quad (33)$$

and this is finite for $\tau = 0$. Hence, the integral on the right of Eq. (21) exists as a mean square Riemann integral. Since the right of Eq. (33) may be differentiated four times with respect to τ at $\tau = 0$, this integral possesses two mean square derivatives as it should. The double integral on the right of the expression just below Eq. (21) may be also rewritten and evaluated:

$$\frac{1}{2}\int_{-\infty}^{\infty} \frac{\bar{P}_Q\omega_0^2 e^{-i\omega\tau}d\tau}{(\omega^2+\omega_0^2)(\omega^2-p_j^2-i2\beta\omega)(\omega^2-p_k^2+i2\beta\omega)} = \frac{\pi\bar{P}_Q\omega_0\,e^{-\omega_0\tau}}{2(p_j^2+\omega_0^2+2\beta\omega_0)(p_k^2+\omega_0^2-2\beta\omega_0)} +$$

$$\frac{2\beta\pi\bar{P}_Q\omega_0^2 e^{-\beta\tau}\,[2(p_j^2-2\beta^2+\omega_0^2)+(p_j^2-p_k^2-4\beta^2)]\cos p_j'\tau}{[(p_j^2-2\beta^2+\omega_0^2)^2+(2\beta p_j')^2][(p_j^2-p_k^2-4\beta^2)^2+(4\beta\,p_j')^2]} -$$

$$\frac{\pi\bar{P}_Q\omega_0^2 e^{-\beta\tau}[(p_j^2-2\beta^2+\omega_0^2)(p_j^2-p_k^2-4\beta^2)-8\beta^2 p_j'^2]\sin p_j'\tau}{p_j'[(p_j^2-2\beta^2+\omega_0^2)^2+(2\beta p_j')^2][(p_j^2-p_k^2-4\beta^2)^2+(4\beta p_j')^2]} = I_{jk}(\tau) \quad (34)$$

for $\tau \geq 0$. For $\tau \leq 0$, interchange j and k and replace τ by $|\tau|$. This must a'so be done in Eq. (33).

Then, provided the expressions

$$\left.\begin{aligned}&\sum_{j=1}^{m}\sum_{k=1}^{n} E\{R_j R_k\}\sin(j\pi x/L)\times \sin(k\pi x/L)I_{jk}(0)\\ &\sum_{j=1}^{m}\sum_{k=1}^{n} E\{R_j R_k\}\sin(j\pi x/L)\times \sin(k\pi x/L)j^2k^2 I_{jk}(0)\end{aligned}\right\} \quad (35)$$

converge for all approaches to the limit, Eq. (21) and the first of Eqs. (29) converge in m.s. and

$$\Gamma_W(x,\tau) = \sum_{j=1}^{\infty}\sum_{k=1}^{\infty} E\{R_j R_k\}\times \sin(j\pi x/L)\sin(k\pi x/L)I_{jk}(\tau) \quad (36a)$$

$$\Gamma_S(x,\tau) = (Eh\pi^2/L^2)^2\sum_{j=1}^{\infty}\sum_{k=1}^{\infty} j^2k^2E\{E_j E_k\}\times \sin(j\pi x/L)\sin(k\pi x/L)I_{jk}(\tau) \quad (36b)$$

The variance for $W(x, t)$ and $S(x, t)$ are given by the formulas

$$\left.\begin{aligned}\sigma_W^2(x) &= \Gamma_W(x, 0)\\ \sigma_S^2(x) &= \Gamma_S(x, 0)\end{aligned}\right\} \tag{37}$$

Case (A): R(x) Deterministic

We have

$$E\{R_j R_k\} = R_j R_k \tag{38}$$

and, since $R(x)$ is known,

$$R_j = (2/L)\int_0^L R(x)\sin(j\pi x/L)\,dx \tag{39}$$

from Eq. (5).

If $R(x)$ is piecewise smooth, as is usually the case with distributed loads, we know that the magnitude of R_j decreases at least as fast as $1/j$ as j increases; hence, we write

$$R_j = \alpha_j(1/j) \tag{40}$$

where α_j is a constant. Combining Eqs. (38) and (40) and substituting in Eqs. (35), we find that each of these expressions has a finite limit. Therefore, by Eqs. (37), we see that the $W(x, t)$ and $S(x, t)$ have finite m.s. values when there is finite power in $Q(t)$.

Now let us go to extremes and assume that $\omega_0 \to \infty$. Eq. (30) and the second of Eqs. (31) are replaced by Eqs. (32). The m.s. Riemann integral

$$\int_{-\infty}^{t} h_j(t-\tau)Q(\tau)\,d\tau \tag{41}$$

still exists since

$$\int_0^\infty\int_0^\infty h_j(\tau_1)h_j(\tau_2)\Gamma_Q{}^\infty(\tau - \tau_2 + \tau_1)\,d\tau_1\,d\tau_2 = (\pi\bar{P}_Q e^{-\beta\tau}/4p_j{}^2)\{\cos p_j'\tau + (\beta/p_j')\sin p_j'\tau\} \tag{42}$$

is finite at $\tau = 0$. The right-hand side of Eq. (42) is twice differentiable with respect to τ at $\tau = 0$ and the second derivative is continuous there; this means that Eq. (41) has a m.s. derivative which is m.s. continuous. The lack of a second m.s. derivative follows because we are now allowing infinite amplitude fluctuations in loading to occur infinitely often in every finite time interval. Eq. (34) becomes

$$I_{jk}{}^\infty(\tau) = \lim_{\omega_0\to\infty} I_{jk}(\tau) = \frac{\bar{P}_Q\beta e^{-\beta|\tau|}}{(p_j{}^2 - p_k{}^2 - 4\beta^2)^2 + (4\beta p_j')^2}\times \left\{4\cos p_j'\tau - \frac{p_j{}^2 - p_k{}^2 - 4\beta^2}{\beta p_j'}\sin p_j'|\tau|\right\} \tag{43}$$

We again find that each expression in Eqs. (35) has a finite limit when $I_{jk}(0)$ is replaced by $I_{jk}{}^\infty(0)$. Therefore, $W(x, t)$ and $S(x, t)$ have finite m.s. values even when there is infinite total power in $Q(t)$ provided that R_j decreases at least as fast as $1/j$ as j increases.

If $R(x)$ represents a single concentrated load at the center, say, then

$$R_j = (2/L)\sin(j\pi/2) \tag{44}$$

and we find that $W(x, t)$ and $S(x, t)$ have finite m.s. values for $\omega_0 < \infty$, but $S(L/2, t)$ does not have a finite m.s. value although $W(x, t)$ still does when $\omega_0 \to \infty$. Hence, for a single concentrated load at the center, the displacement and stress have finite means squares for finite variance of $Q(t)$; the displacement has a finite mean square but $S(L/2, t)$ does not when $Q(t)$ has infinite variance.

Case (B): R(x) Random

We take $R(x)$ to be of second order, m.s. differentiable, with mean $E\{R(x)\} = 0$. If the mean is not zero, it may be treated separately by the procedure given in Case (A), since it is deterministic.

Let

$$E\{R(x)\,R(y)\} = \Gamma_R(x, y) \tag{45}$$

The R_j in Eq. (5) are now random variables. $\Gamma_R(x, y)$ possesses the derivatives $\partial\Gamma_R/\partial x$, $\partial\Gamma_R/\partial y$, and $\partial^2\Gamma_R/\partial x\partial y$. Hence,

$$\left.\begin{aligned}\Gamma_R(x, y) &= \sum_{j=1}^{\infty}\sum_{k=1}^{\infty} E\{R_j R_k\}\sin(j\pi x/L)\times \sin(k\pi y/L)\\ E\{R_j R_k\} &= (4/L^2)\int_0^L\int_0^L \Gamma_R(x, y)\times \sin(j\pi x/L)\sin(k\pi y/L)\,dx\,dy\end{aligned}\right\} \tag{46}$$

Since the limit in the first of Eqs. (46) is independent of how it is approached, Eq. (5) is m.s. convergent.

From the continuity and piecewise smoothness of $\Gamma_R(x, y)$, it follows that $E\{R_j R_k\}$ decreases at least as rapidly as $1/jk$ as j and k increase. The expressions in Eqs. (36) thus converge to finite limits regardless of how the limit is approached; this is still the case when $\omega_0 \to \infty$. Again we see that $W(x, t)$ and $S(x, t)$ have finite m.s. values, or, what is the same thing, finite variances regardless of whether $Q(t)$ has finite or infinite variance provided only that $\Gamma_R(x, y)$ is piecewise smooth as is usually the case in physical applications.[6]

Making the extreme assumption that $R(x)$ is completely random,

$$\Gamma_R(x, y) = K\delta(x - y) \tag{47}$$

where K is a constant. Then

$$\left.\begin{aligned}E\{R_j, R_k\} &= 0 \quad \text{for } j \neq k\\ E\{R_j{}^2\} &= \text{const.}\end{aligned}\right\} \tag{48}$$

$W(x, t)$ and $S(x, t)$ have finite m.s. values as long as ω_0 is finite, as is clear from Eqs. (35). If we go the final step towards unreality and assume that $Q(t)$ has infinite total power with a white noise type of spectrum, then $W(x, t)$ still has a finite m.s., but $S(x, t)$ does not.

(3) Conclusion

The displacement and maximum bending stress in a uniform simply supported Bernoulli-Euler beam with constant distributed external viscous damping have been calculated for a number of random disturbances.

In all cases in which the total power or variance of the time-varying excitation $Q(t)$ is finite, displacement and stress have finite m.s. values. Even if the variance of $Q(t)$ is assumed infinite with P_Q^{∞} as in Eqs. (32), this is still the case provided that when $R(x)$ is deterministic it is piecewise smooth and, when it is random, that $\Gamma_R(x, y)$ be smooth. For a single concentrated force at the center and for a completely random $R(x)$, the bending stress does not have a finite m.s. value when $\sigma_Q^2 = \infty$, although the displacement still does.

Hence, in the cases examined and for assumptions on the random excitation which are physically plausible, the Bernoulli-Euler theory with distributed (constant) external viscous damping predicts finite m.s. displacement and bending stress.

We mentioned earlier that $P_Q(\omega)$ is determined by the random process $Q(t)$, and we chose to work with a process having the $P_Q(\omega)$ given in Eq. (30). Finite total power, one adjustable parameter, and ease in carrying out certain integrations guided our choice. We do not claim that this spectrum merits special attention. It is simply physically plausible and suitable for our purposes. Other spectral densities applicable to gusts, for example, are available.[6] Nonetheless, it does appear reasonable to conclude on the basis of our investigation that any other $Q(t)$ associated with an actual random process should yield finite m.s. displacement and stress for our model. One point not discussed is how the m.s. stress in a Bernoulli-Euler beam and a Timoshenko beam differ as a function of ω_0 when using a $Q(t)$ with the spectral density of Eq. (30). This is a fairly interesting point as it might indicate that it is necessary to use the more complicated model for ω_0 sufficiently large. We hope to discuss this point in a future paper.

References

[1] Press, Harry, and Mazelsky, Bernard, *A Study of the Application of Power-Spectral Methods of Generalized Harmonic Analysis to Gust Loads on Airplanes*, NACA Report 1172, 1954.

[2] Liepmann, H. W., *Extension of the Statistical Approach to Buffeting and Gust Response of Wings of Finite Span*, Journal of the Aeronautical Sciences, Vol. 22, No. 3, p. 197, March, 1955.

[3] Press, Harry, and Houbolt, J. C., *Some Applications of Generalized Harmonic Analysis to Gust Loads on Airplanes*, Journal of the Aeronautical Sciences, Vol. 22, No. 1, p. 17, January, 1955.

[4] Eringen, A. C., *Response of Beams and Plates to Random Loads*, J. Appl. Mech., Vol. 24, No. 1, p. 46, March, 1957.

[5] Diederich, F. W., *The Response of an Airplane to Random Atmospheric Disturbances*, NACA TN 3910, April, 1957.

[6] Saunders, K. D., *A Power-Spectrum Equation for Stationary Random Gusts, Including a Sample Problem*, Journal of the Aeronautical Sciences, Vol. 25, No. 5, p. 295, May, 1958.

[7] Samuels, J. C., and Eringen, A. C., *Response of a Simply Supported Timoshenko Beam to a Purely Random Gaussian Process*, J. Appl. Mech., Vol. 25, No. 4, p. 496, December 1958.

[8] Moyal, J. E., *Stochastic Processes and Statistical Physics*, J. Roy. Statist. Soc., Ser. B., Vol. 11, 1949.

[9] Loève, Michel, *Probability Theory*, Chapter X, D. van Nostrand Co., Inc., New York, 1955.

[10] Van Lear, G. A., Jr., and Uhlenbeck, G. E., *The Brownian Motion of Strings and Elastic Bars*, Phys. Rev., Vol. 38, p. 1583, March, 1931.

On the Estimation of Structural Damping From Aircraft Resonance Tests

(*Continued from page 342*)

The calculation of the response columns in terms of the generalized coordinates from the displacements measured at a sufficient number of points presents the greatest difficulty due to the probable variation in these columns with change in measuring points. The extent of the variation depends ultimately on the quality of the semirigid approximation; a practical procedure would be to calculate the response columns (at any one frequency) from a number of sets of n displacements and to compare the results. Should they not differ greatly, a set of mean response columns could be constructed.

Finally, the matrix of damping coefficients should be rendered symmetrical by averaging corresponding elements before inclusion in the flutter equations; extensive lack of symmetry would indicate failure of the method. Such averaging will also, to some extent, assist the theoretical linear damping mechanism to describe internal dissipation in the physical system which will depend on both frequency of excitation and absolute amplitude of response.

References

[1] Fraejis de Veubeke, B. M., *A Variational Approach to Pure Mode Excitation Based on Characteristic Phase Lag Theory*, North Atlantic Treaty Organisation, AGARD Report No. 39, April, 1956.

[2] Traill-Nash, R. W., *On the Excitation of Pure Natural Modes in Aircraft Resonance Testing*, Journal of the Aero/Space Sciences, Vol. 25, No. 12, pp. 775–778, December, 1958.

Ablation of Reinforced Plastics in Supersonic Flow†

GEORGE W. SUTTON*
General Electric Company

Summary

The ablation characteristics of several reinforced plastics were investigated in the flow of a rocket exhaust. The simulation characteristics for ablation of a vehicle in hypersonic flight are considered, which indicates that the rocket exhaust is generally a more severe environment. The thermal diffusivities of the material were also measured during the ablation tests by means of a new technique. The ablation results are reported as an "effective heat of ablation" which represents the heat blocked or absorbed per unit ablated mass. These ranged from about 10^3 B.t.u./lb. for a silicone-asbestos, to 6×10^3 B.t.u./lb. for plastics reinforced with Refrasil fibers, which are about 96 per cent pure silica.

Symbols

A = cross section of re-entry body
C_D = drag coefficient of re-entry body
C_p = specific heat
H_e = effective heat of ablation
D = diameter of calorimeter
ΔH = enthalpy change per unit volume of reinforced plastic
k = thermal conductivity
M = Mach number
p = pressure
q = "calorimeter" heating rate
V = gas stream velocity
W = weight of re-entry body
x = distance ablated
$\dot{x}$ = ablation rate
t = time
T = temperature
ρ = weight density
α = thermal diffusivity
[ ] = concentration

Subscripts

c = chamber of rocket engine
i = insulator
0 = initial
p = reinforced plastic
s = calorimeter
w = outer wall
1 = ahead of normal shock
2 = immediately behind normal shock
3 = at edge of boundary layer at the stagnation point

Received March 19, 1959.

† This work was performed under the auspices of the U.S. Air Force, Ballistic Missile Division. Presented at the Second Technical Symposium for Ballistic Missiles, June, 1957, at the Ramo-Wooldridge Corporation.

* Manager, Magnetohydrodynamic Power Generation, Space Sciences Laboratory, MSVD.

The author wishes to express his appreciation to Dr. A. V. Grosse of Temple University for testing innumerable material samples in the oxy-cyanogen flame; to T. Jordan and D. Hollinger of the General Engineering Laboratory, G-E, for their painstaking fabrication of the models; to T. Butler, E. Finger, J. Healy, and J. Anabel at the Rocket Engine Test Section, G-E, for their careful conduction of the rocket engine tests; and to J. Segletes for performing the often tedious job of data reduction. Also, the author wishes to thank Dr. J. Farber, Manager of Aerophysics Laboratory Operation, G-E, for suggesting this problem.

Introduction

THE ABLATION METHOD of absorbing aerodynamic heating for hypersonic flight is distinctly different from the conventional heat sink methods, because the heat is not necessarily conducted into the interior of the skin material but is absorbed by the temperature rise of a thin layer near the surface until it melts or vaporizes. Thus, ablation is characterized by a continuous loss of surface material. Therefore, it is desirable for the ablation material to possess both a low thermal conductivity and a large enthalpy change from its initial temperature to the temperature at which it leaves the surface. Although monolithic ceramics generally possess such properties, they are subject to thermal shock and spalling. Hence, it is necessary to consider the ceramic in some other form. This form is suggested naturally by the use of inorganic oxide fibers in the form of reinforcement for thermosetting plastics, which are commonly available. In this study, a number of plastics reinforced with inorganic fibers were investigated for possible use as an ablation material.

A relation that sometimes has been used to determine the rate of ablation, $\dot{x}$, is

$$\dot{x} = q/\Delta H \tag{1}$$

where q is the net heating rate to a nonreacting impermeable wall at the surface temperature of the ablation material, and ΔH is the increase in enthalpy per unit volume between the initial temperature of the material and the temperature of the material when it has been removed from the surface by the ablation process. However, this simplified analysis is inadequate because of the very complex mechanism of ablation of reinforced plastics. The thermal conductivity of most reinforced plastics is quite low; hence, the temperature rise in the plastic is usually confined to a narrow region near the heated surface. In this region the plastic resin decomposes into a gas whose composition is not completely known, and leaves behind a linked carbonaceous structure. The inorganic reinforcing fibers reach a temperature sufficiently high so that they melt

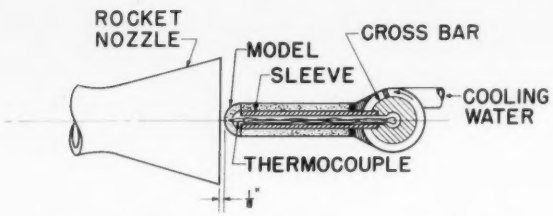

FIG. 1. Schematic diagram of experimental equipment.

into a liquid film which flows along the surface in the direction of the main air flow: the liquid carries with it some of the carbon. The reinforcing fiber may also evolve some gas by evaporation of its constituents.

The gases which are evolved are then injected into the boundary layer, and may alter the convective heat-transfer rate to the gas-material interface. The extent of this alteration and the amount of carbon combusted at the interface are not known. Thus, the convective heat transfer through the interface cannot be calculated without making simplifying assumptions. Furthermore, the liquid film convects some of the heat in the meridional direction so that not all of the heat transfer through the interface at a given point reaches the unheated plastic at that point.

In view of this lack of basic information concerning the mechanism of the ablation process, a series of tests were made to determine the gross ablation rates of several reinforced plastics in the exhaust of a rocket motor. The rocket motor exhaust cannot completely duplicate high-speed flight in air, but several of the more important environmental conditions can be simulated quite well. These include the heat-transfer rate, stagnation-point pressure, density, and skin friction. Of course, the chemical kinetics are not duplicated, and the rocket motor exhaust is notorious for rapid fluctuations in temperature, velocity, and pressure. The question of simulation is treated below in some detail.

The results are reported as the "effective heat of ablation," H_e, which is the ratio of the calorimeter heat transfer to the rate of mass loss. The "calorimeter" heat-transfer rate is defined as the heat-transfer rate to an impermeable non reacting surface having zero emissivity at the same temperature as the surface temperature of the ablating material.

Preparation of Models

The models were 1-in. diameter hollow hemispheres which were individually molded in a set of matched metal molds at high pressure so that the fabrication procedure was representative of that used for larger parts. No laminates were considered, because preliminary testing of custom molded laminates revealed that, when they were heated, the resin between the layers of reinforcement became carbonized, causing premature loss of the reinforcement by delamination. Instead, molding compounds containing the reinforcement in short lengths in random orientation were used. After the hemisphere was fabricated, a cylindrical afterbody was molded onto it. A small hole was drilled partway into the hemisphere from the inside, and a chromel-alumel thermocouple made of 0.010-in. diameter wire was inserted. The hole was then filled with an epoxy resin. Each thermocouple, complete with leads, was calibrated prior to installation.

Two different resins were used: Cincinnati Testing Laboratory 91LD, which is a high-temperature phenolic, and Dow Corning 2106, which is a high-temperature silicone. These two resins were selected on the basis of preliminary tests using an oxy-cyanogen torch. Although some other phenolic resins showed about the same resistance to heating as 91LD, 91LD is more widely known to industry and its properties have been studied extensively. It is reported as having excellent bonding strength to glass. The 2106 is relatively newer, but was reported as having good strength retention at elevated temperatures. However, the fabricator had some difficulty in molding parts from 2106 because of its greater viscosity, which hindered the closing of the mold.

The reinforcements which were used are as follows:

(1) Fiberglas strands, chopped into 1/2-in. lengths. The glass is known as "E" glass.

(2) Raybestos-Manhattan asbestos, No. 325.

(3) Short staple Fiberfrax, which is essentially aluminum silicate. Fibers of this material are difficult to draw, consequently they are blown, resulting in short lengths and very small diameters.

(4) H. I. Thompson Co. Refrasil, P 100. This about 96 per cent pure SiO_2, made by leaching the lower melting flux oxides out of "E" glass fibers. The leaching process causes the fiber to shrink and become porous, reducing the fiber strength considerably.

(5) Type 181 Fiberglas cloth, chopped into 1/2-in. squares. This is a relatively newer method of using glass, and reinforced plastics using this have been used successfully for several high-temperature applications, such as fins, small rocket nozzles, and jet vanes.

The molding compounds were mixed to contain by weight 1/3 resin and 2/3 reinforcement. However, the higher molding pressures which were required to

TABLE 1
Rocket Operating Conditions, Wt. O_2/Wt. fuel = 2.081

p_c, psia	T_c, °R.	p_1, psia	Assumption	V_1, ft. per sec.	M_1	ρ_2/ρ_1	p_2, psia	ρ_2, lb./ft.^{3}	$[O]_3$, Molar %	$[0_2]_3$, Molar %
300	5,850	30	equilibrium	6,900	2.12	3.94	168	6.50×10^{-2}	2.6	10.0
300	5,850	30	frozen	6,640	2.13	3.41	189	7.32×10^{-2}	1.8	9.3
300	5,850	14.7	equlibrium	7,750	2.54	5.24	121	4.63×10^{-2}	3.1	10.2
300	5,850	14.7	frozen	7,440	2.54	4.28	138	5.35×10^{-2}	1.8	9.3

close the mold for the silicones caused some resin flash, and resulted in densities which correspond to 80–90 per cent reinforcement. The specific gravities of the samples are given in Table 3.

Model 4 was not fabricated using the above procedure. Instead, it was made by cementing together two pieces of General Electric Textolite, grade 11508. The purpose of the test was to determine whether stock reinforced plastics had desirable ablation properties, and whether a glued joint would effect the ablation rate. The particular cement which was used was a polyester: Hetron 92 + 10 per cent $CaCO_3$.

Test Method

A schematic of the equipment is shown in Fig. 1. The rocket motor had an exit diameter of 3.75 in., an area ratio of 4, and burned oxygen and 92.5 per cent ethyl alcohol. The nominal weight ratio of oxygen to fuel was selected as 2.08 in order that the products of combustion contain some oxygen. For that mixture ratio, a chamber pressure of 300 psia should result in an exit pressure of about 15 psia, using an equilibrium calculation. However, previous experiences with that particular motor indicate that when the pressure at the lip is atmospheric, the pressure at the exit centerline may be more than two atmospheres.

In order to determine the environmental conditions at the model, extensive thermochemical calculations were made.[1] The results are shown in Table 1, for two different exit pressures and for both equilibrium and frozen flow, because of the uncertainty of the chemical conditions and exit pressure. The density ratio across a normal shock located at the exit is also given, which is useful for calculating the stagnation point inviscid velocity gradient. The range of probable stagnation-point pressure, density, and oxygen concentrations are also given in Table 1.

The model was located well within the first shock diamond in order to prevent shock-wave boundary-layer interaction. The tests were made by igniting the engine and lowering the model into the flow after full thrust was attained. The time required to insert the model was less than 0.1 sec. The exposure time was limited to 5 sec. in order to minimize shape changes of the model. The thermocouple voltage was recorded with an galvanometer oscillograph together with the run duration. The time duration of the test was measured from the time the model was centered in the flow, until shut down of the motor. After each run, the change in shape of the specimen was measured. Only one sample of each material was tested.

The surface brightness temperature was measured with an optical pyrometer, which had been calibrated with a standard lamp placed at the rocket nozzle exit. Brightness temperatures which were measured during some preliminary tests of longer duration indicated that the surface temperature remained constant during the run. Hence, it is assumed that the measured surface temperature during a test is constant during the entire test. The surface emissivities of the ablating surfaces are not known, but there is reason to believe that they are close to unity. The rocket exhaust was almost nonluminous in comparison to the luminosity of the heated model surface. It is assumed that the brightness temperature is the actual surface temperature. The range of the temperature data of Table 3 may be an indication of the uncertainty in these measurements.

Flight Simulation

The validity of the extrapolation of the results to hypersonic flight conditions depends upon the degree of simulation of flight conditions in the rocket exhaust. This question cannot be resolved exactly for two reasons: (1) the chemically reacting flow in both flight and the rocket exhaust are extremely difficult to analyze; and (2) the factors which are responsible for the ablation are not completely known. However, the range of the simulation of the more important environmental factors are discussed below.

(*1*) *Heating Rate*

The "calorimeter" heating rate at the stagnation point of the model was determined during a calibration test by inserting a small slug of silver into a model at the stagnation point. A thermocouple was peened into a small hole in the rear of the silver slug and the surface of the slug was finished flush with the model. The model was lowered into the rocket exhaust flame, and the thermocouple voltage was recorded on an oscillograph with a frequency response of 1,000 cps.

The Fourier heat conduction law was then used to determine the heating rate to the model from the temperature data; this is shown in Fig. 2 as a function of

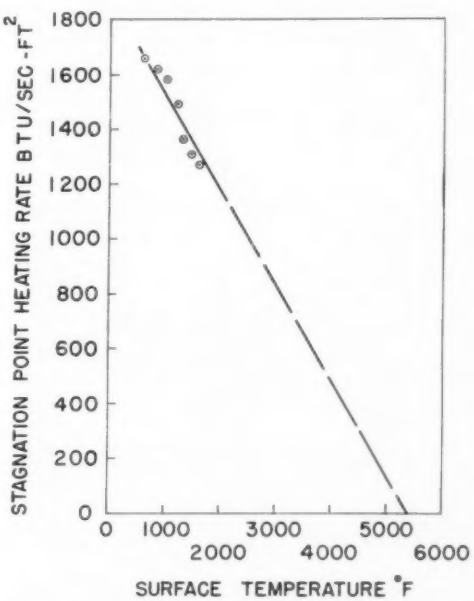

FIG. 2. Calorimeter heating rate in rocket exhaust for mixture ratio of 2.085 and chamber pressure of 293.6 psia.

TABLE 2
Theoretical Molar Oxygen Content at Stagnation Point Pressure and 2,700°F. (p_c = 300 psia)

Wt. ratio of O_2 to fuel	Equilibrium $[O_2]$	Equilibrium $[O]$	Frozen $[O_2]$	Frozen $[O]$
1.62	0%	0%	2.3%	0.9%
1.92	0	0	—	—
2.08	4.42	0	9.3	1.8
2.24	8.77	0	—	—
2.54	15.53	0	16.7	1.0

the calculated instantaneous surface temperature. The curve has been extrapolated linearly to zero heat transfer at the total temperature of the exhaust gas. It can be seen from Fig. 2 that the heat-transfer rates of 800 B.t.u./ft.²-sec. at a surface temperature of 3,000°F., do indeed simulate the heat-transfer rates of hypersonic flight conditions. It is interesting to note that these rates are more than twice as large as those predicted by laminar theory. This may be due to the presence of high frequency fluctuations of the flow velocity and pressure, or the effect of chemical reactions in the boundary layer.

If the silver slug were in perfect contact with the plastic, the heat transfer would be larger by the following factor:

$$q_{\text{actual}}/q_{\text{calorimeter}} = 1 + (16/3\pi^{1/2})(\rho_i C_{p_i}/\rho_s C_{p_s})(\alpha_i t/D^2)^{1/2} \quad (2)$$

which amounts to a 15 per cent correction at most.

(2) *Chemical Simulation*

Because of the presence of combustible hydrocarbons in the resin, it appears necessary to have some oxygen present in the main gas flow. The last two columns of Table 1 indicate that there is slightly over 11 per cent of oxygen at the edge of the boundary layer. However, the real question is the amount of oxygen that would be present at the wall if there were no reactions with the products of pyrolysis. The percentages of oxygen at the wall for a temperature of 2,700°F., which is a typical surface temperature for reinforced plastics, is shown in Table 2 for the assumptions of local equilibrium and frozen composition. It can be seen that a mixture ratio in excess of 2.54 is required to obtain the oxygen content of air. Mixture ratios this high were considered dangerous by the rocket pit operators, so that no tests at this ratio were made. However, the results of tests at ratios of about 2.25 were not significantly different than tests at lower ratios, indicating that the effect of the combustion may be of secondary importance for these plastics.

(3) *Surface Shear Stress*

By use of stagnation-point laminar theory, calculations were made of the ratio of the surface shear stress in the rocket exhaust to that of free flight, as a function of meridional angle on a hemisphere. This ratio is 1.6 when compared to a flight velocity of 20,000 ft. per sec. at 100,000 ft. altitude, and 1.0 at 13,500 ft. per sec. at 60,000 ft. altitude.

(4) *Pressure Gradient*

Since the molten reinforcement is swept downstream by both shear stresses and pressure gradient, it is important to also duplicate the pressure gradient. Now the pressure gradient in the vicinity of the stagnation point of a sphere is given by the negative product of the gas density at the edge of the boundary layer, the square of the stagnation-point inviscid velocity gradient, and the downstream length. It has been shown that the ratio of heat transfer to mass transfer at the stagnation point is independent of the velocity gradient.[2] Hence, the only factor which must be duplicated is the density at the edge of the gaseous boundary layer at the stagnation point. Fig. 3 shows the range of altitude and Mach number which are simulated by the stagnation density of the rocket exhaust.

TABLE 3
Data for Rocket Exhaust Ablation Tests on Reinforced Plastic 1-in. Diameter Sphere-Tangent Cylinders

Model No.	Resin	Reinforcement	Specific Gravity of Reinforced Plastic	Stagnation-Point Ablation, in.	Surface Brightness Temp., °F.	Surface condition at end of Test	Time Duration of Test, sec.	Weight of ratio Oxygen to Fuel	Chamber Pressure, psia
4	Melamine	181 glass cloth	1.81	0.326	2,290	Relatively smooth	6.2	2.28	292
5	91-LD	1/2-in. chopped Fiberglas strands	1.86	0.156	2,560		3.8	2.05	299
6	91-LD	R/M 325 asbestos	1.78	0.198	2,630	Rough	4.7	2.00	300
7	91-LD	Fiberfrax short staple	1.83	0.240	2,810		5.0	2.08	302
8	91-LD	P-100 Refrasil	1.63	0.083	2,790	Cracked	5.0	2.05	303
9	91-LD	1/2-in. chopped 181 glass cloth	1.84	0.206	2,290		4.9	2.24	300
10	DC-2106	1/2-in. Fiberglas strands	1.93	0.199	3,210		5.1	2.32	305
11	DC-2106	R/M 325 asbestos	1.88	0.394	2,870	Cracked	5.1	2.21	297
12	DC-2106	Fiberfrax, short staple	1.80	0.210	3,140	Small cracks	5.0	2.01	307
13	DC-2106	P-100 Refrasil	1.65	0.077	3,140		5.3	1.98	302
14	DC-2106	1/2-in. chopped 181 glass cloth	1.88	0.217	2,920		4.9	2.16	298

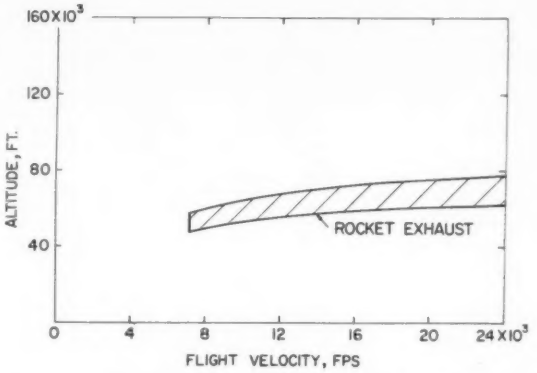

FIG. 3. Altitudes and flight velocities simulated by stagnation-point density in rocket exhaust.

(5) *Pressure*

Table 1 shows the probable range of stagnation pressure p_3, in the rocket exhaust. They are close to the maximum expected for a 5,500 mile range re-entry body with $W/C_D A \sim 10^2$ lb./ft.^{2}.

(6) *Size*

The model size was large enough that the heated region was shallow in comparison to the radius. Thus, the heat conduction in the solid was one-dimensional and the results are applicable to shapes which are much larger. Theory[2] also predicts that the velocity gradient per se has little effect, since the ablation rate and heating rate may both be normalized against the stagnation-point velocity gradient.

(7) *Time*

The length of time required to establish steady-state ablation was less than 0.1 sec. for these tests, as determined by detailed examination of Fastax motion pictures, in comparison to a total run time of about 5 sec. This result is verified by simple ablation theory.[3] Therefore, the starting transient had very little effect on the results.

(8) *Free-Stream Enthalpy*

Since the effect of gaseous mass transfer on heat transfer depends on the free-stream enthalpy,* this should also be duplicated. Unfortunately, this is only 3,320 B.t.u./lb. for the rocket exhaust, which corresponds to a flight velocity of only 12,900 ft. per sec. Thus, the measured results are conservative with respect to flight speeds in excess of 13×10^3 ft. per sec.

Test Results and Data Reduction

The data taken during each test is presented in Table 3. The stagnation point ablation, x, is the axial length of material which was removed during a test. The variation of ablation with meridional angle is shown in Fig. 4. It can be seen that the ablation rate is almost constant up to an angle of 60°, after which it rapidly decreases.

The surface condition of each sample after being tested may be determined from Fig. 5. The surfaces of all samples are quite rough after a test, having a surface roughness of about 2,000 μ in. root mean square. However, during the test, the surface is covered by a relatively smooth molten layer of the reinforcement. The presence of a glued joint had no apparent effect on model 4.

Effective Heat of Ablation

Some early experiments indicated that the ablation rate for a given material varied almost linearly with the "calorimeter" heat-transfer rate. Thus it appears that a logical method of data reduction is to divide the calorimeter heating rate for the surface temperature of each test, as obtained from Fig. 2, by the rate of mass loss. The result is called the "effective heat of ablation."

An average ablation rate was used, obtained by dividing the length ablated by the run time. Actually, there is a starting transient during which time the ablation rate is less than the steady-state rate. Since the transient time is smaller than that required for the model to be lowered into position, this correction has been neglected.

The calculated heats of ablation are shown in Table 4. It can be seen that some models made from phenolic have a slightly lower ablation rate than those

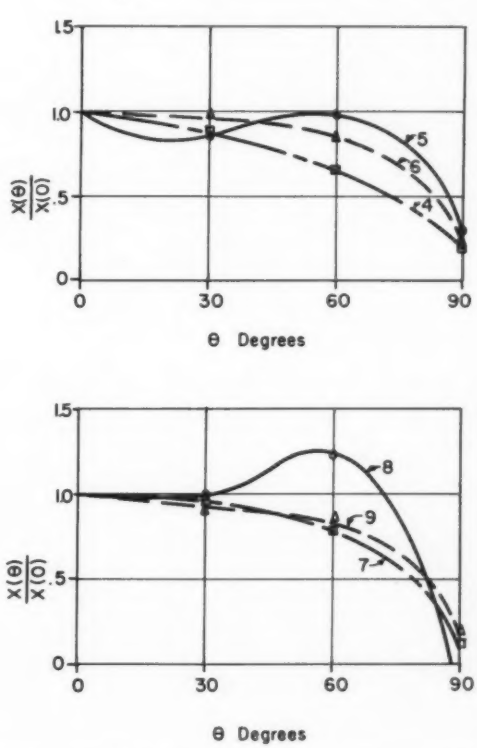

FIG. 4. Variation of ablation rate with meridional angle.

* This was pointed out to the author by Prof. Lester Lees of the California Institute of Technology.

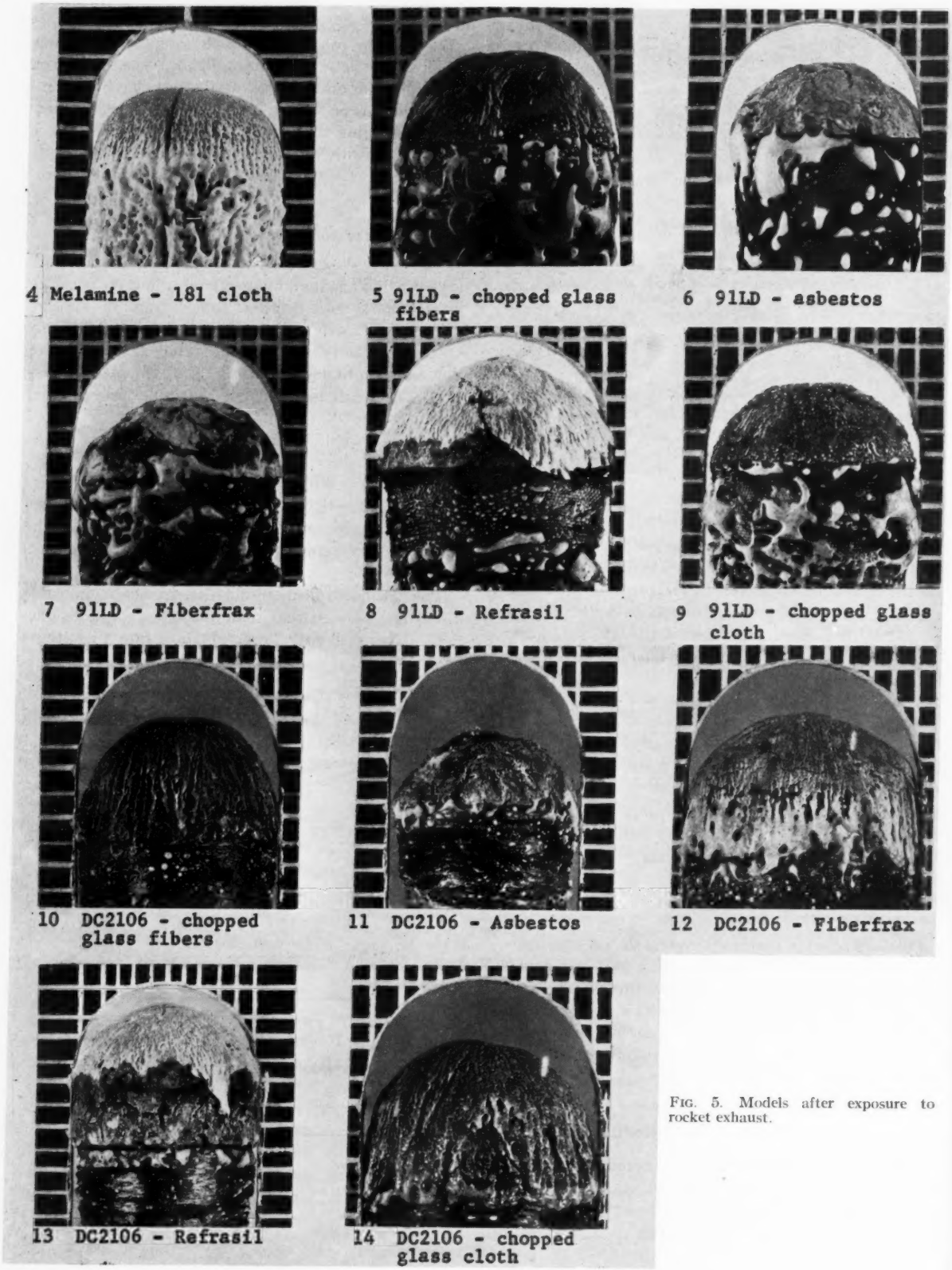
4 Melamine - 181 cloth
5 91LD - chopped glass fibers
6 91LD - asbestos
7 91LD - Fiberfrax
8 91LD - Refrasil
9 91LD - chopped glass cloth
10 DC2106 - chopped glass fibers
11 DC2106 - Asbestos
12 DC2106 - Fiberfrax
13 DC2106 - Refrasil
14 DC2106 - chopped glass cloth

FIG. 5. Models after exposure to rocket exhaust.

TABLE 4
Results of Ablation Tests

Model No.	Resin	Reinforcement	q, Extrapolated "Calorimeter" Heating Rate	H_c, Effective Heat of Ablation, B.t.u./lb.	α_p, Thermal Diffusivity, ft.²/sec.
4	Melamine	181 Glass cloth	1,085	2.2×10^3	
5	91-LD	1/2-in. Fiberglas strands	988	2.5×10^3	
6	91-LD	R/M 325 asbestos	962	2.5×10^3	0.98×10^{-6}
7	91-LD	Fiberfrax short staple	898	1.9×10^3	1.64×10^{-6}
8	91-LD	P-100 Refrasil	908	6.4×10^3	1.47×10^{-6}
9	91-LD	1/2-in. chopped 181 glass cloth	1,085	2.7×10^3	2.52×10^{-6}
10	DC-2106	1/2-in. Fiberglas strands	755	1.9×10^3	2.68×10^{-6}
11	DC-2106				
11	DC-2106	R/M 325 asbestos	877	1.1×10^3	3.31×10^{-6}
12	DC-2106	Fiberfrax short staple	782	2.0×10^3	0.92×10^{-6}
13	DC-2106	P-100 Refrasil	782	6.3×10^3	
14	DC-2106	1/2-in. chopped 181 cloth	860	2.0×10^3	1.25×10^{-6}

made from silicone. However, this difference may not be significant in view of the small number of samples.

Note the high heat of ablation for those samples which contain Refrasil. Fastax motion pictures taken of the tests reveal that for models made with other reinforcements, the molten surface flowed readily; this was not true for the Refrasil, which exhibited little fluidity.

Another way of calculating the effective heat of ablation is to subtract the surface radiation from the calorimeter heat-transfer rate, and then divide by the rate of mass loss. In these tests, the surface emissivity was not measured, and the accuracy of the surface temperature measurements does not warrant this method.

Thermal Diffusivity

For a material with constant thermal properties, the temperature distribution in the reinforced plastic during steady-state ablation is given quite closely by[3]

$$[T(x) - T_0]/(T_w - T_0) = \exp(-\dot{x}x/\alpha_p) \qquad (3)$$

where x is the distance from the melting surface, T_0 is the initial temperature, T_w is the surface temperature, α_p is the thermal diffusivity, and $\dot{x}$ is the ablation rate given by x/t. Now, a thermocouple which is initially at distance x_0 from the surface will progressively move toward the surface. At any time t the distance between the heat surface and the thermocouple is given by

$$x = x_0 - \dot{x}t \qquad (4)$$

Substitution of Eq. (3) into Eq. (2) yields the following expression for the temperature history of the thermocouple:

$$T(t) - T_0 = (T_w - T_0) \exp(-\dot{x}x_0/\alpha_p) \exp(\dot{x}^2t/\alpha_p) \qquad (5)$$

Hence, a semilogarithmic graphical representation of the change of thermocouple temperature vs. time should be a straight line. Semilog plots of the data did fall on a straight line, as a typical plot shows in Fig. 6. For those models for which thermocouple data was available, the thermal diffusivities are given in Table 4. For these values, the temperature profiles as given by Eq. (3) are quite shallow. This is also evident from sections taken of the melamine and phenolic models which are shown in Fig. 7. The darkened area which has been heated is somewhat greater than that predicted by Eq. (3). This is to be expected because of the redistribution of temperature in the model after shut down of the rocket motor. The slight cratering at the center of some of the specimens was probably due to the presence of the thermocouple well.

Discussion

From the test results, it appears that the oxygen content in the rocket exhaust did not have any major effect on the results. Thus, it appears permissible to apply the results to hypersonic flight in air. However, the results should be used with caution because of the small number of samples and possible error in the determination of the surface temperatures. The accuracy of the measured data appears to be ±15 per cent.

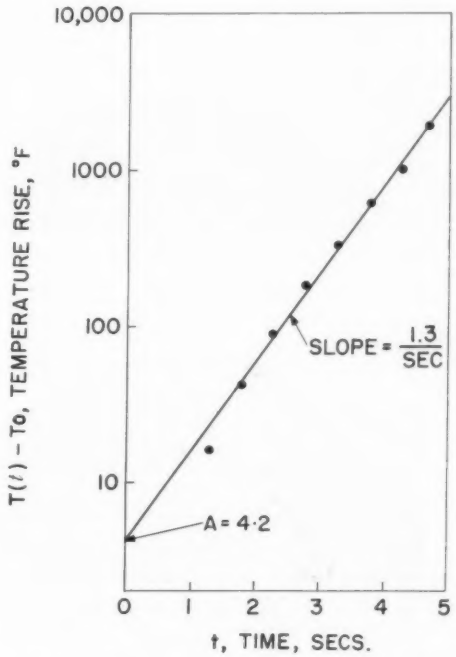

FIG. 6. Temperature rise vs. time for model 8.

The measured thermal diffusivities are somewhat higher than those typical of reinforced plastics at 400°F. The error in this measurement may be quite large due to the disturbing effect of the thermocouple installation on the temperature field.

It is of interest to compare the effective heat of ablation, H_e, to the theoretical enthalpy change of the reinforced plastic. The enthalpy increase for phenolic-silica, including the energy of pyrolysis of the phenolic, is about 1,000 B.t.u./lb.[4] This value is 50 per cent of the measured "heat of ablation," H_e, for phenolic-glass, and only about 20 per cent for phenolic-Refrasil. In the case of glass, the reduction may be caused by the mass-transfer cooling caused by the pyrolysis of the resin. In the case of Refrasil, the molten layer was much more viscous than the glass, which caused the melt to remain longer at the heated region. This resulted in somewhat higher surface temperatures, and may have caused some evaporation of silica. The larger viscosity and the possibility of silica evaporation may account for the decrease in the ablation rate as compared to the Fiberglas. Unfortunately, the models containing Refrasil exhibited some structural weakness, as evidenced by the presence of surface cracks.

The asbestos samples were somewhat poorer in their resistance to ablation. Both developed considerable surface roughness.

Both Fiberfrax models had the same ablation parameter; however, the silicone sample developed some surface cracks.

The Fiberglas models made with phenolic seemed to ablate less than those with silicone. There was not appreciable difference between the models using chopped strands as compared with chopped 181 cloth. However, some plastic fabricators find that the latter is more convenient for molding large shapes.

It is interesting that the melamine-glass cloth model machined from stock Texolite had about the same resistance to ablation as the custom molded parts containing glass. It had the advantage of very shallow heat pene-

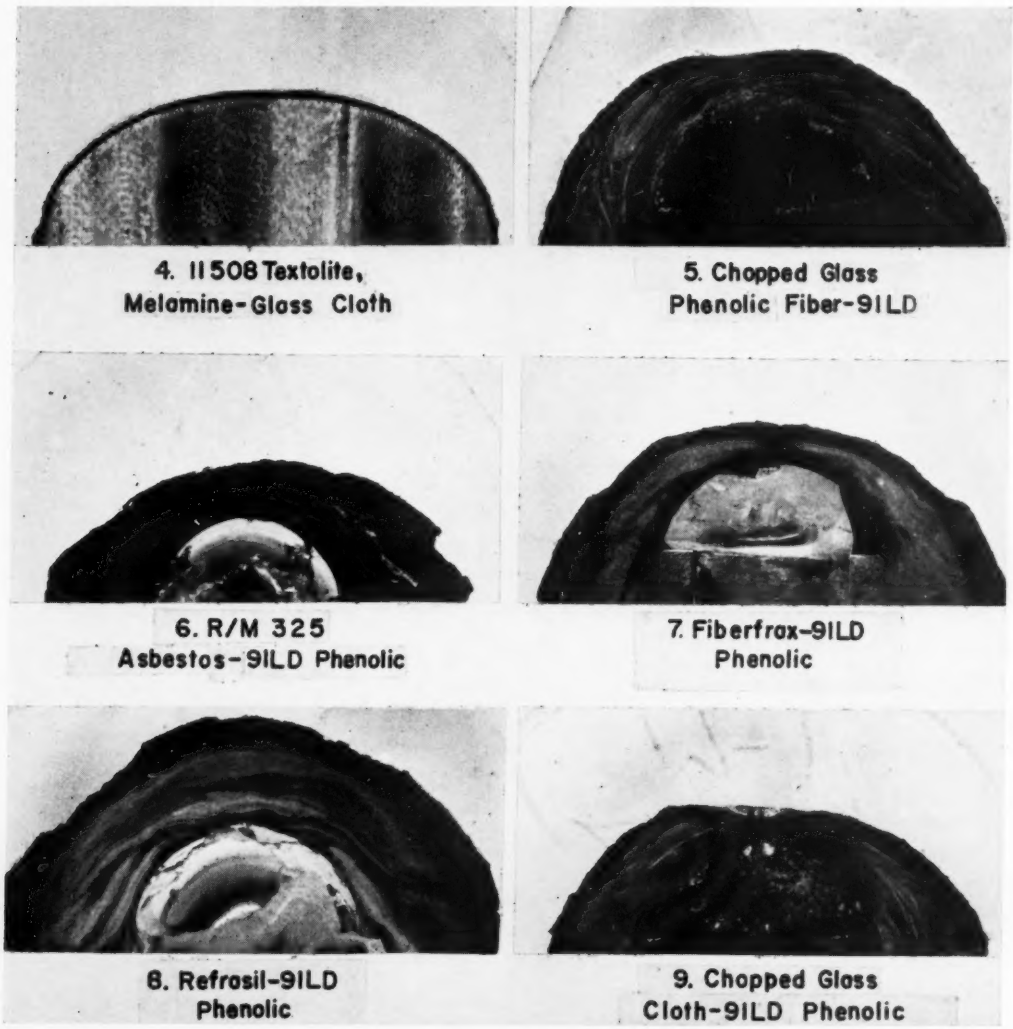

FIG. 7. Sections of the melamine and phenolic models after exposure.

tration, as can be seen from the sectioned model in Fig. 7. In addition, the presence of a glued joint had no apparent effect on the ablation rate. Thus, as an alternate method of fabrication, large shapes may be made by cementing together stock Texolite.

Application to Ablation Design

To use the results in Table 4, one calculates the heating rate to a nonreacting impermeable wall and merely divides this heating rate by the heat of ablation to determine the rate of removal of reinforced plastic, at the stagnation point. This ablation data may be used for calculations of the ablation rate for trajectories for which the heat transfer is varying slowly in comparison with the time required for the ablation rate to adjust. This time is given approximately by[3]

$$\tau \doteq 2 \pi k_p \rho_p C_p [(T_w - T_0)/2q]^2 \qquad (6)$$

where k_p, ρ_p, and C_p are the thermal conductivity, density, and specific heat of the plastic, and q is the heat-transfer rate to the surface. The effect is to slightly overestimate the ablation rate.

This ablation data should not be used for calorimeter heating rates less than 10^2 B.t.u./ft.^{2} sec., since the radiation flux from the surface may equal the aerodynamic heating at surface temperatures below that which will result in appreciable ablation, and the resin will simply decompose.

Conclusions

(1) A rocket motor exhaust may be used to simulate hypersonic heating for flight Mach numbers greater than 8 at 70,000 ft. altitude. For altitudes greater than 70,000 ft. the rocket exhaust is a somewhat more severe environment.

(2) The ablation rates of certain inorganic reinforced plastics are sufficiently low so that they may be used for the thermal protection of re-entry bodies. Data has been presented by which calculations can be made of the required ablation material.

(3) The temperature profile in such an ablating plastic is an inverse exponential when changes in the ablation rate occur slowly in comparison to the time required for the ablation rate to readjust.

(4) The average thermal diffusivity for the temperature range 100–2,000°F. is of the same order of magnitude as values at 400°F.

(5) The largest heat of ablation was exhibited by plastics reinforced with Refrasil, which is 96 per cent silica. This may be due to the high viscosity of molten silica.

(6) All reinforcements, except glass, seemed to suffer from mechanical weakness at elevated temperatures.

(7) No significant difference was discernible in the ablation resistance of melamine, 91-LD, or DC 2106, all of which are high-temperature resins.

References

[1] Munch, N. E., and Youmans, E. H., *Rocket Engine Combustion and Exhaust Flame Calculations for 92½% Water and Liquid Oxygen*, R57AGT317 Flight Propulsion Laboratory Department, General Electric Company, March 15, 1957.

[2] Sutton, G. W., and Scala, S. M., *The Two-Phase Laminar Boundary Layer with Mass Addition—A Study of Melting Ablation*, 1958 Heat Transfer and Fluids Mechanics Institute, Stanford University Press, 1958.

[3] Landau, H. G., *Heat Conduction in a Melting Solid*, Quart. Appl. Math., Vol. 8, No. 1, pp. 81–94, January, 1950.

[4] Vidale, G., General Electric Company MSVD, personal communication.

Foucault Pendulum Effect

(*Continued from page 347*)

pressions (5.5). In this case, particularly for high-speed vehicles, machine computation would be the most expedient method for studying the system errors.

References

[1] Sommerfeld, A., *Mechanics*, Academic Press, New York, 1952.

[2] Wrigley, W., Woodbury, R. B., and Hovorka, J., *Inertial Guidance*, Institute of the Aeronautical Sciences, Fairchild Fund Paper No. FF-16, New York, January, 1957. (This is now out of print; however, a limited number of copies are available from the Librarian, Instrumentation Laboratory, M.I.T.)

Change of Address

Since the Post Office Department does not as a rule forward magazines to forwarding addresses, it is important that the Institute be notified of changes in address 30 days in advance of publishing date to ensure receipt of every issue of the JOURNAL and AERO/SPACE ENGINEERING.

Notices should be printed legibly and sent directly to:

Institute of the Aeronautical Sciences, Inc.

2 East 64th Street, New York 21, N.Y.

Readers' Forum

BRIEF REPORTS of investigations in the aerospace sciences and discussions of papers published in the JOURNAL are presented in this special department. Entries must be restricted to a maximum of 1,300 words or the equivalent of one JOURNAL page including formulas and illustrations. Publication is completed as soon as possible after receipt of the material. The Editorial Committee does not hold itself responsible for the opinions expressed by the correspondents.

Contents

Bending of an Orthotropic Plate Clamped on the Boundary of a Conic Section ..... Y. Ōhasi and T. Suzuki 386

Stagnation-Point Heat-Transfer Measurements in Hypersonic, Low-Density Flow ..... S. E. Neice, R. W. Rutowski, and K. K. Chan 387

Two Analytical Results of Fin-Stabilized Rocket Trajectory Under Quadratic Drag Law .... K. S. Sung and C. Park 388

A Possible "Fully Developed" Hydromagnetic Pipe Flow ..... A. Demetriades 388

Dynamic Effects in Fatigue Testing ..... Richard M. Rowland and James L. Cronin 390

Viscous and Leading-Edge Effects in Hypersonic Flow ..... Robert J. Whalen 391

An Approximation to the Deflections and Strains in a Uniformly Loaded, Clamped, Rectangular Panel Subjected to Very Large Plastic Deformations ..... Joshua E. Greenspon 392

Thermal Stresses in a Long Circular Shell With Axial Temperature Variation ..... D. J. Johns 393

The Approximate Solution of the Equations of Motion of an Airplane Moving in a Vertical Plane .... E. F. Trombley 394

A Further Extension of the Routh-Hurwitz Stability Criteria for Quintic and Sextic Equations .. Herbert Saunders 396

Minor Circle Flight at Large Angles of Inclination ..... W. H. T. Loh 397

On the Unsteady Motion of a Delta Wing in Supersonic Flight ..... M. M. Stanišić 399

Bending of an Orthotropic Plate Clamped on the Boundary of a Conic Section

Y. Ōhasi and T. Suzuki*

Department of Applied Mechanics, The University, Nagoya, Japan

December 29, 1959

SIMPLE SOLUTIONS have been obtained by previous authors[1, 2, 3] for the orthotropic circular and elliptic plates clamped on the boundary and submitted to a uniform lateral load. A similar solution, however, can be easily obtained in more general case of conic sections, since a conic section is generally represented by the equation of the form

$$ax^2 + 2bxy + cy^2 + d = 0 \tag{1}$$

where x, y are the axes of symmetry with respect to the elastic properties of the plate.

The differential equation governing the deflection of an orthotropic plate is[4]

$$D_x(\partial^4 w/\partial x^4) + 2H(\partial^4 w/\partial x^2 \partial y^2) + D_y(\partial^4 w/\partial y^4) = q \tag{2}$$

In the particular case where the lateral load is expressed by a polynomial of x and y, q is given by the expression

$$q = \sum_{m=0}^{r} \sum_{n=0}^{s} q_{m,n} x^m y^n \tag{3}$$

The solution of Eq. (2), which satisfies the required conditions on the boundary, is

$$w = (ax^2 + 2bxy + cy^2 + d)^2 \sum_{m=0}^{r} \sum_{n=0}^{s} C_{m,n} x^m y^n \tag{4}$$

where $C_{m,n}$ is obtained by solving the simultaneous equations;

* The authors wish to express their thanks to Prof. H. Ōkubo for his kind suggestion.

Contributors Please Note

Readers' Forum items must be confined to the equivalent of one page in the *Journal*. Contributions that exceed this limit will be returned to the authors for condensation and rewrite. To avoid inconvenience and delay, please adhere to the following specifications:

(1) Five, double-spaced, typewritten, manuscript pages (8½ by 11 in.), including wide margins, formulas, and headings, equal one printed page.

(2) For every illustration, deduct at least one-half or as much as one manuscript page, depending on the size of the illustration.

$$(m+4)(m+3)(m+2)(m+1)D_x\{a^2C_{m,n}+4abC_{m+1,n-1}+2(ac+2b^2)C_{m+2,n-2}+4bcC_{m+3,n-3}+c^2C_{m+4,n-4}+2adC_{m+2,n}+4bdC_{m+3,n-1}+2cdC_{m+4,n-2}+d^2C_{m+4,n}\}+2(m+2)(m+1)(n+2)(n+1)H\{a^2C_{m-2,n+2}+4abC_{m-1,n+1}+2(ac+2b^2)C_{m,n}+4bcC_{m+1,n-1}+c^2C_{m+2,n-2}+2adC_{m,n+2}+4bdC_{m+1,n+1}+2cdC_{m+2,n}+d^2C_{m+2,n+2}\}+(n+4)(n+3)(n+2)(n+1)D_y\times\{a^2C_{m-4,n+4}+4abC_{m-3,n+3}+2(ac+2b^2)C_{m-2,n+2}+4bcC_{m-1,n+1}+c^2C_{m,n}+2adC_{m-2,n+4}+4bdC_{m-1,n+3}+2cdC_{m,n+2}+d^2C_{m,n+4}\}=q_{m,n},\quad m=0,1,2,\ldots,r,\quad n=0,1,2,\ldots,s \tag{5}$$

In the case of a uniform load of the intensity $q_{0,0}$ the deflection is

$$w=\frac{q_{0,0}}{24a^2D_x+16(ac+2b^2)H+24c^2D_y}(ax^2+2bxy+cy^2+d)^2 \tag{6}$$

In the case of hydrostatic pressure of $q=q_{0,0}+q_{1,0}x+q_{0,1}y$, the corresponding deflection is

$$w=(C_{0,0}+C_{1,0}x+C_{0,1}y)(ax^2+2bxy+cy^2+d)^2 \tag{7}$$

where

$$C_{0,0}=q_{0,0}/\{24a^2D_x+16(ac+2b^2)H+24c^2D_y\},$$
$$C_{1,0}=[\{a^2D_x+2(ac+2b^2)H+5c^2D_y\}q_{1,0}-4b(aH+cD_y)q_{0,1}]/24F,$$
$$C_{0,1}=[\{5a^2D_x+2(ac+2b^2)H+c^2D_y\}q_{0,1}-4b(aD_x+cH)q_{1,0}]/24F,$$
$$F=\{5a^2D_x+2(ac+2b^2)H+c^2D_y\}\{a^2D_x+2(ac+2b^2)H+5c^2D_y\}-16b^2(aD_x+cH)(aH+cD_y)$$

References

[1] Ōkubo, H., *On the Bending of Thin Aeolotropic Plates*, (1st Report), Reports of the Inst. High-Speed Mech., Tōhoku Univ. (in Japanese), Vol. 2, No. 10, p. 105, March, 1950.

[2] Ōhasi, Y., *Bending of a Thin Elliptic Plate of an Orthotropic Material Under Uniform Lateral Load*, ZAMP, Vol. 3, p. 212, 1952.

[3] Timoshenko, S., and Woinowsky-Krieger, *Theory of Plates and Shells*, 2nd Ed., p. 376, McGraw-Hill Book Co., Inc. New York, 1959.

[4] Timoshenko, S., and Woinowsky-Krieger, loc. cit., p. 365.

Stagnation-Point Heat-Transfer Measurements in Hypersonic, Low-Density Flow

S. E. Neice,* R. W. Rutowski,** and K. K. Chan***

Missiles and Space Division, Lockheed Aircraft Corporation, Sunnyvale, Calif.

January 8, 1960

Introduction

In hypersonic, low Reynolds number flow around a blunt body, the boundary-layer thickness approaches the shock-layer thickness (shock standoff distance) within the region of continuum flow.[1] In this instance, the customary boundary-layer approximations no longer apply. Hoshizaki[2] and Probstein[3] have obtained solutions to the incompressible Navier-Stokes equations in the stagnation region of a blunt body in this hypersonic low Reynolds number flow. The results indicate that heat-transfer rates are substantially higher than those predicted by incompressible boundary-layer theory.[4] Probstein indicated that the actual heat-transfer rates would be correspondingly higher than the predictions of Fay and Riddell.[5] These findings are of particular importance in the atmospheric entry phase of recoverable satellites. Such vehicles would spend considerable time in the altitude range from about 500,000 ft. to 250,000 ft., the region where the work of references 2 and 3 apply. A large portion of the total heating would occur in this region, even considering the predictions of reference 5. Any increase in this heating, as indicated by Hoshizaki and Probstein, could alter such a vehicle's performance considerably. The purpose of this note is to describe a series of tests, performed in a reflected-type shock tunnel, which provide stagnation-point heat-transfer data in hypersonic low-density flow characterized by a well-developed viscous shock layer.

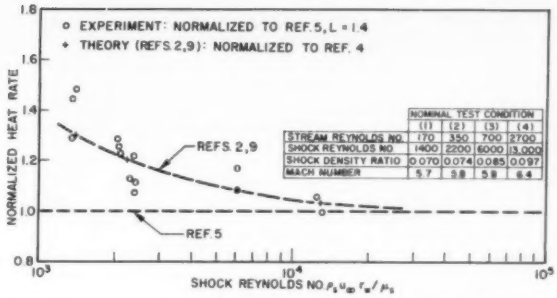
o EXPERIMENT: NORMALIZED TO REF. 5, L = 1.4
+ THEORY (REFS. 2,9): NORMALIZED TO REF. 4
NORMALIZED HEAT RATE
SHOCK REYNOLDS NO. $\rho_s u_\infty r_w/\mu_s$
REFS. 2,9
REF. 5
NOMINAL TEST CONDITION
(1) (2) (3) (4)
STREAM REYNOLDS NO. 170 350 700 2700
SHOCK REYNOLDS NO. 1400 2200 6000 13,000
SHOCK DENSITY RATIO 0.070 0.074 0.085 0.097
MACH NUMBER 5.7 5.8 5.8 6.4

FIG. 1. Nominal test conditions and experimental results.

Apparatus and Tests

Tests were conducted in a reflected-type shock tunnel connected to the downstream end of a 3-inch diameter, combustion driven shock tube. The air in the reflected region is expanded through the conical nozzle and exhausts into a plenum chamber which is initially evacuated. Models used in these tests were two 1-in. radius hemisphere cylinders. The calibration model was instrumented with a pressure transducer to record stagnation pressures. The test model was fitted with a thick film heat-transfer gage as described in reference 6. There was no attempt to "tailor" the reflection conditions. Calibration pressure records indicate that at least 200 microseconds of almost constant flow was obtained in the selected test conditions.

For the purposes of these tests, the tunnel was calibrated at four selected test conditions (Fig. 1) by measurements of the incident shock velocity and the reservoir and stagnation pressures. With these measurements and the assumpion of equilibrium flow, the flow along the centerline was evaluated using tables and charts in reference 7. The flow is undoubtedly not in equilibrium. Using the results of Bray,[8] it is estimated that measured pitot pressures and heat-transfer rates will be less than 10 per cent lower than values measured in the equilibrium free stream. This will have a correspondingly small effect on the indicated test conditions. The lower heat rates are opposite to the effect predicted by Hoshizaki and Probstein. The calibration, therefore, indicates an "effective" equilibrium free-stream condition corresponding to the equilibrium stagnation-point flow.

Results and Discussion

The experimental results are presented in Fig. 1. Here, the ratio of measured heat-transfer rate to the value computed by Fay and Riddell[6] is plotted against the shock Reynolds number based on equilibrium density and viscosity (ρ_s, μ_s) immediately behind the normal shock, but including the free-stream velocity (u_∞) and the body nose radius (r_w) of 1 in. In using the results of reference 5, a Lewis number (L) of 1.4 was used. Corresponding theoretical values are those of Hoshizaki[2] and include the effect of surface slip.[9] The shock-wave density ratio varies from about 0.097 down to 0.072 throughout the test range. Hence, the theoretical points are connected by a dashed line only to indicate the trend with Reynolds number. As shown in Fig. 1, the theoretical predictions of the effect of shock-generated vorticity on stagnation-point heat-transfer rates appear to be borne out by the experimental results.

Present plans are to increase the nozzle area ratio by a factor of two and to decrease the model size to half of that used in the present tests. In future tests, free-stream Reynolds numbers as

* Research Specialist.
**Staff Scientist.
***Aeronautical Engineer.

low as 50 should be obtained, which will extend the test range to the limit of continuum flow.

REFERENCES

[1] Adams, M. C., and Probstein, R. F., *On the Validity of Continuum Theory for Satellite and Hypersonic Flight Problems at Altitude*, Jet Propulsion, Vol. 28, No. 2, pp. 86–89, February, 1958.

[2] Hoshizaki, H., *Shock-Generated Vorticity Effects at Low Reynolds Numbers*, Lockheed Missiles and Space Division, LMSD 48379, Vol. 1, *January, 1959*, (ASTIA No. 210801).

[3] Probstein, R. F., *Continuum Theory and Rarified Hypersonic Aerodynamics*, WADC TN-58-145, July, 1958.

[4] Sibulkin, M., *Heat Transfer Near the Forward Stagnation Point of a Body of Revolution*, Journal of the Aeronautical Sciences, Vol. 19, No. 8, pp. 570–571, August, 1952.

[5] Fay, J. A., and Riddell, F. R., *Theory of Stagnation Point Heat Transfer in Dissociated Air*, Journal of the Aeronautical Sciences, Vol. 25, No. 2, pp. 73–85, February, 1958.

[6] Rutowski, R. W., *Stagnation Point Heat Transfer in a Partially Ionized Gas*, Heat Transfer and Fluid Mechanics Institute, Stanford University Press, pp. 110–125, 1959.

[7] Feldman, S., *Hypersonic Gas Dynamic Charts for Equilibrium Air*. AVCO Mfg. Corp., January, 1957.

[8] Bray, K. N. C., *Atomic Recombination in a Hypersonic Wind-Tunnel Nozzle*, Journal of Fluid Mechanics, Vol. 6, Part 1, pp. 1–32, July, 1959.

[9] Hoshizaki, H., *The Effect of Shock-Generated Vorticity Surface Slip and Temperature Jump on Stagnation Point Heat Transfer Rates*, Journal of the Aeronautical Sciences, Vol. 27, No. 2, February, 1958.

Two Analytical Results of Fin-Stabilized Rocket Trajectory Under Quadratic Drag Law

K. S. Sung and C. Park

Graduate Students, Department of Aeronautical Engineering, Seoul National University, Seoul, Korea

December 29, 1959

THE QUADRATIC drag law in power-off flight

$$m(dv/dt) = -cv^2 - mg \sin \omega$$
$$v(d\omega/dt) = -g \cos \omega$$

where m, v, ω, g, and c are the mass, linear velocity, flight path angle, gravitation, and drag constant, respectively, can be integrated once after the change of variable

$$u = v \cos \omega$$

into the form

$$(2mg/cu^2) + \ln [(1 + \sin \omega)/(1 - \sin \omega)] + 2 \sec \omega \tan \omega = a$$

where a is a constant to be determined from initial condition.

When this is expanded in series form

$$u/u_0 = 1 + \sum_1^\infty a_n \omega^n$$

where $u_0 = \sqrt{2mg/ac}$, the first five coefficients are

$$a_1 = 2/a, \quad a_2 = 6/a^2, \quad a_3 = (1/a) + (20/a^2)$$
$$a_4 = (6/a^2) + (115/2a^4), \quad a_5 = (11/20a) + (30/a^3) + (177/a^5)$$

Integrating once more for endurance, horizontal and vertical distance, respectively, there result

$$t = -(1/g) \cdot \int u \sec^2 \omega \, d\omega = -(u_0/g) \sum_0^\infty b_n \omega^{n+1}/(n+1) + \text{const.}$$

$$x = -(1/g) \cdot \int u^2 \sec^2 \omega \, d\omega = -(u_0^2/g) \sum_0^\infty c_n \omega^{n+1}/(n+1) + \text{const.}$$

$$y = -(1/g) \cdot \int u^2 \sec^2 \omega \tan \omega$$
$$= -(u_0^2/g) \sum_1^\infty d_n \omega^{n+1}/(n+1) + \text{const.}$$

where the first several terms corresponding to the above mentioned five terms are

$$b_0 = 1, \quad b_1 = a_1, \quad b_2 = a_2 + 1, \quad b_3 = a_3 + a_1$$
$$b_4 = a_4 + a_2 - (4/3), \quad b_5 = a_5 + a_3 + (2/3)a_1$$
$$b_6 = a_4 + (2/3)a_1 - (73/45), \quad b_7 = a_5 + (2/3)a_3 + (17/30)a_1$$
$$b_8 = (2/3)a_4 + (2/3)a_1 - (13/45)a_2 - 1.136$$
$$c_0 = 1, \quad c_1 = a_1 + b_1, \quad c_2 = a_2 + a_1 b_1 + b_2$$
$$c_3 = a_3 + a_2 b_1 + a_1 b_2 + b_3$$
$$c_4 = a_4 + a_3 b_1 + a_2 b_2 + a_1 b_3 + b_4$$
$$c_5 = a_5 + a_4 b_1 + a_3 b_2 + a_2 b_3 + a_1 b_4 + b_5$$
$$c_6 = a_5 b_1 + a_4 b_2 + a_3 b_3 + a_2 b_4 + a_1 b_5 + b_6$$
$$c_7 = a_5 b_2 + a_4 b_3 + a_3 b_4 + a_2 b_5 + a_1 b_6 + b_7$$
$$c_8 = a_5 b_3 + a_4 b_4 + a_3 b_5 + a_2 b_6 + a_1 b_7 + b_8$$
$$d_1 = 1, \quad d_2 = c_1, \quad d_3 = c_2 + (1/3), \quad d_4 = c_3 + (1/3)c_1$$
$$d_5 = c_4 + (1/3)c_2 + (2/15), \quad d_6 = c_5 + (1/3)c_3 + (2/15)c_1$$
$$d_7 = c_6 + (1/3)c_4 + (2/15)c_2 + (17/315)$$
$$d_8 = c_7 + (1/3)c_5 + (2/15)c_3 + (17/315)c_1$$
$$d_9 = c_8 + (1/3)c_6 + (2/15)c_4 + (17/315)c_2$$

Another approximation is obtained from the extended quadratic drag law

$$(D/m) + g \sin \omega = e + fv^2$$

This enables the integration of equations of motion. The results are

$$\left.\begin{array}{c} e > 0, \quad f > 0 \\ t = -(1/fV) \arctan w + \text{const.} \\ (g/2e) \ln [1 + (1/w^2)] = \ln \tan [(\omega/2) + (\pi/4)] + \text{const.} \\ s = -(1/2f) \ln (1 + w^2) + \text{const.} \end{array}\right\} \quad (1)$$

where

$$V = \sqrt{e/f}, \quad w = v/V$$

$$\left.\begin{array}{c} e = -e' < 0, \quad f > 0 \\ t = (1/2fV) \ln K + \text{const.} \\ (g/2e') \ln (1 - w^2) = \ln \tan [(\omega/2) + (\pi/4)] + \text{const.} \\ s = 1/f \cdot \ln \sinh [(1/2) \ln K] + \text{const.} \end{array}\right\} \quad (2)$$

where

$$V = \sqrt{e'/f}, \quad K = (w+1)/(w-1), \quad w = v/V$$

and s is the arc length of the flight path.

The heavier the rocket compared with drag and the smaller the angle of flight, the better is the convergence of series method. One example showed the error of about 4 per cent with $\omega = 45°$ and $u_0 = 700$ m.p.h.

The new method can be used for any flight angle except for terminal dive, and its judicious use has brought less error than earlier methods in actual problems.

REFERENCE

[1] Sung, K. S., and Park, C., *The Trajectory of a Fin-Stabilized Rocket* J. Korean Astronautical Soc., Vol. 1, No. 1, pp. 14–19, November, 1959.

A Possible "Fully Developed" Hydromagnetic Pipe Flow*

A. Demetriades

Research Fellow, Guggenheim Aeronautical Laboratory, California Institute of Technology, Pasadena, Calif.

December 29, 1959

RECENT WORK on internal hydromagnetics has revived interest on the action of electromagnetic fields on conducting fluids moving in enclosed ducts. Particularly contributive to the understanding of the interaction between the fluid viscosity and the fields is the study of the end state in the dynamic balance between

* This work was performed in the course of the author's consulting activities at and with the support of the Plasmadyne Corporation, Santa Ana, Calif.

these two agents—the state which, in hydrodynamic language, is called the "fully developed state." Thus, the fully developed flow of a conducting fluid in a channel with parallel, mutually immobile walls immersed in a uniform, essentially unidirectional magnetic field has been studied by Hartmann,[1] Shercliff,[2] and Chang and Lundgren.[3] The Poiseuille flow between two coaxial cylinders with a radial magnetic field has also been investigated by Globe.[4] The present communication presents some results arrived at during the study of the hydromagnetic analogue of the Hagen-Poiseuille flow in a circular pipe.

The problem of the steady laminar, fully developed, electrically nondissipative flow of an incompressible, conducting fluid in a pipe of circular section presents the added difficulty that the magnetic field has to be nonuniform and nonvanishing along at least two of the three cylindrical coordinates (the case of the field everywhere parallel to the pipe axis being inconsequential). Thus, the simple assumptions that the electric field vanishes everywhere, that the magnetic field is everywhere finite, and that the flow is axisymmetric leads to the following equations of momentum balance:

$$\partial p/\partial r = \sigma w B_r B_z \tag{1}$$

$$\partial p/\partial z = (\eta/r)(\partial/\partial r)[r(\partial w/\partial r)] - \sigma w B_r^2 \tag{2}$$

and the equations of Maxwell:

$$(\partial B_r/\partial r) + (B_r/r) + (\partial B_z/\partial z) = 0 \tag{3}$$

$$(\partial B_r/\partial z) - (\partial B_z/\partial r) = \mu\sigma w B_r \tag{4}$$

where p is the pressure; σ, η, and μ, the (constant) conductivity, viscosity, and permeability of the fluid; B_r and B_z the radial and axial components of the magnetic induction, respectively; r and z the cylindrical coordinates illustrated in Fig. 1; and w the axial flow velocity, satisfying the equation of continuity:

$$\partial w/\partial z = 0 \tag{5}$$

Note that in the above equations the electrical current density has been substituted for from the generalized Ohm's law and that, for no ohmic dissipation, the only allowed currents flow in azimuthal circles concentric with the pipe axis. Also note that the pressure in the fluid is now a priori undetermined, in contrast with the channel-flow problem.[1]

Eqs. (1)–(5) are still as general as permitted by the three above mentioned assumptions. A detailed investigation of their mutual compatibility leads to the conclusion that they can be satisfied for two cases only. In the first, the magnetic fields and the axial pressure gradient will have to be functions of both r and z; therefore, all parameters of interest, except the velocity and the viscous shear, will vary not only radially but also along the channel. In the second case, it is found that the equations are compatible if $\partial p/\partial z$ and B_r are functions of r only; without solving the equations themselves, this "compatible" field can be found by inspection to be

$$B_r = 2Ar \tag{6}$$

$$B_z = C - 4Az + B_{z_1}(r) \tag{7}$$

where A and C are constants. This field has the general form shown in Fig. 1. The radial component has a form unaffected

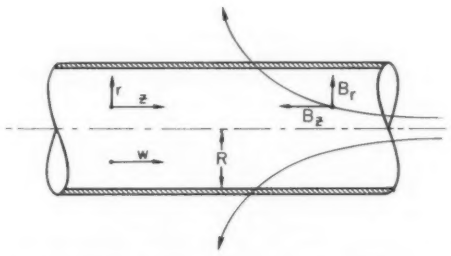

FIG. 1. Problem geometry showing coordinate system (r, z), flow velocity w, and configuration of magnetic field given by Eqs. (6) and (7).

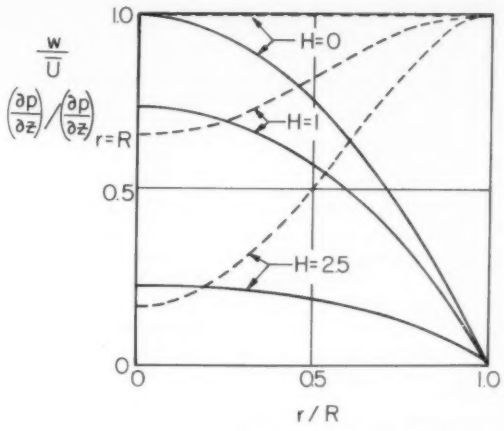

FIG. 2. Axial velocity (solid lines) and axial pressure gradient (dashed lines) for pipe flow under the action of the magnetic field of Eqs. (6) and (7) for various Hartmann numbers.

by the fluid motion, whereas the last term of B_z is found to depend on the magnetic Reynolds number and, hence, represents the amount of "bending" of the magnetic lines due to the motion. Laboratory reproduction of this unique field can be effected by proper choice of the constants A and C.

Two of the boundary conditions necessary for the solution are identical to those of the Hagen-Poiseuille case. The third is that the electrical current vanishes on the pipe wall and the fourth that the axial pressure gradient has a known value on the wall. The solution becomes straightforward once Eqs. (6) and (7) are inserted into Eqs. (1)—(4) and once the following transformations are made:

$$\gamma = (r/R)^2$$
$$\zeta = (r/U)(dw/dr)$$

where R is the pipe radius and U the velocity on the axis in the absence of the field. The velocity is thus obtained from the solution of

$$(d^2\zeta/d\gamma^2) - H^2\zeta = 0 \tag{8}$$

where H is the Hartmann number $H = AR^2\sqrt{\sigma/\eta}$ and is

$$w/U = \left\{[(1-\gamma)/\cosh H] + (1/\cosh H) \times \sum_{\nu=1}^{\infty} [H^{2\nu}(1-\gamma^{2\nu+1})/(2\nu+1)(2\nu+1)!]\right\} \tag{9}$$

The remainder of the pertinent parameters can be obtained easily from Eqs. (1)—(4); for example, the pressure gradient $\partial p/\partial z$ is

$$\partial p/\partial z = (\partial p/\partial z)_{r=R} \left\{[\cosh H\gamma/\cosh H] + (H^2\gamma/\cosh H) \times \sum_{0}^{\infty} [H^{2\nu}(1-\gamma^{2\nu+1})/(2\nu+1)(2\nu+1)!]\right\}$$

The velocity and pressure gradient are plotted in Fig. 2 for various values of the Hartman number.

REFERENCES

[1] Hartmann, J., and Lazarus, F., Kge. Kanske Videnskab Selskab Mat.-fys. Medd. 15, Nos. 6 and 7, 1937. Also see Cowling, T. G., *Magnetohydrodynamics*, pp. 13–17, Interscience Publishers, Inc., New York, N. Y., 1957.

[2] Shercliff, J. A. *Steady Motion of Conducting Fluids in Pipes under Transverse Magnetic Fields*, Proc. Camb. Phil. Soc., Vol. 49, p. 136, 1953.

[3] Chang, C. C., and Lundgren, T. S., *The Flow of an Electrically Conducting Fluid Through a Duct with Transverse Magnetic Field*, 1959 Heat Transfer and Fluid Mechanics Institute, Stanford University Press, Stanford, California, 1959.

[4] Globe, S., *Laminar Steady-State Magnetohydrodynamic Flow in an Annular Channel*, Physics of Fluids, Vol. 2, No. 4, p. 404, July–August, 1959.

Dynamic Effects in Fatigue Testing

Richard M. Rowland and James L. Cronin
Strength Group Engineer, McDonnell Aircraft Corp., and Associate Professor, Institute of Technology, St. Louis, Mo., Respectively
December 1, 1959

TODAY's emphasis on fatigue analysis and fatigue-life predictions requires close examination of the methods used for such testing and predictions. One such method is full-scale testing and fitting the results to existing S-N and modified Goodman diagrams. The validity of such data should be questioned in regard to the influence of the load-cycle time. It is frequently assumed that dynamic effects need not be considered when the input frequency does not approximate the structural natural frequency. Intuitively, this assumption does not appear completely valid. Test techniques are improving to such an extent that within the foreseeable future it will be possible to approach the structural natural frequency with the input frequency. In general, the question arises as to whether the type of force input and the frequency and distribution of these inputs have harmonics that would couple with the structural resonances so as to affect adversely the life predictions.

The periodic functions, I, II, and III (Fig. 1), are made up of linear elements combined in a manner which permits variation of the input distribution within the period. These functions are assumed to be the forcing functions impressed upon a damped single-degree-of-freedom system. The steady-state solution of the differential equation of motion of such a system defines the deformation of the structure as a function of time. For these forcing functions, the steady-state solutions are:

$$y(t)_{\mathrm{I}} = LH + P\{k_2H[(1-k_1)/(1-k_2)] - \sum_{n=1}^{\infty}(2/n\pi)(\sqrt{J}/F)\cos[\theta_1 - \theta_2 + A(t/t_1)]\}$$

$$y(t)_{\mathrm{II}} = (LH/2) + P\{[k_1k_2H/(1-k_2)] - \sum_{n=1}^{\infty}(2H/A^2)(\sqrt{J-2A\sin A + A^2/F})\cos[\theta_3 - \theta_4 + A(t/t_1)]\}$$

$$y(t)_{\mathrm{III}} = L - P\{(4/k_1A^2)\sum_{n=1}^{\infty}(J/2F)\cos[-\theta_4 + A(t/t_1)]\}$$

where

$A = 2n\pi/(1+k_1)$, $J = 2(1-\cos A)$
$B = (1-\lambda^2n^2)/\omega^2(1+k_1)^2$, $L = G(1+k_2)/2k$
$D = 2nc\lambda/\omega(1+k_1)c_c$, $P = G(1-k_2)/2k$
$H = 2/(1+k_1)$, $F = \sqrt{B^2+D^2}$
$\theta_1 = \tan^{-1}\dfrac{2\sin A}{J}$, $\theta_3 = \tan^{-1}\dfrac{\sin A - A\cos A}{1-\cos A - A\sin A}$
$\theta_2 = \tan^{-1}(B/-D)$, $\theta_4 = \tan^{-1}(D/B)$
$\lambda = 2\pi/t_1$

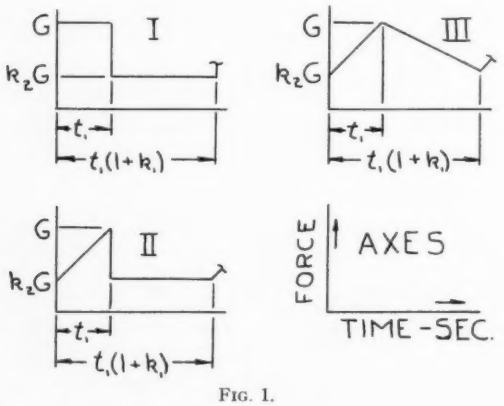

FIG. 1.

k = spring constant of the structure
ω = undamped natural frequency
c/c_c = ratio of the structural damping to the critical damping

The initial term of each solution is the mean value of the input during the period divided by the spring constant of the structure. Assuming that the stress in the structure is linear with deformation, the initial term may be defined as a measure of the mean stress felt by the structure.

The portion of the second term which precedes the brackets may be likewise defined as a measure of the alternating stress felt by the structure.

For functions I and II, the portion of the second term just inside the bracket is a function of the input distribution and of the lower input force limit. When combined with the term preceding the bracket, this term represents a modification to the mean stress, reducing it for function I and increasing it for function II. The series expression represents the response function applied to the alternating stress giving rise to the stress cycles and amplification of this stress. This expression relates the input distribution and loading time to the undamped natural frequency of the structure.

The series for functions I and II converge rather slowly, with the higher harmonics strongly influencing the value of the summation. Examination of six values of λ/ω, from 0.10 to 0.835 with $(1+k_1) = 1.5$, 2.0, 2.5, and 3.0, exhibited the influence of the higher harmonics for all combinations. Four and five cycles of varying amplitude per input cycle resulted. The maximum half-amplitude for function I was 427 per cent and for function II was 327 per cent.

The series for function III exhibited the same characteristics for some combinations of λ/ω and $(1+k_1)$. However, when $(1+k_1) = 2.0$, the first harmonic predominated over the higher harmonics with a half-amplitude of 100 per cent for all values of λ/ω providing that

$$(1+k_1)/(\lambda/\omega) \neq n < 5$$

When this proviso was violated, the higher harmonics predominated. When $(1+k_1) \neq 2.0$, one cycle per input cycle resulted, due to the predominance of the first harmonic, but the range was shifted downward—i.e., both the upper and lower limits were lower than would be predicted for the force limits, thus creating a modification to the mean stress term which is not apparent from the form of the solution.

Thus, these forcing functions can yield results which have the following characteristics:

(a) The ratio of the number of stress cycles to the number of input load cycles exceed unity due to the predominance of the higher harmonics.

(b) Amplification of the alternating stress occurs in such a manner that the stress range, and, hence, the stress limits, are not those associated with the static application of the force limits.

To assure compatibility of test data, the force input should be one which has one stress cycle per input cycle, a predictable mean stress and no amplification of the alternating stress. Neither functions I nor II will yield these results. Function III with the unloading rate controlled to equal the loading rate—i.e., $(1+k_1) = 2.0$ will yield these results.

Fatigue analysis and predictions based upon existing test data can be erroneous unless the type and distribution of the force inputs are compatible. Any testing without proper control can only lead to erroneous conclusions regarding the life of the structure.

Some of the scatter associated with fatigue testing can be attributed to lack of control of the test inputs and also to variations in the parameters, λ/ω and $(1+k_1)$. The results of this investigation showed large differences in the stress range for slight variations in these two parameters.

In conclusion, it would appear feasible to utilize functions I and II for spectrum testing if appropriate controls could be provided. This approach would necessitate the selection of appropriate force limits to maintain the desired stress limits.

Viscous and Leading-Edge Effects in Hypersonic Flow

Robert J. Whalen
Principal Scientist, Flight Sciences Laboratory, Inc., Buffalo, N.Y.
December 11, 1959

THE PURPOSE of this note is to call attention to correlations of existing experimental data on hypersonic viscous and inviscid leading-edge effects by means of parameters proposed by general similitude considerations.

The pressure similitude, according to references 1 and 2, for the hypersonic flow about a two-dimensional* blunt leading-edge slender body may be written (for a perfect gas with constant specific heats):

$$p/p_\infty = f[M_\infty\tau,\ M_\infty^3 k(d/x),\ \chi,\ H_w/H_\infty,\ \gamma,\ Pr] \qquad (1)$$

where M_∞ = free-stream Mach number, τ = thickness ratio, k = nose drag coefficient, $\chi \equiv M_\infty^3\sqrt{c}/\sqrt{Rex}$, H_w = surface total enthalpy, H_∞ = free-stream total enthalpy, γ = specific-heat ratio, and Pr = Prandtl number.

Correlation of existing experimental[3] and numerical[4] results for the inviscid hypersonic flow about a blunt leading-edge body at angle of attack is presented in Fig. 1. The experimental and numerical results are in the $2° \leq |\alpha| \leq 20°$, $6.86 \leq M_\infty \leq 20$, $0.4 \leq |M_\infty\alpha| \leq 7$ range. In this figure, the measured pressure is non-dimensionalized with respect to the "strong" tangent-wedge value. Thus, in the one limit at large angle of attack, the data approach the tangent-wedge value, while in the other limit—i.e.,

$$[M_\infty^3 k(d/x)]^{2/3}/M_\infty^2\alpha^2 \gg 1$$

the data are observed to approach the "strong" blast-wave theory. The relative weak dependence (although this must be verified for smaller $M_\infty\alpha$) on the parameter $M_\infty\alpha$ may be readily observed in Fig. 1. This is due largely to the method of presentation.† A plot of $\Delta p/p_\infty$ vs. $M_\infty^3 k\,(d/x)$ yields the dependence on the parameter $M_\infty\alpha$ (in the form of lines of constant $M_\infty\alpha$) as proposed by the general similitude.[1]

The boundary-layer interaction problem at arbitrary angle of attack may be considered in a similar manner. Correlation of experimental results[3] in the $11.5 \leq M_\infty \leq 19$, $1(1/4)° \leq |\alpha| \leq 11(1/4)°$, $0.4 \leq |M_\infty\alpha| \leq 3.74$, $0.1 \leq \chi \leq 14.5$ range, for both air and helium, is presented in Fig. 2. The data are presented for both the swept and unswept plates correlated on the interaction parameter, χ, based on streamwise conditions—i.e., $\chi \equiv M_\infty^3\sqrt{c}/\sqrt{Rex}$, x = distance from leading edge measured in streamwise direction, since the presence of a spanwise velocity has been shown[5] to have a small (<15 per cent) influence on strong boundary-layer interaction in the $0° \leq \Lambda \leq 60°$ range (Λ = sweep angle). As in the previous blunt-body problem, the experimental data are observed to approach the inviscid "strong" tangent-wedge value for large α and, in the other limit, the strong-interaction value for small α. The strong-interaction value for air is taken as that for $H_w/H_\infty \cong 0.5$, the approximate equilibrium temperature associated with the Ohio State experiments.

The combined viscous and inviscid leading-edge effects are considered in Fig. 3. The experimental results for air[3, 6] are in the $4.3 \leq Re_d \leq 4{,}128$, $5.8 \leq M_\infty \geq 11.5$ range and for helium[4, 7, 8] in the $132 \leq Re_d \leq 19{,}500$, $11.4 \leq M_\infty \leq 23$ range, (Re_d = Reynolds number based on leading-edge thickness). The correlation and approach of the data to both the "strong" blast-wave and "strong" boundary-layer interaction theories may be readily observed.

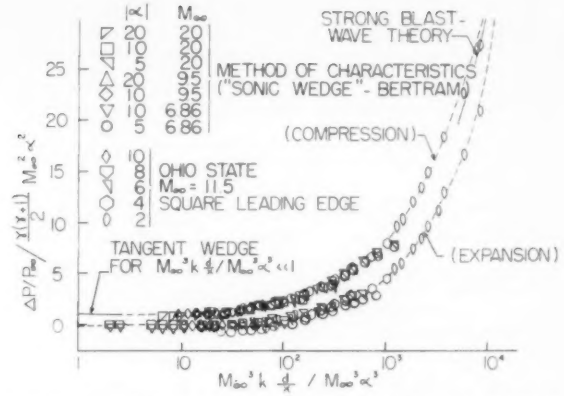

FIG. 1. Inviscid hypersonic flow about blunt leading-edge bodies at angle of attack (air).

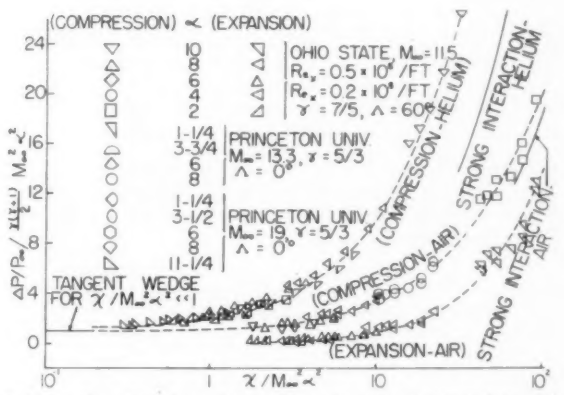

FIG. 2. Boundary-layer interaction at angle of attack (air and helium).

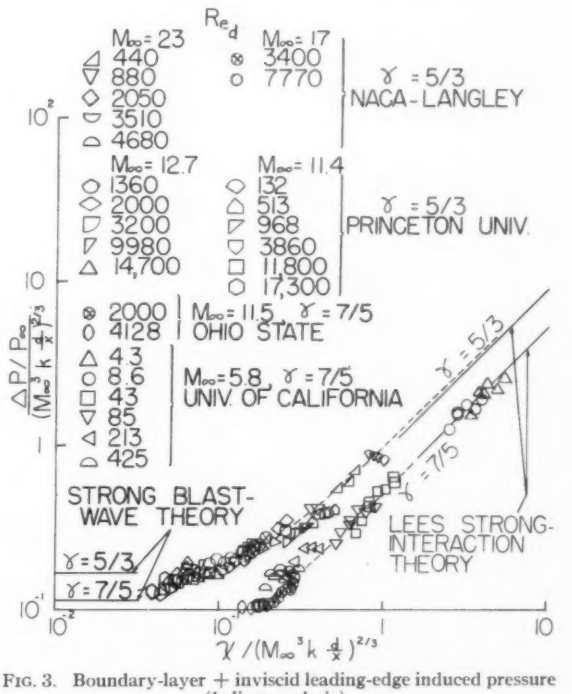

FIG. 3. Boundary-layer + inviscid leading-edge induced pressure (helium and air).

* This restriction is required for the viscous problem in order to avoid specifying the aspect ratio of the geometry under consideration. The parameter for the inviscid hypersonic flow about an axisymmetric geometry is taken as $M_\infty^{3/2}k^{1/2}(d/x)$.

† This form of presentation is, therefore, useful for predicting local pressure distributions on blunt bodies in hypersonic flow.

REFERENCES

[1] Cheng, H. K., *Similitude of Hypersonic Real-Gas Flows Over Slender Bodies With Blunted Noses*, Journal of the Aero/Space Sciences, Vol. 26, No. 9, pp. 575–585, September, 1959.

[2] Hayes, W. D., and Probstein, R. F., *Viscous Hypersonic Similitude*, Journal of the Aero/Space Sciences, Vol. 26, No. 12, pp. 815–824, December, 1959.

[3] Lee, J. D., *Pressure Distribution on a 60° Flat Delta and on a Blunted Flat Plate at a Nominal Mach Number of 11.5*, Ohio State University Rpt. 775, May, 1958.

[4] Bertram, M. H., and Henderson, A., Jr., *Effects of Boundary Layer Displacement and Leading Edge Bluntness on Pressure Distribution, Skin Friction, and Heat Transfer of Bodies at Hypersonic Speeds*, NACA TN 4301, July, 1958.

[5] Whalen, R. J., *Boundary-Layer Interaction on a Yawed Infinite Wing in Hypersonic Flow*, Journal of the Aero/Space Sciences, Readers' Forum, Vol. 26, No. 12, pp. 839–41, December, 1959.

[6] Schaaf, S. A., Hurlbut, F. C., and Talbot, L., *Induced Pressures on Flat Plates in Hypersonic Low Density Flow*, Bell Aircraft Rpt. D143-978-008, January, 1957.

[7] Hammitt, A. G., Vas, I. E., and Bogdonoff, S. M., *Leading Edge Effects on the Flow over a Flat Plate at Hypersonic Speeds*, Princeton University, Aeronautical Engineering Dept. Rpt. No. 326, September, 1955; also Hammitt, A. G., and Bogdonoff, S. M., *Hypersonic Studies of the Leading Edge Effect on the Flow over a Flat Plate*, Jet Propulsion, Vol. 26, No. 4, pp. 241–246, April, 1956.

[8] Henderson, A., and Johnston, P. J., *Fluid-Dynamics Properties of Some Simple Sharp- and Blunt-Nosed Shapes at Mach Numbers From 16 to 24 in Helium Flow*, NASA Memo 5 8-59L, June, 1959.

An Approximation to the Deflections and Strains in a Uniformly Loaded, Clamped, Rectangular Panel Subjected to Very Large Plastic Deformations*

Joshua E. Greenspon
J G Engineering Research Associates, Baltimore, Md.

December 1, 1959

THE ONLY stresses that are of importance in the elastic small-deflection region of plates are those corresponding to bending of the panel. As the load is increased and the plate enters the large-deflection region, the load is resisted by both bending and tension in the middle plane of the panel. As the load is further increased, the tensile stresses become predominant. Finally, when very large deformations occur which are many times the thickness of the panel, the panel may be considered to act as a stretched membrane. In deriving the formulas given here, the following assumptions have been made:

(a) The tension in the panel is constant.

(b) All bending stresses in the panel may be neglected.

(c) Elastic deflections of the panel may be neglected—i.e., no elastic recovery of the deflection or strain takes place after loading.

(d) The strain in the panel is large compared with the strain at the yield point.

The plate is therefore assumed to act as a stretched membrane. The equation of equilibrium of a stretched membrane under uniform static loading is as follows:

$$(\partial^2 w/\partial x^2) + (\partial^2 w/\partial y^2) = -(P_0/T) \tag{1}$$

where w is the lateral deflection, P_0 is the external lateral pressure (load per unit area), and T is the tension per unit length.

Assuming that the boundaries of the membrane remain stationary, the boundary conditions may be written as follows:

$$w = 0 \text{ at } x = 0, \quad x = a, \quad y = 0, \quad y = b \tag{2}$$

Considering only the first term in the series representing the deflection, we obtain

$$w(x, y) = [16P_0b^2/T\pi^4(b^2/a^2 + 1)] \sin(\pi x/a) \sin(\pi y/b) \tag{3}$$

Now, if it is assumed that the strain is due totally to the lateral deflection, the expressions for the strains in the x and y directions are as follows:[1]

$$\epsilon_x = (1/2)(\partial w/\partial x)^2, \quad \epsilon_y = (1/2)(\partial w/\partial y)^2 \tag{4}$$

The maximum deflection occurs at the center of the panel—i.e., at

$$x = a/2, \quad y = b/2$$

and is as follows:

$$w_{max} = 0.164P_0a^2/T\{1 + [1/(b^2/a^2)]\} \tag{5}$$

The maximum strain occurs at the middle of the long side,

$$x = 0, \quad y = b/2$$

is in the direction of the short side, and is (for $b/a > 1$)

$$\epsilon_{max} = 0.132b^2[P_0(b/a)/T(b^2/a^2 + 1)]^2 \tag{6}$$

The assumption that the tension is constant gives

$$T = \sigma_u h \tag{7}$$

where h is the thickness of the panel and σ_u is the ultimate stress.

Tests have been conducted by Day,[2, 3] who obtained ultimate loads, strains, and deflections in rectangular panels.

Table 1 gives comparisons between experimental deflections and strains when the panel has reached its ultimate load or failure load; the strain and deflection is calculated by Eqs. (5) and (6) corresponding to this value of the load. Failure occurred when a crack appeared at the middle of the long side of the panel. An earlier paper[4] contains more extensive comparisons

* This work was partially completed when the author was employed at the David Taylor Model Basin in 1956.

TABLE 1
Comparison of Ultimate Deflections and Strains

The ultimate or failure pressure was reached when a crack appeared in the panel. In the cases considered here, the crack always appeared at the middle of the long side of the panel. This is also the location of the theoretical maximum strain.

σ_u	h	b/a	a	P_0	w_e	w_t	ϵ_e	ϵ_t
61,000	0.113	1.55	13.5	920	2.77	2.82		
70,700	0.119	1.55	13.5	950	2.54	2.38	0.17	0.15
41,800	0.134	1.55	13.5	700	2.44	2.64	0.18	0.19
46,100	0.104	1.55	13.5	600	2.76	2.64		
41,800	0.068	1.55	13.5	435	3.12	3.23		
72,300	0.125	1.55	54	226	9.47	8.44	0.10	0.12
65,000	0.182	1.55	54	245	7.06	6.99	0.07	0.08

σ_u = ultimate stress obtained from coupon test (in psi)
h = thickness of panel (in inches)
b/a = length/width
P_0 = pressure at failure (in psi)
w_e = experimental center deflation at failure (in inches)
w_t = theoretical center deflection for the given failure pressure (in inches)
ϵ_e = experimental edge strain at failure (inches/inch)
ϵ_t = theoretical edge strain for the given failure pressure (inches/inch)

and methods for estimation of ultimate loads using the assumptions given in this note.

References

[1] Timoshenko, S., *Theory of Plates and Shells*, 1st Ed., p. 304, McGraw-Hill Book Co., Inc., New York, 1940.

[2] Day, J. W., *Hydrostatic Pressure Tests on Thin Rectangular Diaphragms 21 Inches by 13½ Inches*, David Taylor Model Basin Rpt. 635, March, 1951.

[3] Day, J. W., *Hydrostatic Pressure Tests on Thin Rectangular Diaphragms 84 Inches by 54 Inches*, David Taylor Model Basin Rpt. 636, April, 1951.

[4] Greenspon, J. E., *An Approximation to the Plastic Deformation of a Rectangular Plate Under Static Load with Design Applications*, International Shipbuilding Progress, Vol. 3, No. 22, pp. 329–340, June, 1956.

Thermal Stresses in a Long Circular Shell With Axial Temperature Variation

D. J. Johns
Lecturer, The College of Aeronautics, Cranfield, England

December 1, 1959

Symbols

B	=	$D_B(1 + \nu_B)$
C	=	$\beta R D_c$
d	=	bulkhead thickness
D	=	flexural rigidity $= E_c t^3/12(1 - \nu_c^2)$ for shell
E	=	Young's modulus
F_m	=	temperature function in shell
M_x, M_ϕ	=	bending moments per unit length about ϕ, x axes, respectively
N_x, N_ϕ	=	stress resultants in x and ϕ directions, respectively
Q_x	=	transverse shear per unit length
r	=	radial coordinate in bulkhead
R	=	radius of shell and bulkhead
t	=	thickness of shell
T	=	temperature rise above strainless state
W	=	radial displacement of shell
x	=	longitudinal shell coordinate (For convention, see Fig. 1)
α	=	coefficient of expansion
β	=	$[3(1 - \nu_c^2)/R^2t^2]^{1/4}$
θ	=	rotation
σ	=	stress
ν	=	Poisson's ratio
ϕ	=	angle denoting positions on shell periphery

Subscripts

B	=	bulkhead
C	=	cylindrical Shell
0	=	at edge of long shell—i.e., $x = 0$

Differentiation with respect to coordinate x denoted by prime—e.g., T_c'.

THE STUDY of thermal stresses in thin, circular, cylindrical shells stiffened by various types of frame or bulkhead, etc., is of considerable current interest. In the unstiffened shells, thermal stresses can arise from radial,[1, 2] circumferential,[1, 2] or axial[2, 3] temperature gradients, and discontinuity stresses can also occur at the junction of the shell with any other member having different thermal-expansion properties and/or temperature distributions.[4–8] This latter problem is investigated here, for a long circular shell, edge-supported on a plane, constant-thickness bulkhead. The axial temperature distribution in the shell is of the form

$$T_c = \sum_{m=0}^{3} F_m x^m$$

and, in the bulkhead, any general radial temperature distribution is assumed.

The fact that the shell and bulkhead are attached at $x = 0$ will induce a system of self-equilibrating forces and moments on both components making the resultant deformations compatible. The extent of this compatibility will depend upon whether the shell is simply supported or clamped at its joint with the bulkhead.

If these self-equilibrating force systems are a transverse shear, Q_0, and a bending moment, M_0, (see Fig. 1) acting at $x = 0$ on the shell, the corresponding system acting on the bulkhead must be $-Q_0$ and $-M_0$. The values of shell and bulkhead deflection and rotation which result can be deduced from references 7 or 9.

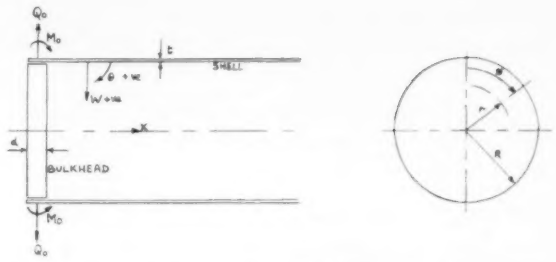

FIG. 1. Semi-infinite shell-bulkhead, showing sign convention.

Clamped Edge Conditions

The total resultant deflections and rotations at $x = 0$ in the shell and $r = R$ in the bulkhead are

$$W_0 = -(1/2\beta^3 D_c)(\beta M_0 + Q_0) + (\alpha_c R/2)\{(T_{c0}'''/\beta^3) + (T_{c0}''/\beta^2) - 2T_{c0}\} \quad (1)$$

$$\theta_0 = (1/2\beta^2 D_c)(2\beta M_0 + Q_0) - (\beta\alpha_c R/2)\{(T_{c0}'''/\beta^3) + (2T_{c0}''/\beta^2) + (2T_{c0}'/\beta)\} \quad (2)$$

$$W_B = [Q_0(1 - \nu_B)R/E_B d] - (2\alpha_B/R)\int_0^R T_B \cdot r \cdot dr \quad (3)$$

$$\theta_B = -M_0 R/D_B(1 + \nu_B) \quad (4)$$

For compatibility of rotations, the result obtained from Eqs. (2) and (4) is

$$M_0 = \frac{(\beta\alpha_c R/2)\{(T_{c0}'''/\beta^3) + (2T_{c0}''/\beta^2) + (2T_{c0}'/\beta)\} - (Q_0/2\beta^2 D_c)}{(1/\beta D_c) + [R/D_B(1 + \nu_B)]} \quad (5)$$

By equating Eqs. (1) and (3), compatibility of deflections is obtained and, together with Eq. (5), yields finally

$$Q_0 = \frac{(2\alpha_B/R)\int_0^R T_B r dr + [\alpha_c R/4(B + C)]\,[(T_{c0}'''/\beta^3)(B + 2C) + (2T_{c0}''/\beta^2)C - (2T_{c0}'/\beta)\cdot B - 4T_{c0}(B + C)]}{\{[(1 - \nu_B)R/E_B d] + (1/4\beta^3 D_c)[(B + 2C)/(B + C)]\}} \quad (6)$$

where

$$B = D_B(1 + \nu_B), \quad C = \beta R D_c$$

From Eqs. (5) and (6), the corresponding stress distributions in both shell and bulkhead may be found.

Simply Supported Edge Conditions

In the foregoing analysis, if $M_0 = 0$ and compatibility of rotations is ignored, Eqs. (1) and (3) yield the result for compatibility of deflections—i.e.

$$Q_0 = \frac{(2\alpha_B/R)\int_0^R T_B r dr + (\alpha_c R/2)\{(T_{c0}'''/\beta^3) + (T_{c0}''/\beta^2) - 2T_{c0}\}}{\{[(1 - \nu_B)R/E_B d] + (1/2\beta^3 D_c)\}} \quad (7)$$

Thermal Stresses in Bulkhead

The stress distribution in a plane circular bulkhead subjected to an arbitrary axisymmetric temperature distribution is given

by reference 1 and also presented in reference 7. In addition to these stresses, there is a uniform stress field caused by the transverse shear Q_0 and a bending stress distribution due to M_0.

Thermal Stresses in Cylindrical Shell

The expression for the resultant shell deflection mode is

$$W = (\alpha_c R/2)\{e^{-\beta x}\{[(T_{c0}'''/\beta^3) + (T_{c0}''/\beta^2)]\cos\beta x - (T_{c0}''/\beta^2)\sin\beta x\} - 2T_c\} + (e^{-\beta x}/2\beta^3 D_c)[\beta M_0(\sin\beta x - \cos\beta x) - Q_0\cos\beta x] \quad (8)$$

The various functions of x in Eq. (8) are tabulated in reference 9, p. 394.

From Eq. (8), the expressions for the various stress couples and stress resultants in the shell may be obtained.

$$N_x = 0 \quad (9)$$

$$N_\phi = (E_c t\alpha_c e^{-\beta x}/2)\{[(T_{c0}'''/\beta^3) + (T_{c0}''/\beta^2)]\cos\beta x - (T_{c0}''/\beta^2)\sin\beta x\} - 2\beta R e^{-\beta x} \times [\beta M_0(\sin\beta x - \cos\beta x) - Q_0\cos\beta x] \quad (10)$$

$$Q_x = -e^{-\beta x}[2\beta M_0\sin\beta x - Q_0(\cos\beta x - \sin\beta x)] - (E_c\alpha_c t/4\beta R)\{e^{-\beta x}\{\cos\beta x(T_{c0}'''/\beta^3) - \sin\beta x[(T_{c0}'''/\beta^3) + 2(T_{c0}''/\beta^2)]\} - (T_c'''/\beta^3)\} \quad (11)$$

$$M_x = (e^{-\beta x}/\beta)[\beta M_0(\cos\beta x + \sin\beta x) + Q_0\sin\beta x] - (E_c\alpha_c t/4\beta^2 R)\{e^{-\beta x}\{\cos\beta x(T_{c0}''/\beta^2) + \sin\beta x[(T_{c0}'''/\beta^3) + (T_{c0}''/\beta^2)]\} - (T_c''/\beta^2)\} \quad (12)$$

$$M_\phi = \nu_c M_x \quad (13)$$

These results will now be applied to a simple example.

Consider the case of a constant axial temperature distribution in the shell and zero temperature rise in the bulkhead—i.e.,

$$T_c = \text{const.}$$
$$T_B = 0$$

Clamped Edge Conditions

Using Eq. (6),

$$Q_0 = -\alpha_c R T_c\{[R(1 - \nu_B)/E_B d] + (1/4\beta^3 D_c)[(B + 2C)/(B + C)]\}^{-1} \quad (14)$$

and from Eq. (5),

$$M_0 = (-Q_0/2\beta)[B/(B + C)] \quad (15)$$

Therefore, the maximum (tensile) stress in the bulkhead is given by

$$\sigma_B = -(Q_0/d) + (6M_0/d^2) = (-Q_0/d)\{1 + (3/\beta d)[B/(B + C)]\} \quad (16)$$

and in the shell the maximum bending stress at the joint is

$$\sigma_0 = |6M_0/t^2| = (3Q_0/\beta t^2)[B/(B + C)] \quad (17)$$

Simply Supported Edge Conditions

Using Eq. (7),

$$Q_0 = -\alpha_c R T_c\{[R(1 - \nu_B)/E_B d] + (1/2\beta^3 D_c)\}^{-1} \quad (18)$$

and the maximum (uniform, tensile) stress in the bulkhead is

$$\sigma_B = -Q_0/d \quad (19)$$

Similarly, the maximum bending stress in the shell occurs at a distance $\beta x = \pi/4$ (reference 9, p. 394) when

$$M_x = +0.323(Q_0/\beta)$$

and the maximum stress is

$$\sigma = |1.9380 Q_0/\beta t^2| \quad (20)$$

Comparing the pairs of Eqs. (14) and (18), (16) and (19), (17) and (20), it is seen that much smaller stresses result from simply supported edge conditions. A similar conclusion should result from any more general analysis.

References

[1] Goodier, H. N., *Thermal Stress and Deformation*, J. Appl. Mech., Vol. 24, No. 3, pp. 467–474, September, 1957.

[2] Kent, C. H., *Thermal Stresses in Thin Walled Cylinders*, ASME Trans., Vol. 53, pp. 167–180, 1931.

[3] den Hartog, J. P., *Temperature Stresses in Flat Rectangular Plates and in Thin Cylindrical Tubes*, J. Franklin Inst., Vol. 222, p. 149, 1936.

[4] Przemieniecki, J. S., *Transient Temperature Distributions and Thermal Stresses in Fuselage Shells with Bulkheads or Frames*, J. RAeS., Vol. 60, pp. 799–804, December, 1956.

[5] Johns, D. J., *Thermal Stress Distributions in Cylindrical Shells Stiffened by Bulkheads or Frames for Arbitrary Temperature Distributions*, College of Aeronautics Note, No. 83, 1958.

[6] Johns, D. J., *Thermal Stress in Short Uniform Cylindrical Shells*, Engineering Materials and Design, Vol. 2, p. 167, March, 1959.

[7] Johns, D. J., *Discontinuity Stresses in Stiffened Cylindrical Shells*, Aircraft Eng., Vol. 31, No. 363, pp. 131–132, May, 1959.

[8] Houghton, D. S., and Chan, A. S. L., *Discontinuity Stresses at the Junction of a Pressurised Spherical Shell and a Cylinder*, College of Aeronautics Note, No. 80, 1958.

[9] Timoshenko, S., *Theory of Plates and Shells*, McGraw-Hill Book Co., Inc., 1st Ed. 1940.

The Approximate Solution of the Equations of Motion of an Airplane Moving in a Vertical Plane*

E. F. Trombley

Applied Mathematics Engineer, General Engineering Laboratory, General Electric Co., Schenectady, N.Y.

September 21, 1959

Summary

An approximate solution for equations of motion of an airplane moving in a given vertical plane is found for climb at constant Mach Number and acceleration at altitude. The designer should find that these approximations conform to the requirements of a quick and accurate design technique.

(1) Introduction

Once the equations of motion are stated, the main problem is to find (*i*) the approximate solution of these equations for a constant Mach Number climb in the variable-temperature region. An immediate consequence of the approximate solution of (*i*) is an approximate solution of (*ii*), a constant Mach number climb in the constant-temperature region, and (*iii*), acceleration in a straight line at constant altitude.

The weight of W of the airplane is considered as a point mass concentrated at the c.g., which moves along a path Γ in a given vertical plane x, h, where x is distance and h is altitude. The external forces are thrust T, lift L, and drag D. The lift is always normal to the path, and the thrust and drag are always tangent to the path. The forces L, T, and D, as well as the specific fuel consumption S, are assumed to be given (in tabular form) as functions of Mach Number and altitude. The use of equilibrium conditions gives the tangential acceleration as

$$dV/dt = g\{[(T - D)/W] - \sin\theta\} \quad (1)$$

and the normal acceleration as

$$V(d\theta/dt) = g[(L/W) - \cos\theta] \quad (2)$$

where θ is the angle that the tangent to Γ makes with the positive x-axis.

The equation for the change of weight due to fuel consumption is

$$dW/dt = -TS \quad (3)$$

The approximate method given here is adequate for the requirements of the designer. An exact solution is not to be expected, since T, L, and D are assumed to be given as experimental data and not in analytical form.

* The preparation of this note was aided by the friendly interest and criticism of Professor M. M. Stanišić.

(2) Solution of Problem (*i*)

From $V = Ma$ (M is Mach number, and a is velocity of sound), it follows that

$$dV/dt = M^2aa' \sin\theta (a' = (da/dh) \neq 0) \quad (4)$$

The application of Eq. (4) to Eq. (1) gives

$$\sin\theta = [1/(1+K)][(T-D)/W] \quad (5)$$

where

$$K = M^2aa'/g$$

From

$$dh/dt = Ma\sin\theta$$

it follows that Eq. (5) is the same as

$$dh/dt = [Ma/(1+K)][(T-D)/W] \quad (6)$$

In the constant-temperature region, $a' = 0$, so the solution of (*ii*) can be obtained from (*i*) by replacing K by 0 in (*i*).

The boundary conditions are

$$\begin{aligned} h &= h_1 \rightarrow t = t_1 = 0 \\ h &= h_2 (h_2 > h_1) \text{ (end of climb)} \\ M &= \text{const.} \end{aligned} \quad (7)$$

Eq. (6) is approximated by

$$dh/dt = (1/2)\{[Ma_1/(1+K_1)][(T_1-D_1)/W_1] + [Ma_2/(1+K_2)][(T_2-D_2)/W_2]\} \quad (8)$$

where the right-hand side of Eq. (8) is the average of the right-hand side of Eq. (6) at h_1 and h_2. Here, 1 and 2 refer to conditions at h_1 and h_2, respectively. Given $\Delta t = t_2 - t_1$ and W_2, the solution of Eq. (8) is

$$\Delta h = (1/2)\{[Ma_1/(1+K_1)][(T_1-D_1)/W_1] + [Ma_2/(1+K_2)][(T_2-D_2)/W_2]\}\Delta t \quad (9)$$

where $\Delta h = h_2 - h_1$.

By setting

$$A = (1/2)(T_1S_1 + T_2S_2) \quad (10)$$

Eq. (3) becomes

$$dW/dt = -A$$

or

$$W_2 - W_1 = -A\Delta t \quad (11)$$

if the approximating technique used on Eq. (1) is also used on Eq. (3). The use of Eq. (11) in Eq. (9), along with some algebraic reductions, results in

$$(W_2/W_1)^2 - \{[(C_1-\Delta h)/C_1] - (C_2/C_1)\}(W_2/W_1) - (C_2/C_1) = 0 \quad (12)$$

where

$$C_i = (1/2A)[Ma_i/(1+K_i)](T_i - D_i)(i = 1, 2)$$

and

$$K_i = M^2a_i'a_i/g$$

The solution of Eq. (12) for W_2 is

$$W_2 = (W_1/2)\left([(C_1-\Delta h)/C_1] - (C_2/C_1) + \sqrt{\{[(C_1-\Delta h)/C_1] - (C_2/C_1)\}^2 + 4(C_2/C_1)}\right) \quad (13)$$

For Δh, small in comparison with C_1, Eq. (13) reduces to $W_2 \approx W_1$.

The horizontal distance traveled while climbing from h_1 to h_2 is obtained by approximating

$$du/dt = g\{[(T-D)/W]\cos\theta - (L/W)\sin\theta\} \quad (14)$$

where $u = V\cos\theta$, by

$$du/dt = (g/2)\{[(T_1-D_1)/W_1]\cos\theta_1 - (L_1/W_1)\sin\theta_1 + [(T_2-D_2)/W_2]\cos\theta_2 - (L_2/W_2)\sin\theta_2\} \quad (15)$$

Let Z equal the right-hand side of Eq. (15). The result of integrating Eq. (17) is

$$u_2 = Z\Delta t + u_1$$

or

$$\Delta u = u_2 - u_1 = Z\Delta t \quad (16)$$

Since $u = dx/dt$, the integration of Eq. (16) gives

$$x_2 = (1/2)Z(\Delta t)^2 + x_1$$

or

$$\Delta\psi = \psi_2 - \psi_1 = (1/2)Z(\Delta t)^2 \quad (17)$$

where $\Delta\psi$ is the distance traveled during the time increment extending for t_1 to t_2. In the above x_1, u_1 and x_2, u_2 are the total distance traveled and the horizontal velocity at times t_1 and t_2, respectively.

(3) The Solution of Problem (*ii*) and Problem (*iii*)

It has been mentioned that, if $K_1 = K_2 = 0$ and $a_2 = a_1 = a$ in problem (*i*), the solution of problem (*ii*) is obtained.

The same techniques applied to problem (*iii*) lead to the equation

$$(W_2/W_1)^2 - \{[(C_1 - \Delta M)/C_1] - (C_2/C_1)\}(W_2/W_1) - (C_2/C_1) = 0 \quad (18)$$

where

$$C_i = (1/2aA)(T_i - D_i)(i = 1, 2) \quad (19)$$

and

$$\Delta M = M_2 - M_1 \quad (20)$$

The boundary conditions are

$$\begin{aligned} t = t_1 = 0 &\rightarrow M = M_1 \\ M &= M_2 \text{ (end of acceleration)} \end{aligned} \quad (21)$$

(4) The Role of Eq. (2)

In problem (*iii*), Eq. (2) reduces to $L = W$. In problems (*i*) and (*ii*), Eq. (3) can be written as

$$d\theta/dt = (g/M)(L/aW)\{(\cos\theta)/a\} \quad (22)$$

or, by the approximating equation,

$$(d\theta/dt) - (g/M)(L/aW) = -(g/2M)\{(\cos\theta_1)/a_1 + (\cos\theta_2)/a_2\} \quad (23)$$

The integration of Eq. (23) yields

$$\Delta\theta = (g/M)\int_0^{\Delta t}(L/aW)d\tau - (g/2M)\{(\cos\theta_1)/a_1 + (\cos\theta_2)/a_2\}\Delta t + \text{const.} \quad (24)$$

where

$$\Delta\theta = \theta_2 - \theta_1$$

Clearly,

$$\Delta\theta = (g/M)\int_0^{\Delta t}(L/aW)dz - (g/2M)\{(\cos\theta_1)/a_1 + (\cos\theta_2)/a_2\} \quad (25)$$

since $\Delta t = 0$ in Eq. (24) yields

$$0 = \text{constant} \quad (26)$$

Thus, in problems (*i*) and (*ii*), Eq. (2) requires that L/aW be a function of t, say $f(t)$, such that Eq. (25) is satisfied, and

$$f(0) = L_1/a_1W_1, \quad f(\Delta t) = L_2/a_2W_2 \quad (27)$$

If $f(t)$ exists, it merely makes the approximating equations compatible; it does not give any additional information because the solution for $t = 0$ and $t = \Delta t$ is required and not the solution for $0 < t < \Delta t$.

(5) Application

For a constant Mach Number climb from an altitude H_1 to an altitude H_2, where $H_1 - H_2$ is large, Δh is chosen such that $H_2 = H_1 + n\Delta h$ (n integer) and such that the above approxi-

mations apply to

$$h_1 = H_1 + m\Delta h$$
$$h_2 = H_1 + (m+1)\Delta h \; (m = 0, 1, \ldots, n-1)$$

The result of proceeding from H_1 to H_2 in steps of Δh gives the required approximate solution for the altitudes H_1 and H_2. The same device is used in problem (*iii*).

A Further Extension of the Routh-Hurwitz Stability Criteria for Quintic and Sextic Equations

Herbert Saunders
Engineer,, Missile and Space Vehicle Department, General Electric Company, Philadelphia, Pa.
February 5, 1960

THIS NOTE is concerned mainly with the necessary and sufficient conditions for stability of linear quintic and sextic equations. Routh[1] presented the first stability criteria in a form requiring a specialized tabulation procedure. Hurwitz[2] simplified Routh's method by employing test determinants. The characteristic equation of the linear system may be represented as

$$f(x) = a_n x^n + a_{n-1}x^{n-1} + \ldots + a_1 x + a_0 = 0 \qquad (1)$$

where $a_0, a_1 \ldots a_n$ are known real constants and a_n is positive. Then the Hurwitz test functions may be expressed in the form

$$T_n = \begin{vmatrix} a_{n-1} & a_{n-3} & a_{n-5} & \cdots \\ a_n & a_{n-2} & a_{n-4} & \cdots \\ 0 & a_{n-1} & a_{n-3} & \cdots \\ 0 & a_n & a_{n-2} & \cdots \\ 0 & 0 & a_{n-1} & \cdots \\ 0 & 0 & a_n & \cdots \\ \cdots & \cdots & \cdots & \cdots \\ \cdots & \cdots & \cdots & \cdots \end{vmatrix} \qquad (2)$$

Recently, Duncan[3, 4] applied these test functions to the sextic and octic equations in determining their stability.

It is immediately apparent that after reducing the complexity of the stability problem, there still remains a tedious amount of necessary work in solving higher order equations. In a further effort at simplification, Higgins and Hogan[5] employ the Hurwitz determinants in conjunction with algebraic manipulation to reduce the necessary number of parameters for a quintic equation to four. Even then, an innumerable number of graphs must be plotted in order to determine the stability of the quintic equations. Duncan[6] derived simple relations between certain expressed polynomials and determinantal forms and tended to further minimize the number of effective parameters.

Since there are no general parameters which hold for all degrees of polynomials, the stability determination becomes more difficult as the power of the polynomial increases. In Eq. (1), let

$$x = (a_0/a_{n-1})^{1/n-1}\, s$$

divide by a_0, and then simplify

$$f(s) = (a_n/a_0)(a_0/a_{n-1})^{n/n-1}s^n + s^{n-1} + \ldots + (a_1/a_0)(a_0/a_{n-1})s + 1 = 0 \qquad (3)$$

$$= A_n s^n + A_{n-1}s^{n-1} + \ldots + A_1 s + A_0 = 0 \qquad (4)$$

For the quintic equation, we establish from Eqs. (3) and (4) the following relations for $A_5 \ldots A_0$

$$\left.\begin{aligned} A_5 &= (a_5/a_0)(a_0/a_4)^{5/4} & A_2 &= (a_2/a_0)(a_0/a_4)^{1/2} \\ A_3 &= (a_3/a_0)(a_0/a_4)^{3/4} & A_1 &= (a_1/a_0)(a_0/a_4)^{1/4} \\ & & A_4 &= A_0 = 1 \end{aligned}\right\} \qquad (5)$$

Following a similar procedure as outlined by Duncan,[6] a polynomial $F(s)$ is derived from $f(s)$ and an additional polynomial $g(s)$; i.e., $F(s) = f(s) + g(s)$.

The related polymonial is

$$g(s) = (A_4 s^4 + A_2 s^2 + A_0)(bs) \qquad (6)$$

Combining Eq. (4) for the quintic and Eq. (5),

$$F(s) = P_5 s^5 + P_4 s^4 + P_3 s^3 + P_2 s^2 + P_1 s + P_0 \qquad (7)$$

where

$$P_5 = A_5 + A_4 b, \quad P_4 = P_0 = 1,$$
$$P_3 = A_3 + A_2 b, \quad P_2 = A_2, \quad P_1 = A_1 + A_0 b$$

Selecting b arbitrarily—i.e., $P_5 = 0$—then

$$P_5 = 0, \quad P_4 = P_0 = A_4 = A_0 = 1,$$
$$P_3 = A_3 - A_2 A_5, \quad P_2 = A_2, \quad P_1 = A_1 - A_5$$

The effective test function of $F(s)$ is

$$T_4' = \begin{vmatrix} P_4 & P_2 & P_0 & 0 \\ P_5 & P_3 & P_1 & 0 \\ 0 & P_4 & P_2 & P_0 \\ 0 & P_5 & P_3 & P_1 \end{vmatrix} > 0 \qquad (8a)$$

Substituting the equivalence for $P_1 \ldots P_5$ and simplifying, it can be shown that $T_4 = T_4'$. Expanding Eq. (8a) for stability

$$T_4' = P_1 P_3 (P_2 - 2) - (P_3 - P_1)^2 > 0 \qquad (8b)$$

A necessary condition of stability follows from Eq. (8b)—i.e., $P_2 > 2$

$$a_2 > 2/(a_0 a_4)^{1/2} \qquad (8c)$$

Eq. (8b) can be simplified to

$$P_2 - (P_1/P_3) - (P_3/P_1) > 0 \qquad (8d)$$

Substituting $l = P_1/P_3$ and $m = P_2$, Eq. (8d) simplifies for stability to

$$m > l + (1/l)$$

where

$$\left.\begin{aligned} l &= [\, a_1 - (a_5 a_0/a_4)]/(a_0/a_4)^{1/2}[a_3 - (a_2 a_5/a_4)\,] \\ m &= a_2/(a_0 a_4)^{1/2} \end{aligned}\right\}$$

The necessary and sufficient conditions for the quintic characteristic equation to be stable are that $T_2' > 0$, $a_5 > 0$, $a_4 > 0$, $a_2 > 0$, $a_0 > 0$ plus a_5 and a_4 be of the same sign.[7]

As discussed by Higgins and Hogan,[5] their procedure necessitates interpolations between the various plots. The H-H method is both time consuming and not as accurate as this note's procedure. This is exemplified by their problem number 3 for the neutral stability.

In a similar fashion, the stability of the sextic equation may be obtained from Eqs. (3) and (4) with the following relations for $A_6 \ldots A_0$:

$$\left.\begin{aligned} A_6 &= (a_6/a_0)(a_0/a_5)^{6/5}, & A_2 &= (a_2/a_0)(a_0/a_5)^{2/5} \\ A_4 &= (a_4/a_0)(a_0/a_5)^{4/5}, & A_1 &= (a_1/a_0)(a_0/a_5)^{1/5} \\ A_3 &= (a_3/a_0)(a_0/a_5)^{3/5}, & A_5 &= A_0 = 1 \end{aligned}\right\} \qquad (9)$$

The related polynomial for the sextic

$$g(s) = (A_5 s^4 + A_3 s^2 + A_1)(bs^2 + c) \qquad (10)$$

Combining Eq. (4) for $n = 6$ and Eq. (10),

$$F(s) = P_6 s^6 + P_5 s^5 + P_4 s^4 + P_3 s^3 + P_2 s^2 + P_1 s + P_0 \qquad (11)$$

where

$$P_6 = A_6 + A_5 b, \quad P_5 = A_5 = P_1 = A_1 = 1,$$
$$P_4 = A_4 + A_3 b + A_1 c$$
$$P_3 = A_3, \quad P_2 = A_2 + A_1 b + A_3 c, \quad P_0 = A_0 + A_1 c$$

Since b and c are chosen arbitrarily, assume $P_6 = P_0 = 0$. Substituting into the effective test function,

$$T_5' = \begin{vmatrix} P_5 & P_6 & 0 & 0 & 0 \\ P_3 & P_4 & P_5 & P_6 & 0 \\ P_1 & P_2 & P_3 & P_4 & P_5 \\ 0 & P_0 & P_1 & P_2 & P_3 \\ 0 & 0 & 0 & P_0 & P_1 \end{vmatrix} > 0 \qquad (12)$$

After simplification, this reduces to

$$P_5P_1[P_4(P_2P_3 - P_1P_4) - P_2^2] = P_5P_1[P_2(P_3P_4 - P_2) - P_1P_4^2] > 0 \quad (13)$$

From Eq. (13), a necessary condition for stability is

$$P_3P_4 > P_2 \quad (14a)$$

Substituting the equivalence for P_2, P_3, and P_4 and simplifying,

$$\therefore 1 + (a_0/a_4)(a_1/a_3) > (a_6/a_4)(a_2/a_5) + (a_2/a_4)(a_6/a_3) \quad (14b)$$

Rearranging Eq. (13) and dividing by $P_1P_4^2$ and simplifying,

$$(P_2/P_4)(P_3/P_1) - (P_2/P_4)^2(1/P_1) > 1 \quad (15a)$$

or

$$q - pq > 1 \quad (15b)$$

where

$$q = P_2P_3/P_1P_4 \quad p = P_2/P_3P_4 \quad (15c)$$

Substituting equivalent values for P_1, P_2, P_3, P_4 and simplifying,

$$q = \frac{(a_2a_5 - a_1a_6) - (a_0a_3a_5/a_1)}{(a_4a_5 - a_3a_6)(a_1/a_3) - (a_0a_5^2/a_3)} \quad (15d)$$

$$p = \frac{(a_2a_5 - a_1a_6) - (a_0a_3a_5/a_1)}{(a_4a_5 - a_3a_6) - (a_0a_3a_5/a_1)} \quad (15e)$$

The necessary and sufficient conditions for the sextic characteristic equation to be stable are T_5', T_3', a_5, a_3, a_1, and a_0 must all be positive where a_6 is considered positive.[7]

It is apparent that an additional necessary condition for stability is that both numerator and denominator of Eqs. (15d) and (15c) be positive. This method may be applied to equations of higher order than the sextic, but it becomes unwieldy and tedious. This has been similarly noticed by Fuller.[7]

References

[1] Routh, E. J., *Dynamics of a System of Rigid Bodies*, Chap. 6, Part II, Dover Publications, New York, 1955.

[2] Hurwitz, A., *On the Condition for Which an Equation Possesses Roots With Negative Real Parts* (in German), Math. Annal. Vol. 46, 1895.

[3] Duncan, W. J., *Stability Criteria with Specicl Reference to the Sextic Equation*, J. RAeS., September, 1954.

[4] Duncan, W. J., *Stability Criteria for the Octic Equation*, J. RAeS., September, 1954.

[5] Hogan, H. A., and Higgins, T. J., *Stability Boundaries for Fifth-Order Servo Mechanisms*, Proc. Nat'l. Electronics Conf., Vol. 11, 1955.

[6] Duncan, W. J., *Note on Test Functions for Stability*, Quart. J. Mech. & Appl. Math., pp. 30–37, March, 1955.

[7] Fuller, A. T., *Stability Criteria for Linear Systems and Realizability Criteria for R C Networks*, Proc. Camb. Phil. Soc., Vol. 53, Part 4, pp. 78–96, 1957.

Minor Circle Flight at Large Angles of Inclination

W. H. T. Loh*
Senior Post Doctoral Fellow, National Science Foundation, Mathematics Department, Manchester University, Manchester, England

September 3, 1959

Symbols

a = const. = $(L/D)(1/2)(C_DA/m)(\sin\lambda_0/\beta)$

b = const. = $\dfrac{\cos\lambda_0}{(L/D)(1/2)(C_DA/m)R_0\sin^2\lambda_0}$

n = const. = $\sin^2\lambda_0$

n' = const. = $1/(1-b)$, for λ_0 close to $\pi/2$, $n' \cong 1$

C = const. = $\cos\theta_f - a\{b\tan^{-1}[\sqrt{(\rho_f/b)^2 - 1}] - \sqrt{\rho_f^2 - b^2}\}$

C' = const. = $\cos\theta_f + a(1-b)\rho_f$

C_1 = const. = $2(D/L)n'$

C_2 = const. = $(\beta/\sin^2\lambda_0)[\cos\theta_f + (a/n')\rho_f] \cong \beta/\sin^2\lambda_0$

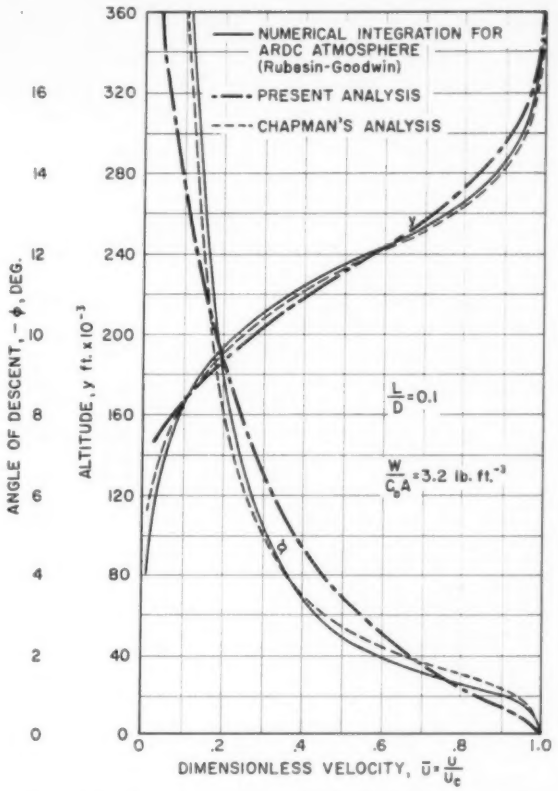

FIG. 1. Angle of descent and altitude-velocity trajectory. Comparison of present approximate analysis with more exact machine calculations for ARDC model atmosphere.

C_3' = const. = $\beta\cos\theta_f + a\beta\rho_f(1-b)$

C_4 = const. = $n'/a\rho_0$

C_5 = const. = $(1/4)C_F'SV_f^2e^{C_1\theta_f}[\rho_f + C_4\rho_0\cos\theta_f]$

C_6 = const. = $(1/4)C_F'SC_4\rho_0V_f^2e^{C_1\theta_f}$

C_7 = const. = $(1/n'\sin\lambda_0)(1/V_f)$

C_8 = const. = $(1/4)C_F'(\rho_f + C_4\rho_0\cos\theta_f)V_f^3$

C_9 = const. = $(1/4)C_F'C_4\rho_0V_f^3$

C_{10} = const. = $\rho_f + C_4\rho_0\cos\theta_f$

C_{11} = const. = $C_4\rho_0$

C_{12} = const. = $K'\sigma^{-(1/2)}V_f^3$ or $6.8\times10^{-6}\sigma^{-(1/2)}V_f^3$

C_{13} = const. = $(4g/\beta V_f^2)n$

C_{14} = const. = $1 - (4g/\beta V_f^2)nF_1(\theta_f)$

C_{15} = const. = $\dfrac{1}{2}\left\{\dfrac{(1+E)(C_1^2+3^2) - 6E}{(C_1^2+1)(C_1^2+3^2)}\right\} \cong \dfrac{1}{C_1^2+1} - \dfrac{3}{C_1^2+3^2}\times\dfrac{1}{C_1^2+1}$

E = const. = $(\beta/C_3\sin^2\lambda_0)^2 \cong 1$

C_{16} = const. = $(1/2)\sqrt{E}\,[1/(C_1^2+2^2)] \cong (1/2)[1/(C_1^2+2^2)]$

C_{17} = const. = $(1/2)E[1/(C_1^2+3^2)] \cong (1/2)[1/(C_1^2+3^2)]$

$F_1(\theta) \cong (\beta/C_3\sin^2\lambda_0)\{C_{15}[C_1\sin\theta - \cos\theta] + C_{16}[(C_1/2)\times\sin 2\theta - \cos 2\theta] - C_{17}\sin^2\theta(C_1\sin\theta - 3\cos\theta)\}$, preferable to use when θ is large

$F_1(\theta) \cong [\ln(\theta/2) + (C_1\theta) + (1/4)(C_1\theta)^2 + (1/18)(C_1\theta)^3]e^{-C_1\theta} - \{[(C_1\theta)^3/720C_1^4] - [(C_1\theta)^2/240C_1^4] + [(1/120C_1^4) + (1/12C_1^2)](C_1\theta) - [(1/120C_1^4) + (1/12C_1^2)]\}$, preferable to use when θ is small

Subscript

f = condition at end of power boost or condition at the beginning of unpowered glide

* On one year's leave of absence from Chance Vought Aircraft, Dallas, Tex.

HYPERSONIC gliders may take off either from earth by rocket boost or from satellite orbits by rocket control. These gliders may fly along a great circle path or along a minor circle path. Solutions for great circle path at all angles of inclination were recently obtained,[1, 4, 5] as were solutions for minor circle path at small angles of inclination.[2, 3] At large angles of inclination, no analytical approximate solutions have been given yet.

Using symbols and assumptions of references 1–5, one obtains the approximate differential equation for minor circle flight at large angles of inclination as:

$$(dV^2/ds) + [2g/(L/D)]\sqrt{\cos^2\lambda_c + \{\sin\lambda_0\cos\theta[1 - (V^2/gR_0\sin^2\lambda_0)] + (V^2/g)(d\theta/ds)\}^2} - 2g\sin\lambda_0\sin\theta = 0$$

$$\sin\alpha \cong \frac{\sin\lambda_0\cos\theta[1 - (V^2/gR_0\sin^2\lambda_0) + (V^2/g)(1/\sin\lambda_0\cos\theta)(d\theta/ds)]}{\sqrt{\cos^2\lambda_0 + \sin^2\lambda_0\cos^2\theta[1 - (V^2/gR_0\sin^2\lambda_0) + (V^2/g)(1/\sin\lambda_0\cos\theta)(d\theta/ds)]^2}}$$

For high-speed re-entry, use may be made of an assumption that, at large angles of inclination, the term

$$\cos\theta[1 - (V^2/gR_0\sin^2\lambda_0)]$$

is relatively small and, consequently, may be neglected. The justification of this assumption is based on the following:

(1) At initial phase of re-entry, the velocity V is close to circular orbital velocity, so that

$$[1 - (V^2/gR_0\sin^2\lambda_0)] \cong 0$$

(provided λ_0 is close to $\pi/2$, which is the case of our major interest).

(2) At terminal phase of re-entry, the angle of inclination θ is close to $\pi/2$, so that

$$\cos\theta \cong \cos(\pi/2) = 0$$

(3) During the middle portion of re-entry,

$$\cos\theta[1 - (V^2/gR_0\sin^2\lambda_c)]$$

remains small because of the offsetting effects of $\cos\theta$ and

$$[1 - (V^2/gR_0\sin^2\lambda_0)]$$

Based on this assumption, the following solutions may be obtained approximately for minor circle flight at large angles of inclination, in a similar manner as those presented in reference 1 and 4 for great circle flight at small and large angles of inclination:

(a) Flight velocity:

$$V^2 = V_f^2[C_{13}F_1(\theta) + C_{14}e^{C_1(\theta_f - \theta)}]$$

(b) Flight altitude and altitude density:

$$y = -(1/\beta)\ln[e^{-\beta y_f} + C_4(\cos\theta_f - \cos\theta)]$$

$$\rho \cong (C' - \cos\theta)/[a(1 - b)]$$

$$\sqrt{(\rho/b)^2 - 1} - \tan^{-1}\sqrt{(\rho/b)^2 - 1} = (C - \cos\theta)/ab$$

(c) Flight distance along flight path:

when

$$C_3^2 > (\beta/\sin^2\lambda_0)^2$$

$$s = \frac{2(1-b)}{\sin\lambda_0\sqrt{C_3^2 - (\beta/\sin^2\lambda_0)^2}} \times \left[\tan^{-1}\sqrt{\frac{C_3 + (\beta/\sin^2\lambda_0)}{C_3 - (\beta/\sin^2\lambda_0)}}\tan\left(\frac{\theta}{2}\right) - \tan^{-1}\sqrt{\frac{C_3 + (\beta/\sin^2\lambda_0)}{C_3 - (\beta/\sin^2\lambda_0)}}\tan\left(\frac{\theta_f}{2}\right)\right]$$

when

$$C_3^2 < (\beta/\sin^2\lambda_0)^2$$

$$s = \frac{(1-b)}{\sin\lambda_0\sqrt{(\beta/\sin^2\lambda_0)^2 - C_3^2}} \times \ln\left\{\left[\frac{C_3\cos\theta + \sqrt{(\beta/\sin^2\lambda_0)^2 - C_3^2}\sin\theta - (\beta/\sin^2\lambda_0)}{C_3\cos\theta_f + \sqrt{(\beta/\sin^2\lambda_0)^2 - C_3^2}\sin\theta_f - (\beta/\sin^2\lambda_0)}\right] \times \left[\frac{C_3 - (\beta/\sin^2\lambda_0)\cos\theta_f}{C_3 - (\beta/\sin^2\lambda_0)\cos\theta}\right]\right\}$$

(d) Flight range:

$$R = (C_3\sin^2\lambda_0/\beta)s - [(1-b)\sin\lambda_0/\beta](\theta - \theta_f)$$

(e) Flight deceleration and maximum deceleration:

$$dV/dt = -(V_f^2/2)[C_2(\rho_f/\rho_0) + (\beta C_1/\sin\lambda_0)(\cos\theta_f - \cos\theta)] \times [C_{13}F_1(\theta) + C_{14}e^{C_1(\theta_f - \theta)}] + g\sin\lambda_0\sin\theta$$

$$(dV/dt)_{max} \overset{*}{\cong} -(V_f^2/2)[C_2(\rho_f/\rho_0) + (\beta C_1/\sin\lambda_0)(\cos\theta_f - \cos\theta_1)]e^{C_1(\theta_f - \theta_1)}$$

$$\theta_1 = \theta_{(dV/dt)_{max}} \overset{*}{\cong} \cos^{-1}\left\{\frac{C_1^2C_3' - \sqrt{C_1^2(\beta^2 - C_3'^2) + \beta^2}}{\beta(C_1^2 + 1)}\right\}$$

(f) Time rate and maximum time rate of average heat input per unit area:

$$dH_{av}/dt = (C_8 - C_9\cos\theta)[C_{13}F_1(\theta) + C_{14}e^{C_1(\theta_f - \theta)}]^{3/2}$$

$$(dH_{av}/dt)_{max} \overset{*}{\cong} (C_8 - C_9\cos\theta_2)e^{(3/2)C_1(\theta_f - \theta_2)}$$

$$\theta_2 = \theta_{(dH_{av}/dt)_{max}} \overset{*}{\cong} \cos^{-1}\left\{\frac{C_1^2C_3' - (2/3)\sqrt{C_1^2(\beta^2 - C_3'^2) + [(2/3)\beta]^2}}{\beta[C_1^2 + (2/3)^2]}\right\}$$

(g) Time rate and maximum time rate of local stagnation region heat input per unit area:

$$dH_s/dt = C_{12}(C_{10} - C_{11}\cos\theta)^{1/2}[C_{13}F_1(\theta) + C_{14}e^{C_1(\theta_f - \theta)}]^{3/2}$$

$$(dH_s/dt)_{max} \overset{*}{\cong} C_{12}(C_{10} - C_{11}\cos\theta_3)^{1/2}e^{(3/2)C_1(\theta_f - \theta_3)}$$

$$\theta_3 = \theta_{(dH_s/dt)_{max}} \overset{*}{\cong} \cos^{-1}\left\{\frac{C_1^2C_3' - (1/3)\sqrt{C_1^2(\beta^2 - C_3'^2) + [(1/3)\beta]^2}}{\beta[C_1^2 + (1/3)^2]}\right\}$$

(h) Total aerodynamic heat input to the vehicle from the beginning to the point concerned:

$$Q \overset{*}{\cong} \left(\frac{1-b}{\sin\lambda_0}\right)\int_{\theta_f}^{\theta}\frac{C_5 - C_6\cos\theta}{C_3 - (\beta/\sin^2\lambda_0)\cos\theta}e^{-C_1(\theta - \theta_f)}\,d\theta$$

$$Q \overset{*}{\cong} \frac{C_5(1-b)\sin\lambda_0}{\beta C_1}(1 - e^{-C_1\theta}), \qquad \text{for } \theta_f \cong 0, \quad \rho_f \cong 0$$

(i) Flight time:

$$t = \int(ds/V) = C_7\int_{\theta_f}^{\theta}[C_{13}F_1(\theta) + C_{14}e^{-C_1(\theta - \theta_f)}]^{-(1/2)} \times \frac{d\theta}{C_3 - (\beta/\sin^2\lambda_0)\cos\theta} \overset{*}{\cong} C_7\int_{\theta_f}^{\theta}\frac{e^{(C_1/2)(\theta - \theta_f)}\,d\theta}{C_3 - (\beta/\sin^2\lambda_0)\cos\theta}$$

The last expression can easily be integrated by graphical means. When $\lambda_0 = \pi/2$, the minor circle becomes a great circle; and all the results reduce respectively to the corresponding results valid for great circle paths at large angles of inclination.[4] If the gravity term is neglected, C_{12} and C_{14} become 0 and 1,

* Minor terms being neglected in the derivation.

respectively; the above solutions are reduced to much simpler forms. Fig. 1 gives a comparison of present approximate analytical closed form solutions with those obtained from more accurate numerical methods.[5] Fairly good agreements were seen. Similar good agreements were also obtained for deceleration, range, and other items of interest.

References

[1] Eggers, A. J., Allen, H. J., and Neice, S. E., *A Comparative Analysis of the Performance of Long Range Hypervelocity Vehicles*, NACA TN 4046, October, 1957.

[2] Loh, W. H. T., *Minor Circle Flight for Boost-Glide Vehicles*, J. ARS, Vol. 29, No. 4, April, 1959.

[3] Loh, W. H. T., *Minor Circle Flight for Orbital-Launched or Boost-Glide Vehicles*, J. ARS, Vol. 29, No. 10, Part 1, October, 1959.

[4] Loh, W. H. T., *Hypervelocity Glider at Large Angles of Inclination*, J. ARS, Vol. 30, No. 2, February, 1960.

[5] Chapman, D. R., *An Approximate Analytical Method for Studying Entry Into Planetary Atmospheres*, NACA TN 4276, May, 1958.

On the Unsteady Motion of a Delta Wing in Supersonic Flight

M. M. Stanišić
Associate Professor, Division of Engineering Sciences, Purdue University, Lafayette, Ind.

November 16, 1959

Summary

Heaslet, Lomax, and Jones[1] have used the Volterra-Green method in order to formulate the steady motion of a wing in supersonic flight. This paper represents an extension of the work in reference 1 to the unsteady motion of a delta wing in supersonic flight.

(1) Object of Investigation

The problem is to find an acceleration potential for the lifting surface. Much work has been done for the last decade in this field. However, if one has to face the problem of approximate determination of the aerodynamic force on the wings, then the higher-order singularities appearing in a kernel function, as has been obtained in many papers in world literature, impose difficulties which cannot always be surmounted by integration by part. The Volterra-Green method, as was shown in reference 1, is very suitable for the formulation of acceleration potential, since singularities obtained in the kernel function using this method will be of low order. Therefore, the work in reference 1 will be extended to the unsteady case.

(2) Solution for the Acceleration Potential Function

Using the linearized theory, the motion of compressible unsteady flow is governed by the equation

$$(1 - M^2)\phi_{xx} + \phi_{yy} + \phi_{zz} - (1/a^2)(2U\phi_{xt} + \phi_{tt}) = 0 \quad (1)$$

where ϕ is the velocity potential function, $M = U/a$ is the Mach number, U is the velocity of the wing, and a is a local velocity of sound. Eq. (1) is satisfied with the function ϕ or any of its derivatives. We assume that the delta wing is placed in a Mach cone and that the wing is flat and rigid. Hence, the position of the wing at any time is given by

$$z = g(x, y)e^{-i\omega t} \quad (2)$$

where ω is the frequency of the wing and $g(x, y)$ is regular everywhere (see Fig. 1).

The nature of the problem formulated by Eq. (1) implies that: (a) $\phi = 0$ on the aftercone

$$\lambda \equiv x^2 - \beta^2(y^2 + z^2) = 0$$

where $\beta^2 = M^2 - 1$; and (b) if

$$\underline{\Omega} = \underline{\Omega}[0, 0, -i\omega g(x, y)e^{-i\omega t}]$$

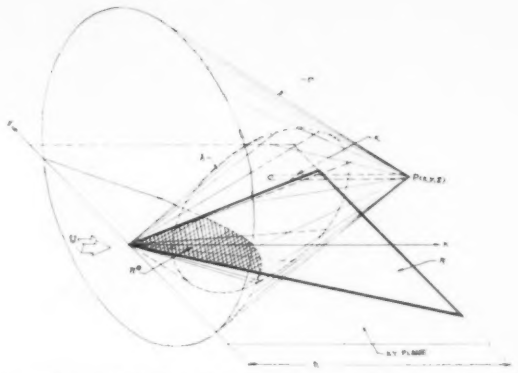

Fig. 1. General view of the geometry of wing plane in cones λ and Γ.

is a velocity of the wing and

$$\bar{C} = \bar{C}(U + u, v, \omega)$$

is velocity of the flow, then[2]

$$w = e^{-i\omega t}[Ug_x(x, y) - i\omega g(x, y)] \quad (3)$$

Using the substitution

$$\phi(x, y, z, t) = \Psi(x, y, z)e^{kx - i\omega t}$$

Eq. (1) leads to

$$(1 - M^2)\Psi_{xx} + \Psi_{yy} + \Psi_{zz} - \Lambda^{*2}\Psi = 0 \quad (4)$$

with

$$k = -[i\omega M/a(1 - M^2)]$$
$$\Lambda^{*2} = \omega^2/a^2(M^2 - 1)$$

Denoting

$$x = X, \quad y = (M^2 - 1)^{-(1/2)}Y, \quad z = (M^2 - 1)^{-(1/2)}Z$$

Eq. (4) becomes

$$L(\Psi) \equiv \Psi_{XX} - \Psi_{YY} - \Psi_{ZZ} + \Lambda^2\Psi = 0 \quad (5)$$

where

$$\Lambda^2 = \omega^2/a^2(M^2 - 1)$$

Now, the Volterra-Green method requires that:

$$\iiint_V \{\sigma L(\Psi) - \Psi L(\sigma)\}\, dV = - \iint_S [\sigma D_{\bar{n}}(\Psi) - \Psi D_{\bar{n}}(\sigma)]df \quad (6)$$

where A is a surface which encloses a volume V.[1, 2, 4] Here, σ is any particular solution of Eq. (5), and $D_{\bar{n}}(\ldots)$ are the modified directional derivatives with respect to the normal on the surface A. However, without loss of generality, we can replace $D_{\bar{n}}(\ldots)$ by $D_\nu(\ldots)$, where $D_\nu(\ldots)$ are modified directional derivatives of the co-normal. Therefore,

$$L(\Psi) = L(\sigma) = 0$$

Then, Eq. (6) reduces to

$$\int_A \int \sigma D_\nu(\Psi)df = \int_A \int \Psi D_\nu(\sigma)df \quad (7)$$

Hence, in order to find Ψ at any point, $P(X, Y, Z)$, from knowledge of the boundary conditions given on the wing surface, we have to choose σ such that

$$\sigma(\Gamma) = 0, \quad (\partial\sigma/\partial\nu)(\Gamma) = 0$$

where Γ is the forecone from point $P(X, Y, Z)$, given by

$$\Gamma \equiv (X - X_1)^2 - \alpha^2 = 0$$

with

$$\alpha^2 = [(Y - Y_1)^2 + (Z - Z_1)^2]$$

Otherwise, the solution cannot be obtained according to this method. Evidently[3]

$$\sigma = \int_0 \cos\,(\Lambda\alpha \sinh\theta)d\theta \qquad \cosh^{-1}[(X - X_1)/\alpha] \tag{8}$$

satisfies conditions for σ on the forecone Γ. However,

$$\Psi(\lambda) = 0;\ (\partial\Psi/\partial\nu)(\lambda) = 0$$
$$\sigma(\Gamma) = 0;\ (\partial\sigma/\partial\nu)(\Gamma) = 0$$

Therefore, the surfaces λ and Γ are excluded from consideration. Evidently, σ possesses a singularity along the axis of a small cylinder K, going from point $P(X, Y, Z)$, parallel to the wing plane. Hence, Eq. (7) can be written as

$$\lim_{\alpha\to 0}\int_K\int [\Psi(\partial\sigma/\partial\nu) - \sigma(\partial\Psi/\partial\nu)]dS + \int_{\pi_\pm{}^*}\int [\Psi(\partial\sigma/\partial\nu) - \sigma(\partial\Psi/\partial\nu)]df = 0 \tag{9}$$

where $ds = 2\pi\alpha\, dX_1$. From Eq. (9) it follows that

$$\lim_{\alpha\to 0}\int_K\int [\Psi(\partial\sigma/\partial\nu) - \sigma(\partial\Psi/\partial\nu)]df = 2\pi \lim_{\alpha\to 0}\int_X^{X_\lambda} \Psi[(\partial\sigma/\partial\nu)(K)]\ \alpha dX_1 \tag{10}$$

However,

$$(\partial\sigma/\partial\nu)(K) = -\Lambda\int_0 \sinh\theta\,\sin(\Lambda\alpha\sinh\theta)d\theta - \frac{(X - X_1)\cos\,[\Lambda\sqrt{(X - X_1)^2 - \alpha^2}]}{\alpha\sqrt{(X - X_1)^2 - \alpha^2}} \qquad \cosh^{-1}[(X - X_1)/\alpha] \tag{11}$$

If $\Lambda = 0$, Eq. (11) is reduced to the equation of steady flow [1]. Therefore, Eqs. (9)–(11) lead to

$$\int_{X_\lambda}^{X}\Psi(X_1, Y, Z)dX_1 = -(1/2\pi)\int_{\pi_\pm{}^*}\int [\Psi(\partial\sigma/\partial\nu) - \sigma(\partial\Psi/\partial\nu)]df \tag{12}$$

Denoting with (′) prime the physical quantities corresponding to the surface $\pi_-{}^*$,

$$\left.\begin{aligned}\sigma = \sigma',\quad \Psi = -\Psi'\\ \partial\sigma/\partial\nu = -(\partial\sigma'/\partial\nu'),\quad \partial\Psi/\partial\nu = -(\partial\Psi'/\partial\nu')\end{aligned}\right\} \tag{13}$$

Hence, differentiating Eq. (12) with respect to X and taking into account Eq. (13), one obtains

$$\Psi(X, Y, Z) = -(1/\pi)\int_{\pi_+{}^*}\int \Psi(X_1, Y_1, 0)(\partial\sigma/\partial\nu)df \tag{14}$$

Moreover,

$$\partial\sigma/\partial\nu = \lim_{Z_1\to 0}(\partial\sigma/\partial Z_1) \tag{15}$$

However, from Eq. (8) it follows that

$$(\partial\sigma/\partial\nu)(\pi_+{}^*) = (Z\Lambda/\alpha)\int_0^{\cosh^{-1}[(X-X_1)/\alpha]} \sinh\theta\,\sin(\Lambda\alpha\sinh\theta)d\theta + \frac{(X - X_1)Z\cos\,[\Lambda\sqrt{(X - X_1)^2 - \alpha^2}]}{\alpha^2\sqrt{(X - X_1)^2 - \alpha^2}} \tag{16}$$

Denoting

$$\Psi(X, Y, Z) = \chi(X, Y, Z)e^{i\omega t}$$

where χ is the acceleration potential and referring to the transformation used previously, one obtains

$$\chi_{(x,\ y,\ z,\ t)} = -(e^{-i\omega t}/\pi)(\partial/\partial x)\times\int_{\pi_+{}^*}\int A(x,\ y,\ 0)K_{x,\ y,\ z;\ x_1,\ y_1,\ 0})dx_1dy_1 \tag{17}$$

where

$$A(x_1, y_1, 0) \equiv \Psi(x_1, y_1, 0)$$

is a source function for three-dimensional unsteady flow and

$$K(x, y, z; x_1, y_1, 0) = (\partial\sigma/\partial\nu)(\pi_+{}^*)$$

is the kernel function. Therefore, the acceleration potential around the delta wing, the objective of this investigation, is formulated.

References

[1] Heaslet, A. M., Lomax, H., and Jones, A. L., *Volterra's Solution of the Wave Equation as Applied to the Three-Dimensional Supersonic Airfoil Problems*, NACA TN 1412, September, 1947.

[2] Stanišić, M. M., *A Remark Concerning the Vibration of a Delta Wing in Supersonic Flight*, Journal of the Aero/Space Sciences, Readers' Forum, Vol. 26, No. 10, October, 1959.

[3] Stanišić, M. M., *On the Oscillation of a Delta Wing in Supersonic Flow*, Doctoral Thesis, submitted to Department of Mathematics, Illinois Institute of Technology, publication of Illinois Institute of Technology, Vol. 7, p. 11, December, 1958.

[4] Stanišić, M. M., *On the Acceleration Potential for the Unsteady Motion of the Compressible Flow Around a Delta Wing in Supersonic Flight*, to be published in Bulletin of Polytechnic Institute of "Jassy," R. P. Roumania.

IAS Twenty-Ninth Annual Meeting

Hotel Astor, New York City, January 23–25, 1961

The scope of the meeting will be broad to cover the many interests of IAS members. The Meetings Committee invites papers to be submitted in any of the scientific fields relating to aeronautics and space.

Members or organizations wishing to have papers considered for presentation at this meeting should submit outlines or summaries to the Meetings Committee, 2 East 64th St., New York 21, N.Y., no later than August 1, 1959.

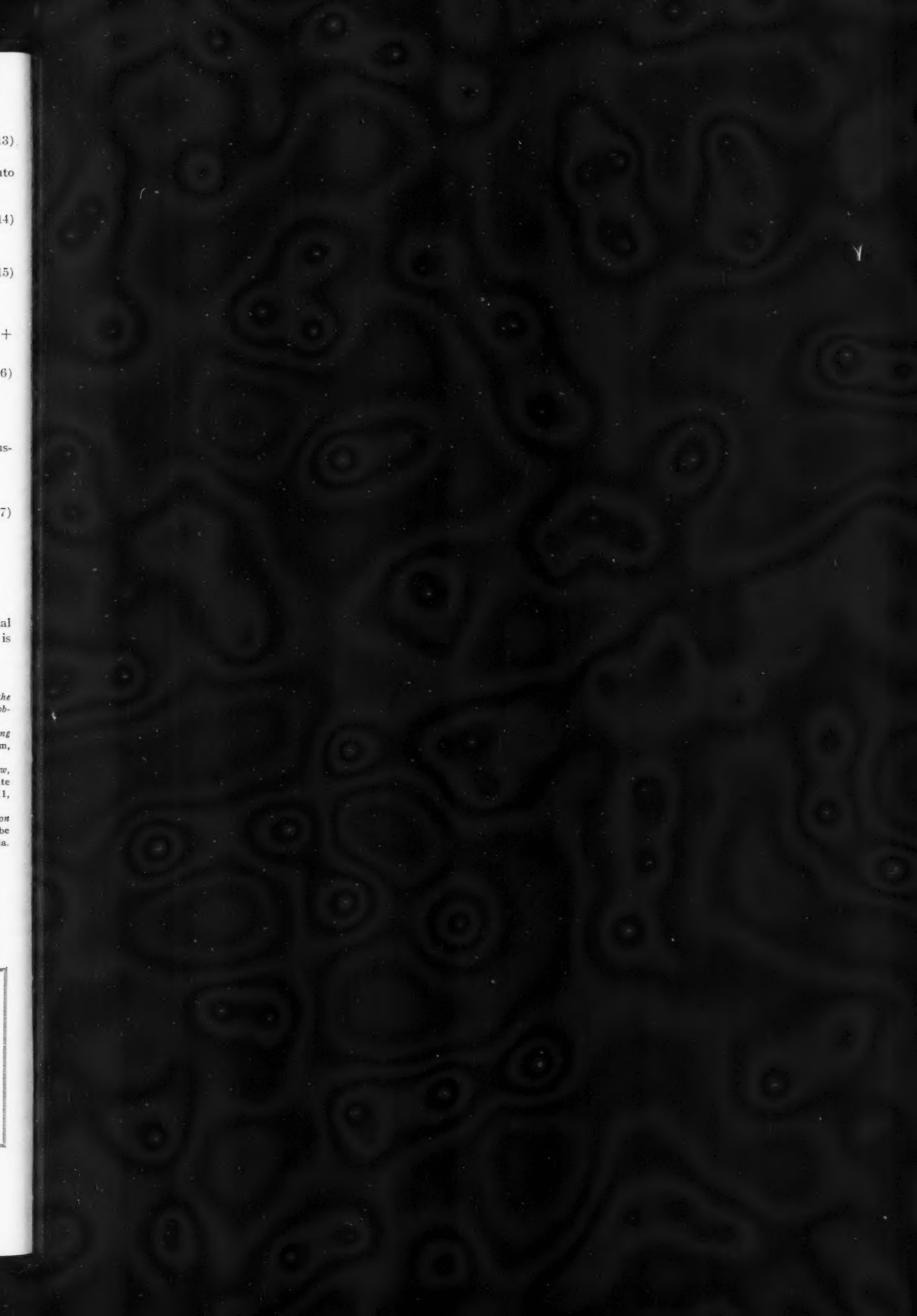

REQUIREMENTS *for* CONTRIBUTIONS

to the publications of the

INSTITUTE *of the* AERONAUTICAL SCIENCES

The Institute of the Aeronautical Sciences invites both members and nonmembers from any country to submit papers for publication in the JOURNAL OF THE AERO/SPACE SCIENCES and AERO/SPACE ENGINEERING. The Institute, following the practice of other societies, does not pay for contributions.

The following directions for the preparation of papers, if followed by authors, will save correspondence, avoid the return of papers for changes, minimize the work of preparation for the printer, and save the expense due to the charges made for "author's corrections."

MANUSCRIPTS: The original typewritten copy of the paper is desired. **To expedite review, an additional copy of both the manuscript and figures should be submitted.** The manuscript must be double or triple spaced on one side of white paper sheets, consecutively numbered. There should be wide margins to allow for the marking of directions to the printer. Correcting, changing, or adding to papers after they are in type is costly. It is, therefore, imperative that papers submitted be in final form. Typographical errors may be corrected on proofs, but if authors wish to add material, they may do so at their own expense. In mailing, drawings may be rolled, but manuscripts should be sent flat. Send by first-class mail (register if you wish for your own protection) to the Editorial Office, Institute of the Aeronautical Sciences, 2 East 64th Street, New York 21, N.Y. All manuscripts will be examined by the Editorial Committee and by the Editor. Authors will be advised as promptly as possible whether the paper is acceptable for publication.

TITLES: The title of the paper should be brief. The name and initials of the author should be written as he prefers. The use of the full name of an author is advocated because of the frequent duplication of initials and surnames which sometimes makes it difficult to establish the identity of the author. This is particularly important for large annual indexing and abstracting services. All titles and degrees or honors are omitted. The name of the organization with which the author is associated should be placed after his name on a separate line. The date on which the paper is received will be inserted by the Editor. The author's title or position should be indicated in a footnote.

SUMMARIES OR ABSTRACTS: An abstract to be printed at the beginning should accompany each article. It should be adequate as an *index* and as a *summary*. It should contain a statement of major conclusions reached, since summaries in many cases constitute the only source of information used in compiling scientific reference indexes. Abstracts printed in other journals, especially foreign, in most cases consist of summaries from printed papers. The summary should explain as adequately as possible the major conclusions to a nonspecialist in the subject and should contain from 100 to 300 words, depending on the length of the paper.

SUBHEADINGS: Subheadings should be inserted by the author at frequent intervals. The work of editorial preparation will be simplified by the author's provision of many subheadings.

MATTER USUALLY DELETED: Photographs or illustrations of little technical interest and not showing advances in general practice. Too detailed tabular matter (general results of such tables may be included in the text). Lengthy descriptions of materials or processes or of preliminary experiments or theories that preceded final results; salient features only are of interest.

REFERENCES: References should be numbered consecutively and grouped together at the end of the manuscript, with only the corresponding number being mentioned in the text. The arrangement should be as follows. For books: [1] Durand, W. F., *Aerodynamic Theory*, 1st Ed., Vol. 1, p. 23; Julius Springer, Berlin, 1934. For magazines: [1] England, C. R., Crawford, A. B., and Mumford, W. W., *Some Results of a Study of Ultra-Short-Wave Transmission Phenomenon*, Proc. IRE, Vol. 20, No. 12, pp. 481–482, March, 1933. Please give author, title, edition, volume, number, page, publisher, and place and date of publication as indicated. Omission of one required fact causes much extra editorial work and possible inaccuracies.

ILLUSTRATIONS: Illustrations should accompany manuscripts, and each should always be referred to in the text by number. Drawings or graphs should not be larger than 12 × 16 inches, and must be made with jet black India ink on white paper or tracing cloth, the latter being preferred. *Do not use typewriter for lettering.* The smallest lettering on 8 × 10 inch figures should be no less than $^1/_4$ inch high. Cross-section paper (white with black lines) may be used, but it should not have more than 4 lines per inch. If finer ruled paper is used, the major division lines should be drawn in with black ink, omitting the finer divisions. In the case of finely ruled paper, only blue-lined paper can be accepted. *Tracing paper and blueprints* are not acceptable. Lettering and all markings must be large enough to be readable after reduction to single-column width ($3^1/_{16}$ in.). Mail rolled or flat; never fold. Drawings that cannot be reproduced (including pencil drawings) will be returned to the author for redrawing, thus delaying publication of the paper. Photographs should be distinct and show clear black and white contrasts. They must be on glossy white paper. Avoid round or oval photographs.

CAPTIONS AND LEGENDS: Legends or captions must accompany each drawing or photograph submitted. If written on the drawing or photograph, they should be placed below and well outside the part to be reproduced. Each table should have a caption such as Table 1, Table 2, Table 3, etc. Captions should be complete in themselves so as to make the data intelligible to the reader without reference to the text. A duplicate list of captions for figures should be included as the last page of the manuscript. Use "Fig. 1" (not Figure 1), "Figs. 3 and 4," etc., in both the text and the numbering of illustrations. In the text, "Eq. (1)" or "Eqs. (1) and (2)" is used, not "Equation (1)." In captions, legends, and in table headings, write all words in full; do not abbreviate, except for "Fig." and "Eq."

MATHEMATICAL WORK: Formulas may be typewritten or carefully written in pen and ink, the writing to be large enough so that it can be marked for the printer. Considerable space for marking should be allowed above and below all equations. All complicated equations should be repeated on separate sheets with plenty of space left for marking. The solidus should be used for simple fractions appearing within the text. Make all expressions clear to the typesetter. Greek letters used in formulas should be clearly designated by name in the margin of the manuscript. The difference between capital and lower-case letters should be clearly distinguished and care taken to avoid confusion between zero (0) and the letter (o), between the numeral (one) and the letter (ell) and the prime (′), between alpha and a, kappa and k, u and mu, v and nu, n and eta. All subscripts and exponents should be clearly distinguished. Avoid complicated exponents and subscripts. Dots and bars over letters or mathematical expressions should also be avoided. When it is necessary to repeat a complicated expression, it should be represented by some convenient symbol.

SYMBOLS AND ABBREVIATIONS: The symbols recommended in the American Standard Association "Letter Symbols for Aeronautical Sciences," ASA Y10.7—1954, should be used wherever practicable. All symbols should be clearly written and carefully checked. Standard abbreviations should be used, and it should be noted that most abbreviations are lower case, such as m.p.h., b.m.e.p., i.h.p. b.hp., hp., etc.

Corporate Members

of the

Institute of the Aeronautical Sciences

AC SPARK PLUG DIVISION, GENERAL MOTORS CORPORATION

ACADEMY OF AERONAUTICS

AEROJET-GENERAL CORPORATION

AEROLAB DEVELOPMENT COMPANY

AERONCA MANUFACTURING CORPORATION

AERONUTRONIC SYSTEMS, INC.

AEROQUIP CORPORATION

AGAWAM AIRCRAFT PRODUCTS, INC.

ALLIED RESEARCH ASSOCIATES, INC.

ALLISON DIVISION, GENERAL MOTORS CORPORATION

ALUMINUM COMPANY OF AMERICA

AMERICAN AIRLINES, INC.

AMERICAN BOSCH ARMA CORPORATION

AMERICAN STEEL & WIRE DIVISION, UNITED STATES STEEL CORPORATION

AMOCO CHEMICALS CORPORATION

AMPHENOL-BORG ELECTRONICS CORPORATION

ANDERSON, GREENWOOD & CO.

ARDE ASSOCIATES

ASSOCIATED AVIATION UNDERWRITERS

AUTOMATION INDUSTRIES, INCORPORATED

AVCO RESEARCH LABORATORY

AVIEN, INC.

BEECH AIRCRAFT CORPORATION

BELL AIRCRAFT CORPORATION

BENDIX AVIATION CORPORATION

BOEING AIRPLANE COMPANY

BOOZ, ALLEN & HAMILTON

BULOVA RESEARCH AND DEVELOPMENT LABORATORIES, INC.

CANADAIR, LTD.

THE CESSNA AIRCRAFT COMPANY

CHANCE VOUGHT AIRCRAFT, INCORPORATED

THE CHASE MANHATTAN BANK

CHICAGO AERIAL INDUSTRIES, INC.

THE CLEVELAND PNEUMATIC INDUSTRIES, INC.

CONTINENTAL MOTORS CORPORATION

CORNELL AERONAUTICAL LABORATORY, INC.

CURTISS-WRIGHT CORPORATION

DANIEL, MANN, JOHNSON, & MENDENHALL

THE DECKER CORPORATION

DEL MAR ENGINEERING LABORATORIES

DELCO-REMY DIVISION, GENERAL MOTORS CORPORATION

DOAK AIRCRAFT COMPANY, INC

DOUGLAS AIRCRAFT COMPANY, INC.

DZUS FASTENER COMPANY, INC

EASTERN AIR LINES, INC.

EATON MANUFACTURING COMPANY

EDO CORPORATION

ELASTIC STOP NUT CORPORATION OF AMERICA

ENGINEERING SUPERVISION COMPANY

FAIRCHILD CAMERA AND INSTRUMENT CORPORATION

FAIRCHILD ENGINE AND AIRPLANE CORPORATION

THE GARRETT CORPORATION

GENERAL APPLIED SCIENCE LABORATORIES, INC.

GENERAL DYNAMICS CORPORATION

GENERAL ELECTRIC COMPANY

GENERAL PRECISION EQUIPMENT CORPORATION

G. M. GIANNINI & CO., INC.

GIANNINI PLASMADYNE CORPORATION

THE B. F. GOODRICH COMPANY

GOODYEAR AIRCRAFT CORPORATION

GRUMMAN AIRCRAFT ENGINEERING CORPORATION

HYDRO-AIRE, CO.

INSURANCE COMPANY OF NORTH AMERICA COMPANIES

INTERNATIONAL BUSINESS MACHINES CORPORATION

THE INTERNATIONAL NICKEL COMPANY, INC.

ITT LABORATORIES, DIVISION OF INTERNATIONAL TELEPHONE AND TELEGRAPH CORPORATION

JANITROL AIRCRAFT, A DIVISION OF MIDLAND-ROSS CORPORATION

JOHNS-MANVILLE SALES CORPORATION

WALTER KIDDE & COMPANY, INC.

KOLLSMAN INSTRUMENT CORPORATION

LAVELLE AIRCRAFT CORPORATION

LEAR, INCORPORATED

C. W. LEMMERMAN, INC.

LIBRASCOPE DIVISION OF GENERAL PRECISION, INC

THE LIQUIDOMETER CORPORATION

LOCKHEED AIRCRAFT CORPORATION

LOEWY-HYDROPRESS DIVISION OF BALDWIN-LIMA-HAMILTON CORPORATION

THE MARQUARDT CORPORATION

THE MARTIN COMPANY

McDONNELL AIRCRAFT CORPORATION

MELPAR, INC.

MELPAR, INC.

MINNEAPOLIS-HONEYWELL REGULATOR COMPANY

NATIONAL CREDIT OFFICE, INC.

NORTH AMERICAN AVIATION, INC.

NORTHROP CORPORATION

NUCLEAR DEVELOPMENT CORPORATION OF AMERICA

PAN AMERICAN WORLD AIRWAYS, INC.

THE RALPH M. PARSONS COMPANY

PESCO PRODUCTS DIVISION, BORG-WARNER CORPORATION

PHILLIPS PETROLEUM COMPANY

PIASECKI AIRCRAFT CORPORATION

RADIO CORPORATION OF AMERICA
ASTRO-ELECTRONIC PRODUCTS DIVISION
DEFENSE ELECTRONIC PRODUCTS

RAMO-WOOLDRIDGE DIVISION, THOMPSON RAMO WOOLDRIDGE INC.

REPUBLIC AVIATION CORPORATION

ROHR AIRCRAFT CORPORATION

PAUL ROSENBERG ASSOCIATES

RYAN AERONAUTICAL COMPANY

SANDBERG-SERRELL CORPORATION

SHAFER BEARING DIVISION, CHAIN BELT COMPANY

SHELL OIL COMPANY

SIMMONDS PRECISION PRODUCTS, INC.

SOCONY MOBIL OIL COMPANY, INC.

SOLAR AIRCRAFT COMPANY

SOUTHWEST PRODUCTS CO.

SPACE TECHNOLOGY LABORATORIES, INC.

R. DIXON SPEAS ASSOCIATES

SPERRY GYROSCOPE COMPANY DIVISION OF SPERRY RAND CORPORATION

STANDARD OIL COMPANY OF CALIFORNIA

STANDARD OIL COMPANY (INDIANA)

STANDARD-THOMSON CORPORATION
CLIFFORD MANUFACTURING DIVISION

STANLEY AVIATION CORPORATION

THIOKOL CHEMICAL CORPORATION

THOMPSON RAMO WOOLDRIDGE INC.

TRANS WORLD AIRLINES, INC.

TURBO PRODUCTS, INC.

UNION CARBIDE CORPORATION

UNITED AIR LINES, INC.

UNITED AIRCRAFT CORPORATION

UNITED STATES AVIATION UNDERWRITERS, INC.

VERTOL AIRCRAFT CORPORATION

VITRO CORPORATION OF AMERICA

WESTERN GEAR CORPORATION

WESTINGHOUSE ELECTRIC CORPORATION

WYMAN-GORDON COMPANY

YOUNG RADIATOR COMPANY